Université de Liège - Faculté de médecine

Département des sciences biomédicales et précliniques

Identification of myoferlin as a component of mitochondria-associated membranes and discovery of a new function in calcium transfer in PDAC cell lines

Sandy Anania

GIGA-Cancer – Metastases Research Laboratory

Sart-Tilman

Liège, Belgique

Année académique 2021-2022

Thesis submitted for the obtention of the degree of Doctor of Philosophy in Biomedical and Pharmaceutical Sciences

Jury Members :

Christine Gilles (Présidente), Maître de recherche FNRS – Université de Liège

Michael Herfs (Secrétaire), Chercheur qualifié FNRS – Université de Liège

Jennifer Rieusset (Membre externe), Directrice de recherche – Université Claude Bernard Lyon 1

Thierry Arnould (Membre externe), Professeur ordinaire – Université de Namur

Pascal De Tullio (Membre interne), Directeur de recherche FNRS – Université de Liège

Nor Eddine Sounni (Membre interne), Maître de recherche FNRS – Université de Liège

Olivier Peulen (Promoteur), Chargé de cours – Université de Liège

Vincenzo Castronovo (Co-promoteur), Professeur ordinaire – Université de Liège

Abstract

Pancreatic cancer is one of the deadliest cancers, with a five-year survival rate being less than 9%. This low survival rate is explained by the late diagnosis and the inefficient treatments. Therefore, developing new therapeutic strategies is needed to improve the survival of patients with pancreatic cancer. In this context, targeting cancer cell metabolism has been proposed as a promising approach, since cancer cells adapt their metabolism to face challenging environmental conditions and to fit their needs for proliferation. Many proteins have been proposed as therapeutic targets, where their targeting enables to create a metabolic imbalance, sensitizing cancer cells to other therapeutics treatments. One of these proteins, named myoferlin, is overexpressed in pancreatic cancer, where it influences cell metabolism. Indeed, myoferlin silencing in pancreatic cancer cells impairs lysosomes integrity, endosomal trafficking and also decreases mitochondrial respiration, which is associated with a fragmented network. Since mitochondria have been reported as key actors for proliferation, relapse and resistance to chemotherapy, we aimed at investigating the role of myoferlin in mitochondrial metabolism and dynamics. We first hypothesized that myoferlin was directly involved in mitochondrial dynamics and metabolism by being present on this organelle and by interacting with proteins involved in mitochondrial dynamics. Interestingly, we found that myoferlin is interacting with MFNs, proteins involved in mitochondrial fusion. However, our results suggested that myoferlin is unlikely located on mitochondria but is rather located in the membranes associated with this organelle. Due to its peculiar structure and reported function in the cell, we investigated a potential function for myoferlin in calcium transfer between endoplasmic reticulum and mitochondria. Our results showed that myoferlin silencing significantly reduces the mitochondrial calcium level upon stimulation, probably through its interaction with IP3R3. This discovery improves our comprehension of myoferlin function in cancer biology and could be extended to other myoferlin functions in a non-cancer context.

Remerciements

Je voudrais tout d'abord remercier le Professeur Vincent Castronovo pour m'avoir permis de réaliser ma thèse au sein de son laboratoire. Merci d'avoir toujours cru en moi.

Je tenais évidement à remercier mon promoteur, le Professeur Olivier Peulen, pour m'avoir conseillée durant ma thèse.

Je voudrais ensuite remercier le Docteur Akeila Bellahcène. Merci pour vos nombreux conseils lors de nos nombreuses réunions du lundi.

Je ne peux pas clôturer ces quatre années de thèse sans dire merci aux membres de mon laboratoire. Shihui, tu m'as beaucoup aidée durant ces quelques mois au LRM et j'espère que tout se passe pour le mieux en ce moment pour toi. Raphaël et Yasmine, votre optimisme inégalable me surprendra toujours. Je vous souhaite le meilleur pour vos dernières années de thèse.

Ensuite, je voudrais remercier la MG team pour tous les beaux moments que l'on a passés ensemble : Assia, tu as été un vrai pilier pour moi, ma grande sœur de galère. Jordan, même si tu n'es là que depuis récemment, j'ai apprécié nos conversations et j'espère vraiment que ta thèse pourra aboutir. Victoria et Fanny, je suis très heureuse de voir à quel point vous vous êtes adaptées aux exigences du laboratoire et je suis certaine que ça se passera très bien pour vous dans les prochaines années. Je voudrais aussi remercier Naïma et Ferman pour leur présence, le LRM sans vous n'est pas le LRM. Merci aussi à Véronique pour la logistique au laboratoire.

Ensuite, je voudrais remercier toutes les autres personnes qui se sont investies dans ma thèse. Je voudrais tout d'abord remercier le Professeur Marc Thiry pour avoir relu une partie de ma thèse et m'avoir fait évoluer sur le fond et les idées. Sans vous, ce travail ne serait pas aussi abouti. Je voudrais aussi remercier le Docteur Di Valentin pour avoir pris le temps de m'expliquer certains concepts relatifs aux plasmides. Merci aussi au Docteur Arnaud Blomme pour nos conversations mais aussi pour m'avoir aidée dans ce travail, notamment en acceptant de me donner des microlitres précieux d'anticorps. Je voudrais ensuite remercier le Docteur Stéphanie Herkenne. Grâce à notre conversation, tu m'as aidée à débloquer mon projet et à le faire avancer. Tu m'as guidée sur les points clés à aborder. Je voudrais aussi remercier le Docteur Yelena Sargsyan pour m'avoir fourni son protocole sur les flux calciques.

De plus, je tenais à remercier mes amis et ma famille pour leur soutien. Je voulais d'abord remercier mes jumeaux de thèse, Romain et Olivier. Merci d'avoir été là pour moi. Vous avez sans aucun doute contribué à l'aboutissement de ce travail. Meghan et Sébastien, je ne peux pas ne pas vous remercier pour votre soutien durant ma thèse. Merci d'avoir été là pour moi dans les moments difficiles de ma vie. Sushi, sans toi, cette thèse n'aurait jamais abouti, tu as toujours été là pour moi, tu m'as aidée à me relever et tu m'as encouragée à aller au bout des choses. Évidemment, je remercie aussi Sacha et je n'oublierai jamais notre séance de tournage au CHU, quelle expérience ! Elif et Malika, nous avons fait nos études ensemble et j'ai vu nos chemins diverger après le master. Vous êtes vraiment une source d'inspiration pour moi. Maintenant, je suis prête à explorer d'autres facettes amusantes de la recherche après ma thèse, et ça c'est en partie grâce à vous. Elizabeth, merci d'avoir été là pour moi durant cette thèse. Je suis contente de voir que tu es prête à passer aussi par là. Je serai là pour toi durant ta thèse, tu peux compter sur moi si tu as besoin d'aide.

Ensuite, je voudrais remercier le Docteur Martin Farnir qui a été un ami, un confident, un collaborateur mais surtout mon compagnon. Que serait ce travail sans toi ? Je me suis souvent posée la question. Tu as été là pour moi dans les moments difficiles, tu m'as toujours écoutée et soutenue et tu m'as encouragée à aller jusqu'au bout. Mais au-delà de cette écoute et de tous les beaux moments passés ensemble, tu as activement participé à ce travail, je n'oublierai jamais toutes nos soirées à travailler et à réfléchir à mon projet. J'espère que notre collaboration continuera encore longtemps.

Je voudrais aussi remercier ma famille car, sans eux, je n'aurais jamais pu réaliser une thèse. Maman, merci pour tout ce que tu as fait pour nous, j'espère que tu es fière de nous de là-haut. Merci aussi à mon Papa et Nadine, pour m'avoir soutenue sur tous les plans durant ma thèse. Je suis heureuse d'avoir une famille comme vous.

Je voudrais finalement remercier les membres de mon jury qui ont accepté de lire et d'évaluer ce travail. Je suis très honorée de pouvoir le partager et en discuter avec vous. Je tenais aussi à remercier les membres de mon comité de thèse pour tous leurs conseils qui ont contribué à l'amélioration de ce travail.

Je tenais aussi à remercier le FNRS, le CIRM ainsi que la fondation Léon Fredericq pour avoir accepté de me financer durant ces quatre ans.

Content

Content ix
1. Introduction 3
1.1. Structure and functional role of the pancreas 3
1.2. Pancreatic Cancer 6
1.2.1. Etiology and risk factors of pancreatic cancer 8
1.2.2. Development of PDAC 9
1.2.3. Diagnosis, staging and treatment of PDAC 11
1.2.4. Overview of PDAC metabolism 15
1.3. Mitochondria-associated membranes 19
1.3.1. Mitochondrial structure and metabolism 20
1.3.2. Structure and function of the endoplasmic reticulum 23
1.3.3. Structure and composition of MAMs 24
1.3.4. Technical approaches to investigate MAMs 27
1.3.5. Role of MAMs in cellular functions 29
1.3.6. Implication of MAMs in diseases 46
1.4. Myoferlin 50
1.4.1. Myoferlin, a member of the ferlin family 51
1.4.2. Transcriptional regulation and alternative splicing of myoferlin 52
1.4.3. Structure of ferlins 53
1.4.4. Calcium, C2 domains and interaction with phospholipids 54
1.4.5. Myoferlin's functions in a non-cancer context 56
1.4.6. Myoferlin in cancer 59
1.4.7. Subcellular localizations of myoferlin 65
2. Aim of the project 69
3. Material and methods 73
3.1. Cells and chemicals 73
3.2. Cell culture 76
3.3. Small interfering RNA transfection 76
3.4. Plasmid preparation and transfection 77
3.5. Western blotting 78
3.6. Immunofluorescence 79
3.7. Colocalization studies 79
3.8. Proximity ligation assay 81
3.9. Co-immunoprecipitation 82

3.10. Mitochondrial enrichment using Qiagen kit 82
3.11. Subcellular fractionation using percoll gradient 83
3.12. Ultrastructural analysis 84
3.13. Oxygen consumption rate analysis 85
3.14. Calcium flow 85
3.15. WST1 assay 86
3.16. Indirect fluorescence resonance energy transfer 86
3.17. Statistical analysis 86
4. Results 91
4.1. Part I: myoferlin interacts with proteins involved in mitochondrial fusion in PDAC cell lines 91
4.1.1. Endogenous myoferlin is present in mitochondrial crude extract and colocalizes partly with mitochondria 92
4.1.2. Endogenous myoferlin is in proximity with mitochondrial fusion machinery in pancreas cancer cell lines 95
4.1.3. Myoferlin interacts with mitofusins in pancreas cancer cells 101
4.1.4. Myoferlin colocalizes but does not interact with mitofusins in normal cells 102
4.1.5. Part I: limitations of the study 104
4.1.6. Part I: conclusions and discussion 105
4.2. Part II: myoferlin is located in MAMs, where it plays a role in calcium transfer and interacts with IP3R3 109
4.2.1. Myoferlin is unlikely to be located on mitochondria of PDAC cell lines 109
4.2.2. Myoferlin is found in MAMs of PDAC cell lines 115
4.2.3. Myoferlin silencing impacts mitochondrial Ca^{2+} level upon histamine stimulation 117
4.2.4. Myoferlin silencing does not impair ER integrity 121
4.2.5. Myoferlin silencing does not impact abundance of MAMs proteins related to Ca^{2+} signaling 123
4.2.6. Myoferlin silencing has no impact on ER-Mitochondrial contact sites 124
4.2.7. Myoferlin interacts with IP3R3, a protein involved in Ca^{2+} signaling in MAMs 133
4.2.8. The overall survival of patients with PDAC is correlated with *ITPR3* expression 141
4.2.9. Myoferlin expression is significantly correlated to *ITPR3* expression in pancreatic cancer but not in normal pancreas. 142
4.2.10. Investigation of myoferlin silencing on mitochondrial metabolism 144
4.2.11. Part II: limitations of the study 147
4.2.12. Part II: conclusions and discussion 148
5. General conclusion and discussion 153
5.1. Myoferlin localization with respect to mitochondria 153

5.2. Myoferlin silencing and calcium transfer at MAMs 154
5.3. Myoferlin, calcium transfer and mitochondrial metabolism 156
5.4. Myoferlin and mitochondrial dynamics: from the perspective of MAMs 156
5.5. Considerations about other potential functions for myoferlin in MAMs 158
5.6. Cell metabolic profile: is there a relationship with MAMs? 159
5.7. Extension to other cancers and non-cancer tissues 160
5.8. Contributions of other myoferlin localizations within the cell 160
5.9. Therapeutic perspectives 162
6. References 165
7. Supplemental figures 193
Associated publications 199

List of abbreviations

$[Ca^{2+}]_c$: cytosolic calcium concentration 34
$[Ca^{2+}]_{ER}$: ER calcium concentration 34
$[Ca^{2+}]_{mt}$: mitochondrial calcium concentration 34
ACAT1: acyl-coenzyme-A cholesterol acyl-transferase-1 16
AD: Alzheimer disease 20
ADM: acinar-to-ductal metaplasia 10
AKT: protein kinase B 24
AMPK: AMP-activated protein kinase 37
ANOVA: one-way analysis of variance 86
ANT: adenine nucleotide translocase protein 33
APAF-1: apoptotic protease activating factor-1 33
ATF6: activating transcription factor 6 45
ATGs: autophagy-related proteins 43
ATP: adenosine triphosphate 15
BAK: BCL-2 homologous killer protein 33
BAX: BCL-2 associated-X 33
BCA: bicinchoninic acid 78
BCL-2: B-cell lymphoma-2 33
BCL-XL: B-cell lymphoma-extra-large 33
BIP: binding immunoglobulin protein 44
BOK: BCL-2 related ovarian killer 149
BRCA1: breast cancer type 1 susceptibility protein 1 8
BRCA2: breast cancer type 1 susceptibility protein 2 8
Ca^{2+}: calcium 20
CAFs: cancer-associated fibroblasts 15
CAV1: caveolin-1 42
CDKN2A: cyclin dependent inhibitor 2A 8
CHOP: transcription factor C/EBP-homologous protein 45
CM: crude mitochondrial fraction 83
CMAMs: crude MAMs 83
COX8: cytochrome c oxidase subunit 8 78
CSCs: pancreatic cancer stem cells 18
CYP11A1: cytochrome P450 cholesterol side chain cleavage enzyme 42
$Dist_{ER\text{-}M}$: distance between mitochondria and ER 125
DMEM: Dulbecco's modified Eagle's medium 76
DNM2: dynamin-2 31
DRP1: dynamin-related protein 1 31
EGF: epidermal growth factor 60
EGFR: epidermal growth factor receptor 14
EHD2: Eps15 homology domain 2 56
eIF2α: eukaryotic translation factor-2α 45
EPHA2: the ephrin type-A receptor-2 62
ER: endoplasmic reticulum 16
ERAD: ER-associated degradation pathway 44
ERK-1/2: extracellular regulated kinase-1/2 59
ER-MCSs: ER-mitochondria contact sites 20

ERMICC: ER-mitochondria contact coefficient 125
ETC: electron transport chain 18
$FADH_2$: reduced flavin adenine dinucleotide 37
FAK: focal adhesion kinase 60
FATE-1: fetal and adult testis-expressed transcript protein 26
FBS: fetal bovine serum 76
FBXL2: F-box/LRR-repeat protein 47
FCCP: carbonyl cyanide-p-trifluoromethoxyphenylhydrazone 85
FDA: food and drug administration 14
FER1: fertilization defective-1 protein 51
FER1L3: fer-1-like family member 3 50
FIS1: mitochondrial fission 1 protein 31
FOLFIRINOX: Folinic Acid, Fluorouracil, Irinotecan, Oxaliplatin 12
FRET: fluorescence resonance energy transfer 95
GAPDH: glyceraldehyde-3-phosphate dehydrogenase 73
GLUD1: glutamate dehydrogenase 1 17
GLUT1: glucose transporter 1 16
GOT1: aspartate aminotransferase 1 17
GRP75: 75 kDa glucose-regulated protein 25
GRP78: 78-kDa glucose-regulated protein 73
GTP: guanosine-5'-triphosphate 30
HA: hemagglutinin 73
HER2: human epidermal growth factor receptor-2 13
HK1: hexokinase 1 16
HK2: hexokinase 2 16
HNSCC: head and neck squamous cell carcinoma 59
HPV: human papilloma virus 62
HR: heptad repeats (domain) 30
HSC70: heat shock cognate-71 kDa protein 73
HSP70: heat shock protein-70 44
ICQ: intensity correlation quotient 79
IDH: isocitrate dehydrogenase 21
IGF-1: insulin-like growth factor 1 57
IGF1R: insulin-like growth factor 1 receptor 57
IMM: inner mitochondrial membrane 21
IP3: inositol triphosphate 35
IP3Rs: inositol 1,4,5-triphosphate receptors 24
IPMN: intraductal papillary mucinous neoplasms 9
IRE1: inositol requiring enzyme 1 44
JNK: c-Jun N-terminal kinase 59
KRAS: kirsten rat sarcoma viral oncogene homolog 9
MAMs: mitochondria-associated membranes 19
MAPK: mitogen-activated protein kinase 57
MAVS: anti-viral signaling protein 44
Mcl-1: myeloid cell leukaemia-1 protein 48
MCN: mucinous cystic neoplasms 9
MCTP: multiple C2 domain and transmembrane region proteins 54
MCU: mitochondrial calcium uniporter 36

MDH1: malate dehydrogenase 1 17
MERCS: mitochondria-ER contact sites 20
MET: mesenchymal to epithelial transition 59
MFF: mitochondrial fission factor 31
MFN: mitofusin 30
MICU1: the EF-hand Ca2+-sensing proteins 1 39
MICU2: the EF-hand Ca2+-sensing proteins 2 39
MiD49: mitochondrial dynamics proteins 49 31
MiD51: mitochondrial dynamics proteins 51 31
MKL1/2: megakaryoblastic leukemia 1 and 2 52
MMPs: matrix-metalloproteinases 59
mPTP: mitochondrial permeabilization transition pore 33
mTOR: mammalian target of rapamycin 14
NCLX: Na+/ Ca2+/Li+ exchanger 37
NCX: Na+/ Ca2+ exchanger 34
NFAT: nuclear factor of activated T-cells 52
NLRP3: NLR family pyrin domain containing 3 44
OCR: oxygen consumption rate 37
OMM: outer mitochondrial membrane 21
OPA1: optic atrophy protein 1 30
OR: odds ratio 8
ORAI1: calcium release-activated calcium channel protein 1 35
ORP: oxysterol binding proteins like 40
OXPHOS: oxidative phosphorylation 15
p63: transformation-related protein 63 62
PA: phosphatidic acid 40
PACS-2: phosphofurin acidic cluster sorting protein-2 25
PAF: paraformaldehyde 79
PALB2: partner and localizer of BRCA2 8
PanIN: pancreatic intraepithelial neoplasia 9
PAX: paxillin 60
PC: phosphatidylcholine 40
PCC: Pearson coefficient correlation 79
PD: Parkinson disease 20
PDAC: pancreatic ductal adenocarcinoma 6
PDH: pyruvate dehydrogenase 21
PE: phosphatidylethanolamine 40
PEMT: PE methyl-transferase 40
PERK: PKR-like ER kinase 45
Per_M: mitochondrial perimeter 125
PET: polyethylene terephthalate 60
Pinch-1: particularly interesting new Cys-His protein 1 60
PIP2: phosphatidylinositol 4,5 biphosphate 35
PLA: proximity ligation assay 81
PLC: phospholipase C 35
PM: purified mitochondrial fraction 83
PMAMs: purified MAMs fraction 83
PMCA: plasma membrane Ca2+-ATPase 34

PRSS1: serine protease 1 9
PS: phosphatidylserine 40
PS-1: presenilin-1 49
PS-2: presenilin-2 49
PSD: PS decarboxylase 40
PTEN: phosphatase and tensin homolog 24
PTPIP51: protein tyrosine phosphatase interacting protein 51 26
Pyk2: proline-rich tyrosine kinase 2 27
RAB32: Ras-related protein Rab32 43
ROI: regions of interest 79
ROS: reactive oxygen species 15
RR: relative risk 8
RT: room temperature 78
RTK: receptor tyrosine kinases 50
RyR: ryanodine receptor 35
S1R: Sigma-1 receptor 42
SDS: sodium dodecyl sulfate 78
SERCA: sarcoendoplasmic reticulum calcium-ATPase 26
siRNA: small interfering RNA 76
SMAD4: mothers against decapentaplegic homolog 4 10
SP1: specificity protein 1 73
SRCC: Spearman's rank correlation coefficient 79
SRF: serum response factor 62
STAT3: signal transducer and activator of transcription 3 62
STIM1: stromal interaction molecule-1 35
STX17: SNARE protein syntaxin-17 43
TCA: tricarboxylic acid 16
TEM: transmission electron microscopy 116
TGF: tumor growth factor 60
Tie-2: tyrosine-protein kinase receptor tie-2 59
TOM20: mitochondrial import receptor subunit TOM20 homolog 73
TP53: tumor protein p53 10
TRPCs: transient receptor potential channels 35
TTF: thyroid transcription factor 62
UPR: unfolded protein response 44
VAPB: vesicle-associated membrane protein-associated protein B 26
VDAC1: voltage-dependent anion channel 1 33
VDACs: voltage-dependent anion channels 21
VEGF: vascular endothelial growth factor 59
VEGFR-2: vascular endothelial growth factor receptor-2 59
XBP1: X-box-binding protein-1 45
α-KGDH: alpha-ketoglutarate 21

Introduction

1. Introduction

1.1. Structure and functional role of the pancreas

The pancreas is an organ of the digestive system, handling exocrine and endocrine functions. This organ is located in the upper abdomen, behind the stomach and close to the small intestine. It can be anatomically divided into three parts: the head, the body and the tail (1).

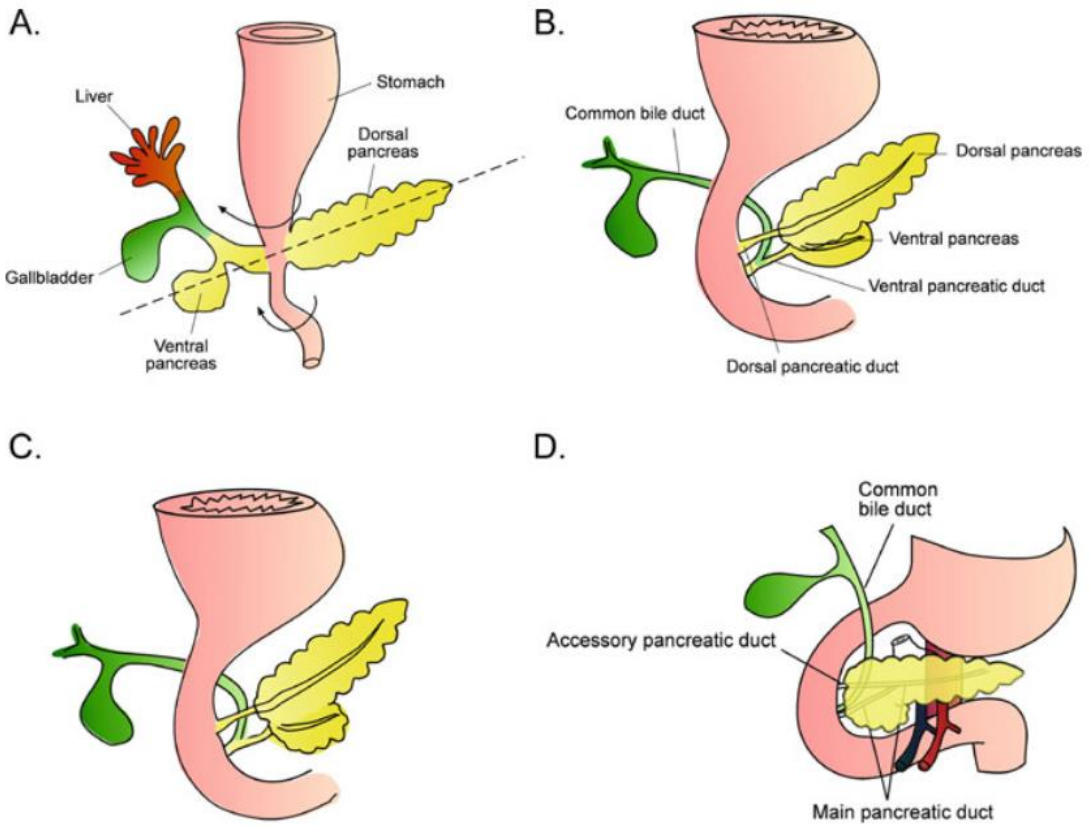

Figure 1-1. Development of the pancreas. (A) The dorsal and ventral pancreatic buds develop in opposite directions from the foregut. During the seventh week of gestation, the stomach and the duodenum rotate. (B-C) As a consequence of the rotation, the ventral bud fuses with the "head" part of the dorsal bud. (D) The ducts from the ventral and dorsal pancreas fuse and give rise to the main pancreatic duct, running the entire length of the pancreas. A part of the dorsal duct does not fuse with the ventral duct, forming the accessory pancreatic duct. The picture is from the publication of Leung *et al.* (2010) (1).

Embryologically, during the fourth week of human gestation, the pancreas begins to develop from two endoderm lined primordial buds of the duodenum (Figure 1-1). On one hand, the dorsal bud extents, forming the pre-head, body and tail of the pancreas. On the other hand, the ventral bud arises next to the hepatic diverticulum and the biliary system. During the seventh gestation week in human, the stomach and the duodenum rotate. Thus, the ventral bud fuses with the "head" part of the dorsal bud, forming the pancreas. In addition, ducts from

the ventral and dorsal pancreas fuse and give rise to the main pancreatic duct, which runs the entire length of the pancreas, from the tail to the head. This duct will allow the secretions from the exocrine pancreas to reach the duodenum, in order to digest food. A part of the dorsal duct does not fuse with the ventral duct, forming the accessory pancreatic duct (also named the duct of Santorini). At later stages, the pancreas will continue to mature through a process of branching morphogenesis (1).

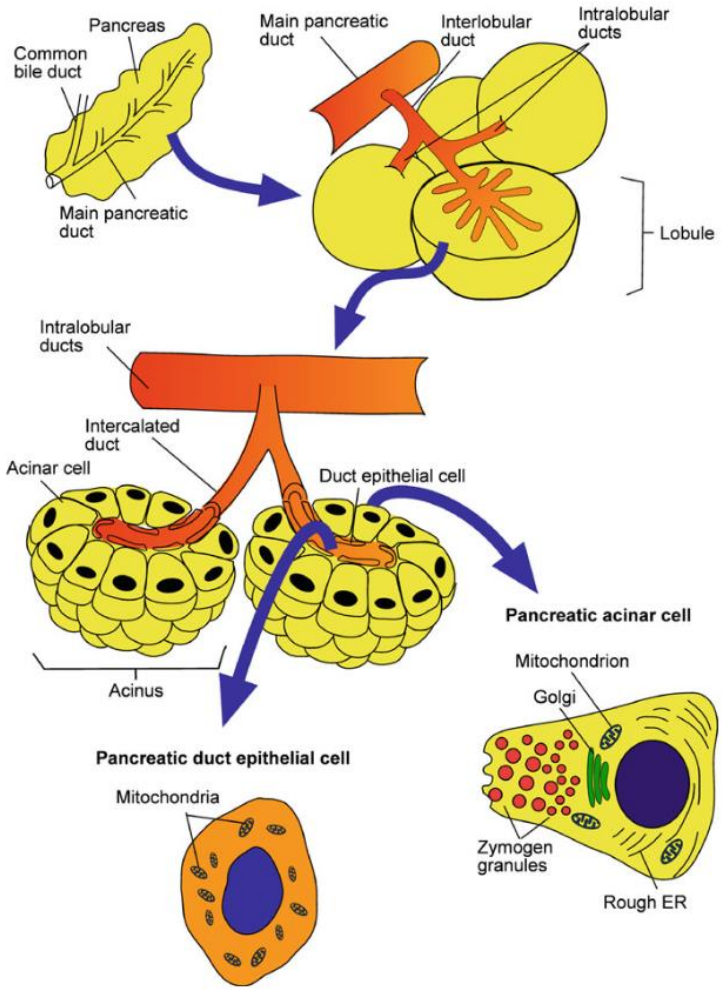

Figure 1-2. Structure of the exocrine pancreas. The lobules are constituted of several acini, being the assembly of acinar cells. Those last ones secrete a pancreatic juice which is conveyed to the main pancreatic duct. From the acinar cells to the main pancreatic duct, the secretions are transported to the intercalated ducts, then to the interlobular ducts and, finally, to the extralobular ducts. Both pancreatic acinar and ductal cell are represented. The picture is from the publication of Leung *et al.* (2010) (1).

In the mature pancreas, 80-85% of the organ's mass is constituted of lobular structures, participating in the secretory function (Figure 1-2). Those lobules are constituted of several acini, themselves being the assembly of acinar cells. They are interconnected by ducts, allowing the secretions to reach the duodenum, through the main pancreatic duct. From the acini to the main duct, the secretions are first conveyed to the intercalated ducts, then to the interlobular

ducts and finally to the extralobular ducts. The place where the main pancreatic duct discharges the secretions to the duodenum is named the major duodenal papilla (or the ampulla of Vater), while the accessory pancreatic duct allows the secretions to reach the duodenum through the accessory papilla (1,2).

Histologically, two main basic elements are observed in the pancreas: the Langerhans islets, involved in the endocrine function of the pancreas, and the secretory cells, representing 80-85% percent of the pancreatic mass and being involved in the secretion of pancreatic juice and enzymes (1). Five varieties of cells can be found in the Langerhans islets (1): (i) the alpha cells that produce the hormone glucagon, which is released when the blood glucose level is low. (ii) The beta cells, which are the dominant cell type in the islets, releasing insulin to lower the level of glucose in blood (insulin favors the uptake of glucose by the peripheral tissues, such as adipose and skeletal muscle tissues, and prevents glucose production by the liver). (iii) The delta cells, that secrete the somatostatin, inhibiting the overproduction of insulin or glucagon. (iv) The PP cells secrete the pancreatic polypeptide hormone, involved in satiety and appetite. (v) And finally, the epsilon cells, responsible of the ghrelin secretion, also involved in appetite, intestinal motility and feeding behaviors (1,3). In accordance with their endocrine functions, the pancreatic islets are highly vascularized, receiving ~ 10-15% of the total pancreatic blood flow (1). Dysfunction of the endocrine pancreas is associated with diseases such as type-2 diabetes. This disease is characterized by an insulin resistance, associated with a reduced capacity of the beta cells to produce insulin. Thus, patients with type-2 diabetes also present high glucose level in blood (4).

Besides its endocrine function, the pancreas has also an exocrine activity involving acinar and ductal cells. On one hand, acinar cells produce four families of enzymes: the glycosidases, the lipases, the nucleases and proteases, able to digest, respectively, carbohydrates, fats, nucleic acids and proteins. Those cells are polarized, with the apical part being directed toward the acinus lumen, and are associated to each other by tight-junctions. In accordance with their secretory function, acinar cells have abundant mitochondria, developed endoplasmic reticulum and Golgi apparatus. In addition, they contain zymogen granules, composed of digestive enzymes under the form of precursors, including trypsinogen, chymotrypsinogen and procarboxypeptidases. In order to hydrate the protein-rich secretions from acinar cells, a juice, composed of NaCl, is produced. Briefly, the Cl^- is driven towards the acinar lumen, followed by

Na^+ flow through the tight junctions. *In fine*, this osmotically draws water to the lumen, creating the pancreatic juice. Once secreted in the duodenum, the trypsinogen is activated by enterokinase, produced by enterocytes. Then, the activated trypsin can activate itself and other enzymes such as chymotrypsinogen and procarboxypeptidases. Thanks to the proenzyme (the precursors), the "autodigestion" of the pancreas is avoided. In patients with mutations such as *PRSS1* mutation, the pancreatic enzymes are overactivated, leading to inflammation of the pancreas, named pancreatitis (1). On the other hand, the exocrine function of the pancreas also involves ductal cells, responsible for the secretion of sodium bicarbonate, which neutralizes the acidic pH of the gastric chyme, in the duodenum. This prevents damages to the duodenum mucosa and provides optimal pH for the activity of pancreatic enzymes. Therefore, dysfunction of ductal cells can lead to ulcers and maldigestion (1).

In the following work, we will discuss of pancreatic cancer, which can arise from the exocrine (for instance, ductal adenocarcinoma) or endocrine (depending on the cell type; insulinoma, glucagonoma, etc…) pancreas. Because the ductal adenocarcinoma is the most frequent type of pancreatic cancer, with low survival, we will mainly focus on this type of pancreatic cancer.

1.2. Pancreatic Cancer

In 2020, according to the Global Cancer Observatory of the World Health Organization (https://gco.iarc.fr/), 495.773 patients have been diagnosed worldwide with pancreatic cancer **(Figure 1-3)**. Furthermore, it is estimated that the five-year survival rate is of ~9%, making it the seventh leading cause of cancer-related death worldwide **(Figure 1-4)** (5,6) (https://gco.iarc.fr/). Incidence and mortality of pancreatic cancer are correlated with increasing age and with gender, men being more prone to develop the disease (7). The etiology is complex and multifactorial but smoking, alcohol consumption, family history, type-2 diabetes and obesity have been associated with a higher risk of developing pancreatic cancer (7). This cancer can be subdivided in two main categories: pancreatic ductal adenocarcinoma (PDAC), which arises from the exocrine part of the pancreas, and which is the most common (90-95% of cases) and aggressive type of pancreatic cancer; and the pancreatic neuroendocrine tumor which arises from the endocrine part of the pancreas and which is less common (6). Most of the time, diagnosis of PDAC occurs at very late stages and metastases have already spread, making the surgery impossible (8). Chemotherapy is therefore proposed to lower the burden

but the benefit is only temporary (8). In this work, we will focus on the pancreatic adenocarcinoma subtype because of its poor prognosis and high frequency.

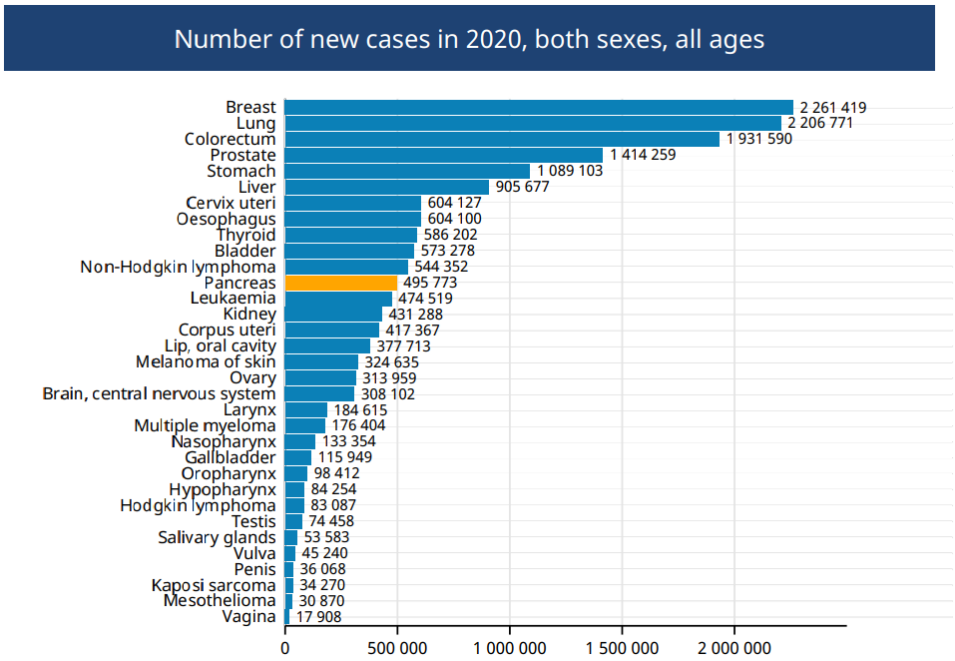

Figure 1-3. Estimated number of new cases in 2020 from various types of cancers worldwide, including both males and females and all ages. The number of new cases for pancreatic cancer is highlighted in yellow. (https://gco.iarc.fr/).

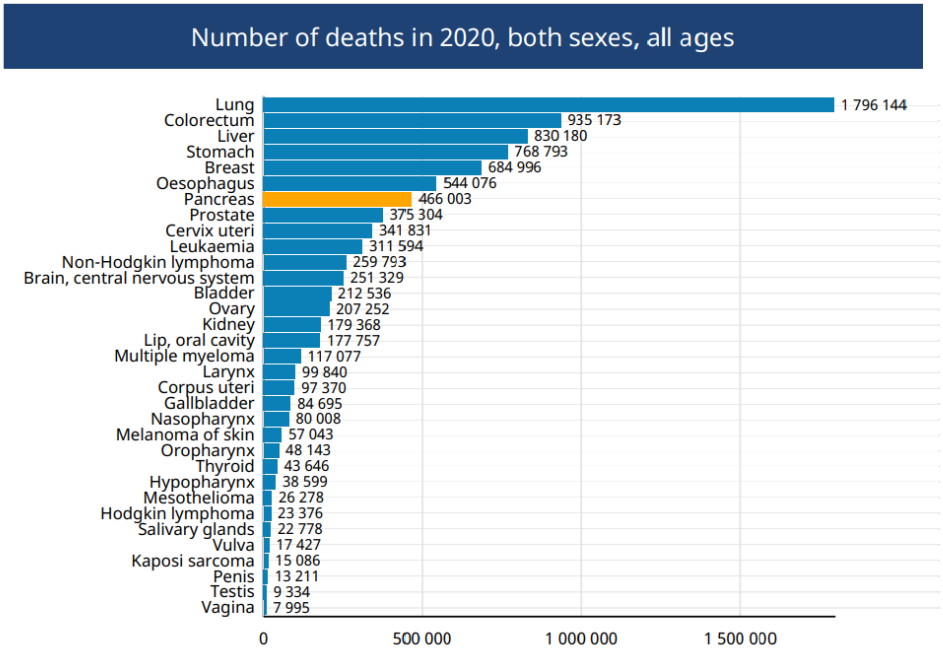

Figure 1-4. Number of deaths from various types of cancers worldwide in 2020, for both sexes and all ages. Pancreatic cancer, highlighted in yellow, was the seventh leading cause of cancer-related death. (https://gco.iarc.fr/).

1.2.1. Etiology and risk factors of pancreatic cancer

Two categories of risk factors for pancreatic cancer have been identified: the modifiable and non-modifiable factors. Smoking, alcohol consumption, obesity, type-2 diabetes, diet, and occupational exposures (for instance, nickel exposure) constitute some external and modifiable factors, while gender, age, ethnicity, family history, infections and genetic are intrinsic factors that cannot be modified (6,9).

Among **modifiable factors**, smoking is the major environmental factor for pancreatic cancer (6,10). Compared to never-smoker, smokers increase their risk of developing PDAC (odds ratio (OR) = 1.72; 95% confidence interval: 1.39-2.12) (11). In addition to smoking, alcohol also represents another risk factor for developing pancreatic cancer (6,9). Indeed, drinking more than nine glasses of alcohol per day is considered as high alcohol consumption and significantly increases the risk of developing the disease compared to people drinking less than one glass per day (OR = 1.6; 95% confidence interval: 1.2-2.2) (9). However, no increased risk is observed in low to moderate alcohol consumers, except if they are smoking, suggesting intertwine effects of both alcohol and cigarette (6). Another modifiable and external factor is obesity (6,9). Indeed, many studies have shown that being overweight can increase the risk of developing pancreatic cancer (6,9). The diet can also impact the risk (6). For instance, red meat consumption (120 g/day) has been positively associated with risks of developing pancreatic cancer (relative risk (RR) = 1.13; 95% confidence interval: 0.93-1.39) (6,12). Furthermore, some studies have shown that some compounds used to conserve the meat such as nitrosamines, nitrite or N-nitroso, may increase the risk of developing the digestive disease (6,13). On the opposite, consuming vegetables was reported to have protective effects against pancreatic cancer (6).

Family history, genetic, gender and age are **non-modifiable factors** associated with pancreatic cancer (6,9). It is estimated that 5 to 10% of patients with pancreatic cancer have a family history (6). The risk is increased if the patient has a first degree relative with pancreatic cancer (6,14). This risk doubles if there are two relatives with the disease and can rise 32-fold and higher if the number of relatives presenting the cancer is more than two (6,15). Cases of inherited pancreatic cancer are usually related to germ-line mutations in genes such as *breast cancer type 1 susceptibility protein 1 and 2* (*BRCA1* and *BRCA2* respectively), *partner and localizer of BRCA2* (*PALB2*) or *cyclin dependent inhibitor 2A* (*CDKN2A*). Finally, chronic

pancreatitis can also increase the risk of developing pancreatic cancer (6). For instance, patients with *serine protease 1* (*PRSS1*) gene mutations and related pancreatitis are more likely to develop pancreatic cancer (6).

1.2.2. Development of PDAC

Years before the apparition of the first symptoms (such as jaundice, loss of weight and abdominal pain) and diagnosis, pancreatic lesions arise, grow and evolve progressively into invasive PDAC **(Figure 1-5)** (16). Those precursor lesions are named the pancreatic intraepithelial neoplasia (PanIN) and can be classified in three categories: the low, intermediate and high grades (16). PanIN-1a and -1b are part of the low-grade category and are characterized by minimal cytological and architectural atypia while, PanIN-3 is an advanced lesion with severe atypia and is called "carcinoma *in-situ*" (16). On a side note, PanIN constitutes the main type of lesion leading to PDAC. However, even if it is less frequent, other types of lesions such as intraductal papillary mucinous neoplasms (IPMN) and mucinous cystic neoplasms (MCN) can develop into PDAC (17).

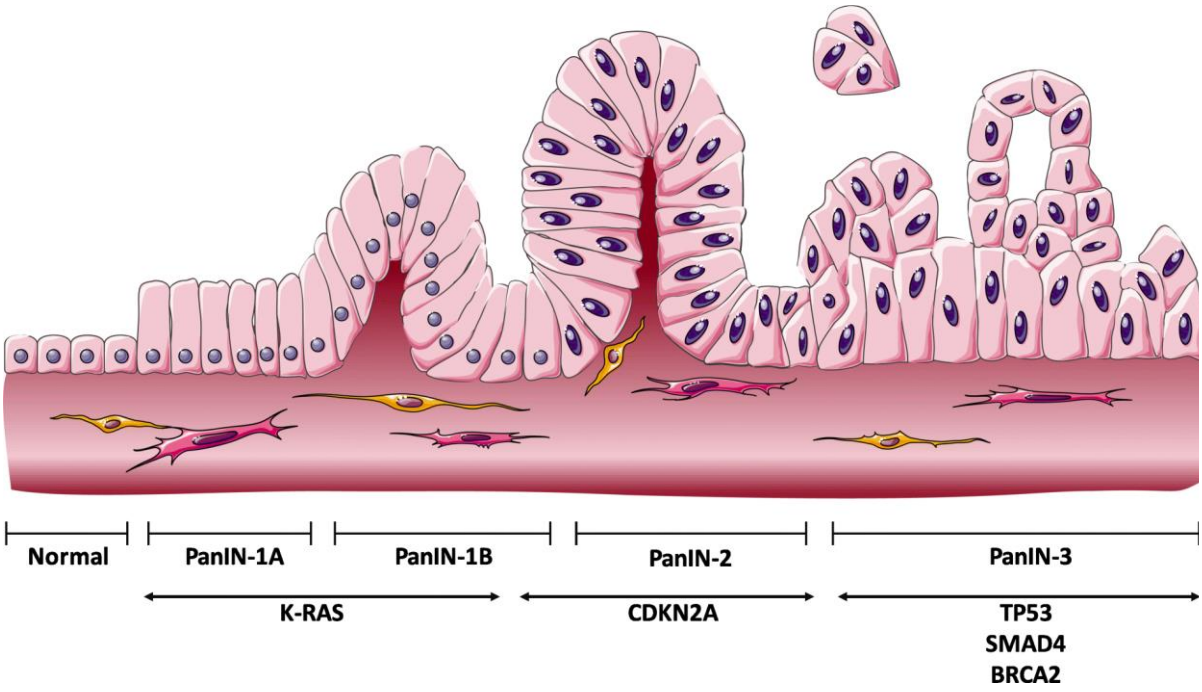

Figure 1-5. Development of PDAC from normal pancreas to PanIN-3. Driving mutations involved in tumorigenesis such as *KRAS*, *CDKN2A* or *TP53* are represented in accordance with the PanIN status. The picture is from Daoud *et al.* (2019) (18).

The study of PanIN lesions is essential to find new strategies allowing early detection (and prevention) of PDAC. It has been identified that the *kirsten rat sarcoma viral oncogene homolog* (*KRAS*) gene is mutated in 70-85% of cases, initiating early PanIN-1 stage **(Figure 1-5)** (16,19). In PDAC, the main mutation found in KRAS (in ~80 % of cases) is the G12D mutation, meaning that

the glycine at position 12 is replaced by an aspartic acid (20). This small GTPase is anchored to the plasma membrane and creates a bond between growth factor receptors and intracellular pathways involved in cell survival and proliferation (19). In some cancers, the mutant KRAS is permanently bound to GTP in its activated form. Therefore, the pro-survival and proliferative downstream signaling pathways, such as the AKT/PI3K or the MAPK pathways, are constitutively activated (19). Although *KRAS* mutations have been involved in PanIN initiation, studies performed on transgenic mice showed that only 20% of mice with mutated *KRAS* develop pancreatic cancer even if 100% of those mice had developed PanIN lesions, suggesting that *KRAS* mutation alone is not sufficient to drive PanIN into pancreatic cancer (19). Indeed, other driving mutations on genes such as the *tumor protein p53* (*TP53*), the *mothers against decapentaplegic homolog 4* (*SMAD4*), and the *CDKN2A* are involved in tumorigenesis (Figure 1-5): PanIN lesions in transgenic mice mutated for *KRAS* and *TP53* evolve into PDAC in more than 99% of cases, meaning that the succession of mutations in proto-oncogenes and tumor suppressor genes is required for tumorigenesis (19).

Even if the name pancreatic ductal adenocarcinoma may suggest that the cellular origin of PDAC is ductal cells, the cellular origin of PDAC is still under debate (17). In fact, recent studies performed in engineered mouse models, reported that PDAC may emerge either from pancreatic embryonic precursors, ductal cells or acinar cells, all of them being capable to give rise to the cancer (Figure 1-6) (17,21,22). PDAC cells display ductal features, explaining why ductal cells were initially considered as the origin of PDAC (17). Nevertheless, it is now known that acinar cells can undergo acinar-to-ductal metaplasia (ADM) and give rise to PDAC (21). In addition, it seems that the cellular origin of PDAC may influence the disease progression. Indeed, in their study published in 2019, Lee *et al*. showed that acinar cells, mutated for *KRAS* and *TP53* in mice model, lead to invasive PDAC (22). Nonetheless, they required prolonged time to develop into PDAC compared to ductal cells mutated for the same genes (22). Moreover, it seems that mutated-ductal cells can give rise to PDAC without formation of PanIN lesions, while acinar cells seem to be systematically associated with those lesions (Figure 1-6) (23). Nevertheless, the possibility that ductal cells can develop into PDAC through PanIN lesions cannot be excluded regarding actual scientific knowledge (17,23).

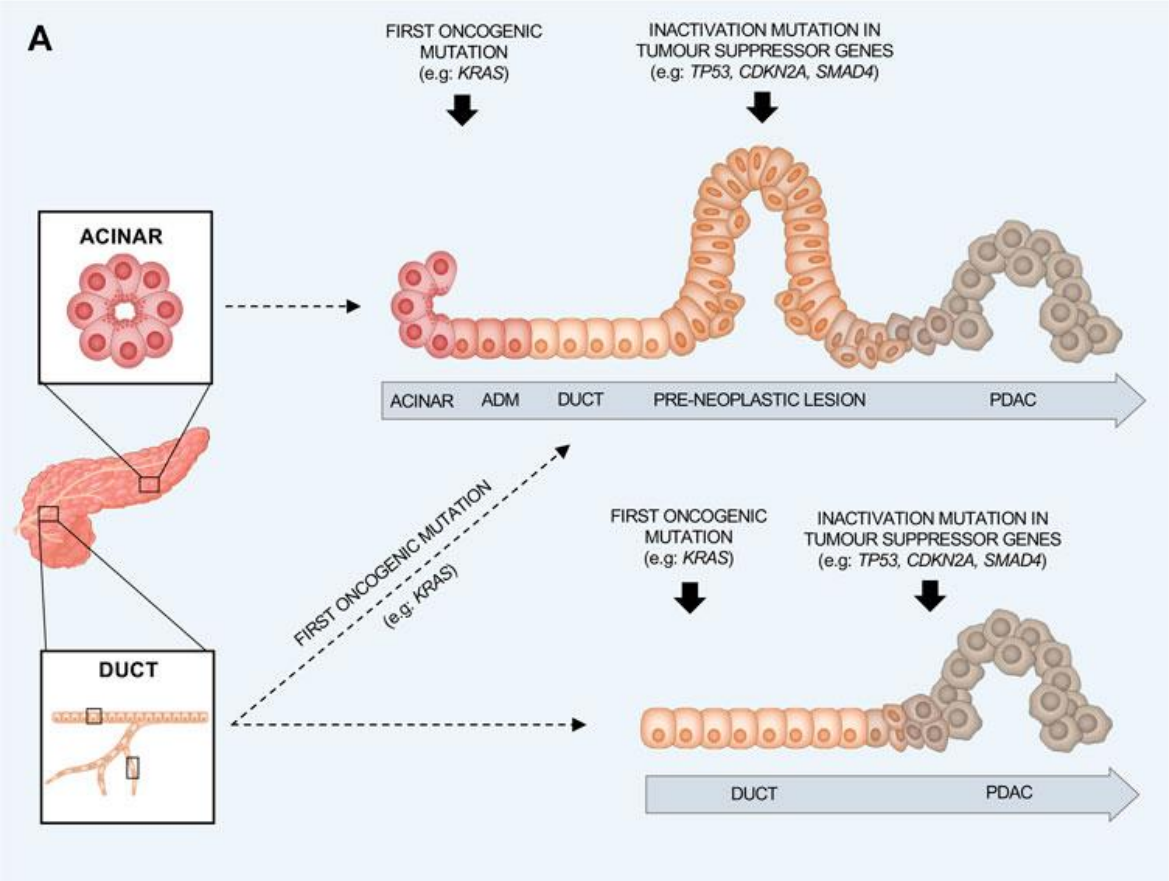

Figure 1-6. PDAC can originate from acinar or ductal cells. Acinar cells (top) will undergo an ADM, which becomes irreversible upon *KRAS* mutation. The resulting ductal-like cells will evolve into PanIN lesions, and finally, PDAC. If the cellular origin of the tumor arises from ductal cells (bottom), the tumoral development is thought to be faster, without formation of PanIN lesions. Nevertheless, the possibility that ductal cells can develop into PDAC through PanIN lesions cannot be excluded. Adapted from Malinova *et al*. (2021) (17).

1.2.3. Diagnosis, staging and treatment of PDAC

1.2.3.1. Diagnosis and staging of PDAC

Patients with pancreatic cancer usually exhibit unspecific symptoms such as epigastric pain, cachexia and jaundice (24). In case of pancreatic cancer suspicion, an abdominal CT-scan is performed to check the presence of a pancreatic mass (25). Moreover, in order to corroborate the lesion and to appraise the degree of differentiation, a biopsy is harvested (25). Based on imaging, the extent of the cancer is assessed using the TNM score, established on three parameters: the T parameter gauges the size of the tumor. Whether the cancer has reached or not the lymphatic system is assessed by the N parameter. And finally, the presence of metastases is determined by the M parameter (25). According to the TNM score, the cancer is classified in three categories: the resectable, limited resectable or non-resectable cancers (25).

This is summarized in (Table 1). The cancer is considered as non-resectable when it has reached the vascular system and when there is the presence of metastases (25,26).

Table 1. TNM score. According to the size of the tumor (T), the spread to lymph nodes (N) or the presence of metastases (M), a stage from 0 to IV is established. Based on the stage, the tumor is classified as (borderline) resectable or unresectable.

Stages	Tumour (T)	Nodes (N)	Metastasis (M)	Surgery
Stage 0	Tis	N0	M0	
Stage IA	T1	N0	M0	Resectable
Stage IB	T2	N0	M0	Resectable - Borderline resectable
Stage IIA	T3	N0	M0	
Stage IIB	T1, T2, T3	N1	M0	
Stage III	T1, T2, T3 T4	N2 Any N	M0	Unresectable
Stage IV	Any T	Any N	M1	Unresectable

1.2.3.2. Standard treatments of PDAC

Because in 80% of cases, patients are diagnosed at late stages, the tumor is not resectable (8). In this situation, the 5-year survival rate is below 5% (27,28). Nevertheless, even if the benefit is only of a few months, chemotherapies, such as FOLFIRINOX, which is a combination of molecules, including Folinic Acid (improves the effect of Fluorouracil by promoting optimal binding to the thymidylate synthase), Fluorouracil (a nucleoside metabolic inhibitor, interfering with DNA and RNA synthesis; it inhibits the thymidylate synthase by competitive binding, and its metabolites incorporate into DNA and RNA), Irinotecan (inhibits the type-I topoisomerase, preventing ligation of the single strand break) and Oxaliplatin (induces crosslinking of macromolecules such as DNA, preventing its replication and transcription) can be administrated. In addition, gemcitabine (after being metabolized, gemcitabine inhibits the ribonucleotide reductase, involved in deoxynucleoside triphosphate synthesis and incorporates into DNA, further inhibiting DNA synthesis) or gemcitabine combined with paclitaxel (impacts mitosis by preventing microtubules depolymerization), can also be used to prolong the survival (Figure 1-7) (8,25,29–34). On the opposite, for the 20% of remaining cases with limited or fully resectable tumors, the surgery can be performed (8,25). Naturally, this decision considers the patient's comorbidities and performance status (25). In case of a resectable tumor, the surgery is directly performed without neo-adjuvant therapy if the global patient's health allows it (8,25). If the tumor is considered as borderline for resection, a neo-adjuvant treatment such as radio-

chemotherapy or chemotherapy alone may be administrated (8,25). This is followed by surgery, if a positive response from the patient after neo-adjuvant treatment is observed (Figure 1-7) (25). It is worth mentioning that, even for patients undergoing surgery, the risk of relapse is high. Indeed, 76.7% of patients with resected tumor experiment a relapse within 2 years after the surgery (27,28).

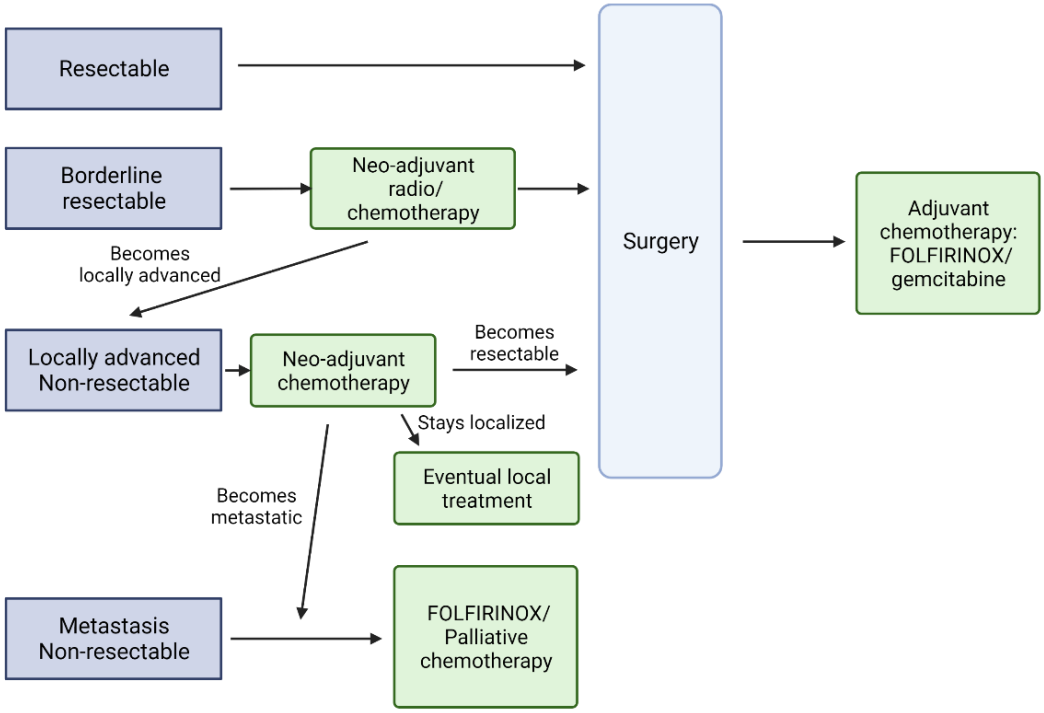

Figure 1-7. Treatment strategy according to the resectable, borderline resectable and non resectable status of the tumor (with or without metastases). If the tumor is resectable, the surgery can directly be performed (rare situation). This is followed by adjuvant chemotherapy (usually FOLFIRINOX). If the tumor is borderline resectable or non-resectable (without metastases), neo-adjuvant chemotherapy is administrated. It is followed by surgery if the tumor becomes resectable. For advanced diseases, palliative chemotherapy is administrated. The picture was created with BioRender.com

1.2.3.3. Targeted therapy in PDAC

As opposed to chemotherapy, targeted therapy specifically targets molecules involved in cancer progression. One example of targeted therapy is the use of Trastuzumab, a monoclonal antibody, in human epidermal growth factor receptor-2 (HER2) positive breast cancer (35,36). Indeed, in some breast cancers, HER2 is highly expressed, leading to abnormal tumor growth (36). The monoclonal antibody Trastuzumab blocks HER2 and, as a consequence, downstream signaling pathways involved in tumor progression are under-stimulated (36). Studies showed that the use of Trastuzumab in combination with chemotherapy improved the relative overall

survival by 37% and increased the 10-year survival from 75 to 84% (35). However, even if those therapies have demonstrated satisfactory results for some cancers, in the case of PDAC, targeted therapy only improves the overall survival by a few days. Indeed, the only targeted therapy approved by the food and drug administration (FDA) for patients with advanced pancreatic cancer is the Erlotinib (https://www.fda.gov/). This molecule inhibits the epidermal growth factor receptor (EGFR), which is often overexpressed in PDAC (37). Because the EGFR is involved in cell proliferation, apoptosis and division, its inhibition reduces tumor growth and metastasis (37). It is noteworthy to point out that the mutation in *KRAS* (occurring in ~ 85% of cases in PDAC (16,19)) is associated with a lack of sensitivity for the drug. Indeed, KRAS is part of downstream signaling pathways of the EGFR (38). According to the study of Moore *et al.* published in 2007, the combination of Erlotinib and gemcitabine increases the median survival time of patients with PDAC by approximatively ten days (6.24 months versus 5.91 months for the gemcitabine-Erlotinib versus gemcitabine-placebo) (39). Moreover, the one-year survival rate increased from 17% to 23% when Erlotinib was used with gemcitabine (39). Even if the use of Erlotinib prolonged the survival, the benefit remains minor. Notably, in Belgium, the Erlotinib is not used to treat pancreatic cancer.

In that regard, having a better understanding of PDAC biology and finding new therapeutic targets for this disease are needed. Since cancer cells exhibit uncontrolled cell proliferation, they adapt their energy metabolism to support their growth and division (40–42). In addition, cancer cells have to face challenging environmental conditions such as the lack of nutrients and hypoxia, which require metabolic adaptations (40–42). This reprogramming of energy metabolism in cancer cells has been described in 2011 by Hanahan *et al.* as an emerging hallmark (40). Therefore, targeting cancer cell metabolism, in order to create a metabolic imbalance able to slow down cell proliferation and sensitize them to other therapies, is currently under investigations. In this context, numerous metabolic pathways have been investigated, such as the mammalian target of rapamycin (mTOR) pathway, often involved in cancer metabolism (43). Unfortunately, targeting the mTOR pathway has demonstrated toxic side effects in clinical trials, highlighting the important role of this pathway in normal proliferating cells (43). In this context of cancer cell metabolism, our team studies a protein, named myoferlin, overexpressed in PDAC compared to non-cancer tissues, where it is barely detectable (44). Such an expression profile makes this protein a good candidate for targeted

therapy, especially since myoferlin has also been associated with cancer cell metabolism (45–49). Before introducing myoferlin, the following sections will approach the hallmarks of PDAC metabolism and the relationship existing between metabolism and inter-organelle communication.

1.2.4. Overview of PDAC metabolism

PDAC is characterized by an exacerbated desmoplasia that represents up to 90% of the tumor volume. Desmoplasia is constituted of cancer-associated fibroblasts (CAFs) that, under activation, deposit a large amount of extracellular matrix. This accumulation of extracellular matrix is responsible for the hypovascularisation observed in PDAC and represents a barrier for immune cells and chemotherapeutic compounds (16). As a consequence of desmoplasia and resulting hypovascularisation, pancreatic cancer cells are submitted to nutrient starvation, hypoxia and metabolic stress (50). To survive to those extreme conditions, cancer cells adapt their behavior and metabolism, for instance, by increasing autophagy and switching to glycolysis (50).

Indeed, since its discovery in the 20s by Otto Warburg, it is now known that cancer cells switch their metabolism towards glycolysis, even in the presence of oxygen (Figure 1-8) (51). Despite the fact that glycolysis is less efficient for adenosine triphosphate (ATP) production than oxidative phosphorylation (OXPHOS), it is thought to confer advantages to proliferating cells by providing them biosynthetic precursors needed for nucleotides or proteins, thus supporting their growth (50). In addition, ATP obtained by glycolysis is produced faster than via mitochondrial respiration, which can confer advantages under competitive environments (52). Another consequence of this so-called Warburg effect is the acidification of the tumoral environment by lactate production. This acidification of the tumoral microenvironment is thought to alter the tumor-stroma interface, allowing the invasion of surrounding tissues by cancer cells (52). In addition to environment acidification, the high glycolysis rate might indirectly provide elevated ratios of $NADPH,H^+/NADP^+$ (for instance through the pentose phosphate pathway or the “single carbon” pathway) needed for the reactive oxygen species (ROS) detoxification (52). Indeed, ROS level is elevated in cancer due to hypoxia, high metabolic rate and genetic alterations. Moderate levels of ROS can favor tumor progression, for instance, by inducing DNA mutations. However, excessive amounts of ROS can be harmful for cancer cells, explaining their need for ROS detoxification (53).The Warburg effect is also influenced by

mutations found in cancers (50). For instance, oncogenic KRAS upregulates the glucose transporter-1 (GLUT1), increasing glucose influx inside the cell. It also upregulates the expression of hexokinase 1 and 2 (HK1 and HK2), increasing glycolysis rate, and drives glucose intermediates into glycolysis side-paths such as the pentose phosphate pathway, to support biomass synthesis (54). In addition, mutations in *TP53*, *SMAD4* or the activation of the hypoxia inducible factor-1 subunit alpha (HIF-1α) pathway all contribute and favor the Warburg effect (50).

Another characteristic found in PDAC is their increased reliance on **lipid synthesis and/or uptake (Figure 1-8)** (50). This confers building blocks for membrane formation, signaling molecules, or post-translational modifications of proteins (55). Furthermore, it is a non-negligible source of energy for the cell, required for migration and metastasis (50). Compared to normal cells relying mainly on dietary fat, some cancer cells produce more than 90% of their own triacylglycerol fatty acids (55,56). This observation is well illustrated by the study of Daemen *et al.* published in 2015, where the metabolite and transcriptional profile of 38 pancreatic cancer cell lines showed three main metabolic subtypes, including a glycolytic and a lipogenic one (57). While the glycolytic subtype depended more on glycolysis, the lipogenic one was characterized by high levels of metabolites and enzymes involved in cholesterol, steroid and lipid synthesis as well as OXPHOS (57). As for the Warburg effect, this increased reliance on lipid metabolism observed in PDAC is also modulated by oncogenes such as KRAS (58). In parallel to the *de novo* lipid synthesis, PDAC cells enhance their uptake of cholesterol and store it as cholesteryl-ester. Indeed, cholesterol is a major constituent of plasma membrane lipid rafts, which modulates cell signaling. This explains why in PDAC the acyl-coenzyme-A cholesterol acyl-transferase-1 (ACAT1) is highly expressed and associated with cancer progression (55). This enzyme is also highly enriched in the contacts existing between endoplasmic reticulum (ER) and mitochondria (59).

Besides glucose and lipid metabolism, PDAC cells also rewire their **amino acid metabolism** (50). In this context, glutamine constitutes a good example **(Figure 1-8)** (50). Indeed, in non-cancer cells, glutamine is converted into glutamate and then into alpha-ketoglutarate to fuel the tricarboxylic acid (TCA) cycle (50). However, in cancer cells, glutamate is preferentially rewired toward the aspartate/malate pathway, the end products being pyruvate and an elevated ratio of $NADPH,H^+/NADP^+$ (50). This pathway helps for the detoxification of ROS and, therefore,

maintains the cell redox homeostasis (50). As for lipid or glucose metabolism, KRAS plays a major role in this rewiring. On one side, it downregulates the glutamate dehydrogenase (GLUD1), which converts glutamate into alpha-ketoglutarate, while on the other side, it upregulates the aspartate aminotransferase 1 (GOT1) and the malate dehydrogenase 1 (MDH1), that participate to the aspartate/malate pathway (50).

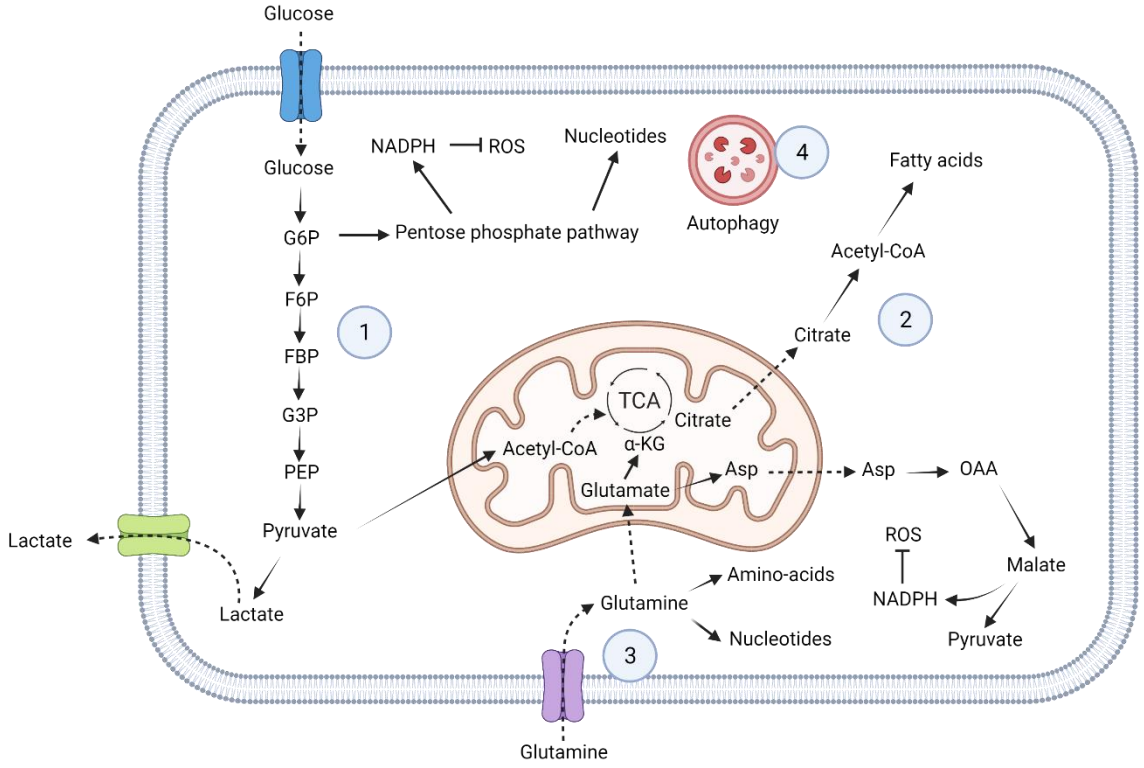

Figure 1-8. Major metabolic pathways in PDAC. **(1)** PDAC proliferative cells sustain their metabolic needs thanks to the Warburg effect. **(2)** Some PDAC cells rely exclusively on lipogenesis, providing them non-negligible sources of energy. **(3)** PDAC-specific glutamine metabolism: in PDAC, glutamine is preferentially converted into aspartate, then into oxaloacetate, malate and finally into pyruvate. This results in a high $NADPH,H^+/NADP^+$ ratio, allowing ROS detoxification. **(4)** The metabolic needs of the cell are supported by autophagy (and macropinocytosis). G6P: glucose-6-phosphate; F6P: fructose-6-phosphate; FBP: fructose biphosphate; G3P: glyceraldehyde-3-phosphate; PEP: phosphoenolpyruvate; Asp: aspartate; OAA: oxaloacetate; α-KG: alpha-ketoglutarate; TCA: tricarboxylic acid cycle; ROS: reactive oxygen species. The picture was created with BioRender.com

Furthermore, PDAC have been characterized by their enhanced **autophagy and macropinocytosis (Figure 1-8)** (50). While autophagy is often anti-tumorigenic in normal cells and at early stages of cancer development, it becomes beneficial for cancer cells at later stages (50). Indeed, inhibition of autophagy in PDAC suppresses growth and proliferation (50). This is explained by the fact that, under nutrient deprivation, cancer cells use autophagy (and macropinocytosis) to recycle sugars, amino acids, fatty acids and other molecules through anabolic pathways (50). Interestingly, the cells adapt themselves in a sustained manner,

meaning that even after restoring nutrients, an enhanced level of autophagy is still observed (50). This could be explained by the involvement of oncogenes such as *KRAS*, known to favor autophagy. Indeed, KRAS can suppress autophagy through the PI3K/AKT/mTOR pathway, while it can promote autophagy through the MAPK pathway. In cancer cells, an upregulation of the MAPK pathway and downregulation of the PI3K/AKT/mTOR axis, promoting the KRAS-induced autophagy was reported (60). In the literature, it has been proposed to target autophagy in combination with chemotherapy. However, this strategy was not successful due to a compensation through macropinocytosis. Therefore, inhibition of both macropinocytosis and autophagy has been proposed as a more successful approach (50).

Finally, during decades, the scientific community believed that cancer cells switched their metabolism to glycolysis because their mitochondria were not functional (51). However, this belief has been questioned and, today, it is known that, even if mitochondrial respiration is often repressed in cancer cells, it remains perfectly functional (51). For instance, in 2020, Hollinshead *et al*. showed that, unlike cell lines derived from less hypoxic tumors such as lung and colon, PDAC cell lines were able to proliferate under severe hypoxia (61). Interestingly, under anoxia, the cells stopped proliferating but were able to maintain their viability for several days. Those results suggest that a minimal oxygen concentration is required in PDAC cellular processes to maintain growth and that PDAC cells establish strong metabolism adaptation to sustain viability in the absence of oxygen. By creating mitochondrial DNA-deficient cells for key respiratory chain catalytic subunits, they were able to show that PDAC cell lines, under severe hypoxia, required functional electron transport chain (ETC) to maintain growth, demonstrating the importance of mitochondria in PDAC (61). In addition to this study, pancreatic cancer stem cells (CSCs), that have been involved in cancer relapse and metastasis, have been recently shown to be highly dependent on oxidative metabolism and to display a low energetic flexibility. Indeed, researchers showed that those cells, relying exclusively on OXPHOS, were unable to efficiently produce ATP from glycolysis upon mitochondrial inhibition with metformin (62). This lead CSCs to apoptosis, while a small fraction of CSCs survived because of an intermediate metabolic status (62). Similar studies highlighted mitochondria in pancreatic cancer as a promising therapeutic target. Indeed, in their report, Masoud *et al*. showed in 2020 that PDAC cell lines with a high OXPHOS capacity were more resistant to gemcitabine. Moreover, treating

those cells with phenformin, an inhibitor of the mitochondrial respiratory complex I, was able to re-sensitize them to gemcitabine (63).

In the context of mitochondrial targeting as a therapeutic strategy, a growing interest for the interconnections existing between mitochondria and other organelles, such as ER, emerged (64,65). Indeed, it has been demonstrated that those contacts constitute real metabolic platforms, with distinct lipid and protein compositions, where exchanges of metabolites occur (64–66). Cancer cells use those metabolic platforms to fit their metabolic needs and to avoid apoptosis (64–67). Interestingly, researchers found that proteins involved in those contacts were often modulated or overexpressed by cancer cells (65,68,69). Some studies showed that targeting proteins located in those contacts negatively impacted tumor progression, by creating metabolic stress or sensitizing cells to apoptosis (70,71). Additionally, a recent publication showed that mitochondria from neuroblastoma cells, obtained from patients after the diagnosis or after cancer relapse, did not present differences in DNA content, size or shape (72). However, the contacts existing between mitochondria and ER were modified, conferring apoptotic resistance to cancer cells responsible of the relapse (72). This study highlighted the importance of communication between organelles in cancer. Even if studying the physical and metabolic interconnections existing between organelles seems promising, researchers only recently began to study those interconnections in the context of cancer. Therefore, it probably remains lot of proteins, functions and modulations related to those contacts that should be investigated in cancers and that will probably be discovered in future years. In this work, we studied a protein named myoferlin in the context of PDAC metabolism, and more precisely, in the context of mitochondrial metabolism. We first believed this protein to be located on mitochondria. Nevertheless, our investigations prompted us to wonder whether myoferlin was located in the metabolic platforms existing between organelles. In the following section, such metabolic platforms, the mitochondria-associated membranes (MAMs), will be described in more details.

1.3. Mitochondria-associated membranes

Membrane contact sites between organelles have been recently defined by Scoranno *et al.* in 2019. To be considered as a contact site, the membranes in association should: (a) not fuse

together, (b) display protein tethering, (c) fulfil a function and (d) have a specific proteome/lipidome (73).

The term MAMs designates the membranes in contact with mitochondria. Therefore, considering strictly the meaning of MAMs, this includes plasma membranes (74,75) and organelles such as ER (76), lysosomes (77,78), and peroxisomes (79). Ideally, MAMs should englobe all of the overmentioned organelles. However, the term MAMs is often used in the literature to designate exclusively the membrane of ER in association with mitochondria (80). When referring to the specific ER-mitochondria tethering, the terms of mitochondria-ER contact sites (MERCS) or ER-mitochondria contact sites (ER-MCSs) are often used in the literature (81,82). Even if the terminology MAMs or MERCS (as well as ER-MCSs) refers slightly to different concepts, MAMs referring to the ER membrane in contact with mitochondria and MERCS to the contact sites, those terms are usually used to designate the same concept, being the association of ER with mitochondria (83). In the present work, the term MAMs will be mainly used to refer to the association between both organelles.

Since its discovery in the late 50's (84), efforts to understand and characterize MAMs function have emerged. Nowadays, it is known that contacts between ER and mitochondria largely influence cell metabolism and fate. MAMs have been described in many cellular processes including mitochondrial dynamics, apoptosis, lipid synthesis, calcium (Ca^{2+}) transfer, autophagy and inflammation. In addition, this metabolic platform has been associated with pathologies such as cancer, diabetes, Alzheimer (AD) and Parkinson (PD) diseases (85,86).

The present section briefly describes mitochondria and ER. This is followed by a review of the structure and the specific constituents of MAMs as well as their main functions. In addition, the way MAMs influence and participate in pathologies such as cancer, neurodegenerative and metabolic diseases is approached.

1.3.1. Mitochondrial structure and metabolism

The mitochondrion is an organelle found in eukaryotic cells. It is responsible for the aerobic respiration where the oxygen is the final electron acceptor. It is used to produce energy under the form of ATP. Because mitochondria harbor their own DNA and exhibit a specific double-membrane structure, it is thought that the presence of this organelle in eukaryotic cells is the result of endosymbiosis (87).

Mitochondria are delimited by two distinct membranes: the outer mitochondrial membrane (OMM) which surrounds the inner mitochondrial membranes (IMM). The space between those membranes is named the intermembrane space (87). On one side, the OMM is more permeable than the IMM because of the presence of numerous porins, allowing the passive diffusion of molecules smaller than 6 kDa (88). Interestingly, the main type of porin located on the OMM is the voltage-dependent anion channels (VDACs), representing more than 50% of OMM proteins and allowing the entry of ions and uncharged molecules into the inter-membrane space (88). On the other side, the IMM is less permeable. It contains proteins involved in the ETC. Moreover, one particularity of the IMM is the presence of invaginations named cristae. Those structures increase the IMM surface and thus, the amount of proteins involved in the OXPHOS. Finally, the space delimited by the IMM is called the mitochondrial matrix, where the TCA or Krebs cycle occur (87).

Mitochondria use the pyruvate produced by glycolysis. This last one is a metabolic pathway found in eukaryotic and prokaryotic cells that converts glucose into pyruvate to provide energy. Through this metabolic process, occurring in the cytosol, two net molecules of ATP, pyruvate and NADH, H+ are produced from one molecule of glucose. The pyruvate produced through glycolysis may enter the mitochondria where it is processed into acetyl-Coenzyme A to feed the TCA cycle (Figure 1-9). Pyruvate, can cross the OMM through porin, such as VDACs, and then the IMM through a specific symport with proton, the mitochondrial pyruvate carrier, to enter the mitochondrial matrix (88). Once in the matrix, the molecule is oxidized by the pyruvate dehydrogenase (PDH) into acetyl-Coenzyme A. The Krebs cycle starts when acetyl-Coenzyme A reacts with oxaloacetate to produce citrate and ends when the malate is oxidized into oxaloacetate to re-start the cycle. There exist three steps where the intermediates of the TCA cycle are oxidized with the production of NADH, H+ or FADH2. Indeed, in addition to malate oxidation, the isocitrate is oxidized by the isocitrate dehydrogenase (IDH) into alpha-ketoglutarate (α-KGDH), which is in turn, oxidized by the alpha-ketoglutarate dehydrogenase into succinyl-CoA. Consequently, the succinyl-CoA is converted into succinate thanks to the succinate dehydrogenase with the production of GTP. Next to the production of NADH, FADH2 is also produced during the sixth step of the TCA cycle through the oxidation of succinate into fumarate. FADH2 and NADH, H+ provide electrons to the ETC (89).

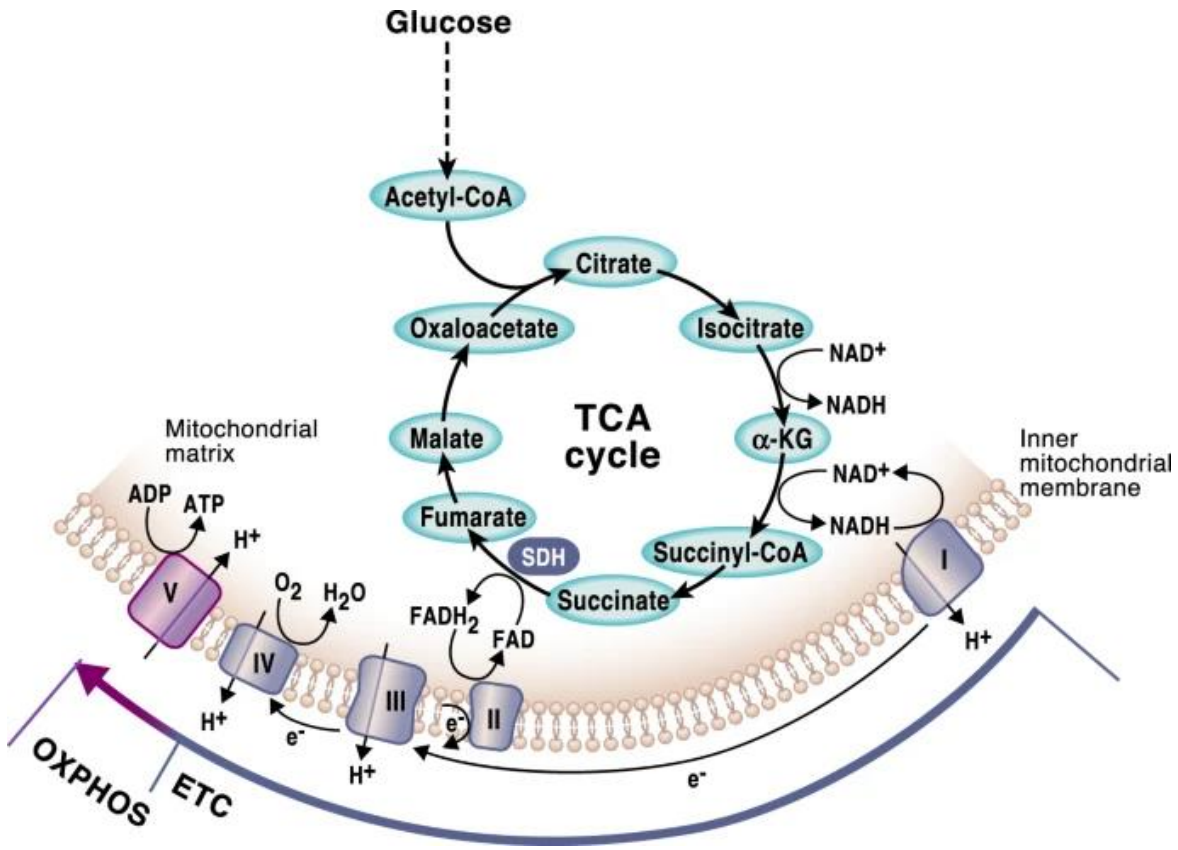

Figure 1-9. Representation of the TCA cycle and OXPHOS. The Krebs cycle starts when acetyl-Coenzyme A (Acetyl-CoA) reacts with oxaloacetate to produce citrate and ends when the malate is oxidized into oxaloacetate to re-start the cycle. NADH, H+ or FADH2 are generated by the TCA cycle and provide electrons to the ETC. The transport of electrons through complexes I, III and IV allows H^+ pumping from the matrix to the intermembrane space, creating an electrochemical gradient across the IMM. This accumulation of protons in the intermembrane space is required for the proper activity of the ATP synthase. Most of the protons from the intermembrane space return to the matrix through the ATP synthase, synthetizing ATP from ADP and inorganic phosphate. The picture is from the publication of Martinez-Reyes and Chandel (2020) (89).

The ETC chain is a set of protein complexes located in the IMM (Figure 1-9). There are four complexes composing this chain: the complex I, II, III and IV. The chain starts when the complex I oxidizes the NADH, H+ into NAD+, while the complex II accepts the electrons from FADH2, generated during the TCA cycle. Then, the electrons from the complex I and II transit to the complex III thanks to the ubiquinone/ubiquinol, also known as coenzyme Q. Following this step, the electrons are carried to the complex IV thanks to the cytochrome c. At the end of the process, the complex IV passes the electrons to the oxygen, forming water. The transport of electrons through complex I, III and IV allows H+ pumping from the matrix to the intermembrane space, creating an electrochemical gradient across the IMM. This accumulation of protons in the intermembrane space is required for the proper activity of the ATP synthase. Indeed, most of the protons from the intermembrane space return to the matrix through the

ATP synthase, synthetizing ATP from ADP and inorganic phosphate. Combined together, the ETC and the passage of protons through the ATP synthase constitute the "OXPHOS" (90).

As explained in this work, mitochondria are in contact with other organelles such as endoplasmic reticulum. Those contacts are known to influence mitochondrial metabolism. For instance, Ca^{2+}, which is transferred from the ER to the mitochondria, acts as a cofactor of some enzymes of the TCA cycle. Before describing those contacts in more details, the ER is briefly approached.

1.3.2. Structure and function of the endoplasmic reticulum

The endoplasmic reticulum is an organelle characterized by continuous membranes that can be divided into distinct subdomains such as tubules or sheets (Figure 1-10). Fission and fusion of the network participate to the ER dynamics, involving proteins such as reticulons and atlastin (91). While the branched tubules, found at cell periphery, mainly correspond to smooth endoplasmic reticulum, the flat sheets, located near the nuclear region, often correspond to rough endoplasmic reticulum. This last one is enriched in ribosomes and is involved in synthesis, folding and post-translational modifications of proteins. On the other hand, smooth ER is often associated with Ca^{2+} handling (see section *Calcium transfer at MAMs modulates cellular metabolism*) and lipid synthesis (see section *MAMs participate to ER stress relief*) (92).

Ribosomes play an important role in protein synthesis. They interact with mRNA in the cytosol and dock to the ER membrane, where they deliver proteins for the secretory pathway. The newly synthesized proteins, harboring a signal peptide, are recognized by a signal recognition particle (SRP), which binds to its receptor on the ER. After docking to the ER membrane, the protein is translated in the ER. Once in the ER lumen/membrane, the proteins undergo proper folding by the chaperones. As discussed in the *MAMs participate to ER stress relief* section, unproper folding can lead to ER stress and activate the UPR response. In accordance with their functions, some proteins are retained in the ER, while others are packed and sent to the Golgi apparatus for final destinations (92).

The ER is also involved in lipid synthesis and participates to the detoxification of drugs or alcohol. For instance, the synthesis of glycerophospholipids, sphingolipids and triglycerides has been described on the ER membrane. The newly synthesized lipids can be transported to final destinations through vesicles or contacts with other organelles such as mitochondria. This

transfer of lipids occurring between ER and mitochondria is described in the *Lipid transfer occurs at MAMs and participates to mitochondrial membrane integrity* section (94). In the following section, the functional aspect of those membranes in association with mitochondria will be approached.

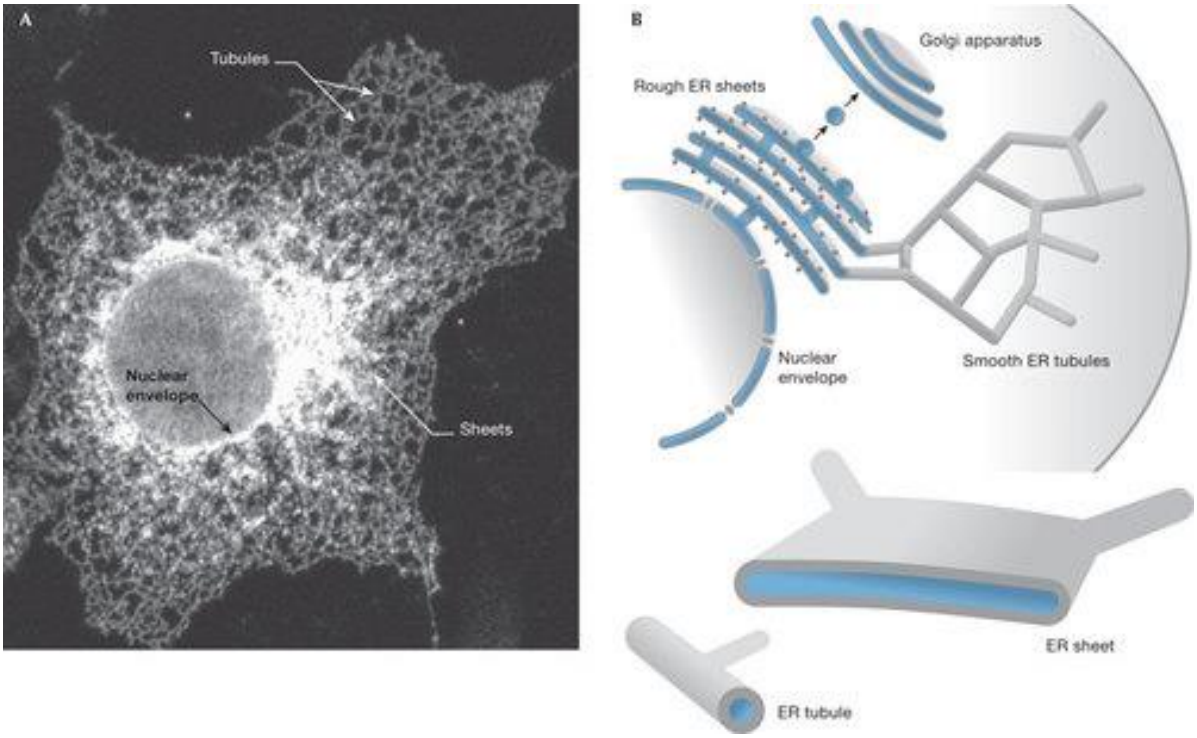

Figure 1-10. Endoplasmic reticulum (ER) structure. **(A)** Immunostaining of ER showing the ER tubules at the cell periphery and the ER sheets near the perinuclear region. **(B)** schematic representation of the ER tubules and sheets. The picture is from the publication of Park and Blackstone (2010) (93).

1.3.3. Structure and composition of MAMs

MAMs structure and composition are closely related to their functions (Figure 1-11). For instance, in relation with their function in lipid transfer, lipids such as cholesterol, ceramides and sphingolipids as well as proteins involved in lipid synthesis and phospholipid transfer are found to be enriched in MAMs (see *Lipid transfer occurs at MAMs and participates to mitochondrial membrane integrity* section) (80). In addition to their function in lipid transfer, MAMs are involved in Ca^{2+} transfer. Therefore, proteins, such as VDACs and the inositol 1,4,5-triphosphate receptors (IP3Rs) as well as proteins involved in their modulation, such as the phosphatase and tensin homolog (PTEN) or the protein kinase B (AKT), were described in those cellular regions (96) (see section *Implication of MAMs in diseases*). VDACs and IP3Rs are channels located, respectively, on the OMM and on the ER membrane. In MAMs, those

channels are in proximity, allowing efficient Ca^{2+} transfer from the ER to the mitochondria. In order to stabilize those proteins, a linker, the 75 kDa glucose-regulated protein (GRP75), creates a bridge between them. Whereas VDACs and IP3Rs were not reported to interact with each other, GRP75 was shown to interact with both VDACs and IP3Rs (97) (see section *Calcium transfer at MAMs modulates cellular metabolism*).

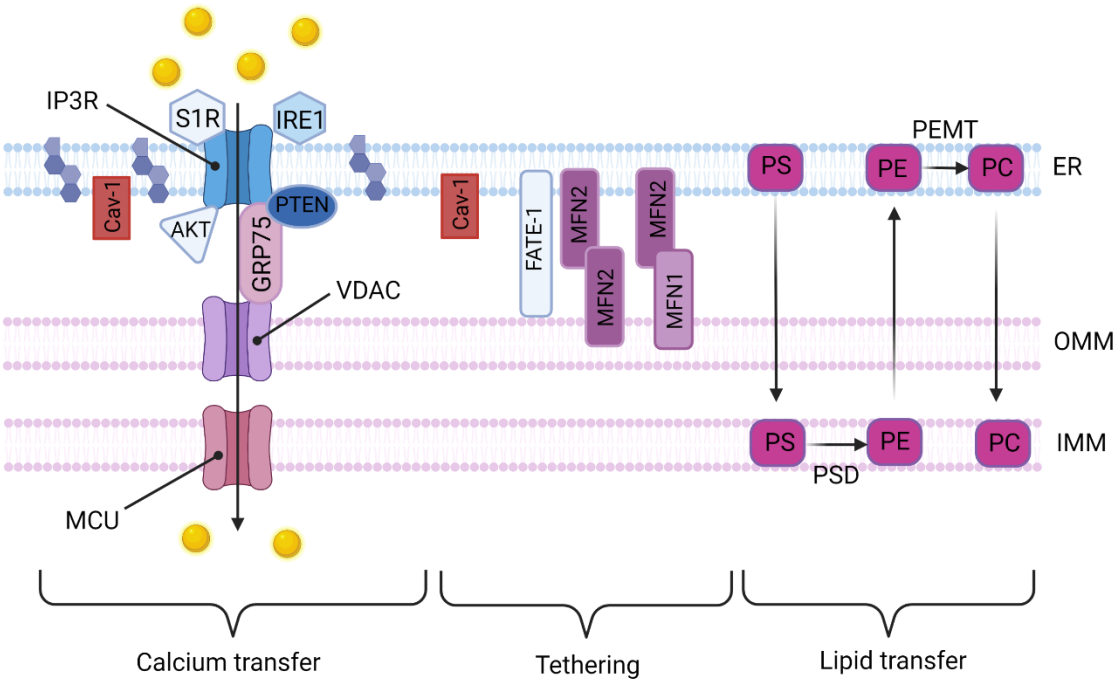

Figure 1-11. Protein composition of MAMs and their related functions. MFN1 and MFN2 tether the membranes of ER and mitochondria, which is essential for efficient Ca^{2+} and lipid transfer. IP3Rs and VDAC1 allow Ca^{2+} transfer between both ER and mitochondria. The stabilization of the VDAC1-IP3Rs axis is assured by linker proteins such as GRP75. Ca^{2+} transfer can be modulated by proteins such as AKT, PTEN or S1R. Proteins involved in lipid synthesis, and transfer, such as PEMT or PSD, are also found in MAMs. The picture was made with BioRender.com

Furthermore, in order to allow Ca^{2+} and lipid transfer between both organelles, an optimal distance between ER and mitochondria is required. Some proteins such as MFN2 and phosphofurin acidic cluster sorting protein-2 (PACS-2) have been described at MAMs, where they participate to the tethering of both organelles (96). In 2008, MFN2 silencing has been reported to increase the distance between ER and mitochondria and, by consequence, to decrease the transfer of Ca^{2+} between both organelles (98). Nonetheless, the contrary has also been reported, where MFN2 silencing enhanced the contacts between ER and mitochondria, thus, increasing the transfer of Ca^{2+} (99). In the study published by Filadi *et al.* in 2015, a model was proposed, where MFN2 would prevent Ca^{2+} overload and toxic effects on the cells (99). Due to those discrepancies, in 2016, Naon *et al.* re-evaluated the effect of MFN2 depletion on

MAMs (100). They found similar results to Scorrano and his team in 2008 (98), where MFN2 reduced ER-mitochondria contact sites (100). Nevertheless, despite the study published by Naon *et al*. in 2016 (100), further investigations are probably needed to clarify this point. Besides MFN2, there is also the interaction of the vesicle-associated membrane protein-associated protein B (VAPB), located on the ER, with the protein tyrosine phosphatase interacting protein 51 (PTPIP51), located on mitochondria (101,102). In the literature, overexpression or silencing of those proteins was shown to increase or decrease, respectively, the contacts between ER and mitochondria. Moreover, PACS-2, a protein involved in membrane trafficking, was also reported in MAMs (103). Its depletion was shown to induce mitochondrial fragmentation and to uncouple ER from mitochondria. Conversely, the overexpression of PACS-2 has been associated with enhanced ER-mitochondria contact sites (96,103,104). In addition, it was reported that PACS-2 could regulate the activity of calnexin, which is a protein found in MAMs. Since calnexin regulates the activity of the sarcoendoplasmic reticulum calcium-ATPase (SERCA) pump, located on the ER, the redistribution of calnexin to the plasma membrane, upon *PACS-2* knockdown, influenced the Ca^{2+} dynamics between ER and mitochondria (105). On the opposite, proteins such as the fetal and adult testis-expressed transcript protein (FATE-1) have been described as MAMs spacers (96,106). Disruption of MAMs tethering have been reported to impact mitochondrial dynamics and metabolism, showing the importance of tethering proteins (100,107).

In the literature, even if this definition tends to evolve with time, the distance between ER and mitochondria should be less than 30 nm to be considered as a contact (108). Moreover, the optimal distance between ER and mitochondria is estimated to be about 15 nm. Nevertheless, the optimal distance between organelles must also take into consideration whether this is rough or smooth ER in contact with mitochondria, the cell line on which the study is performed and the environment. Indeed, since MAMs are involved in cell metabolism, the environment may impact the cell requirements and thus, MAMs ultrastructure (96,109). Impairment of this last one can have major effect on MAMs function such as defective Ca^{2+} signaling, as observed in AD, diabetes or PD (98). In addition to MAMs ultrastructure, the overmentioned parameters (for instance, cell lines or environment) may also influence “MAMs frequency”. Indeed, the proportion of mitochondrial membranes in contact with ER is estimated to be approximately

20% (110). However, this proportion may vary according to the model used and cell metabolism.

The interest for the existence of inter-organelle communication and its impact on cell metabolism and function is relatively new. This is only since recently that diseases such as cancer, PD, AD or even diabetes have been associated with inter-organelle communication such as MAMs (111–114). As described previously, many proteins have already been identified in MAMs. Nonetheless, our comprehension and knowledge about proteins involved in MAMs is still limited. For instance, even in 2022, new MAMs proteins are being identified, such as the proline-rich tyrosine kinase 2 (Pyk2) protein, recently reported in MAMs of hippocampal neurons (115). In this work, we studied a protein named myoferlin. The silencing of this protein has been shown to impact mitochondrial metabolism of PDAC cell lines (47). In order to identify the underlying mechanism, we aimed at identifying myoferlin localization in relation with mitochondria. As it will be approached in this work, our research lead us to investigate the presence of myoferlin in MAMs.

Before describing in more details the functional aspect of MAMs, the techniques commonly used to study MAMs are briefly approached.

1.3.4. Technical approaches to investigate MAMs

In order to study MAMs composition, isolation using cell fractionation has been used for the first time in 1990 by Vance (116). Using this technique, crude mitochondria are collected and further centrifuged, allowing the obtention, on the one hand, of a purified mitochondrial fraction and, on the other hand, a fraction containing organelles associated to mitochondria, being mainly ER. This technique is a gold standard to assess the presence of proteins in MAMs fractions and to evaluate, under specific conditions, how the abundance of those proteins may vary in the cells and in MAMs (117,118). It can also be used in association with mass-spectrometry to identify unknown proteins (119–121). Nevertheless, one limitation of this technique is the contamination with other organelles, which can affect result interpretations.

Techniques based on fluorescence can also be used to assess whether a protein is located in MAMs or the contacts between ER and mitochondria (98,122). Probes, plasmids or antibodies can be used for those purposes. The advantage of fluorescence-based techniques is the visual assessment of the protein of interest regarding ER and/or mitochondria. Depending on the

tools used, those techniques may even allow visualization of MAMs in living cells. It is also less time consuming than techniques such as TEM, where image analysis is often laborious. Nevertheless, microscope resolution constitutes a limitation and can impact result interpretations. To overcome this issue, some strategies have been developed, such as the fluorescence resonance energy transfer (FRET) (73), irreversible split fluorescent probes (73,123) or the use of reversible fluorescent reporters (73,124). This allows the detection of fluorescence where the ER is in proximity with mitochondria. Even if those techniques allow us to visualize MAMs, they constitute challenging approaches and cannot compete with TEM resolution for MAMs visualization.

In the MAMs research field, TEM is commonly used for the visualization of ER-mitochondria contact sites. Thanks to its resolution, it allows to quantify the distance between ER and mitochondria, the length of the ER membrane in contact with mitochondria and the mitochondrial perimeter (73,100). Nevertheless, this technique is time consuming for image analysis and cannot be performed on living cells.

The proximity ligation assay (PLA) is another technique often used to study MAMs. Similarly to immunofluorescence assays, one pair of primary antibodies are used against proteins of interest, followed by the addition of secondary antibodies conjugated to DNA oligonucleotides. Then, hybridizing connector oligonucleotides are added. They bind to the DNA oligonucleotides from the secondary antibodies, if they are in proximity. Following this step, a ligase creates a circular template for rolling circle amplification. Finally, the amplified DNA is detected using some fluorescent probes. In 2016, Tubbs and Rieusset provided an exhaustive protocol to study ER-mitochondria interactions by PLA on fixed cells (125). The authors proposed couples of proteins that could be used to study MAMs, such as the couple IP3R1 and VDAC1 as well as GRP75 and VDAC1. The advantage of this technique is its simplicity and rapidity, assessing alterations in contact sites. Nevertheless, this technique requires specific antibodies to avoid false positive signals. In addition, signals can be detected if less than 40 nm separate proteins of interest. Thus, upon small variations in distance between proteins, signals could still be detected, creating false negative results (125).

Besides the structural study of MAMs, some techniques also allow us to investigate functional alterations of MAMs. For instance, since MAMs have been involved in Ca^{2+} transfer, it is possible to study this transfer using probes or plasmids in living cells (see sections *Calcium transfer at*

MAMs modulates cellular metabolism and *Plasmid preparation and transfection*). Those tools allow the assessment of ER, cytosolic or mitochondrial Ca^{2+} level upon stimulation. It is particularly interesting as it is known that dysfunctional Ca^{2+} transfer to mitochondria can impact their metabolism. In the literature, a way to study this relationship between Ca^{2+} and mitochondrial metabolism has been published by Hajnoczky *et al.* in 1995, where vasopressin injection induced an increase in mitochondrial Ca^{2+} level and thus, mitochondrial dehydrogenases activity (126). This link was established using microscopy.

Besides Ca^{2+} transfer, MAMs have also been involved in lipid exchanges. One strategy to study lipid transfer between both organelles is to use radioactive isotopes ([3-^{3}H] Serine) and to check for the formation of PS, PE or PC by thin layer chromatography from different fractions (for instance, crude mitochondria or pure mitochondria) (116). In their article published in 2022, Peter *et al.* proposed the MATALIC method, where enzymes, able to tag phospholipids of interest, are send to ER or mitochondria (127). If the phospholipids are tagged twice, it means they were transferred between both organelles. In this case, the detection of tags was performed by mass-spectrometry.

1.3.5. Role of MAMs in cellular functions

1.3.5.1. MAMs are involved in mitochondrial dynamics

Mitochondria were often described as small, static, individual entities. However, thanks to imaging, it is known that mitochondria form a dynamic network that can undergo fission and fusion events (128). The fusion is characterized by the union of two mitochondria while the fission designates the division of one mitochondrion into two individual organelles (128). The concept of mitochondrial dynamics relies on the equilibrium between fission and fusion events (128). For instance, an excess of fusion or a lack of fission both lead to an apparent hyperfused network while an excess of fission or a lack of fusion both lead to a fragmented network. This dynamic depends on the cell type, the specific needs of the cell and the environment (128,129). Namely, under nutrient deprivation, mitochondria fuse to allow distribution of matrix components and to increase the surface of the IMM, and by consequence, the OXPHOS (128,130). On the opposite, fragmented mitochondrial networks have been described in high nutrient environment, cell division, apoptosis and prolonged stress (128,130,131).

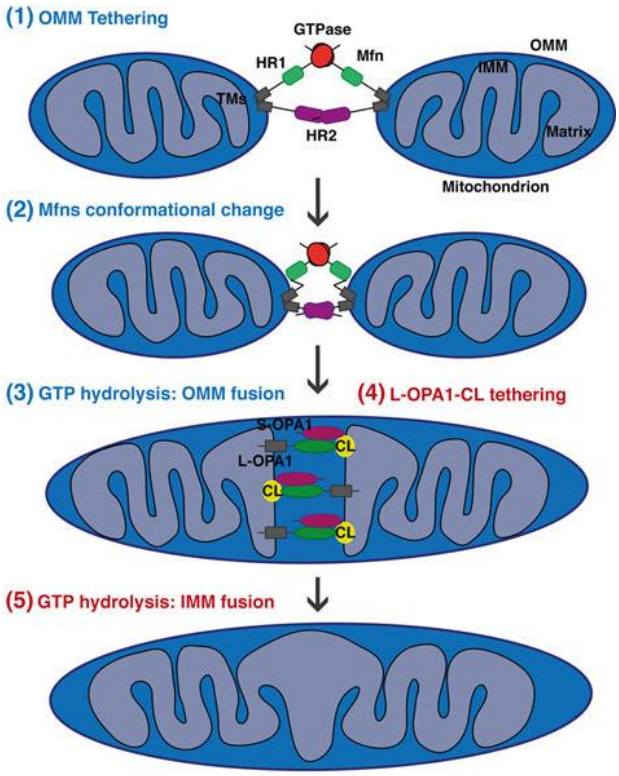

Figure 1-12. Steps leading to mitochondrial fusion. (1) MFNs tether mitochondria prior to fusion thanks to their HR domains. (2) Following this step, MFNs change their conformation and (3) GTP is hydrolyzed, leading to OMM fusion. Thanks to S-OPA1 and L-OPA1 as well as cardiolipin (CL), both IMMs fuse (4). This process involves GTP hydrolysis (5). This figure is adapted from Tilokani *et al*. (2018) (128).

Mitochondrial fusion is a fast event, occurring in less than 2 minutes and involving proteins such as mitofusins (MFNs) and optic atrophy protein 1 (OPA1) (Figure 1-12). While MFNs are involved in the OMM fusion, OPA1 participates to the IMM fusion (128,132,133). To allow the fusion, mitochondria have to be in proximity, where MFNs can accumulate and tether both mitochondria by forming hetero- or homo-typic complexes (128,133). This is followed by guanosine-5'-triphosphate (GTP) hydrolysis, triggering OMM fusion. Indeed, MFNs are GTPases, harboring a transmembrane domain, allowing MFNs insertion in the OMM. In addition, those proteins have a cytosolic N-terminal GTPase domain, allowing membrane fusion, and cytosolic C-terminal heptad repeats (HR) domains, allowing tethering (128,133). The MFNs family encompasses MFN1 and MFN2, each protein coming from distinct genes. Both MFNs are involved in mitochondrial fusion and have been described on mitochondria (134). However, differences exist between MFN1 and MFN2. For instance, MFN1 has been reported to have a higher GTPase activity and a higher efficiency for mitochondrial tethering than MFN2 (134). In addition, while MFN1 has been reported only on mitochondria, MFN2 has also been reported on the ER, and more precisely in MAMs, where it participates to the tethering

between both mitochondria and ER (98,135). Such tethering is essential to preserve the metabolic integrity of the platform. Beside MFNs, the IMM fusion requires the OPA1 GTPase, which supports IMM fusion through GTP hydrolysis. OPA1 is a protein located in the IMM, encompassing several isoforms required for IMM fusion, such as the isoforms S and L. Furthermore, OPA1-mediated fusion requires cardiolipin, a phospholipid enriched in the IMM (128,133). As it will be discussed in the *Lipid transfer occurs at MAMs and participates to mitochondrial membrane integrity* section, MAMs are involved in mitochondrial membrane integrity and can impact cardiolipin synthesis (80).

Mitochondrial fission is a multistep process, requiring the action of the ER as well as cytosolic and mitochondrial proteins (Figure 1-13) (128). During the first step of mitochondrial fission, the ER wraps around mitochondria, allowing actin to polymerize between both organelles. This is followed by constriction, reducing the mitochondrial diameter. Once the diameter is reduced, the cytosolic dynamin-related protein 1 (DRP1) is recruited by the OMM where it forms a ring-like structure around mitochondria. Due to its GTPase activity, DRP1 hydrolyzes GTP and further decreases mitochondrial diameter. Because DRP1 cannot bind directly the phospholipids, it is recruited by adaptor proteins located on the OMM (128). Those proteins accumulate at fission sites and include the mitochondrial fission factor (MFF), the mitochondrial fission 1 (FIS1) protein and the mitochondrial dynamics proteins 49 and 51 (MiD49 and MiD51) (136). Finally, in order to divide completely the mitochondria, another GTPase has been reported to be recruited at the fission site where it hydrolyzes GTP and finalizes the constriction (137). This protein, the dynamin-2 (DNM2), is involved in intracellular membrane trafficking, vesicle formation and endocytosis (128,138). Nevertheless, the role of DNM2 in mitochondrial fission has been recently challenged (139,140). In their study, Fonseca *et al.* showed that DNM2 knockdown cells (as well as triple-knockout cells for DNM1, DNM2 and DNM3) were still able to undergo mitochondrial fission. On the opposite, they observed a defect in mitochondrial fission upon DRP1 knockdown, showing the importance of DRP1 for fission while DNM2 seems to be dispensable (140).

As aforementioned, MAMs are involved in mitochondrial fission processes by constricting mitochondria prior to fission. In addition, some publications reported that Ca^{2+} transfer occurs between ER and mitochondria to allow IMM fission. Indeed, in their study published in 2017, Chakrabarti *et al.* demonstrated that rapid and elevated increase of Ca^{2+} in the matrix lead to

IMM constriction and mitochondrial fission (141). This Ca^{2+} -mediated mitochondrial fission has been shown to occur before the intervention of DRP1 and to be independent of this pathway (141). This observation was confirmed by another study, where Ca^{2+} overload conducted to a fragmented mitochondrial network, while mitochondrial Ca^{2+} depletion lead to an hyperfused mitochondrial network (142,143). In parallel, this is only since recently that mitochondrial fusion has been associated with MAMs. Indeed, in their article published in 2020, Abrisch *et al*. showed that mitochondrial fusion machinery also assembles at MAMs to modulate mitochondrial morphology. Interestingly, they found that 88% of mitochondrial fusion events occurred in those subcellular regions (144).

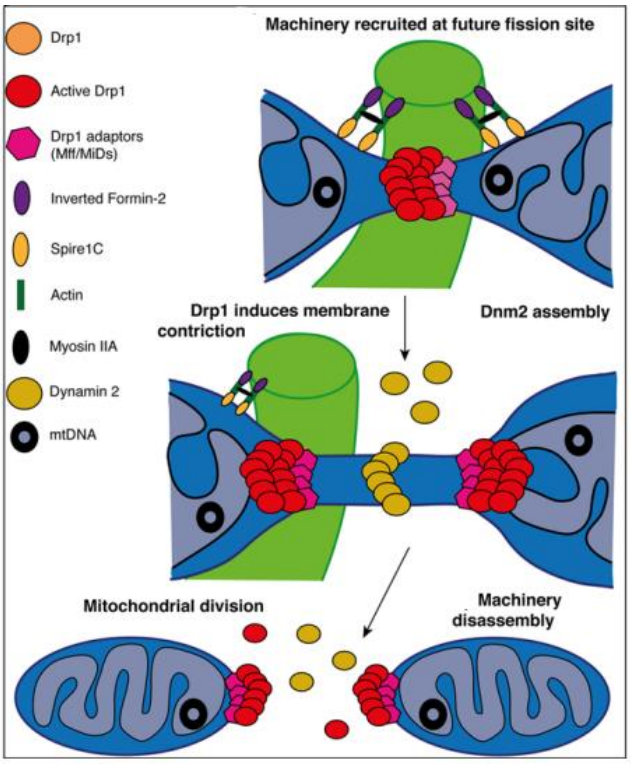

Figure 1-13. Mitochondrial fission. ER (in green) wraps around mitochondria to allow a first constriction. The constriction is achieved by actin polymerization between ER and mitochondria. This step is followed by the recruitment of DRP1 on the OMM thanks to adaptor proteins such as MFF or MIDs. After GTP hydrolysis by DRP1 and further constriction, the DNM2 protein finalizes the mitochondrial fission. This figure is adapted from Tilokani *et al*. (2018) (128).

1.3.5.2. Role of MAMs in cell death

Apoptosis is a programmed form of cell death that can occur through different pathways. One of those pathways involves mitochondria and is named the intrinsic pathway (145). As suggested by its name, this pathway induces cell death in response to intrinsic stimuli such as

ER stress, hypoxia, metabolic stress or DNA damages (146). Because it has been associated with MAMs, the following section describes the intrinsic pathway.

At the early stage of apoptosis, the pro-apoptotic BCL-2 associated-X and BCL-2 homologous killer proteins (BAX and BAK) accumulate and permeabilize the OMM, allowing proteins located in the intermembrane space, such as cytochrome c, to escape mitochondria (145). Once in the cytosol, cytochrome c associates with the procaspase-9 and the apoptotic protease activating factor-1 (APAF-1) into apoptosome. This triggers the activation of caspase-3 and caspase-7, which induces DNA fragmentation and cell death. BAX and BAK proteins are regulated by the B-cell lymphoma-2 and -extra-large (BCL-2 and BCL-XL) anti-apoptotic proteins by direct interaction (145). Those proteins have been extensively described in cancer as they promote cell survival. Besides BAX and BAK OMM permeabilization, the formation of the mitochondrial permeabilization transition pore (mPTP) has also been reported (147). In apoptotic conditions, the voltage-dependent anion channel 1 (VDAC1) and the adenine nucleotide translocase (ANT) proteins, which do not usually interact, form the mPTP channel. It allows the entry of water and ions into the mitochondrial matrix and provokes the matrix swelling and the dissipation of the mitochondrial electrochemical gradient (147). Therefore, the production of ATP is reduced and, as a consequence of mitochondrial swelling, the OMM breaks, leading to cytochrome c release into the cytosol (148,149).

Interestingly, Ca^{2+} has been described as leading to PTP formation. Under high level of Ca^{2+} in the mitochondria, Ca^{2+} interacts with cyclophilin D, a protein involved in PTP regulation, and conducts to PTP formation (148). MAMs have been associated with apoptosis due to their ability to act as a Ca^{2+}-delivery platform for mitochondria **(Figure 1-14)** (64–67). Indeed, modulation or alteration of MAMs can lead to mitochondrial Ca^{2+} overload and, thus, to cell death. It is worth mentioning that cyclophilin D has been shown to modulate Ca^{2+} transfer at MAMs by being part of a protein complex with key proteins involved in Ca^{2+} signaling (111,150). In cancer cells, Ca^{2+} transfer at MAMs is optimized to fit the metabolic needs and also to avoid apoptosis (64–67). Interestingly, this modulation of Ca^{2+} transfer at MAMs by cancer cells is often associated with (proto-)oncogenes, such as BCL-2 or the AKT (151).

Additionally, mitochondrial fission has also been associated with apoptosis. In their report, Frank *et al*. showed in 2001 that cells undergoing apoptosis displayed a fragmented mitochondrial network (152). The inhibition of DRP1 prevented mitochondrial fragmentation

as well as the release of cytochrome c and, by consequence, apoptosis (152). However, other studies have shown that, even if DRP1 inhibition reduced cytochrome c release and mitochondrial fission, it does not prevent BAX and BAK-induced apoptosis (153). Despite the controversy, those results may suggest that mitochondrial fission is closely related to apoptosis (152).

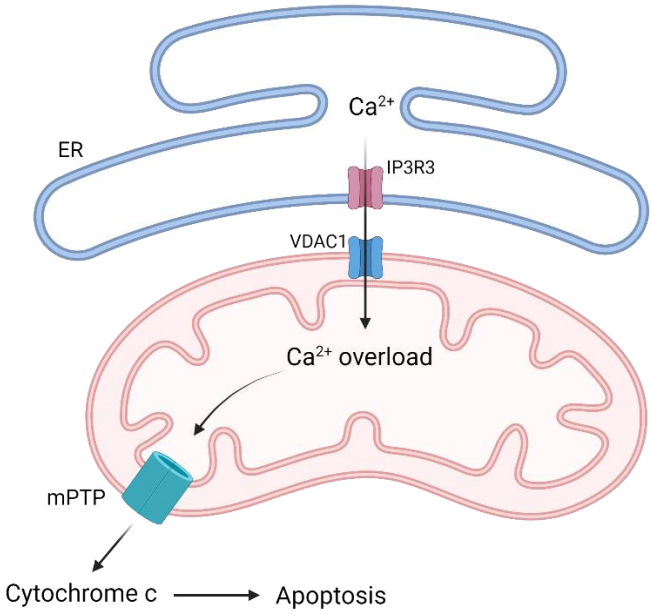

Figure 1-14. MAMs and intrinsic apoptosis. Mitochondrial Ca^{2+} overload induces the formation of mPTP, allowing cytochrome c release and apoptosis. Since MAMs constitute metabolic platforms where Ca^{2+} transfer occurs, they participate to apoptosis. Created with BioRender.com

1.3.5.3. Calcium transfer at MAMs modulates cellular metabolism

The intracellular Ca^{2+} concentration varies according to its localization **in the cell (Figure 1-15)**. In order to sense faint variations in Ca^{2+} as a signal, cytosolic Ca^{2+} has to be maintained at low concentration of approximatively $[Ca^{2+}]_c$= 0.1 µM **(Figure 1-15)** (154,155). To achieve this goal, Ca^{2+} is extruded out of the cell thanks to the plasma membrane Ca^{2+}-ATPase (PMCA) and the Na^+/Ca^{2+} exchanger (NCX), located on the plasma membrane (154,155). In addition, the cell pumps Ca^{2+} into the ER by the SERCA pump. Indeed, the ER is the main intracellular Ca^{2+} store, where the $[Ca^{2+}]_{ER}$ can reach up to 500 µM in resting conditions **(Figure 1-15)** (154). In addition to the ER, mitochondria can accumulate Ca^{2+}upon stimulation but in a lesser extent. Indeed, in resting conditions, the mitochondrial Ca^{2+} concentration ($[Ca^{2+}]_{mt}$) is similar to the $[Ca^{2+}]_c$, but under high level of Ca^{2+} in the cytosol (0.2-5 µM), $[Ca^{2+}]_{mt}$ can rise up to 100 µM **(Figure 1-15)**

(155). Therefore, even if mitochondria do not play a role of intracellular Ca^{2+} store as the ER does, they modulate Ca^{2+} signaling thanks to their ability to accumulate reasonable amounts of Ca^{2+} (156). Remarkably, this buffering capacity can modulate Ca^{2+} propagation inside the cell. For instance, in pancreatic acinar cells, mitochondria create a perinuclear ring which acts as a firewall, preventing the propagation of Ca^{2+} signaling from the apical to the basal region of the cell **(Figure 1-15)** (156,157).

Many stimuli including membrane depolarization, mechanical stress, extracellular or intracellular messengers can lead to a $[Ca^{2+}]_c$ increase (154,155). This phenomenon is mediated by Ca^{2+} channels located on the plasma membrane, such as transient receptor potential channels (TRPCs) mainly found in non-excitable cells, or by the release of Ca^{2+} from the ER through the IP3Rs or by the ryanodine receptor (RyR) in the case of sarcoplasmic reticulum (154,155). A good illustration of a process involving IP3Rs and TRPCs is the effect of **histamine stimulation** on Ca^{2+} signaling **(Figure 1-15)**. Indeed, upon histamine binding to its G-protein coupled receptor, the phospholipase C (PLC) is activated (154,158). Activated PLC cleaves the phosphatidylinositol 4,5 biphosphate (PIP2) into inositol triphosphate (IP3) and diacylglycerol. While diacylglycerol contributes to TRPCs activation, IP3 diffuses throughout the cytosol and binds to its receptor (IP3R) located on the ER, allowing Ca^{2+}release in the cytosol. Once completed, the cell has to restore its basal ER Ca^{2+} level. This phenomenon is named the store-operated Ca^{2+}entry, which is mediated by the stromal interaction molecule-1 (STIM1) and the calcium release-activated calcium channel protein 1 (ORAI1), both located in plasma membrane-ER contact sites **(Figure 1-15)** (154). In order to restore basal $[Ca^{2+}]_c$, Ca^{2+} is extruded out of the cell thanks to PMCA and NCX channels and, in parallel, is pumped back into the ER thanks to the SERCA pump **(Figure 1-15)**. Interestingly, cell stimulation with histamine in a Ca^{2+}-free medium conducts to a rise of $[Ca^{2+}]_{mt}$. Because of the Ca^{2+}-free medium, the observed increase of $[Ca^{2+}]_{mt}$ is related to the internal Ca^{2+} stores, which are closely apposed to mitochondria (154,155). In this context, MAMs play an important role in Ca^{2+} transfer between both ER and mitochondria, creating a synapse-like structure. Such structures allow efficient Ca^{2+} transfer to mitochondria (126,159).

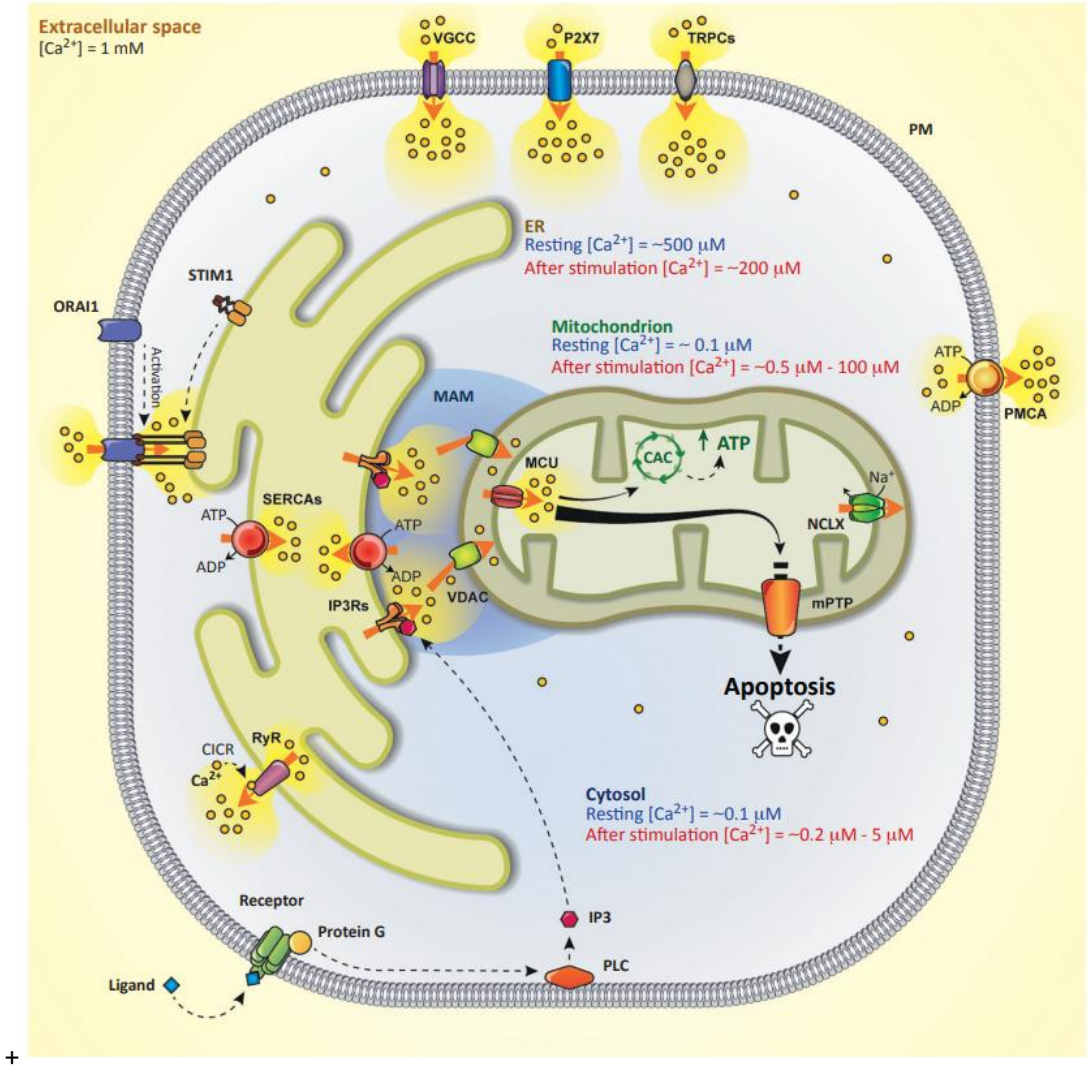

Figure 1-15. Cytosolic and mitochondrial Ca^{2+} concentration in the cell at resting conditions is ~0.1 µM, while in ER, this concentration is about ~500 µM. To maintain low cytosolic Ca^{2+} concentration, the excess of Ca^{2+} is pumped out of the cell thanks to the PMCA or pumped in the ER thanks to the SERCA pump. Upon stimulation, the PLC is activated, resulting in the production of IP3. This last one diffuses in the cytosol until it binds to its receptor (IP3R) located on the ER. This induces Ca^{2+} release from the ER. The transfer of Ca^{2+} to mitochondria can efficiently occur at the contact sites existing between ER and mitochondria (MAMs). Ca^{2+} enters mitochondria through VDAC and MCU, where it regulates mitochondrial respiration and ATP production. If the Ca^{2+} concentration is sustained in time and elevated, it could cause apoptosis. The Ca^{2+} concentration after stimulation is annotated in red. This illustration comes from Giorgi *et al.* (2018) (154).

Effective **Ca^{2+} transfer occurring at MAMs** is crucial for bioenergetic, apoptosis and mitochondrial dynamics (141,154). This is ensured by an optimal distance (usually < 30 nm) separating both ER and mitochondria membranes (83). Under stimulation (e.g. histamine), Ca^{2+} is released through IP3Rs and is brought into mitochondria through VDAC1. In order to maximize and facilitate Ca^{2+} exchange, IP3Rs and VDAC1 create a physical bridge, stabilized by the GRP75 (97,160,161). Once in the intermembrane space, Ca^{2+} ions accumulate and create high Ca^{2+} microdomains, allowing the opening of the mitochondrial calcium uniporter (MCU) located on the IMM. Due to the presence of electrochemical gradient across the IMM (-180

mV), Ca^{2+} enters the mitochondrial matrix (154). Nevertheless, it is soon extruded from mitochondria thanks to the $Na^+/Ca^{2+}/Li^+$ exchanger (NCLX) located on the IMM. This channel allows the exchange of Na^+ for Ca^{2+}. However, in order to avoid accumulation of Na^+ inside the matrix, the cation is exchanged for H^+ by the Na^+/H^+ exchanger located on the IMM. Thus, under $[Ca^{2+}]_c$ increase or Ca^{2+} release from ER at MAMs, the pattern of $[Ca^{2+}]_{mt}$ over time is transient and resembles a narrow peak (155).

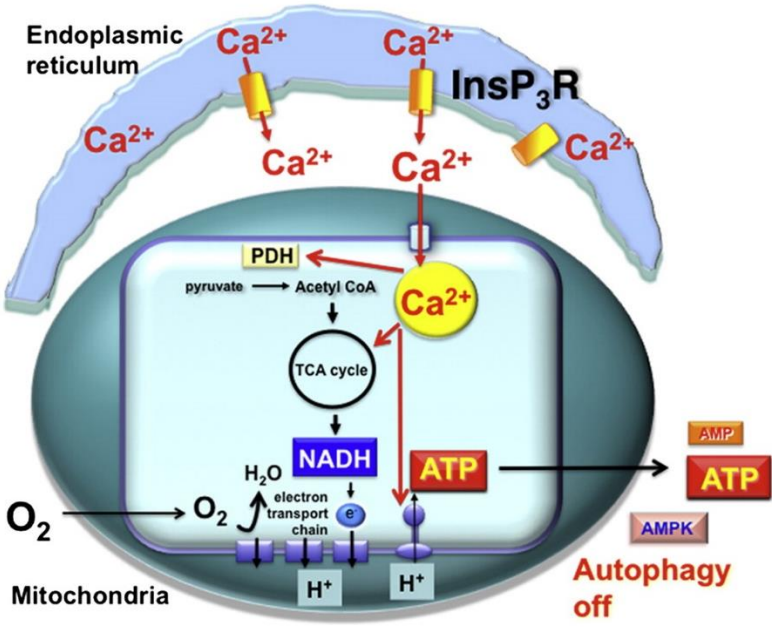

Figure 1-16. Ca^{2+} transfer at MAMs regulates mitochondrial respiration and ATP production. Ca^{2+} acts as a cofactor of enzymes involved in the TCA cycles and is involved in the PDH phosphorylation. Reduced Ca^{2+} transfer at MAMs results in decreased ATP production and activation of AMPK, which leads to increased autophagy. This illustration comes from Cardenas *et al.* (2010) (162).

It is was reported that **Ca^{2+} strongly influences mitochondrial bioenergetic** by enhancing ATP production and OXPHOS **(Figure 1-16)** (160). Indeed, this cation stimulates activity of the IDH and α-KGDH as well as the ATP synthase (160,163,164). Moreover, the phosphatase responsible of PDH dephosphorylation and activation is dependent on Ca^{2+} (165). Therefore, if mitochondria run out of Ca^{2+}, the TCA cycle slows down its activity, producing less $NADH,H^+$ and reduced flavin adenine dinucleotide ($FADH_2$) required for the ETC. As a result, the oxygen consumption rate (OCR) is reduced as well as the ATP production (160). This can lead to AMP-activated protein kinase (AMPK) activation and pro-survival autophagy (154). Considering the fact that mitochondria are less sensitive to cytosolic Ca^{2+} fluctuation, their dependency on

MAMs for Ca^{2+} supply is significant, meaning that MAMs impairment can greatly impact the cell bioenergetic (126,159). Muscle contraction is a perfect illustration of the relationship existing between Ca^{2+} and cellular bioenergetic. Indeed, under muscular contraction, the cell requires large amounts of ATP. This demand is, in part, reached thanks to the proximity existing between mitochondria and sarcoplasmic reticulum, allowing Ca^{2+} supply to mitochondria and, by consequence, increased ATP production (166). The study of Combot *et al.* published in 2022 also illustrates this relationship (167). In their study, they investigated a protein named seipin, which is enriched in the ER membrane of MAMs. This protein was interacting with Ca^{2+} regulators in MAMs and its deficiency impaired mitochondrial Ca^{2+} import. This lead to reduced ATP production and level of TCA cycle intermediates (citrate, alpha-ketoglutarate, fumarate, malate and succinate). Those observations were also reported by Ding *et al*. in 2018, where they showed that seipin promoted lipogenesis by controlling Ca^{2+} transfer between ER and mitochondria (168). Indeed, upon seipin deficiency, *NCLX* knockdown reversed the lipogenesis deficiency.

As mentioned in the *Role of MAMs in cell death* and *MAMs are involved in mitochondrial dynamics* sections, Ca^{2+} is also involved in apoptosis and mitochondrial fission, meaning that Ca^{2+} has both beneficial and detrimental effects on the cell (141,154). In fact, accurate and fine tuning of Ca^{2+} signaling is essential for cell fate and metabolism. In this context, MAMs and its relative role in Ca^{2+} transfer have been associated with disorders such as cancer, PD, and AD (85,86).

As already mentioned, key proteins are involved in Ca^{2+} transfer at MAMs. They include IP3Rs, VDACs and MCU. VDACs are abundant proteins of approximatively 30-35 kDa, located on the OMM. Three isoforms (VDAC1, VDAC2 and VDAC3) are expressed in mammals and display specific characteristics such as gating threshold, localization and interaction with proteins (160,169,170). VDACs are not homogeneously distributed in the OMM and the main isoform located in MAMs is VDAC1 (97,160,171). For this reason, we will focus mainly on this isoform. As indicated by its name, VDAC1 is a voltage-dependent channel. *In vitro* studies, performed with purified VDAC1 and artificial lipid bilayers, revealed that between -30 to +30 mV, VDAC1 is in a high conductance state, often referred to as open-state. In this range of potentials, VDAC1 is permeable to small (<5 kDa) neutral molecules, and to negatively charged molecules such as ADP or ATP as well as inorganic phosphate (160). Beyond this range, the channel

changes its conformation and becomes gated. Interestingly, this change of conformation reduces the permeability for negatively charged and small neutral molecules, while it increases the conductance for Ca^{2+} (160). Despite the fact that *in vitro* studies provide us with essential information for the understanding of voltage-dependent channels, the conformation of VDAC1 under physiological conditions is still unclear and under debate (160). In parallel to voltage dependency, VDAC1 is modulated by other mechanisms. Indeed, some metabolites such as $NADH^{+}$ or some domains of interacting proteins may close the porin by occlusion. Moreover, Ca^{2+} itself has the capacity to increase its own conductance by binding to VDAC1. Finally, the lipid composition of the OMM, the protein interactions and the post-translational modifications, such as phosphorylation, also modulate the porin conformation (160,169,170).

Beside VDAC1, MCU is a 40 kDa protein located on the IMM, allowing Ca^{2+} entry into the mitochondrial matrix. This protein is found in all mammalian tissues but its activity varies among tissues according to interacting partners (155,172,173). A high $[Ca^{2+}]$ is required for the channel opening, explaining why the correct alignment of IP3R3-VDAC1-MCU proteins leads to Ca^{2+} loading into mitochondrial matrix (155,174,175). MCU is modulated by proteins such as the EF-hand Ca^{2+}-sensing proteins 1 and 2 (MICU1 and MICU2), conducting to the channel opening under increasing $[Ca^{2+}]$ (155). Compared to the SERCA pump, MCU has a lower affinity for Ca^{2+} but its transport rate for the cation is higher, meaning that the SERCA pump is more suitable to respond to modest elevation of $[Ca^{2+}]_c$ (155). Remarkably, MCU silencing modulates the cell metabolism by reducing ATP production and OXPHOS activity (176). This observation highlights once again the connection existing between Ca^{2+} and mitochondrial metabolism.

Finally, the last channel often described in Ca^{2+} transfer at MAMs is IP3R. This channel is the result of homo- or hetero-tetramerization of four subunits encoded either form *the Inositol 1,4,5-Trisphosphate Receptor Type 1, 2 or 3* genes (*ITPR1*, *ITPR2* or *ITPR3* genes, respectively) and giving rise to IP3R1, IP3R2 or IP3R3 proteins (177). This homo- or hetero-tetramerization is thought to confer diversity for IP3Rs. Indeed, all IP3R isoforms do not display the same properties. For instance, they do not have the same affinity for IP3, IP3R2 having the highest affinity for this molecule, while IP3R3 has the lowest affinity (178). In addition, post-translational modifications of isoforms also contribute to the complex diversity of IP3Rs. Those channels are located on the ER and also on the Golgi apparatus, where they allow Ca^{2+} release from those organelles (178,179). All the IP3R subunits must bind IP3 to allow the opening of

the channel (178). The IP3Rs Ca^{2+} release can be regulated, for instance, by cytosolic and ER Ca^{2+}, phosphorylation, ATP and also by proteins such as BCL-2 or BCL-XL (178). As mentioned previously, IP3Rs are found in MAMs, where they promote efficient Ca^{2+} transfer (180). Historically, the main IP3R isoform studied in MAMs was IP3R3, because it was found to be abundant in MAMs (180,181). Nevertheless, recent studies showed that IP3R1 as well as IP3R2 can also be found in MAMs (182).

1.3.5.4. Lipid transfer occurs at MAMs and participates to mitochondrial membrane integrity

ER has been described as the major place for phospholipid synthesis in the cell (80). Thanks to specific enzymes located on its external phospholipid layer, the ER synthetizes the majority of phospholipids required for membrane integrity. Once synthesized, phospholipids are conveyed to their final destinations through vesicular or non-vesicular transport. The ER can establish membrane contacts with other organelles, such as mitochondria, to allow phospholipid exchanges (80). Indeed, even if mitochondria can synthetize some of their own phospholipids such as phosphatidylethanolamine (PE), they require phosphatidylserine (PS), phosphatidylcholine (PC) and phosphatidic acid (PA) from the ER (183). As a side note, because mitochondria were not considered as being part of the endomembrane system, it was reported to establish contact sites with ER to allow phospholipid exchanges. Nevertheless, it is now known that mitochondria generate mitochondrial-derived vesicles, being for instance targeted to lysosomes, endosomes or peroxisomes (184).

More specifically, the interplay between ER and mitochondria allows the transfer of PS to the mitochondria where it is converted to PE thanks to the PS decarboxylase (PSD). A fraction of PE is then sent back to the ER where it is converted to PC by the PE methyl-transferase (PEMT). Finally, PC is sent to the mitochondrial membrane, where it participates to its integrity **(Figure 1-17)** (80). In addition to this exchange to provide PS and PC to mitochondria, another process involving oxysterol binding proteins like (ORP) 5 and 6 allows the transfer of PS to mitochondria via the interaction with the PTPIP51 located in the OMM. Depletion of ORP5 and 6 has been shown to impact mitochondrial morphology and respiration, suggesting a role of lipid transfer on mitochondrial dynamics and metabolism (185).

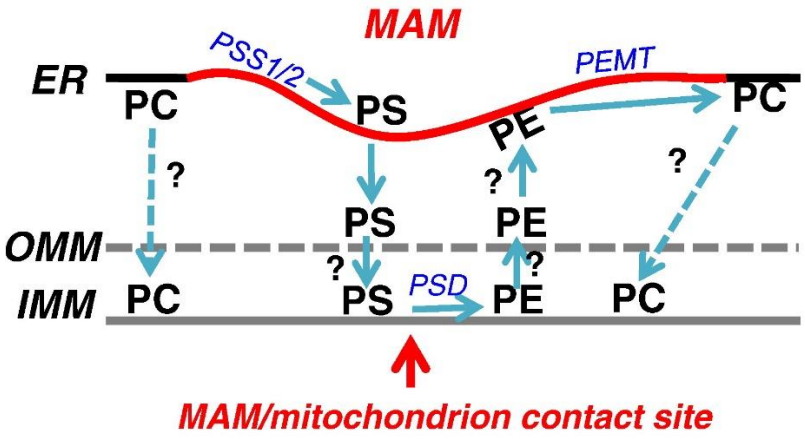

Figure 1-17. Phospholipid transfer occurring at MAMs and participating to mitochondrial membrane integrity. PS is transferred to mitochondria, where it is converted to PE thanks to the PSD. Then, a fraction of the PE is conveyed to the ER and converted into PC thanks to the PEMT. Finally, the PC is transferred to the mitochondria. Dotted lines and question marks represent undefined pathways. The picture is from the publication of Jean.E.Vance (2014) (80).

Besides **phospholipid transport**, MAMs also allow the transfer of PA from ER to mitochondria **(Figure 1-18)**. Even if mitochondria have the capacity to synthetize PA, the majority of mitochondrial PA originates from the ER. Once in the mitochondria, PA is used as a precursor of cardiolipin, a very important and specific phospholipid component of the IMM as it regulates several mitochondrial processes such as Ca^{2+} signaling, ETC activity, apoptosis and ROS signaling (186). Without close and functional membrane apposition, this lipid transfer would not take place and would impair **cardiolipin synthesis**, required for mitochondrial integrity (183).

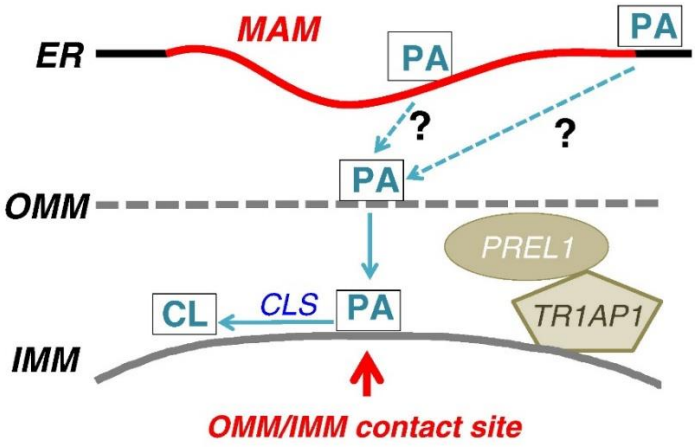

Figure 1-18. Transfer of PA from ER to mitochondria occurring at MAMs. Once transferred to mitochondria, the PA is converted into cardiolipin (CL) thanks to the cardiolipin synthase (CLS). PREL1 and TR1AP1 are part of a protein complex able to transfer PA from the OMM to the IMM. Dotted lines and question marks represent undefined pathways. The picture is from the publication of Jean.E.Vance (2014) (80).

In addition to phospholipid exchange, MAMs participate to **steroid synthesis**. After entering the cell or being synthetized *de novo* in the ER, cholesterol may be used by the cell or stored in lipid droplets. Storage in lipid droplets requires cholesterol esterification by the ACAT1 enzyme

which is enriched in MAMs and even used as a MAMs marker (187). Cholesterol can also be transported to the IMM where it is converted to pregnenolone, a hormone precursor, by the cytochrome P450 cholesterol side chain cleavage enzyme (CYP11A1). The cholesterol translocation from the OMM to the IMM is achieved by a protein complex located in MAMs. Once synthetized, the pregnenolone is sent back to the ER where it can be used for further reactions (80,188).

Additionally, similarly to lipid rafts found on the plasma membrane, MAMs are enriched in cholesterol, sphingolipids and ceramides, supporting their role as a platform for lipid transfer (189). Cholesterol clustering in MAMs has been shown to be a protein-mediated process. Sigma-1 receptor (S1R) is an ER transmembrane chaperone protein, containing two sterol-like binding domains able to attach cholesterol and induce its clustering in MAMs (190). Due to its high abundance in MAMs, S1R has been validated and often used as a MAMs marker (118,189).

Alongside S1R, another protein named caveolin-1 (CAV1) has been found in MAMs. CAV1 has been extensively studied in lipid raft dependent-endocytosis, where it plays a role of scaffolding protein (191). However, its role in MAMs has been less investigated. In 2016, Sala-Vila *et al.* have identified CAV1 as enriched in MAMs of healthy mouse livers. The absence of CAV1 lead to a mitochondrial fragmented network. Proteomic studies performed on MAMs extracts showed that CAV1 knock-out mice displayed a reduced amount of proteins involved in steroid metabolism and cholesterol biosynthesis. Interestingly, this reduced amount of proteins was only visible in MAMs extracts and not in total cell extracts, suggesting a role of CAV1 in protein sorting at MAMs (95). In addition, the presence of CAV1 in MAMs is believed to regulate cholesterol transfer towards mitochondria. Indeed, the absence of CAV1 leads to an accumulation of cholesterol in mitochondria, resulting in impaired respiration as well as glutathione activity and increased of ROS production (192).

1.3.5.5. MAMs are involved in autophagosome formation and mitophagy

Autophagy is a process responsible for the recycling of cytosolic components. While this process is found at basal level in cell, allowing turnover of cytoplasm constituents, it is also induced during nutrient starvation (193). Autophagy is a complex multistep process and whether it is beneficial or detrimental for the cell depends largely on the context. For instance, in PDAC, autophagy sustains survival and proliferation of cancer cells (194). However, even if it

represents an advantage for those cells, exacerbated and prolonged autophagy is detrimental, leading to cell death (195).

At cellular level, autophagy, referred here to as macro-autophagy, consists of several steps and starts with the formation of an "isolation membrane" also named phagophore. This phagophore encloses a portion of the cytoplasm by folding on itself, forming an autophagosome. The fusion of autophagosomes with lysosomes for the degradation of cytosolic components leads to the formation of autolysosomes, also called autophagolysosomes (196). At the end of the process, sugars, amino acids, fatty acids and nucleotides obtained from molecule degradation are recycled through anabolic pathways or used to generate energy (193,196,197). Those steps are regulated by specific sets of proteins including the autophagy-related proteins (ATGs) that participate in formation and development of autophagosomes (196). Interestingly, the origin of membranes leading to autophagosome formation is still unknown but recent evidences show that MAMs could initiate their formation (196). Indeed, in their report, Hamasaki *et al.* showed in 2013 that ATG14 and ATG5, which are markers of autophagosome formation, are localized in MAMs under nutrient starvation (198). Interestingly, they found that MAMs disruption under MFN2 or PACS-2 silencing prevented ATG14 and ATG5 localization at MAMs. They also found that the SNARE protein syntaxin-17 (STX17) was responsible for ATG14 recruitment in ER-mitochondria contact sites. Surprisingly, STX17 knockdown cells presented an accumulation of phagophores while almost no autolysosomes were observed (198). Later, it has been shown that STX17 participated to the induction of a non-canonical mitophagy through the recruitment of ATG14 at MAMs (199). In addition, Gelmetti *et al.* showed in 2017 that PTEN-induced kinase 1 (PINK1) and Beclin-1, both involved in mitophagy, relocalized at MAMs following mitophagy induction. This promoted ER-mitochondria tethering and autophagosome formation (200). Alongside the discovery of Hamasaki and Gelmetti, the Ras-related protein RAB32 (RAB32) has also been identified in contact sites between ER and mitochondria where it triggers degradation of MAMs in a process called *MAM-phagy,* showing a new process involved in MAMs regulation (201). Finally, inhibition or silencing of IP3Rs and MCU leads to a strong induction of autophagy. Indeed, preventing Ca^{2+} transfer to mitochondria could reduce ATP production, resulting in AMPK activation and autophagy induction (202).

1.3.5.6. Proteins involved in inflammation and anti-viral responses are localized in MAMs

Besides its role in lipid metabolism, Ca^{2+} transfer, mitochondrial dynamics, apoptosis and autophagy, MAMs are also involved in inflammation, by providing critical sites for inflammasome formation. Indeed, upon elevated ROS production by mitochondria, the NLR family pyrin domain containing 3 (NLRP3) protein activates and relocates from the ER and the cytosol to MAMs, in order to efficiently sense the presence of ROS. There, it associates with adaptor proteins and caspases, forming inflammasomes. (203,204). Besides NLRP3, MAMs have also been involved in antiviral response. One example implies the mitochondria anti-viral signaling protein (MAVS) located on the OMM (119,203). Localization studies found that the major place for MAVS signaling exists in contacts between ER and mitochondria (119,205). In a model proposed by Vazquez et *al.* in 2015, MAVS is maintained inactive in MAMs by proteins such as MFN2 (206). Upon virus infection, MAVS becomes activated and oligomerized, forming a signaling complex and triggering antiviral response (206).

1.3.5.7. MAMs participate to ER stress relief

The ER is the main site for chaperone-assisted folding and post-translational modifications. Proteins synthesized by ER-bound ribosomes are destined to the Golgi apparatus, plasma membrane, extracellular space as well as to the ER itself (207). Once delivered into the ER lumen, proteins undergo post-translational modifications and should be folded properly into a correct three-dimensional conformation by ER chaperone proteins (207). The chaperone heat shock protein-70 (HSP70) and the binding immunoglobulin protein (BIP) are the most abundant proteins in ER and exert important functions (207). For instance, BIP plays a major role in protein folding by avoiding protein aggregation. In addition to chaperones, pathways involved in degradation, such as the ER-associated degradation pathway (ERAD), avoid unfolded protein accumulation (207).

However, some situations such as hypoxia, nutrient deprivation or aberrant Ca^{2+} level (208) may conduct to overload of unfolded proteins, which could be toxic and lead to cell death. The large amount of unfolded proteins triggers a substantial stress which is referred to as “ER stress” (207). In response to the ER stress and in order to restore protein folding capacity, a process called unfolded protein response (UPR) is initiated. Three main actors, located on the ER, participate to this response: the inositol requiring enzyme 1 (IRE1), the PKR-like ER kinase

(PERK) and the activating transcription factor 6 (ATF6) (207). IRE1 and PERK share similarities in structure and response. IRE1 triggers the activity of the transcription factor X-box-binding protein-1 (XBP1) that, in turn, increases the ER capacity for protein folding and degradation. On the other hand, PERK phosphorylates the eukaryotic translation factor-2α (eIF2α). This globally suppresses protein translation, with the exception of the transcription factor 4 (ATF4) mRNA, which is preferentially translated (207,209). The purpose of the UPR is to restore ER homeostasis and ensure cell survival. However, if the ER stress is sustained and severe, signaling pathways switch in favor of apoptosis. For instance, under sustained activation of PERK, the transcription factor C/EBP-homologous protein (CHOP) is upregulated and induces transcription of gene involved in apoptosis regulation (207).

Remarkably, MAMs have been involved in a metabolic response observed during ER-stress (109,111). Indeed, in order to function properly, chaperone proteins require large amounts of ATP (210) and Ca^{2+} as a cofactor (207). Under ER stress, synthesis of ER chaperones increases to overcome accumulation of unfolded proteins. As a consequence, the number of contacts between ER and mitochondria expands, allowing higher mitochondrial Ca^{2+} uptake. Consequently, the OCR rises and mitochondria produce more ATP, helping the cell to relieve the ER stress (211). This adaptive response, with Ca^{2+} as a key actor, is of major importance as blocking IP3Rs increases cell death upon ER stress (211).

In addition, several studies showed that the alteration of MAMs components impaired ER stress management, confirming the importance of ER-mitochondria coupling. Indeed, in addition to its role in lipid composition, S1R is also involved in Ca^{2+} homeostasis. In resting condition, S1R interacts with BIP but, upon stimulation or ER Ca^{2+} release, S1R dissociates from BIP and interacts with IP3R3, which results in prolonged Ca^{2+} signaling. The upregulation of S1R has been shown to counteract ER stress, while its depletion favors apoptosis (212). Furthermore, the protein MFN2, which is involved in mitochondrial dynamics, is also a major component of MAMs where it tethers both ER and mitochondria. MFN2, but not MFN1 deletion, has been shown to exacerbate ER stress and to induce cell death (213,214). Finally, it has been demonstrated that IRE1α has the ability to distribute IP3Rs at MAMs by working as a scaffold (215). Through this function, IRE1α modulates mitochondrial Ca^{2+} uptake and thus, metabolism (215). Altogether, those studies show the importance of MAMs regulation through Ca^{2+} transfer in response to ER stress.

1.3.6. Implication of MAMs in diseases

As mentioned previously, MAMs participate in several cellular functions such as lipid transfer, autophagy, inflammation, response to ER stress and Ca^{2+} dynamics. Therefore, impairment of MAMs can have dramatic effects on cell physiology (66). For instance, MAMs disruption has been associated with diseases such as PD, AD and cancers (66). In the following work, we will mainly focus on cancer and briefly approach PD and AD disorders.

MAMs have been associated with cancer in numerous studies, where they are involved in cell proliferation and resistance to apoptosis (64). In this context, Ca^{2+} is a key modulator. While a sustained and a high level of Ca^{2+} inside mitochondria triggers apoptosis, its shortage conducts to a drop in ATP production, leading to AMPK activation and, eventually, cancer cell death (64,65). Therefore, it is not surprising that channels such as IP3R3, MCU and VDAC1, playing key roles in Ca^{2+} dynamics in MAMs, have been reported in cancer progression (64,65).

Several studies demonstrated the importance of IP3R3 in cancer progression and some of them have even discussed about "cancer addiction" to this protein (70). In this context, IP3R3 has been found to be overexpressed in several type of cancers such as colorectal (216), breast (68), renal (69) and bile duct (70) cancers. In the study conducted by Shibao *et al.* in 2010, IP3R3 was not present in normal colorectal mucosa, but was only found in colorectal cancer tissues. In addition, they showed a significantly reduced survival of patients displaying a higher expression of IP3R3. Interestingly, knockdown of this channel in colon cancer cell lines enhanced apoptosis (216).This discovery was confirmed in 2019 by Rezuchova *et al*. who demonstrated the importance of IP3R3 for cancer cell survival, proliferation and tumor growth in colon cancer (69). In a similar study published in 2022 on breast cancer, researchers found that the expression of IP3R3 was significantly higher in breast cancer tissues compared to normal ones and was accompanied by a significant reduction of the overall survival (68). Finally, those observations were also confirmed in cholangiocarcinoma, where IP3R3 silencing decreased cell proliferation by prolonging the S phase of the cell cycle and finally induced cell necrosis (70).

This effect on cell proliferation and death has been associated with IP3R3 capacity to regulate cellular bioenergetics thanks to Ca^{2+} transfer to mitochondria (67,112,162,217–219). Indeed, fueling the TCA cycle does not only provide energy to the cell but also biosynthetic precursors required for proliferation. Altogether, those results demonstrate the ability of some cancer cells to cope with IP3R3 upregulation and to use this feature at their advantage to fulfil their

metabolic needs. Therefore, targeting IP3Rs in cancer seems to be a promising therapeutic approach. In their study published in 2016, Cardenas *et al.* showed that inhibition of IP3Rs impaired mitochondrial metabolism and induced a bioenergetic crisis involving AMPK in both tumorigenic and non-tumorigenic cell lines **(Figure 1-19)**. However, cell death was mainly observed in tumorigenic cells. Interestingly, non-cancer cells stopped their cell cycle in the G1 phase while cancer cells progressed in cell cycle, leading to mitotic cell death. The authors proposed that cancer cells undergoing mitosis are not able to cope with the energetic crisis due to their capacity to bypass cell cycle checkpoints (for instance, with *TP53* mutations) **(Figure 1-19)** (67). Even if those results provide a better comprehension regarding the importance of Ca^{2+} signaling for cancer cells, further studies considering the proliferative state and the genetic background of the tumor should be performed.

On the other hand, IP3Rs modulation can also contribute to apoptosis resistance. Indeed, BCL-2 has been shown to directly target all IP3R isoforms, decreasing their ability to transfer Ca^{2+} to mitochondria and protecting cells from apoptosis. Remarkably, in chronic lymphocytic leukemia cells, the use of peptide, resembling and acting as a competitor of IP3Rs, disrupts interaction of BCL-2 with the channel. As a consequence, an elevated $[Ca^{2+}]_{mt}$ was observed in cancer, but not in normal cells (which depend less on BCL-2), and drove cells to apoptosis (220). Moreover, *KRAS* (G13D mutation) colon cancer mutated cells have been described as being less sensitive to apoptosis thanks to the downregulation of Ca^{2+} signaling occurring at MAMs and involving IP3Rs (217). Finally, it is worth mentioning that AKT, which is often over-activated in cancer, is able to phosphorylate IP3Rs in order to prevent Ca^{2+} release from the ER and thus protect cells from apoptosis (151). Whereas PTEN negatively regulates AKT activity by dephosphorylation of PIP3 into PIP2, it has also been reported in MAMs, where it interacts with IP3Rs and favors Ca^{2+} transfer to mitochondria. In their publication, Bononi *et al.* hypothesized that PTEN may counteract the activity of AKT by dephosphorylation of IP3Rs (221). Furthermore, in their study published in 2017, Kuchay *et al.* showed that PTEN competes with the F-box/LRR-repeat protein 2 (FBXL2) for IP3R3 binding, preventing IP3R3 degradation and thus, favoring Ca^{2+} transfer to mitochondria (222).

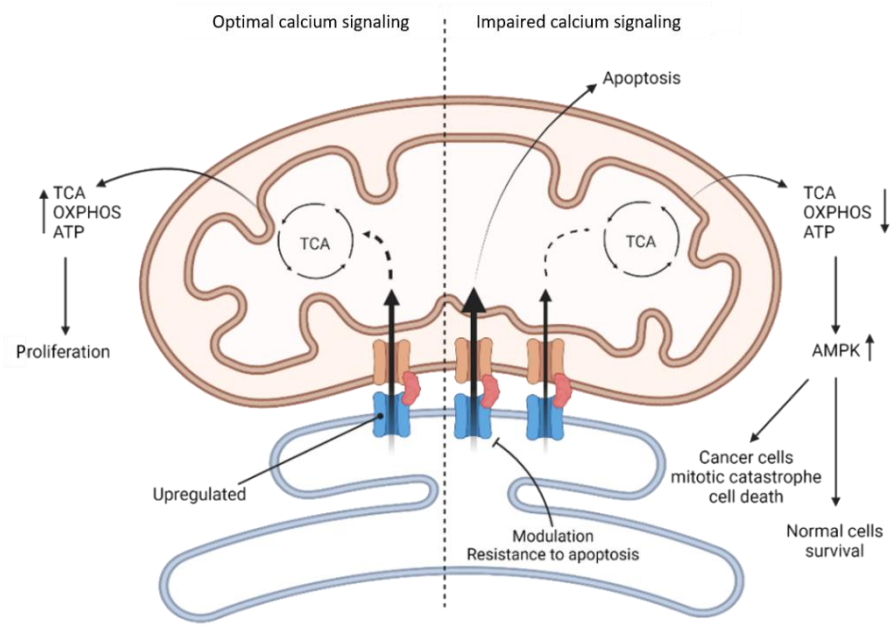

Figure 1-19. When Ca^{2+} signaling reaches the metabolic needs of cancer cells, it sustains their proliferation through optimal ATP and biosynthetic precursors production. Proteins involved in Ca^{2+} transfer at MAMs are often upregulated but also modulated to avoid apoptosis. Impaired regulation of Ca^{2+} signaling at MAMs can lead to cancer cell death, through Ca^{2+} overload inside mitochondria or through reduced mitochondrial Ca^{2+} "uptake". Reduced levels of Ca^{2+} inside mitochondria lead to AMPK activation and mitotic catastrophe for cancer cells. Picture created with BioRender.com

In addition, VDAC1 has also been associated with cancer through its role in Ca^{2+} signaling (223). This mitochondrial protein appears to be overexpressed in several cancers and to promote cancer cells proliferation and tumor growth (224). As for IP3Rs, VDAC1 can be modulated by other proteins including BCL-2 or BCL-XL (225–227). Those interactions have been reported as preventing apoptosis by limiting Ca^{2+} entry inside mitochondria of MEFs (mouse embryonic fibroblast) cells (225). However, the opposite has also been reported in breast cancer cells, where the interaction of BCL-2 and BCL-XL with VDAC1 promotes migration by favoring mitochondrial metabolism through Ca^{2+} signaling (226). Finally, in lung cancer cell lines, VDAC1 has been shown to interact with the myeloid cell leukaemia-1 protein (Mcl-1) to promote cell migration, without impacting proliferation, through a Ca^{2+} dependent-ROS production (228).

Although it is not strictly speaking located in MAMs, MCU is a major player in Ca^{2+} signaling occurring between ER and mitochondria. Comparably to IP3Rs and VDAC1, MCU is associated with cancer, as described in the study of Tossato *et al.* in 2016, where MCU promoted tumor growth and metastasis in breast cancer (229). Moreover, a recent article published in 2020 demonstrated that MCU-induced mitochondrial Ca^{2+} uptake promotes mitochondrial

biogenesis, resulting in tumor growth in colon cancer (230). In PDAC, MCU promotes metastasis and confers resistance to metabolic stress in a cystine-dependent manner. Paradoxically, MCU-overexpressing PDAC exhibits features of cystine-deprived cells and becomes more prompt to ferroptosis (231).

In conclusion, those channels are required for cell metabolism and tumor growth. However, their modulation by cancer cells is also associated with resistance to apoptosis, highlighting a "bivalent" role in cancer and the importance of accurate and fine regulation of Ca^{2+} signaling. This also demonstrates that Ca^{2+} handling largely depends on the cell type, the nature of the tumor, the genetic background and the metabolic needs of the cell. In addition, it is worth mentioning that no studies in regards to expression and patients' survival for IP3R3 in pancreatic cancer have been published yet. In the present work, based on data available online, we briefly approach this question.

Alongside cancer, MAMs have been involved in neurodegenerative diseases including Alzheimer disease (AD). This pathology is the first leading cause of dementia in adults and is characterized by an accumulation of amyloid-ß plaques and intracellular tangles composed of hyperphosphorylated tau (232). This accumulation of plaques and tangles leads to a progressive neuronal loss, associated with cognitive impairment. Interestingly, proteins involved in AD such as ɤ-secretase, presenilin-1 and -2 (PS-1 and PS-2, respectively) are found in MAMs. It has been shown that mutated PS-1 and -2, which are associated with higher risks for AD, lead to the opening of IP3Rs, resulting in intracellular Ca^{2+} flooding and a higher production of amyloid-ß (232). Some pieces of evidence indicate that MAMs participate in the early development of AD, which could explain the aberrant homeostasis, lipid metabolism, mitochondrial function and autophagy observed in AD (233). Currently, MAMs are the subject of investigations for this pathology (234,235).

Parkinson disease (PD) is the second most prevalent neurodegenerative disease. It is characterized by the loss of dopaminergic neurons due to the cytosolic accumulation of misfolded α-synuclein, forming aggregates named Lewis bodies (232). Interestingly, the α-synuclein is found in MAMs where it modulates mitochondrial morphology. Mutations in α-synuclein reduce the apposition of the ER with mitochondria, impacting MAMs-related functions. Such impaired apposition is accompanied by impaired mitochondrial function, being

a characteristic of PD (113,232). Therefore, PD is also a good example of how MAMs dysfunctions can influence or participate in pathologies.

Alteration of MAMs integrity has also been associated with **metabolic disorders** such as **obesity or type-2 diabetes** (96). Indeed, alterations of MAMs have been observed in insulin-resistant hepatocytes as well as obese and diabetic mice (96,236). Interestingly, pharmacological or genetic targeting of cyclophilin D (see section *Role of MAMs in cell death*), a protein involved in Ca^{2+} signaling in MAMs, induces insulin-resistance and impairs insulin signaling in human primary hepatocytes. A rescue, by overexpressing cyclophilin D, was shown to improve the sensitivity to insulin (96,237). Equivalent observations were made upon MFN2 deficiency, where MFN2 overexpression also improved sensitivity to insulin (238). Furthermore, the use of antidiabetic drugs, in diabetic mice, decreased insulin resistance and also restored ER-mitochondria contact sites (238,239). In the literature, impaired Ca^{2+} transfer at MAMs have been proposed as leading to insulin resistance, by impacting insulin signaling (96). Finally, a recent study published in 2022 by Beaulant *et al.* showed that diet-induced obese mice displayed higher distance between ER and mitochondria. Interestingly, those mice developed **steatosis** and resistance to insulin (236). Upon a reverse diet, the communication between ER and mitochondria was restored, with improvement of insulin sensitivity and steatosis. In healthy mice, disruption of MAMs using the spacer FATE-1 impaired insulin sensitivity and induced steatosis, while using linker in diet-induced obese mice prevented glucose intolerance (236). This shows the importance of ER-mitochondria contact sites in metabolic disorders

1.4. Myoferlin

Myoferlin, also named fer-1-like family member 3 (FER1L3), is a protein from the ferlin family. It was discovered for the first time in skeletal muscle in 2000 (240). This protein harbors a unique and rare structure with multiple C2 domains, known to bind membrane in a Ca^{2+} dependent manner (241).

This large type-II transmembrane protein of approximatively 230 kDa is found in many subcellular structures such as plasma membrane, late and early endosomes as well as ER and lysosomes (240,242,243). In accordance with its localization, myoferlin has been shown to play a role in intracellular trafficking of receptors such as the receptors tyrosine kinases (RTK) (244,245).

The FER1L3 is involved in membrane fusion and repair of normal cells (246). Interestingly, myoferlin has been found to be overexpressed in several cancers such as breast and pancreatic cancers (44,247). Its depletion strongly reduces cell migration, invasion and proliferation *in vitro* and decreases tumor size and metastasis *in vivo.* Recent studies highlighted myoferlin as a promising therapeutic target thanks to the use of myoferlin-targeting drugs (45,46).

In the literature, myoferlin has also been associated with mitochondrial dynamics and metabolism in pancreatic cancer (47,49). This observation was correlated with migratory capacity of PDAC cell lines (48). However, as it is described in the following chapter, the cellular mechanism linking myoferlin to mitochondria is still unknown. For this reason, and because no study investigated the localization of myoferlin with respect to this organelle, we aimed to clarify this point.

The present section reviews the structure and the particular functions of myoferlin in a physiological context. In addition, the way myoferlin influences and participates in pathologies such as cancer is approached.

This section is an update on the following publication: "Peulen O, Rademaker G, Anania S, Turtoi A, Bellahcène A, Castronovo V. Ferlin Overview: From Membrane to Cancer Biology. Cells. 2019 Sep;8(9):954." https://doi.org/10.3390/cells8090954

1.4.1. Myoferlin, a member of the ferlin family

Myoferlin, as indicated by its name, is a member of the ferlin family (248). Six proteins have been identified as being part of this family and all of them have common characteristics such as the presence of multiple C2 domains (248). Proteins from the ferlin family all harbor a name in reference to their parental ortholog, the fertilization defective-1 protein (FER1), found in the *Caenorhabditis elegans* worm and involved in spermatid motility (248). The first discovered member of the family corresponds to the FER1L1, the second corresponds to the FER1L2 and so on, until six. Dysferlin, a major and well-studied member of this family, corresponds to the FER1L1, while otoferlin is referred to by the name FER1L2 and myoferlin by FER1L3 (248). Nowadays, despite extensive efforts, the role of ferlins in cell biology remains poorly understood. It is known, however, that dysferlin mutations are involved in myopathies such as the Limb-Girdle muscular dystrophy 2B and that otoferlin mutation is involved in deafness (249,250). Recently, myoferlin gain-of-function variant has been associated with a new type of

hereditary angioedema (251). In addition, myoferlin has been associated with cancer diseases (44,247). However, in the case of cancer, no genetic alterations of myoferlin have been described.

1.4.2. Transcriptional regulation and alternative splicing of myoferlin

Ferlin genomic organization has not been extensively investigated. Nevertheless, valuable information can be obtained from protein databases. In *Caenorhabditis elegans*, *FER1* gene is approximately 8.6 kb in length and composed of 21 exons (252). In humans, the *dysferlin* gene is composed of 55 exons, and encodes 19 splice variant transcripts. The *Otoferlin* gene contains 47 exons and encodes 7 splice variants (253). According to the UniProt database (https://www.uniprot.org/), eight isoforms are obtained from alternative splicing for myoferlin. The first isoform, considered as the canonical one, has a predicted molecular weight of 234,709 kDa. The second isoform has a predicted molecular weight of 229,855 kDa, while the third, fourth, fifth, sixth, seventh and eighth have predicted molecular weights of 233,324 kDa, 160 kDa, 179,551 kDa, 233,477 kDa, 49.720 kDa and 46.697 kDa, respectively. In the literature, there are few studies investigating myoferlin isoforms. In the publication of Blomme *et al.* from 2016, the authors described an enrichment of two bands corresponding to myoferlin in their exosome fractions. One of the bands had a molecular weight of ~ 230 kDa, while the other had a molecular weight of ~ 175 kDa. The authors attributed those bands to the isoforms one and five of myoferlin, respectively (254). Regarding the lack of knowledge about myoferlin isoforms, it would be of interest to confirm their existence and to investigate their function in cells.

In the literature, myoferlin has been described as being overexpressed in several types of cancers (44,247,255). Myoferlin plays a role in receptors trafficking, cell proliferation and migration in cancers (45,46,48,244). Its targeting or silencing also reduces tumor size and metastases (45,46). Nevertheless, why, when and how myoferlin is overexpressed in some type of cancers is still mysterious. In the literature, there are few publications describing transcription factors responsible of myoferlin expression. In 2010, Demonbreun *et al.* found that the myoferlin promoter had several binding sites for the nuclear factor of activated T-cells (NFAT). They suggested that upon membrane injury, the intracellular Ca^{2+} concentration increases, activating NFAT. This last one would promote myoferlin expression, leading to membrane resealing mediated by vesicle fusion (256). In 2017, Hermanns *et al.* identified myoferlin as a target gene of the Megakaryoblastic leukemia 1 and 2 (MKL1/2) transcription

factors, involved in hepatocellular carcinoma growth (257). They found that myoferlin was downregulated upon diminished activity of MKLs. In accordance with other studies (244), the authors found that myoferlin downregulation was associated with a high level of phosphorylated EGFR, impacting downstream signaling pathways (257).

1.4.3. Structure of ferlins

Ferlins structural organization is unique and rare by its repetition of C2 domains able to bind Ca^{2+} ions but also because it encompasses other unique regions such as the FerA or FerB domains (258). A typical ferlin protein contains a transmembrane region at C terminal. In addition, only a small portion of those proteins has been shown to be exposed in the extracellular space when they are located on plasma membrane. The other side constitutes a cytosolic portion, harboring multiple C2 domains, participating in a Ca^{2+} dependent manner, to the membrane organization **(Figure 1-20)** (258). In addition, the cytosolic fraction of ferlins can harbor SH3 domains, involved in protein-protein interaction, FerA and FerB domains, a highly conserved Fer1 domain and finally, a DysF domain that could be involved in phospholipids binding (240,248,258). However, ferlin members do not systematically contain all aforementioned domains. In this context, a classification, considering the presence of the DysF domain, has been elaborated. The type I ferlin group englobes ferlins possessing DysF such as myoferlin, dysferlin and the Fer1L5, while the type II ferlin group contains the otoferlin, the Fer1L4 and the Fer1L6 members. In similarity with DysF, the FerA domain is only found in the type I ferlin group **(Figure 1-20 and Figure 1-21)** (248,259). The function of DysF, FerA, FerB and Fer1 domains remains nowadays obscure. For this reason, finding their individual and synergic functions in relation with C2 domains could provide a better understanding of ferlin roles in cell biology. Furthermore, even though our comprehension of C2 domains has evolved during last decades, a gap still remains between the functional/structural and the biological role of C2 domains. The following section approaches our current knowledge of C2 domains in the context of the ferlin family.

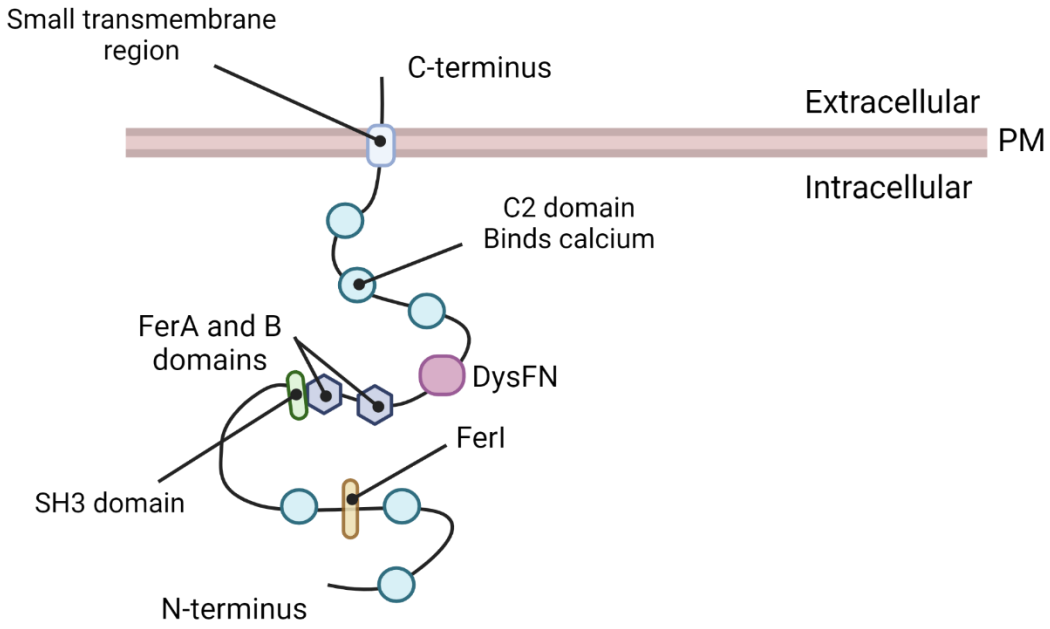

Figure 1-20. Representation of a ferlin protein on the plasma membrane (PM). The small C-terminus region is exposed to the extracellular space. The cytosolic fraction harbors multiple C2 domains as well as FerA, FerB and FerI, SH3 and DysF (DysFN in the picture) domains. On a side note, only ferlins from the type-I ferlin group display DysF and FerA domains. The picture was created with BioRender.com

1.4.4. Calcium, C2 domains and interaction with phospholipids

C2 domains are ~130 amino acids long, independently folded modules, found in several eukaryotic proteins. The typical C2 domain is composed of a beta-sandwich made of 8 beta-strands coordinating Ca^{2+} ions, participating to their ability to bind phospholipids (260). However, some C2 domains have lost their capacity to bind Ca^{2+} but still bind membranes (261). A large variety of proteins containing C2 domains have been identified, and most of them are involved in membrane biology, such as vesicular transport (synaptotagmin), GTPase regulation (Ras GTPase activating protein) or lipid modification (PLC) (262). Nevertheless, few protein families harbor more than five C2 domains as the ferlins do. Indeed, only three vertebrate protein families contain more than two C2 domains: the multiple C2 domain and transmembrane region proteins (MCTP) (263), extended synaptotagmins (264), and the ferlins. Notably, C2 domains nomenclature in the ferlin family begins from the amino to the carboxy terminal by C2A, C2B, …, and C2F domains **(Figure 1-21)** (248). Moreover, it is interesting to mention that a C2 domain is more similar to other C2 domains at a similar position in ortholog proteins than it is to the other C2 domains within the same protein (265).

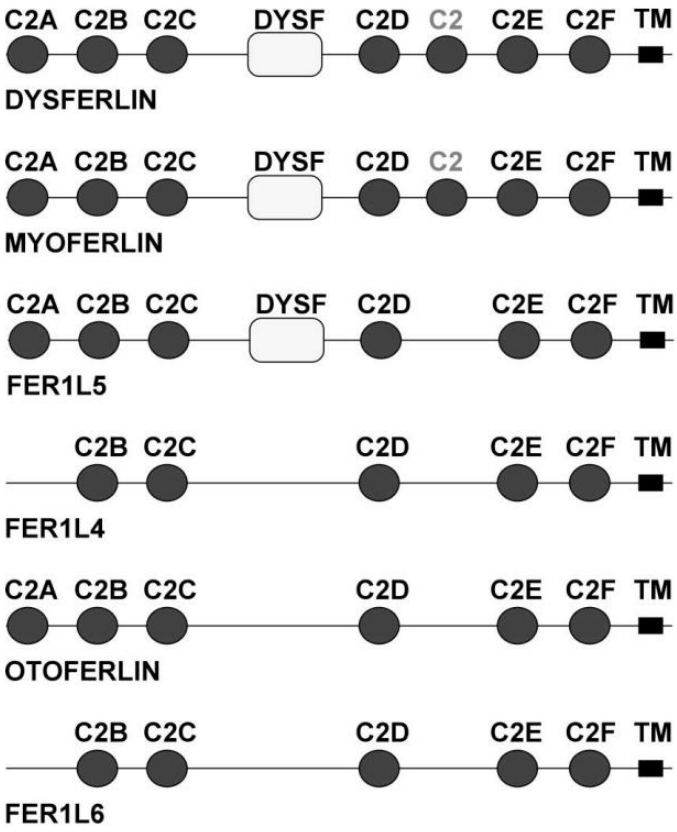

Figure 1-21. Representation of ferlin structure. TM represents the transmembrane region (C-terminus). Ferlins harbor multiple C2 domains. The numeration of C2 domains begins at the N-terminus region (C2A, … until C2F at the C-terminus region). Dysferlin, myoferlin and FER1L5 proteins display a DysF domain, while FER1L4, otoferlin and FER1L6 do not display this domain. The picture is from Posey *et al*. (2011) (248).

Experimentally, myoferlin C2A was the single C2 domain able to bind to phospholipid vesicles. A significant presence of negatively charged PS was required for this interaction. Myoferlin C2A binding to PS-containing vesicles did not occur with Ca^{2+} concentration similar to the one observed in the basal physiological condition (0.1 µM). Indeed, the half-maximal binding was observed at 1 µM (241), suggesting that the C2A domain is involved in specific processes inside the cell requiring Ca^{2+} release from intracellular stock, like the ER does. When cells are stimulated by various means, including depolarization and ligand binding, the cytosolic Ca^{2+} concentration increases up to 1 µM or more, similar to the one required by myoferlin C2A domain to bind lipids. It appears that dysferlin C2A domain has the same binding properties as myoferlin C2A domain. However, its half-maximal lipid binding is higher (4.5 µM) (241). Thanks to a fluorescent probe able to reflect the degree of membrane organization, Marty *et al*. were able to show that myoferlin, as well as dysferlin and otoferlin, are able to influence lipid packing of vesicles. The experiments conducted with individual recombinant Ferlin's C2A-C domains demonstrated that all of them are able to increase lipid order (266). In addition, this property

is enhanced by the presence of Ca^{2+} and requires negatively charged phospholipids. The authors concluded that ferlins are probably able to actively sculpt membranes, increase membrane curvature and thus, facilitate membrane fusion and fission processes. Ferlin proteins also contain a FerA domain recently described as a four-helix bundle fold with its own Ca^{2+}-dependent phospholipid-binding activity (267). On the opposite of C2 domains, the FerA domain is able to bind a phospholipid mixture containing 100% PC, meaning that negatively charged phospholipids are not required for FerA interaction with membranes (267).

1.4.5. Myoferlin's functions in a non-cancer context

1.4.5.1. Myoblast fusion

Dysferlin and myoferlin have a specific temporal pattern of expression in muscle development. Myoferlin is highly expressed in myoblasts that have elongated prior to fusion to syncytial myotubes. After fusion, myoferlin expression is decreased. The dysferlin expression increases concomitantly with the fusion and maturation of myotubes **(Figure 1-22)** (241,246,246). A proteomic analysis revealed the interacting partners of dysferlin during muscle differentiation (268). It appeared that the number of partners decreases during the differentiation process, while the core-set of partners is large (115 proteins). Surprisingly, the dysferlin homolog myoferlin was consistently co-immunoprecipitated with dysferlin. The gene ontology analysis of the core-set proteins indicates that the highest ranked cluster is related to vesicle trafficking (268). In the C2C12 myoblast model, immunoprecipitation experiments showed that myoferlin interacts with the Eps15 homology domain 2 (EHD2) protein apparently through its C2B domain **(Figure 1-23)** (245). EHD2 is involved in endocytic recycling. It was inferred that the interaction between EHD2 and myoferlin might indirectly regulate disassembly or reorganization of the cytoskeleton that accompanies myoblast fusion (245).

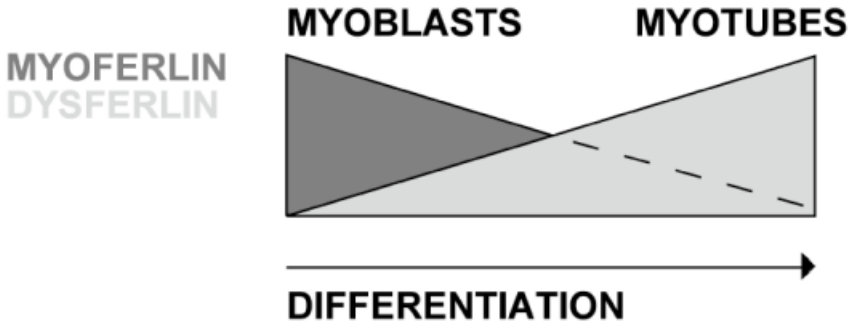

Figure 1-22. Myoferlin and dysferlin expression in myoblasts and myotubes. While myoferlin expression is high in myoblasts and decreases during differentiation, dysferlin expression increases during differentiation into myotubes. The picture is from Posey *et al*. (2011) (248).

In mouse skeletal muscles, myoferlin was found at the nucleus and plasma membrane (240). It was highly expressed in myoblasts before their fusion to myotubes (240,246) and found to be highly concentrated at the site of apposed myoblast and myotube membranes, and at site of contact between two myotubes (246). Myoblast fusion requires a Ca^{2+} concentration increase to 1.4 µM (269), similar to the one reported for myoferlin C2A binding to phospholipids (241). Myoferlin-null mice show impaired myoblast fusion *in vitro*, and display smaller muscles and smaller myofibers *in vivo* (246). Altogether, these observations support a role for myoferlin in the maturation of myotubes and the formation of large myotubes that arise from the fusion of myoblasts to multinucleated myotubes.

Interestingly, myoferlin-null mice are unresponsive to insulin growth factor-1 (IGF-1) for the myoblast fusion to the pre-existing myofibers (Figure 1-23). Mechanistic experiments indicate a defect in IGF-1 internalization and a redirection of the insulin growth factor receptor (IGF1R) to the lysosomal degradation pathway instead of recycling. As a consequence, myoferlin-null myoblasts lack the IGF1-induced increase in AKT and mitogen-activated protein kinases (MAPKs) activity downstream to IGFR (270).

1.4.5.2. Muscle repair

Myoferlin expression is also up regulated in damaged myofibers and in surrounding mononuclear muscles and inflammatory cells (256). As it was observed for dysferlin, myoferlin can be cleaved by calpain to produce a mini-myoferlin module composed of the C2E and C2F domains (271). Interestingly, this mini-myoferlin module bears structural resemblance to synaptotagmin, a well-known actor in synaptic vesicle fusion with the presynaptic membrane (272).

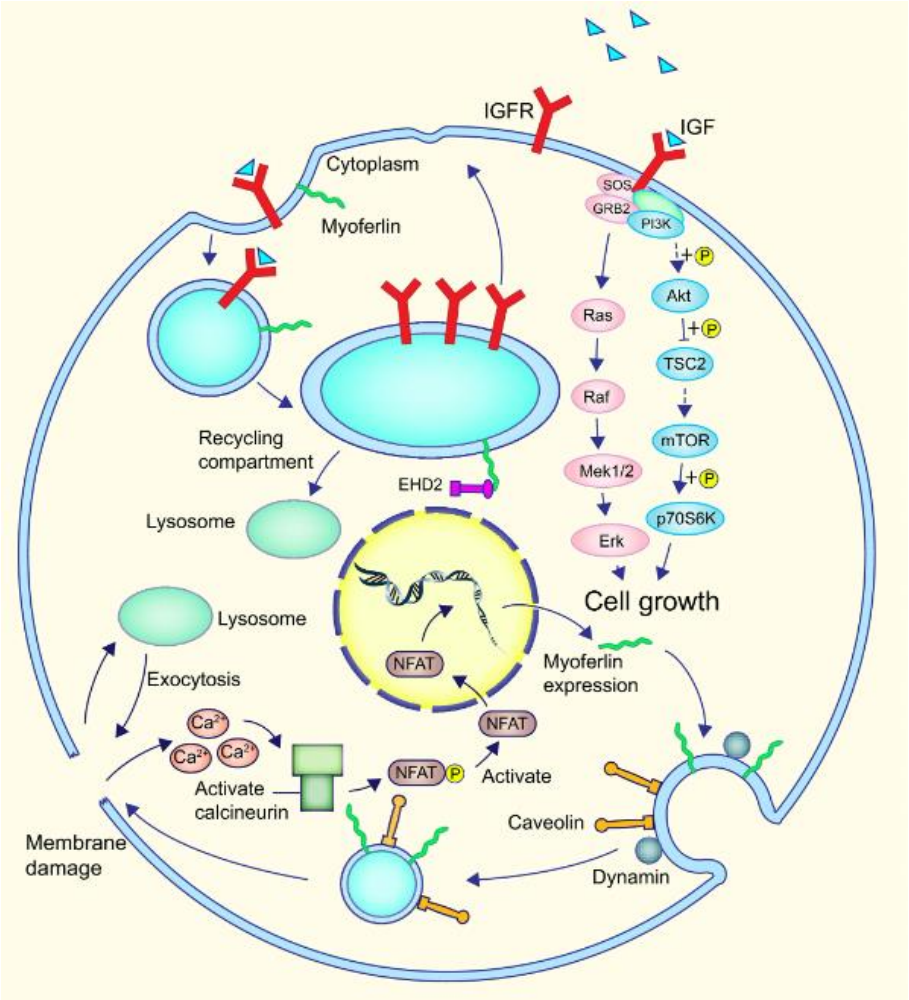

Figure 1-23. Role of myoferlin in muscle cells. Myoferlin participates to endosomal recycling and interacts with EHD2. Upon myoferlin silencing, the IGFRs recycling is impaired and directed to the lysosomal degradation pathway. As a consequence, the cell responds less to IGF stimulation, which is associated with a decreased activity of the MAPKs and AKT pathways. This impacts growth and differentiation of muscle cells. Myoferlin is also involved in membrane damage repair. Upon membrane injury, the intracellular Ca^{2+} concentration increases, activating the calcineurin and NFAT. This last one promotes myoferlin expression, leading to membrane resealing mediated by vesicles fusion. This picture is from the publication of Zhu *et al.* (2019) (230).

The defects in myoblast fusion and muscle repair observed in myoferlin-null mice are reminiscent of what was reported in muscle lacking nuclear factor of activated T-cells (Figure 1-23). Demonbreun and colleagues suggested that in injured myofibers, the membrane damages induce an intracellular increase of Ca^{2+} concentration producing a calcineurin-dependent NFAT activation and subsequent translocation to the nucleus. The activated NFAT can therefore bind to its response element on the myoferlin promoter (256).

1.4.5.3. Membrane resealing of endothelial cells

Bernatchez and colleagues reported that dysferlin and myoferlin are abundant in caveolae-enriched membrane microdomains/lipid rafts isolated from human endothelial cells and are highly expressed in mouse blood vessels (273,274). As observed for muscle cells, myoferlin

regulates the endothelial cell membrane resealing after physical damage. In endothelial cells, myoferlin silencing reduces or abolishes the extracellular regulated kinase-1/2 (ERK-1/2), c-Jun N-terminal kinase (JNK) or PLCγ phosphorylation by vascular endothelial growth factor (VEGF), resulting from a loss of vascular endothelial growth factor receptor-2 (VEGFR-2) stabilization at the membrane. Indeed, myoferlin silencing causes an increase in VEGFR2 polyubiquitination, which leads to its degradation (273). Another angiogenic tyrosine kinase receptor, the tyrosine-protein kinase receptor tie-2 (Tie-2), is significantly less expressed at the plasma membrane when myoferlin is silenced in endothelial cells (275). In this case, it appears that proteasomal degradation plays a minor role in the down regulation of the receptor. Strikingly, G-protein coupled receptors seemed unaffected by the decrease of myoferlin expression, suggesting a selective effect on RTKs. It was also reported that in endothelial cells, myoferlin is required for an efficient clathrin and caveolae/raft-dependent endocytosis, and is co-localized with DNM2 (276).

1.4.6. Myoferlin in cancer

Beside its role in myoblast fusion and membrane repair, myoferlin has been described in pathology such as cancers. Indeed, myoferlin was experimentally discovered as highly expressed in several tumor tissues including the pancreas (277), breast (278), kidneys (278), and head and neck squamous cell carcinoma (HNSCC) (279). This expression was confirmed at a protein level in tumor tissue and/or cell lines from the pancreas (44,280), breast (281,282), lungs (282), melanoma (282), hepatocellular carcinoma (257), HNSCC (255), clear cell renal carcinoma (283,284), and endometroid carcinoma (285). In the following section, in order to have a global vision of myoferlin in cancer, its role in several types of cancers is first described, followed by a focus on PDAC.

The first study highlighting myoferlin in the progression of **breast cancer** was published in 2011 (247), eleven years after the first publication on myoferlin in myoblasts by Davis and his collaborators **(Figure 1-24)** (240). In this study, a mathematical model was proposed to examine the role of myoferlin in breast cancer cell invasion. This model confirms the experimental observation of decreased invasion of the myoferlin-null breast MDA-MB-231 cell line, and predicts that the pro-invasion effect of myoferlin may be partly mediated by matrix-metalloproteinases (MMPs) **(Figure 1-24)** (247). The model was further validated *in vitro* suggesting a mesenchymal to epithelial transition (MET) when myoferlin was knockdown

(Figure 1-24) (286,287). Using the same cell model, Blackstone and colleagues showed that myoferlin depletion increases cell adhesion to polyethylene terephthalate (PET) substrate by enhancing focal adhesion kinase (FAK) and its associated protein paxillin (PAX) phosphorylation (Figure 1-24) (288). Interestingly, myoferlin was reported as regulating cell migration through a tumor growth factor-β1 (TGF-β1) autocrine loop (Figure 1-24) (289). Recently, similar results in regard to MMPs were reported in melanoma (290). Myoferlin expression was first correlated with vasculogenic mimicry in patients, then its *in vitro* depletion in A375 cell line impaired vasculogenic mimicry, migration, and invasion by decreasing MMP-2 production.

Several pieces of evidence, obtained from normal endothelial cells, indicate that myoferlin is involved in RTKs recycling (Figure 1-24). It was shown that MDA-MB-231 and -468 cells depleted for myoferlin are unable to migrate and to undergo EMT upon epidermal growth factor (EGF) stimulation. The authors discovered that myoferlin depletion alters the EGFR fate after ligand binding, most probably by preventing phosphorylated-EGFR degradation (244).

The co-localization of myoferlin with CAV1 (244), the main component of caveolae considered as a metabolic hub (291) prompted researchers to investigate the implication of myoferlin in energy metabolism (Figure 1-24). In this context, the authors showed in triple-negative breast cancer cells that myoferlin-silencing leads to an accumulation of monounsaturated fatty acids (C16:1). Its depletion further decreases oxygen consumption switching the cell metabolism toward glycolysis (49). This was the first report regarding the role of myoferlin in mitochondrial function and cell metabolism.

Several breast cancer cell lines and tissues showed a calpain-independent myoferlin cleavage, regardless of cell injuries and subsequent Ca^{2+} influx (292). The resulting cleaved myoferlin increases ERK phosphorylation in an overexpressing HEK293 system (Figure 1-24). It would be of interest to further study the link between mini-myoferlin and *KRAS* mutated cancers as ERK is a mid-pathway signaling protein in this context.

In accordance with previous publications related to myoferlin in breast cancer, a recent study, published in 2020, showed an interaction of myoferlin with the particularly interesting new Cys-His protein 1 (Pinch-1), a protein involved in cell adhesion (293). In order to prove the existing interaction between myoferlin and Pinch-1, the authors co-immunoprecipitated both proteins and showed that the interaction occurs via the LIM-2 domain of Pinch-1 and the C2D-E-F

domains of myoferlin (293). In addition, the absence of Pinch-1 decreases myoferlin abundance through proteasomal degradation. Interestingly, Pinch-1 silencing limits breast cancer cells proliferation, migration and endothelial cell tube formation *in vitro* and reduces tumor size and metastasis *in vivo*. Those phenomena are dependent on the Lim-2 domain previously shown as interacting with myoferlin (293).

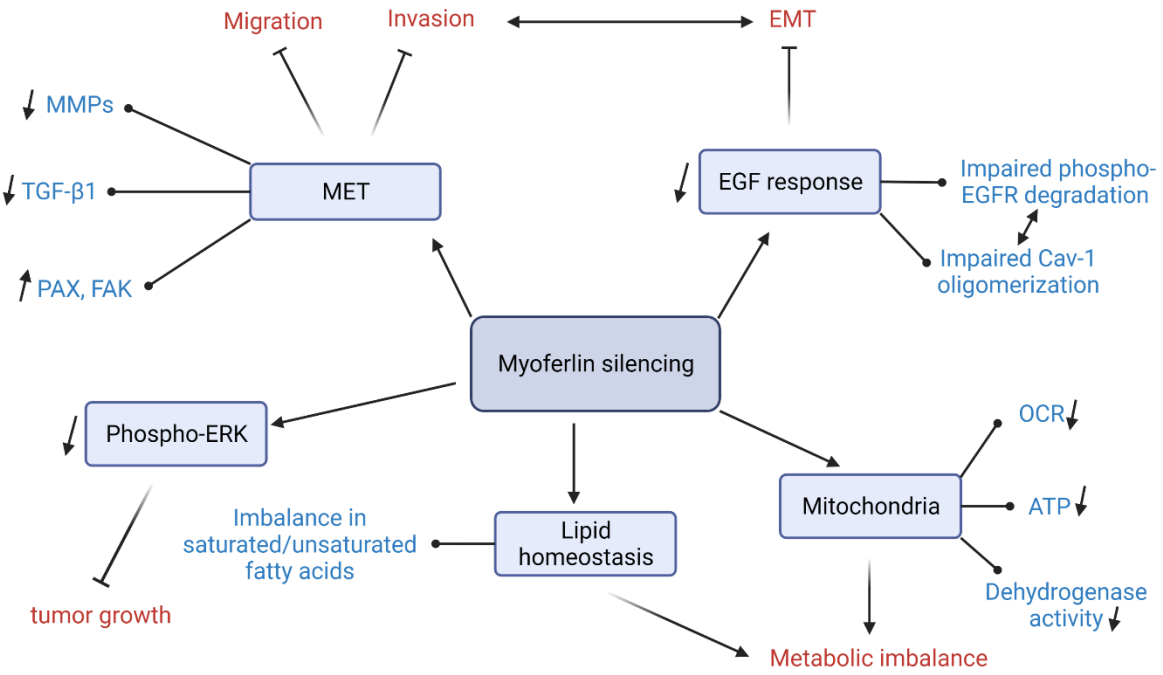

Figure 1-24. Impact of myoferlin silencing on breast cancer cells. Myoferlin silencing induces a MET, characterized by a decreased in MMPs as well as TGF-ß1 expression and an increase in PAX and FAX. This prevents cells from migration and invasion. In addition, myoferlin-silenced cells do not induce an epithelial to mesenchymal (EMT) transition upon EGF stimulation (which is associated to invasion and migration). Studies showed that impaired degradation of EGFR (associated with impaired CAV1 oligomerization) is responsible for the lack of response to EGF stimulation. Furthermore, myoferlin silencing has been shown to impact mitochondrial metabolism, characterized by a decrease in OCR, ATP and dehydrogenase activity, creating a metabolic imbalance. Impaired lipid homeostasis, characterized by an imbalance in saturated/unsaturated fatty acids also participates to the metabolic imbalance. Finally, ERK is less activated upon myoferlin silencing in HEK293 cell line. Those results could be extended to cancer cells, explaining partly the reduced tumor growth. The picture was created with BioRender.com

Finally, Zhang *et al.* in 2018 discovered a new molecule exerting an anti-metastatic effect in breast cancer (46). This molecule, named WJ460, impairs cell migration and proliferation *in vitro*, while it strongly reduces tumor mass and metastasis *in vivo* and improves the overall survival of mice (46). Strikingly, this molecule has been shown to bind the C2D domain of myoferlin and to impair endocytic recycling as described previously under myoferlin silencing in breast cancer. This discovery about myoferlin targeting in breast cancer may open new doors in clinical practice and demonstrates once again the interest of studying myoferlin in the context of cancer (46).

In mice bearing solid Lewis Lung Carcinoma tumors, the intratumoural injection of myoferlin siRNA mixed with a lipidic vector reduces the tumor volume by 73%. The observed reduction is neither the consequence of a difference in blood vessel density nor of VEGF secretion. However, a significant reduction of the proportion of the Ki67-positive cells indicates a decrease in cell proliferation (282). Myoferlin was reported as expressed in human non-small cell lung cancer tissues where it was correlated with VEGFR2, thyroid transcription factor (TTF)-1 and transformation-related protein 63 (p63), especially in the low stage tumors (283).

In the hepatocellular carcinoma cell lines, the silencing of the transcriptional coactivator of the serum response factor (SRF), MKL1/2, induces a reduction in myoferlin gene expression. It was shown by chromatin immunoprecipitation that MKL1/2 binds effectively to the myoferlin promoter (257). As in other cancer types, hepatocellular carcinoma requires myoferlin to proliferate and perform invasion or anchorage-independent cell growth. Its depletion enhances EGFR phosphorylation, in agreement with the concept of myoferlin being a regulator of RTK recycling.

A myoferlin expression pattern was investigated in oropharyngeal squamous carcinoma. It was reported that myoferlin is overexpressed in 50% of the cases and significantly associated with worse survival. Moreover, human papilloma virus (HPV)-negative patients have significantly higher expressions of myoferlin. A subgroup survival analysis indicates the interaction between these two parameters as HPV-negative has the worst prognosis when myoferlin is highly expressed. Nuclear myoferlin expression appears to be highly predictive of the clinical outcome and associated with IL-6 and NANOG overexpression (255). Upon HNSCC cell line stimulation with IL-6, myoferlin dissociates from EHD2 and binds activated signal transducer and activator of transcription 3 (STAT3) to drive it in the nucleus. The observation was extended to breast cancer cell lines (279). Finally, a recent study published in 2021 found myoferlin as being highly overexpressed in nasopharyngeal carcinoma where it influences proliferation, invasion and migration. Moreover, as described in breast cancer, myoferlin knockdown sustains EGFR phosphorylation upon EGF stimulation. The authors also demonstrated that EGFR and the ephrin type-A receptor-2 (EPHA2) co-immunoprecipitate with myoferlin (294).

In gastric cancer, myoferlin has been proposed as a promising biomarker and therapeutic target. Indeed, this protein has been found to be overexpressed in oxaliplatin-resistant gastric

cancer. Its expression was significantly correlated with poor prognosis and its knockdown repressed stem cell features, tumor growth, cell migration and resistance to oxaliplatin (295).

Finally, it is interesting to mention that a new drug, the YQ456, resembling WJ460 and 6y, was also found to attenuate colorectal cancer progression. In colorectal cancer, a high expression of myoferlin was associated with poor survival (45,296). As described for WJ460 and 6y in breast and pancreatic cancer, the small molecule YQ456 is able to interact with the C2D domain of myoferlin and to reduce cell migration, invasion and proliferation *in vitro* as well as metastasis, tumor mass and blood vessels formation *in vivo*. Surprisingly, the authors reported for the first time an interaction of myoferlin with RAB32 and explained that this interaction counteracts DRP-1 activation and the resulting mitochondrial fission. Thus, the authors suggested that treating cells with YQ456 may induce a disruption of the myoferlin-RAB32 complex, resulting in mitochondrial fission, reduced OCR and enhanced mitophagy. However, the link between myoferlin and rab32 needs to be clarified as mentioned in the article (45).

In pancreatic ductal adenocarcinoma, myoferlin was shown to be overexpressed in high grade in comparison to low grade PDAC (280). Patients with high myoferlin have a significantly worse prognosis than those with low myoferlin (280,297). This observation of myoferlin overexpression in pancreatic cancer was in accordance with the proteomic study performed on PDAC by Turtoi *et al*., in 2011 (44). The discovery of myoferlin overexpression prompted researchers to investigate its role in PDAC (Figure 1-25). Experiments undertaken with pancreatic cell lines and siRNA-mediated silencing demonstrated that myoferlin is requested to maintain a high proliferation rate. Myoferlin was reported as a key element in VEGFA exocytosis by PDAC cell lines, correlating with microvessel density in PDAC tissue (Figure 1-25) (298). In addition to its role in angiogenesis, myoferlin has been associated with PDAC metabolism. Indeed, in agreement with the results published by Blomme *et al*. in 2017 in breast cancer, myoferlin-silenced cells exhibit reduced mitochondrial respiration, impaired morphology and fragmented mitochondrial network (Figure 1-25) (47,49). This discovery was extended and confirmed in colon cancer, where myoferlin silencing also protects cells from apoptosis in *TP53*-mutated cells (296). The concept claiming that metastatic dissemination relies on oxidative phosphorylation is broadly accepted (299,300). Based on these reports, Rademaker *et al.* discovered in 2019 that myoferlin is highly expressed in PDAC cells with a high metastatic potential, where it was correlated with mitochondrial respiration (48).

In parallel to the discovery of WJ460 in breast cancer, a small molecule named 6y has been shown to exert anti-metastatic effect in PDAC **(Figure 1-25)**. As for the WJ460, 6y is interacting with myoferlin, showing this time the interest of myoferlin-targeted therapy in PDAC (301). In 2022, Rademaker *et al.* showed that using WJ460 in PDAC reduces mitochondrial respiration and leads to a fragmented mitochondrial network. This was associated with impaired mitochondrial morphology and increased mitophagy. Interestingly, treating PDAC cell lines with WJ460 did not induce apoptosis. Instead, it triggers a ferroptosis-like cell death **(Figure 1-25)** (302). This ferroptosis-like cell death could be associated with increased mitophagy observed upon myoferlin targeting and the role of myoferlin in lysosome membrane integrity. Indeed, in 2021, Gupta *et al.* demonstrated the importance of myoferlin for lysosome function as well as lysosomal membrane protection against damages **(Figure 1-25)** (243).

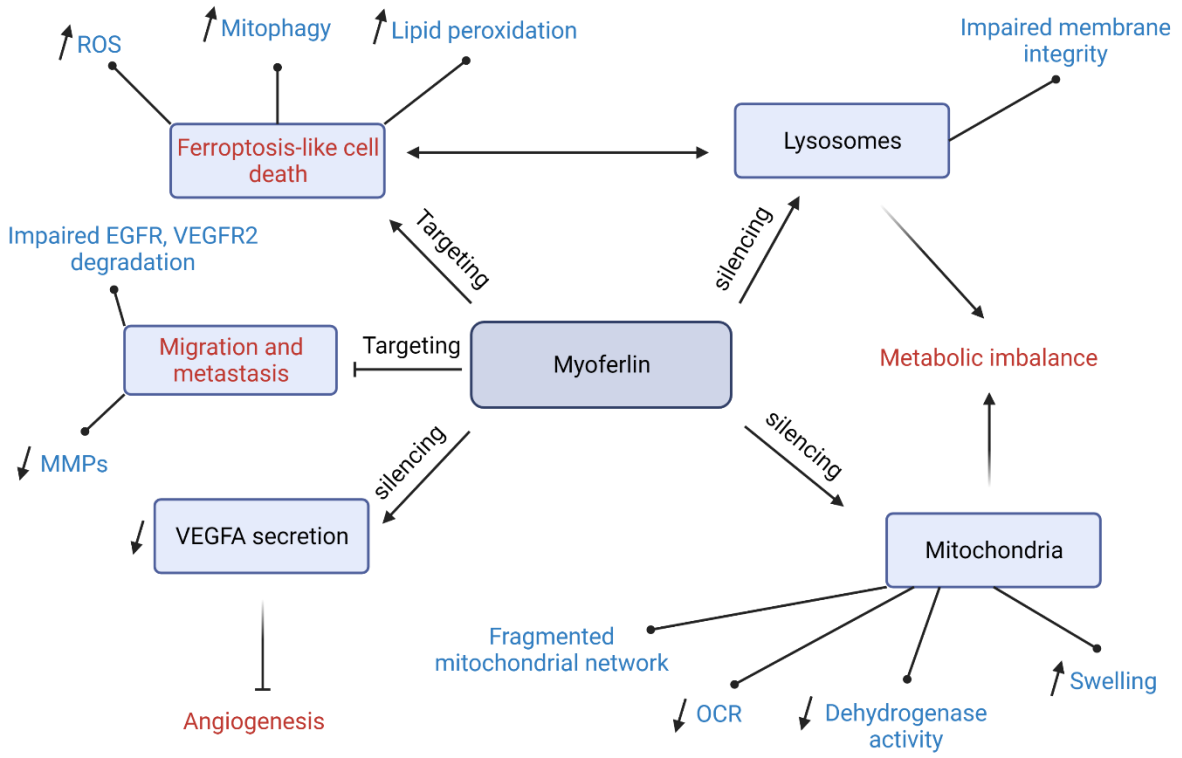

Figure 1-25. Impact of myoferlin silencing/targeting in PDAC cells. Myoferlin targeting induces a ferroptosis-like cells death, characterized by increased ROS, mitophagy and lipid peroxidation. It also impacts cell migration and reduces metastasis in mouse model. This impact on migration and metastasis is believed to be associated with decreased MMPs expression and impaired EGFR, VEGFR degradation. Additionally, myoferlin silencing in PDAC cells reduces their secretion of VEGFA, which is associated with angiogenesis. Myoferlin has also been shown to protect lysosome membranes. Therefore, myoferlin silencing impairs their membrane integrity, that could participate to a metabolic imbalance. Finally, myoferlin silencing also impacts mitochondrial dynamics, respiration, morphology and decreases dehydrogenase activity. The picture was created with BioRender.com

1.4.7. Subcellular localizations of myoferlin

Even if our comprehension is improving, subcellular localization of myoferlin remains unclear. For instance, it is only since 2021 that the presence of myoferlin in lysosomes of PDAC cell lines was clearly proved (243). Another example is the lack of knowledge regarding the potential localization of myoferlin on mitochondria. Indeed, myoferlin has been shown to interact with RAB32 in colon cancer (45) or to influence respiration and mitochondrial network in pancreatic and breast cancer (47,49). However, until this work, no studies had investigated myoferlin presence on this organelle. This means that, even if our understanding of myoferlin localization in the cell becomes more accurate with time, some gaps remain.

When myoferlin was discovered in skeletal muscle for the first time in 2000 by Davis *et al.*, they found that the ferlin member was located at the plasma membrane but also in the nucleus (240). Plasma membrane localization was further confirmed in several reports (245,246,303), with the additional notion that myoferlin accumulates at sites of membrane fusion between myoblasts (246). On the other hand, the fact that IL-6 stimulation induces myoferlin translocation into the nucleus also further confirmed its presence in this region (279). Since 2002, the observation of myoferlin in the cytoplasm, and more precisely in cytoplasmic vesicles, was described by the group of Davis (241). However, no accurate studies about myoferlin subcellular localization had been performed until 2016 (242). In their study, Redpath and his collaborators showed the presence of exogenous myoferlin on the plasma membrane but also in intracellular regions using immunofluorescence techniques. Indeed, they described a bright labeling for the plasma membrane but also for the perinuclear region and cytoplasm. After investigation, they found that myoferlin was partly colocalizing with calreticulin, which is a marker of ER, at the perinuclear region. They also observed colocalization, still in the perinuclear region, with the Golgi apparatus and trans-Golgi network, confirming the previous reports of myoferlin in the Golgi apparatus of cancer cell lines and normal airway epithelium (282,304). Moreover, they found strong colocalization between the ferlin member and RAB5 as well as RAB7 markers, corresponding to early and late endosomes markers respectively. Surprisingly, myoferlin only sporadically colocalized with LAMP1-positive lysosomes in C2C12 (mouse, myoblasts), Cos-7 (monkey, kidney) and HEK293 (human, embryonic kidney) cells (242). Those results were confirmed by Gupta *et al.* in 2021, where they showed that exogenous myoferlin was not present in HEK293 lysosomes (243). However, they identified the

exogenous protein in lysosomes of PDAC cell lines where it maintains membrane integrity (243). Finally, myoferlin was also described in exosomes from PDAC and breast cancer cell lines. Myoferlin silencing rendered exosomes inefficient for nucleic acids delivery and altered migration and proliferation of the targeted cells (254). This is all summarized in Figure 1-26.

In conclusion, myoferlin has been described in many subcellular localizations such as plasma membrane, late and early endosomes, lysosomes, exosomes but also the Golgi apparatus and endoplasmic reticulum (240,242,243,254). Nevertheless, even if a clear link has been established between myoferlin and mitochondrial dynamics as well as metabolism (45,47,48,296), there was no study investigating myoferlin localization in the context of mitochondria. Therefore, we strongly believe that a better understanding of protein localization within the cell can provide us precious information about its biological function. For this reason, we wanted to clarify myoferlin position in accordance with mitochondria and we wanted to understand how this protein influences mitochondrial metabolism and dynamics.

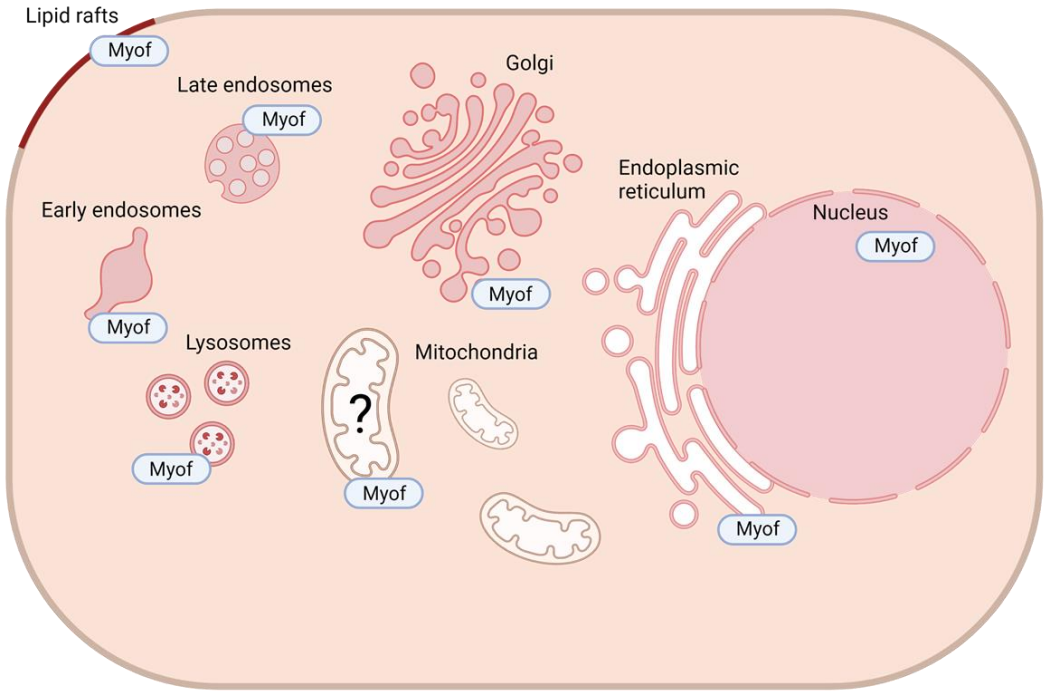

Figure 1-26. Myoferlin localization within the cell. Myoferlin has been reported on plasma membrane, where it is enriched in the lipid rafts, on late and early endosomes, on lysosomes of PDAC cell lines, on the Golgi apparatus, on the ER and in the nucleus. Whether myoferlin is localized on mitochondria is unknown. The picture was created with BioRender.com

AIM OF THE PROJECT

2. Aim of the project

PDAC is an aggressive type of cancer, with a 5-year survival rate being lower than ~9% (305). Due to its late diagnosis, the surgery, being considered as the only curative treatment, is possible in less than 20% of cases (8,25). Among patients benefiting from surgery, it is estimated that 76.70% will experiment a relapse within two years, while for patients diagnosed at late stages (>80% of cases), palliative chemotherapy is often administrated (25,27,28). Unfortunately, there is no effective chemotherapy or targeted therapy for this cancer (8,39). Therefore, there is a real need to have a better comprehension of PDAC biology, allowing us to find the Achilles' heel of cancer cells. In that regard, one proposed strategy is to target cancer cell metabolism (43). Indeed, cancer cells adapt their energy metabolism to support their growth and division but also to face challenging environmental conditions such as the lack of nutrients and hypoxia (40–42). Thus, targeting cancer cell metabolism, in order to create a metabolic imbalance able to slow down cell proliferation and sensitize them to other therapies, is currently under investigations.

In that context, our team studies a protein named myoferlin. This protein is overexpressed in PDAC and its silencing/targeting has been reported to impact cancer cell metabolism, proliferation and migration *in vitro* (47–49,302). In a mouse model, targeting myoferlin using small compounds reduces the number of metastasis and tumor size (45,46,301). In addition, it increases the overall survival, without showing toxic side effects on mice (45,46,301). Therefore, myoferlin targeting seems to be a promising therapeutic target. Nevertheless, our comprehension of myoferlin functions in the cell remains limited and the underlying mechanisms explaining the effect of myoferlin targeting are still unknown. For instance, it has been reported that myoferlin silencing leads to a fragmented mitochondrial network and to a reduced mitochondrial respiration (47). However, no mechanisms have been described. Since mitochondria have been involved in PDAC relapse and tumor growth, we aimed at understanding the mechanism linking myoferlin silencing to mitochondrial dynamics and metabolism (61–63).

As a first attempt, we investigated whether myoferlin was directly implicated in mitochondrial dynamics and metabolism. Thus, we tried to identify whether myoferlin was located on mitochondria and whether it was interacting with proteins involved in mitochondrial dynamics

(see *Part I: myoferlin interacts with proteins involved in mitochondrial fusion in PDAC cell lines*). Our investigations finally prompted us to investigate a potential localization for myoferlin in MAMs. Due to its rare structure with multiple C2 domains able to bind Ca^{2+} and phospholipids, we hypothesized that myoferlin could play a role in Ca^{2+} signaling at MAMs, explaining the impact on mitochondrial metabolism and dynamics observed upon its silencing (see *Part II: myoferlin is located in MAMs, where it plays a role in calcium transfer and interacts with IP3R3*) (241).

MATERIAL AND METHODS

3. Material and methods

3.1. Cells and chemicals

The investigations performed in this work were based on PDAC cell lines (Panc-1, PaTU8988T, BxPC-3 and MiaPaCa-2), on human pancreatic normal epithelial cell line (HPNE) and on murine undifferentiated myoblast cell line (C2C12). PaTu8988T (ACC162) were purchased from the Leibniz-Institute (DSMZ, Braunschweig, Germany) while HPNE (CRL- 4023) were purchased from the American Type Culture Collection (ATCC, Virginia, USA). Panc-1 (CRL-1469), BxPC-3 (CRL-1687), MiaPaCa-2 (CRL-1420) and C2C12 (CRL-1772) were generous gifts from Prof. Muller and Burtea (NMR Laboratory, University of Mons, Belgium), Prof. Bikfalvi (Inserm U1029, Bordeaux, France), Prof. De Wever (Laboratory of Experimental Cancer Research, University of Gent, Belgium) and Prof. Francaux (University of Louvain, Louvain la Neuve, Belgium) respectively. Antibodies against hemagglutinin (HA, 3724S), AMPK (2795), phospho-AMPK (2535), GRP75 (clone D13H4, 3593), mitochondrial import receptor subunit TOM20 homolog (TOM20, clone D8T4N, 42406), calreticulin (clone D3E6, 12238), GLUT1 (12939), BIP (3177), IRE1 (3294), XBP1s (12782), PERK (5683), ATF4 (11815) and CHOP (2895) were from Cell Signaling (Danvers, MA). Vinculin (sc-25336), Myoferlin (clone D-11, sc-376879), Myoferlin (clone K-16, sc-51367), S1R (sc-137075), MFN1 (H-65, sc-50330), specificity protein 1 (SP1, sc-17824), and heat shock cognate 71 kDa protein (HSC70, sc-7298) antibodies were purchased from Santa-Cruz Biotechnology (Dallas, TX). 78-kDa glucose-regulated protein (GRP78, also known as BIP, MAB4846) and mitochondria (Clone 113-1, MAB1273) antibodies were obtained from R&D systems (Minneapolis, MN) and Millipore (Burlington, MA), respectively. Myoferlin (identified here under as HPA - HPA014245) was from Sigma (Bornem, Belgium). VDAC1 (clone 20B12AF2, ab14743), PDHα1 (clone EPR11098, ab168379), phospho-PDHα1 (ab92696), glyceraldehyde-3-phosphate dehydrogenase (GAPDH, ab8245), total OXPHOS cocktail (ab110413) and MFN1/2 antibody (clone 3C9, ab57602) were from Abcam (Cambridge, UK). Antibody against IP3R3 (PA5-88758) was from Invitrogen (Waltham, USA). The antibodies used for the UPR were a generous gift from Dr. Arnaud Blomme (GIGA stem cells, ULiège). The list of antibodies used in this work is presented on Table 2. All reagents were purchased from Sigma (Bornem, Belgium), unless mentioned otherwise.

Antibodies	Source	Identifier
Rabbit anti-IP3R3 (polyclonal)	Invitrogen, Thermo Fisher Scientific	Cat# PA5-88758, RRID: AB_2805108
Rabbit anti-GRP75 (monoclonal)	Cell Signaling Technology	Cat# 3593, RRID: AB_2120328
Rabbit anti-AMPK (polyclonal)	Cell Signaling Technology	Cat# 2795, RRID: AB_560856
Rabbit anti-Phospho-AMPK (monoclonal)	Cell Signaling Technology	Cat# 2535, RRID: AB_331250
Rabbit anti-TOM20 (monoclonal)	Cell Signaling Technology	Cat# 42406, RRID: AB_2687663
Rabbit anti-calreticulin (monoclonal)	Cell Signaling Technology	Cat# 12238, RRID: AB_2688013
Rabbit anti-GLUT1 (monoclonal)	Cell Signaling Technology	Cat# 12939, RRID: AB_2687899
Rabbit anti-HA (monoclonal)	Cell Signaling Technology	Cat# 3724, RRID: AB_1549585
Rabbit anti-BIP (monoclonal)	Cell Signaling Technology	Cat# 3177, RRID: AB_2119845
Rabbit anti-IRE1 (monoclonal)	Cell Signaling Technology	Cat# 3294, RRID: AB_823545
Rabbit anti-XBP1s (monoclonal)	Cell Signaling Technology	Cat# 12782, RRID: AB_2687943
Rabbit anti-PERK (monoclonal)	Cell Signaling Technology	Cat# 5683, RRID: AB_10841299

Rabbit anti-ATF4	Cell Signaling Technology	Cat# 11815, RRID: AB_2616025
Mouse anti-CHOP (mouse)	Cell Signaling Technology	Cat# 2895, RRID: AB_2089254
Mouse anti-Myoferlin (monoclonal)	Santa-Cruz Biotechnology	Cat# sc-376879
Goat anti-Myoferlin (polyclonal)	Santa-Cruz Biotechnology	Cat# sc-51367, RRID: AB_2148879
Mouse anti-Vinculin (monoclonal)	Santa-Cruz Biotechnology	Cat# sc-25336, RRID: AB_628438
Mouse anti-S1R (monoclonal)	Santa-Cruz Biotechnology	Cat# sc-137075, RRID: AB_2285870
Rabbit anti-MFN1 (polyclonal)	Santa-Cruz Biotechnology	Cat# sc-50330, RRID: AB_2250540
Mouse anti-SP1 (monoclonal)	Santa-Cruz Biotechnology	Cat# sc-17824, RRID: AB_628272
Mouse anti-HSC70 (monoclonal)	Santa-Cruz Biotechnology	Cat# sc-7298, RRID: AB_627761
Rabbit anti-Myoferlin (polyclonal)	Sigma-Aldrich	Cat# HPA014245, RRID: AB_1848495
Mouse anti-Mitochondria (monoclonal)	Millipore	Cat# MAB1273, RRID: AB_94052
Mouse anti-GRP78 (monoclonal)	R and D Systems	Cat# MAB4846, RRID: AB_2233235
Mouse anti-VDAC (monoclonal)	Abcam	Cat# ab14734, RRID: AB_443084

Rabbit anti-PDHα1 (monoclonal)	Abcam	Cat# ab168379
Rabbit anti-Phospho-PDHα1 (polyclonal)	Abcam	Cat# ab92696, RRID: AB_10711672
Mouse anti-GAPDH (monoclonal)	Abcam	Cat# ab8245, RRID: AB_2107448
Mouse anti-OXPHOS cocktail (monoclonal)	Abcam	Cat# ab110413, RRID: AB_2629281
Mouse anti-MFN1/2 (monoclonal)	Abcam	Cat# ab57602, RRID: AB_2142624

Table 2. List of antibodies used in this work. Antibodies species, clonality, source and identifiers are specified.

3.2. Cell culture

Panc-1 cells were cultured in Dulbecco's modified Eagle's medium (DMEM, Lonza, Basel, Switzerland) supplemented with 10% fetal bovine serum (FBS). Miapaca-2 and C2C12 were maintained in DMEM supplemented with 10% FBS, 1mM sodium pyruvate and 4mM L-glutamine. PaTu8988T were cultured in DMEM supplemented with 5% FBS, 5% horse serum and 2mM L-glutamine. BxPC-3 were maintained in RPMI1640 supplemented with 10% FBS, 1mM sodium pyruvate, 10mM HEPES and 2.5g/L of glucose. HPNE required a medium composed of 75% DMEM, 25% M3 (Incell Corporation LLC, San Antonio, TX), 2.5% FBS, 0.01% epidermal growth factor, 2mM L-glutamine and 1g/L of glucose. The cells were cultured in a humidified 5% CO2 incubator, at 37◦C and were used between passage 1 and passage 10. The cells were tested monthly for mycoplasma thanks to lab-made reagents.

3.3. Small interfering RNA transfection

The cells were transfected with 20nM small interfering RNA (siRNA) using Ca^{2+} phosphate. The medium was replaced 16 h after transfection, media replacement was considered as time 0. All experiments were performed 48 h after transfection. Myof#1 - 5' CCCUGUCUGGAAUGAGAUUUU 3' and Myof#2 - 5' CUGAAGAGCUGUGCAUUATT 3' siRNA were

used to target myoferlin while the irrelevant siRNA - 5' CUUACGCUGAGUACUUCGAUU 3' was used as transfection control. All siRNA were purchased from Eurogentec (Liège, Belgium).

3.4. Plasmid preparation and transfection

pCDNA3.1-Myoferlin HA (273), a plasmid encoding for human myoferlin cDNA with a C-terminal HA-tag was constructed by William Sessa (Addgene plasmid #22443). CMV-mito-R-GECO1 was a construction from Robert Campbell (Addgene plasmid # 46021) (306) (Figure 3-1). pCDNA3.1-Myoferlin HA or CMV-mito-R-GECO1 plasmids were amplified in DH5alpha or DH10B bacteria, respectively. Bacteria were cultured in classical LB medium, supplemented with ampicillin (100 µg/ml), overnight at 37°C in an agitating incubator (200 rpm). pCDNA3.1-Myoferlin HA plasmid purification was performed using the PureYield™ Plasmid Maxiprep System (A2393) from Promega (Fitchburg, WI). Purification of CMV-mito-R-GECO1 was performed using the NucleoBond Xtra Maxi kit (740424.50) and the NucleoSnap Finisher kit (740434.50) from Macherey Nagel (Düren, Germany) with the help of the GIGA viral platform. Panc-1 or MiaPaCa-2 cells were transiently transfected with 1 µg of plasmid using 2.5 µL Lipofectamine 2000 (Invitrogen, Carlsbad, CA) as reported by the manufacturer's recommendation. The medium was replaced 4h after transfection. 48h after transfection, both Panc-1 and MiaPaCa-2 cells were selected with 600 µg/ml of G-418 for 7 days. Antibiotic pressure using G-418 solution was maintained at a concentration of 200 µg/ml for cell culture. To address CMV-mito-R-GECO1 plasmid localization on mitochondria, we used a MitoTracker Green dye (M7514, Thermo Fisher Scientific, Waltham, USA), at a final concentration of 200nM, which was a generous gift from Dr. Laurent Nguyen (GIGA Stem Cells, ULiège).

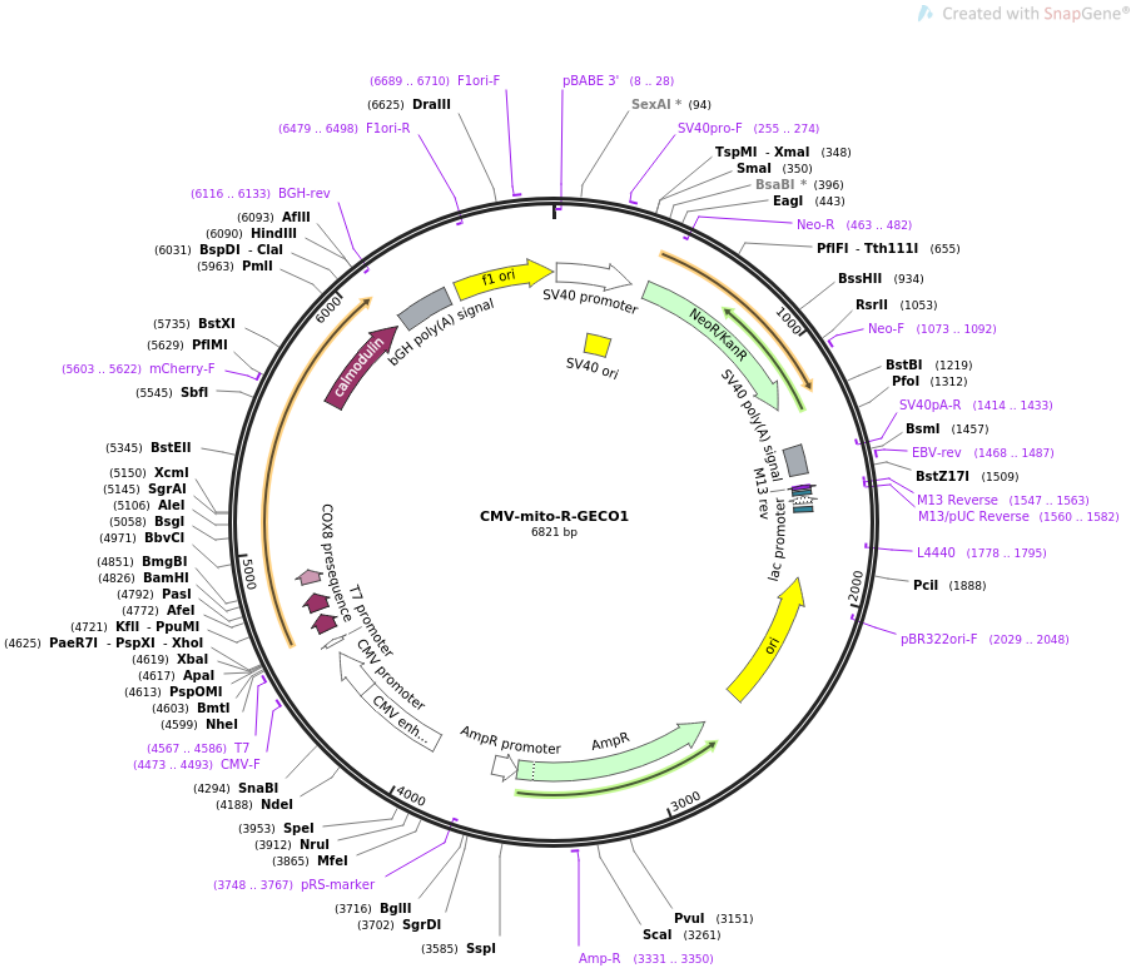

Figure 3-1. CMV-mito-R-GECO1 plasmid (Red intensiometric Ca^{2+} indicator). The plasmid codes for a fusion protein involving cytochrome c oxidase subunit 8 (COX8) and calmodulin. The picture is from https://www.addgene.org/.

3.5. Western blotting

Protein samples were solubilized in 1% sodium dodecyl sulfate (SDS) supplemented with phosphatase and protease inhibitors. Bicinchoninic acid (BCA) protein assay kit (Thermo Scientific, Waltham, MA) was used for protein quantification. Proteins were denatured in Laemmli's buffer during 5 min at 99°C. Samples were loaded on sodium dodecyl sulfate polyacrylamide gel for migration and were then electro-transferred on PVDF membrane during 90 min at room temperature (RT) or overnight at 4°C. Membranes were blocked for 1 h according to antibody manufacturers' instructions. Then, they were incubated overnight at 4°C with primary antibodies (dilution 1:1000) and probed with corresponding secondary antibodies linked to horseradish peroxidase (dilution 1:3000) for 1 h at RT. The revelation was performed using chemiluminescent reagents (ECL western blotting substrate, Thermo Scientific, Waltham,

MA or clarity western ECL substrate, Bio-Rad, California, USA). Quantifications were performed by densitometric analysis using ImageJ software (307) and HSC70 was used as a loading control.

3.6. Immunofluorescence

Regarding part I of the *Results* section (see *Part I: myoferlin interacts with proteins involved in mitochondrial fusion in PDAC cell lines*), cells ($6x10^4$) were seeded on sterilized glass coverslips. After 24 h, cells were washed once with PBS and fixed with ice-cold methanol-acetone (4:1) during 10 min. Then, cells were washed twice with PBS and were blocked for 30 min in 2% bovine serum albumin diluted in PBS. After blocking, coverslips were incubated during 2 h with primary antibodies (dilution 1:100 in BSA-PBS) at RT in a humidified chamber. This step was followed by three washes in 2% BSA-PBS. Coverslips were then incubated with corresponding Alexa Fluor 488 or Alexa Fluor 546 conjugated secondary antibodies (Invitrogen, Molecular Probes, Carlsbad, CA) in a humidified chamber for 45 min (dilution 1:1000 in BSA-PBS). Nuclei counterstaining was performed using hoechst DNA probe (0.01g/L, Calbiochem, San Diego, CA). Pictures were acquired using Nikon A1R confocal microscope or LSM880 Airyscan Elyra Microscope (Zeiss, Oberkochen, Germany).

In part II of the *Results* section (see *Part II: myoferlin is located in MAMs, where it plays a role in calcium transfer and interacts with IP3R3*), the same protocol than in part I was used for immunofluorescence, except for the fixation, blocking and permeabilization steps. Indeed, cells were fixed with paraformaldehyde (PAF) 4% (pH 7,4) for 20 min. After washing, the cells were blocked and permeabilized for 30 minutes with a solution containing 5% BSA - 0,5% saponin - PBS. Antibodies were diluted in 1% BSA - 0,1% saponin - PBS solution.

3.7. Colocalization studies

Regarding part I of the *Results* section (see *Part I: myoferlin interacts with proteins involved in mitochondrial fusion in PDAC cell lines*), immunofluorescence images were deconvoluted using online NIS-elements (Nikon). Colocalization analyses were first performed, without selection of regions of interest (ROI), using correlation methods: Pearson coefficient correlation (PCC), Spearman's rank correlation coefficient (SRCC), Manders' colocalization coefficients (M1 and M2), and intensity correlation quotient (ICQ), thanks to EzColocalization ImageJ plugin (308). The background was automatically identified according to the Costes method. Then, we used "distance between objects"-based methods: distance analysis (centers of mass of channel 1

objects inside channel 2 masks), parametric analysis of the Ripley's K function, and non-parametric Ripley's analysis (SODA), thanks to colocalization studio plugin in Icy software (309). A 5-pixel maximal limit was used as threshold.

The coefficients are described below:

- The PCC quantifies the correlation between two data sets, in our case channels, assuming a linear correlation between the two. An obvious limitation is when the data sets are correlated but not in a linear manner. The PCC takes values between -1 and +1, with -1 being a perfect linear anti-correlation, +1 a perfect linear correlation and 0 no correlation (310,311).
- The SRCC is an improvement upon the PCC. Indeed, the correlation is quantified without assuming a linear correlation. This method assesses the relation between the two data sets by comparing their ordering. For instance, monotonous relationships will have a maximum score. Conversely, periodic relations such as sine function will have a reduced score. The SRCC takes values between -1 and +1, with -1 being a perfect monotonous anti-correlation, +1 a perfect monotonous correlation and 0 no correlation (311,312).
- The Manders coefficients assess the proportion of pixels from one data set colocalizing with the other. Conversely to PCC and SRCC, Manders' method is not based on mathematical relations between two sets but rather represents the colocalization. The Manders coefficients vary from 0 to 1, 0 being no overlapping of the signal and 1 being complete overlapping of the signal (313).
- The ICQ assesses the correlation between the intensities of two data sets. These intensities are compared to their respective means. Comparably to the SRCC, the ICQ does not assume a linear correlation. It ranges from -0.5 to 0.5, -0.5 being a complete anti-correlation of the intensities, -0.5 being the complete correlation of intensities and 0 being no correlated variation of the intensities (random staining) (314).
- The parametrization of Ripley's K function relies on Ripley's K function, which represents the clustering of objects as function of their relative distance. In 2015, Lagache *et al.* have defined a parametrization of this function allowing to estimate the proportion of objects in one channel colocalizing with those in the second (this will be referred to as *Ripley's K* in the figures) as well as the mean distance between these objects (this will be referred to as *distance (K function)* in the figures). The specificity of this method is

that it assesses the relation between objects without requiring them to be located at the exact same spot (315).

- The SODA method is also based on Ripley's K function. Nevertheless, rather than adjusting a parametric function, the values are compared to the expectation in the case of normally distributed random objects. Therefore, SODA in the figures represents the probability of colocalization between objects. The method provides the probability of colocalization between objects (labelled *SODA* in the figures) with a mean distance between these objects (labelled *distance (SODA)* in the figures) (316).
- The center of mass analysis represents the proportion of objects of which the center of mass in the first channel overlaps with object in the second channel (315).

In part II of the *Results* section (see *Part II: myoferlin is located in MAMs, where it plays a role in calcium transfer and interacts with IP3R3*), we focused mainly on Manders 'method (313). The goal was to assess myoferlin localization on mitochondria. Therefore, we needed a method focused on relative position rather than correlation. In part I of the *Results* section, we used Manders' method to assess myoferlin localization on mitochondria. Nevertheless, we used the whole picture as ROI and Costes method for threshold, this can be a problem and lead to an overestimation of the coefficients. Indeed, we observed that the automatic threshold estimation was often too low, leading to the inclusion of non-specific signals such as background noise. Consequently, using Costes method without selecting any ROI can produce an overestimation of colocalization coefficients, which does not represent the biological staining. To address this issue, we wrote a script based on JACoP ImageJ plugin to standardize the results and make them comparable (317). This was enforced by keeping consistent threshold values throughout the set of images. In addition, individual cells were used as ROI. For images randomization, the rows were randomly permutated and the same was done with columns, creating a randomized image. The scripts are available on https://github.com/Yuglut/ImageJ-Colocalisation-Analyses. Scripts were written by Dr. Martin Farnir (Center for Fusion, Space and Astrophysics, Warwick, UK).

3.8. Proximity ligation assay

The Duolink proximity ligation assay (PLA) kit (Sigma, Bornem, Belgium) was used according to the manufacturer's instructions. Primary antibodies were used at dilution 1:75 (Myoferlin-

MFN1/2) or 1:100 (others). Oligonucleotides conjugated secondary antibodies were provided by the kit allowing detection of a red signal if less than 40nm separates both proteins of interest. Pictures were acquired using a Nikon A1R confocal microscope. In each microscopic field, proximity dots were counted using ImageJ software (307) and divided by the number of nuclei in order to calculate an average proximity dots number per cell. To analyze the PLA, we wrote a script to automatically analyze the data in a standardized way. The script is available on https://github.com/Yuglut/ImageJ-PLA-Analyses. The script was written by Dr. Martin Farnir (Center for Fusion, Space and Astrophysics, Warwick, UK).

3.9. Co-immunoprecipitation

Proteins were extracted using a non-denaturing buffer containing Tris-HCl pH 8 (20mM), NaCl (137mM), NP40 (1%), EDTA (2mM) and supplemented with protease inhibitors. Following extraction, proteins were incubated under rotation at 4°C during 30 min and were centrifuged at 14 000g for 15 min at 4°C to eliminate cell debris. 5 µg antibodies were incubated overnight with 500 µg of the protein extract (except for the IP performed from MAMs extracts, where 250 µg were incubated). We used isotype IgG as control (Thermo Scientific, Waltham, MA). Then, protein A/G magnetic beads (Thermo Scientific, Waltham, MA) were added and incubated at 4°C under rotation for 2 h. After three washes with a low salt buffer containing SDS (0.1%), Triton X-100 (1%), EDTA (2mM), Tris-HCl pH 8 (20mM) and NaCl (150mM) and one wash of high salt buffer composed of SDS (0.1%), Triton X-100 (1%), EDTA (2mM), Tris-HCl pH 8 (20mM) and NaCl (450mM), proteins were eluted from magnetic beads using Laemmli's buffer and then processed for western blotting.

3.10. Mitochondrial enrichment using Qiagen kit

Mitochondrial isolation kit (Qiagen, Hilden, Germany) was used according to the manufacturer's instructions. Briefly, $2x10^7$ washed cells were suspended in lysis buffer in order to disrupt the plasma membrane. After centrifugation (1000g, 10 min, 4°C), the supernatant contained cytosolic proteins while the pellet was composed of intact mitochondria, endoplasmic reticulum and other compartmentalized organelles. The pellet was suspended in disruption buffer and homogenized in a potter with a glass pestle (15 strokes). After centrifugation (1000g, 10 min, 4°C), nuclei, cell debris and unbroken cells were pelleted while the microsomes and mitochondria were contained in the supernatant. The supernatant was

then centrifuged (6000g, 10 min, 4°*C*) and the obtained pellet was resuspended in mitochondrial purification buffer. The mitochondrial suspension was pipetted on a purification solution. After centrifugation (14 000g, 10 min, 4°*C*), mitochondria were pelleted and harvested. All fractions were processed for further western blotting experiments.

3.11. Subcellular fractionation using percoll gradient

This experiment was based on the protocol published in 2016 by Lewis *at al.* (118). $8x10^6$ cells were seeded on 150 mm dishes and placed in an 5% CO2 incubator, at 37°C (confluency: 80%). In total, ~40 dishes per experiment were used. 24h after the seeding, the cells were placed on ice and washed once with ice-cold PBS. Then, they were detached from the dishes by scrapping and centrifuged for 5 min at 500g. The resulting pellet was suspended in HB buffer (10 mM HEPES, pH 7.4, and 0.25 M sucrose) and homogenized with Teflon glass homogenizer for 30 strokes. After centrifugation (5 min, 600g), the supernatant was kept aside (supernatant 1) and the pellet was again suspended in HB buffer, homogenized for 15 strokes and centrifuged for 5 min at 600g. The resulting supernatant was pooled with supernatant 1. The pellet constituted P1 fraction, representing non-lysed cells, nuclei and cell debris. Following this step, supernatant 1 was centrifuged for 20 min at 10 300g. The resulting supernatant (supernatant 2) was ultracentrifuged for 60 min at 100 000g, giving a cytosolic (supernatant) and microsome (pellet) fractions. In parallel, the pellet obtained by centrifugation from supernatant 1, constituting crude mitochondrial fraction (CM), was resuspended in IM buffer (5 mM HEPES, pH 7.4, 250 mM mannitol, 0.5 mM EGTA) and placed on percoll medium (25 mM HEPES, pH 7.4, 225 mM mannitol, 1 mM EGTA, 30 % Percoll (v/v)). Following this step, centrifugation for 30 min at 95 000g was performed. MAMs and mitochondria were collected using Pasteur pipettes (MAMs formed a white layer near the top of the tube). Then, MAMs were suspended in IM2 buffer (25 mM HEPES, pH 7.4, 225 mM mannitol, 1 mM EGTA) and centrifuged for 10 min at 6 300g. On one hand, the pellet was harvested as crude MAMs (CMAMs). On the other hand, the resulting supernatant was centrifuged for 1h at 100 000g. The white membrane at the bottom of the tube following centrifugation was harvested as purified MAMs fraction (PMAMs). In parallel, mitochondria obtained from centrifugation on percoll medium were washed three times with IM buffer. The pellet obtained from washing constituted purified mitochondrial fraction (PM). The protocol is represented and summarized on **Figure 3-2**. During the experiment, samples were kept on ice and centrifugations were performed at 4°C.

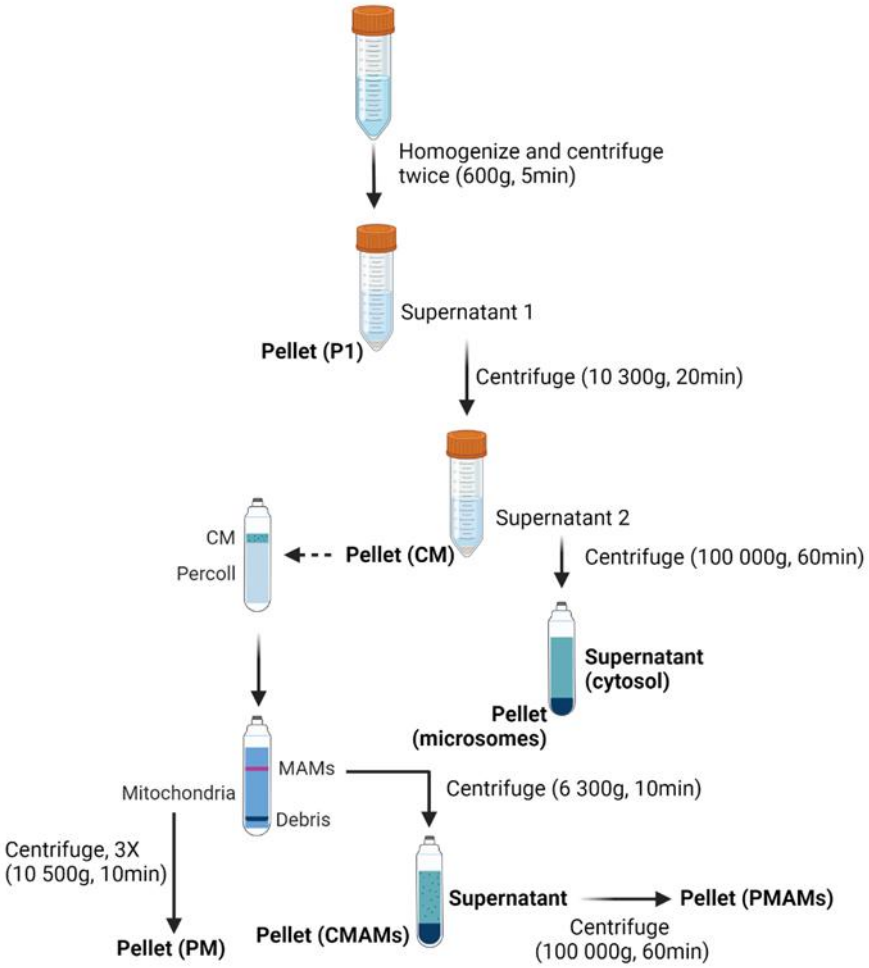

Figure 3-2. Subcellular fractionation. Representation of the protocol used for MAMs purification. PM: pure mitochondria, CMAMs: crude MAMs, PMAMs: pure MAMs. The picture was created with BioRender.com

3.12. Ultrastructural analysis

Panc-1 cells were fixed for 90 min at room temperature with glutaraldehyde (2.5%) in a Sörensen phosphate buffer (0.1 M, pH 7.4) and post-fixed for 30 min with 2% osmium tetroxide. Samples were dehydrated in graded ethanol and embedded in Epon. Thanks to a Reichert Ultracut S ultramicrotome, ultrathin sections were obtained and contrasted with uranyl acetate and lead citrate. Acquisitions were performed with a Jeol (Tokyo, Japan) JEM-1400 transmission electron microscope at 80 kV. Pictures were acquired by Pr. Marc Thiry (Cellular and Tissular Biology, ULiège). Morphometric measurements were performed using ImageJ software (307). The length of the ER interface in contact with mitochondria, the mitochondrial perimeter as well as the distance between both organelles were measured. For calculations of

mitochondria–ER distance, a minimum distance of 30 nm between both organelles was required to be consider as a contact. Since the pictures used for the analyses were limited (< 15 pictures by conditions) and not randomly chosen, precaution for results interpretation should be taken.

3.13. Oxygen consumption rate analysis

OCR were measured with a Seahorse XFp extracellular flux analyzer (Agilent, Santa Clara, CA, USA). siRNA-transfected cells were seeded (10 000 cells per well) in XFp mini-plates and allowed to attach overnight. For mitochondrial OCR analysis, cells were kept in unbuffered serum-free DMEM (Basal DMEM, Agilent) supplemented with pyruvate (1 mM), glutamine (2 mM), glucose (10 mM), pH 7.4 at 37 °C, and ambient CO_2 for 1 h before the assay. During the assay, cells were successively stressed with oligomycin (1 µM), carbonyl cyanide-p-trifluoromethoxyphenylhydrazone (FCCP, 1.0 µM), and rotenone/antimycin A (0.5 µM each) mix. Results were normalized according to the cell number evaluated by Hoechst (2 µg/mL) incorporation after cold methanol/acetone fixation.

3.14. Calcium flow

200 000 cells (stably transfected with the CMV-mito-R-GECO1 plasmid, see section *Plasmid preparation and transfection*) were seeded on glass bottom dishes (Ibidi, 81158, Gräfelfing, Germany) 24h prior to experiment. The next day, the cells were washed once with PBS and the medium was replaced by calcium-free medium (NaCl (145 mM), KCl (4 mM), HEPES (10 mM), glucose (10 mM), MgCl2 (2 mM), EGTA (1 mM)). Then, the dishes were placed on Nikon A1R microscope stage in a humidified chamber with 5% CO_2, at 37°C. Once the cells were placed in the chamber, we waited for 10 minutes before starting the experiment. Pictures acquisition occurred every 5 seconds (a cycle represents the time between two acquisitions). After 50 seconds, a calcium-free buffer containing histamine was injected (100 µM, final concentration of histamine). Pictures acquisition continued for 50 additional cycles until fluorescence returned to its starting value. The detailed protocol for calcium flow experiment was generously shared by Dr. Yelena Sargsyan (University of Bielefeld, Göttingen, Germany).

For the analyses, we assessed fluorescence intensity value over time (Fn) for each cell and we normalized it to the first frame (F0) of the time-lapse (Fn/F0), which allows comparisons between conditions. Those analyses were performed with ImageJ (307). A script, which is

available on https://github.com/Yuglut/ImageJ-Timelapse-CalciumFlow-Analysis, was written to automate and standardize the analyses. The script was written with the help of Dr. Martin Farnir (Center for Fusion, Space and Astrophysics, Warwick, UK).

3.15. WST1 assay

$9x10^3$ cells were seeded per well of a 96-well plate. 24h hours later, WST-1 reagent (Roche, Mannheim, Germany) was diluted in culture medium (1:10) and the absorbance at 450 and 620 nm was measured during 120 min at 37 °C using a Spectramax plate reader (Molecular Devices, Sunnyvale, CA, USA). Following measurement, cells were fixed with cold methanol/acetone and incubated with Hoechst (2 µg/ml) for normalization.

3.16. Indirect fluorescence resonance energy transfer

All samples were processed as described in the *Immunofluorescence* section. The Alexa Fluor 488-conjugated secondary antibody was selected as the donor fluorophore while the Alexa Fluor 546-conjugated secondary antibody was selected as the acceptor (Invitrogen, Molecular Probes, Carlsbad, CA, USA). As a positive control, two secondary antibodies were used, both targeting rabbit anti-myoferlin (HPA) primary antibody, and carrying acceptor or donor fluorophore. Finally, as a negative biological control, proteins from distinct compartments, the nuclear factor SP1 and the plasma membrane transporter GLUT1 were selected. Images were acquired with a LSM880 Airyscan Elyra Microscope (Zeiss, Oberkochen, Germany). The FRET ratio was calculated as described by Guala *et al*. in 2018 (318).

3.17. Statistical analysis

For parametric analyses, according to the number of experimental conditions to compare, unpaired t-test or one-way analysis of variance (ANOVA) were performed. For multiple comparisons, Dunnett's or Tukey tests were applied. When the data were not following a normal distribution, non-parametric tests were carried out. The test of Mann-Whitney was used to compared two groups, while the test of Kruskal-Wallis was used to compare more than two groups. A p-value < 0.05 was considered as statically significant. Survival analyses were performed according to Kaplan–Meier on TCGA PanCancer Atlas cohort (n=177) thanks to the https://kmplot.com/ website. An automatic cut-off was used. Survival curves were compared using the log-rank test. For seahorse statistical analyses, a two-way ANOVA was performed.

RESULTS

Part I: myoferlin interacts with proteins involved in mitochondrial fusion in PDAC cell lines

Adapted from:

Myoferlin Is a Yet Unknown Interactor of the Mitochondrial Dynamics' Machinery in Pancreas Cancer Cells

Sandy Anania, Raphaël Peiffer, Gilles Rademaker, Alexandre Hego, Marc Thiry, Louise Deldicque, Marc Francaux, Naïma Maloujahmoum, Ferman Agirman, Akeila Bellahcène, Vincent Castronovo, Olivier Peulen

Cancers 2020, 12(6), 1643; https://doi.org/10.3390/cancers12061643

4. Results

4.1. Part I: myoferlin interacts with proteins involved in mitochondrial fusion in PDAC cell lines

Myoferlin, also named FER1L3, is a protein from the ferlin family. It was first discovered in skeletal muscle in 2000 (240). This protein harbors a unique and rare structure with multiple C2 domains known to bind membranes in a Ca^{2+} dependent manner (241). FER1L3 is involved in membrane fusion and repair of normal cells (246). Interestingly, myoferlin has been found to be overexpressed in several cancers including PDAC (44,247) and recent studies highlighted myoferlin as a promising therapeutic target thanks to the use of myoferlin-targeting drugs (45,46). Myoferlin silencing or targeting strongly reduces cell migration, invasion and proliferation *in vitro* and decreases tumor size and metastasis *in vivo* (46,48,286,287). Thus, myoferlin overexpression in PDAC confers advantages to cancer cells and this might be related, at least in part, to its role in cell metabolism. Indeed, in the literature, myoferlin has been associated with mitochondrial dynamics and metabolism in pancreatic cancer (47,49). This observation was correlated with the migratory capacity of PDAC cell lines (48). Upon myoferlin silencing, PDAC cell lines exhibit a fragmented mitochondrial network, which is associated with a decrease in mitochondrial respiration (47). Knowing that there is a growing number of publications showing the importance of mitochondrial respiration for cell proliferation, tumor growth, cancer resistance and cancer relapse in PDAC, we decided to investigate the potential relationship existing between myoferlin and mitochondria (61,63,319). Myoferlin is a large type-II transmembrane protein of approximatively 230 KDa, found in many subcellular structures such as plasma membrane, late and early endosomes as well as ER and lysosomes (240,242,243). Thus, myoferlin has been described in secretory and endocytic pathways. However, there is no report showing a direct involvement of myoferlin with mitochondria. In this study, we first aimed at investigating whether myoferlin is located on mitochondria and whether it interacts with MFNs. Indeed, since myoferlin has been shown to interact with GTPases such as RAB7, we thought myoferlin could also interact with MFNs on mitochondria and promote mitochondrial fusion. Thus, upon myoferlin silencing, a lack of fusion would occur, leading to a fragmented mitochondrial network (45,47,254).

4.1.1. Endogenous myoferlin is present in mitochondrial crude extract and colocalizes partly with mitochondria

It was previously shown that myoferlin silencing impairs mitochondrial network in Panc-1 cells (47). Thus, we decided to use the same cell line to investigate the potential mitochondrial localization of endogenous myoferlin **(Figure 4-1A)**. Using differential centrifugation steps (Qiagen kit), we prepared a mitochondrial extract. The abundance of a mitochondrial-specific 60 kDa protein (clone 113-1) indicated a 4.7-fold enrichment factor in comparison to whole cell extract. Interestingly, the mitochondrial crude extract contained several myoferlin isoforms, displaying a 1.6-fold increase compared to the whole cell extract. Even if its relative abundance decreased by 30%, GRP78 was still detectable in the mitochondrial crude extract, suggesting a microsomal contamination.

These results prompted us to perform immunofluorescence staining to explore myoferlin localization inside Panc-1 cells. For this purpose, we used a goat polyclonal myoferlin antibody (K-16). As previously reported (242), myoferlin staining appeared as a punctuated signal spread all over the cytoplasm, with a higher density close to plasma membrane **(Figure 4-1B)**. Nevertheless, no bright labeling was observed at the perinuclear region as described by Redpath *et al.* in 2016 (242). Correlative colocalization analyses of deconvoluted images revealed a partial colocalization between myoferlin (K-16) and mitochondrial signals **(Figure 4-1C)**. While correlation coefficients (PCC and SRCC) showed only a weak association (~0.20), Manders' colocalization coefficients (M1 and M2) indicated an intermediate colocalization (>0.50). The first Manders' coefficient, M1, describes the proportion of myoferlin pixels co-occurring with mitochondrial pixels, and vice-versa for M2. Interestingly, several myoferlin-positive structures were identified in contact with mitochondria **(Figure 4-1D,E)**. Even if it was infrequent, some myoferlin staining seemed to be located between mitochondrial sections, being close to each other and resembling potential mitochondrial fusion sites **(Figure 4-1D,E)**. Myoferlin and mitochondria colocalization was also assessed by "distance between objects"-based methods **(Figure 4-1F)**. Based on these methods, the proportion of myoferlin-positive objects (N = 4286) colocalizing with mitochondrial-object (N = 459), with a mean distance of 2 pixels ranging from 0 to 5 pixels, was below 10% (SODA).

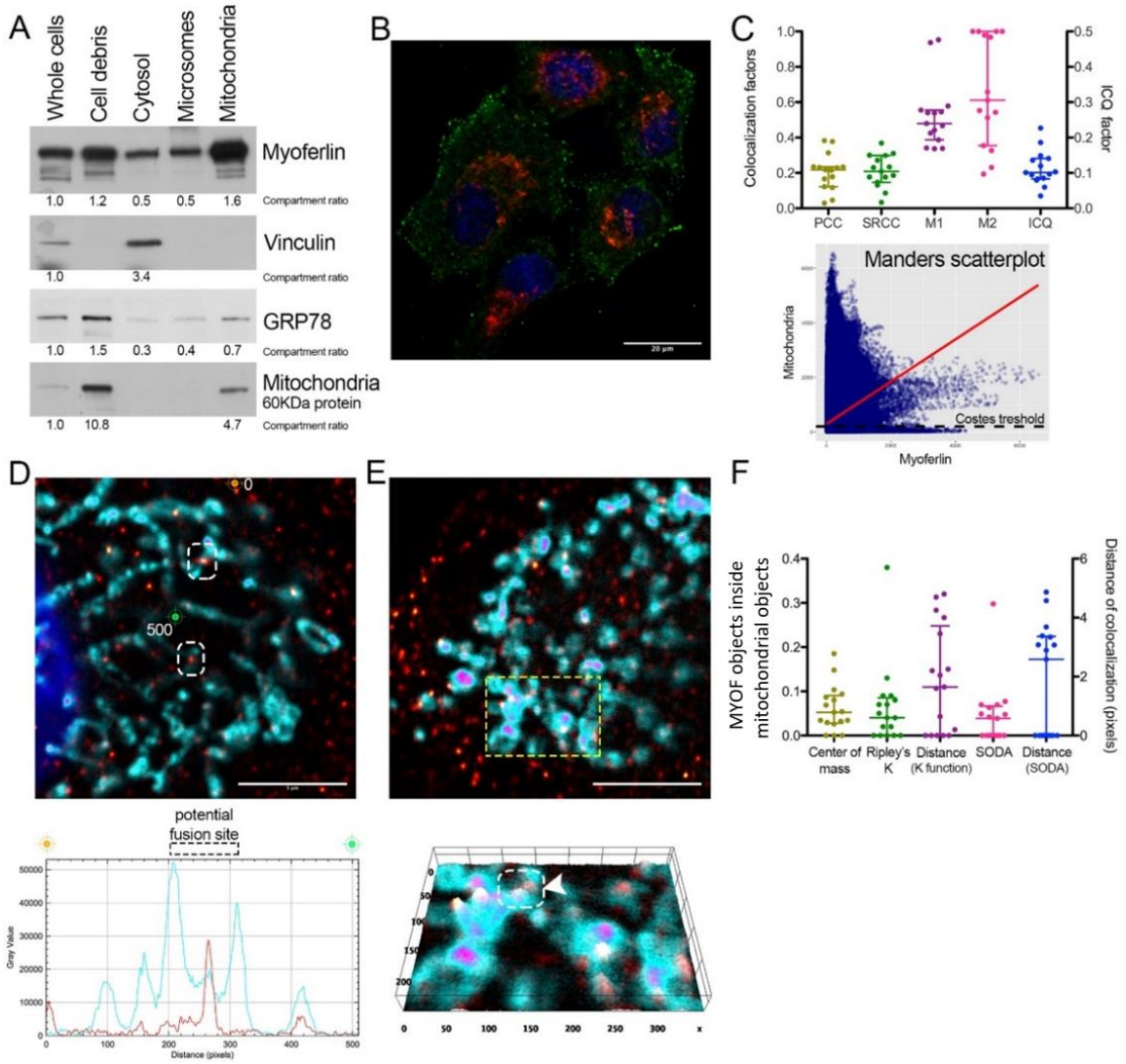

Figure 4-1. Myoferlin colocalizes with mitochondria in Panc-1 cells. **(A)** Western blot of 6 µg protein samples from whole Panc-1 cells and several cellular compartments isolated from Panc-1 cells. Myoferlin, vinculin, GRP78, and a 60 kDa mitochondrial protein were detected on the same membrane. Compartment relative quantification was performed using ImageJ software (307); **(B)** representative confocal image of nuclei (blue), myoferlin (K-16—green) and mitochondria (113-1—red) immunofluorescence. Scale bar = 20 µm; **(C)** Pearson (PCC), Spearman rank (SRCC) correlation coefficients, Manders' colocalization coefficients (M1,M2), and intensity correlation quotient (ICQ) calculated on 17 independent microscopic fields. Manders scatterplot, associated with its linear regression (red line), shows the correlation between the intensity of each pixels in each channel. **(D,E)** Deconvoluted confocal image of nuclei (blue), myoferlin (K-16—"hot" red scale), mitochondria (113-1—"cold" cyan scale). Scale bar = 5 µm. Regions surrounded by white dashed boxes are putative mitochondrial fusion sites. **(D)** Channel intensity profile was established following the segment between orange (0-pixel position) and green (500-pixel position) cross marks; **(E)** The region surrounded by a yellow dashed box was used to generate the 2D intensity profile. Regions surrounded by a white dashed box and marked by white arrow head was looking as a putative mitochondrial fusion site; **(F)** percentage of myoferlin-positive objects (N = 4286) with the center of a mass overlapping mitochondrial objects (N = 459), a percentage of myoferlin-positive objects colocalizing with mitochondrial objects calculated by fitting of the Ripley's K function or by statistical object distance analysis (SODA). Colocalization distances in pixels were measured in both cases. All experiments were performed as three independent biological replicates. The median ±interquartile range is represented.

In addition, we decided to use an additional myoferlin polyclonal antibody raised in rabbits (HPA) (Figure 4-2). In accordance with results obtained using myoferlin K-16 antibody, myoferlin was in proximity with mitochondria (Figure 4-2A). The PCC showed a correlation of ~20%

between myoferlin and mitochondria stainings, while colocalization coefficients such as Manders' coefficients were of ~60%. Finally, the proportion of myoferlin objects colocalizing with mitochondria objects (SODA) was of ~20%.

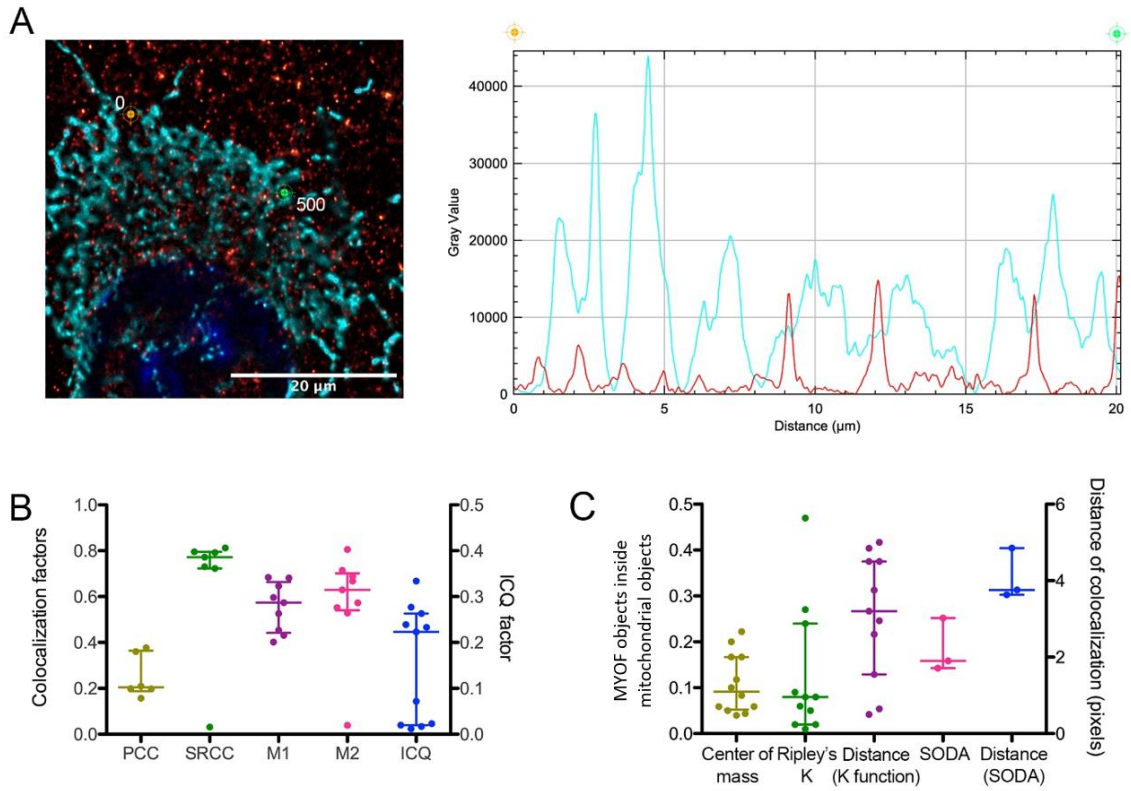

Figure 4-2. Myoferlin colocalizes with mitochondria in Panc-1 cells. **(A)** Deconvoluted confocal image of nuclei (blue), myoferlin (HPA - "hot" red scale), mitochondria (113-1 - "cold" cyan scale). Scale bar = 20 µ m. Channel intensity profile was established following the segment between orange (0-pixel position) and green (500-pixel position) cross marks. **(B)** Pearson (PCC), Spearman rank (SRCC) correlation coefficients, Manders' colocalization coefficients (M1, M2), and intensity correlation quotient (ICQ) calculated on 11 independent microscopic fields. **(C)** Percentage of myoferlin-positive objects (N=7365) with center of mass overlapping mitochondrial object (N=273), percentage of myoferlin positive objects colocalizing with mitochondrial objects calculated by fitting of the Ripley's K function or by statistical object distance analysis (SODA). Colocalization distances in pixels were measured in both cases. The median ±interquartile range is represented.

4.1.2. Endogenous myoferlin is in proximity with mitochondrial fusion machinery in pancreas cancer cell lines

Owing to the known function of myoferlin in membrane fusion, we decided to evaluate the colocalization of myoferlin with components of the fusion machinery: MFNs. We thus performed immunofluorescence using myoferlin (K-16) and MFN1 antibodies (H-65) **(Figure 4-3A)**. It is worth mentioning that the MFN1 antibody (H-65) recognized MFN1 but also MFN2 by western blot. Correlation coefficients **(Figure 4-3B)** showed a strong association between stainings. The PCC almost reached 80% of correlation, while Manders' coefficients reached 100% of colocalization. Conversely, the "distance between objects"-based methods **(Figure 4-3C)** revealed that ~20% of the myoferlin-positive objects (N = 7128) colocalized with a MFN1-positive object (N = 369) with a mean distance of ~3 pixels, ranging from 0 to 5 pixels (SODA).

We decided to use another myoferlin antibody raised in rabbit (HPA) and a MFN1/2 polyclonal antibody (3C9) raised in mouse in order to further investigate whether myoferlin colocalized with MFNs **(Figure 4-4)**. This time, using the HPA antibody, myoferlin labeling was observed at the plasma membrane and also near the perinuclear region, while the MFN1/2 labeling highlighted a structure resembling the one of mitochondria **(Figure 4-4A)**. The PCC coefficient was of ~40%, while Manders' coefficients were of ~80%. Finally, the proportion of myoferlin objects inside MFNs objects was of ~ 60% **(Figure 4-4C)**. Even though those results should be taken carefully due to the method employed (see *Part I: limitations of the study*), they suggested that myoferlin was in proximity with MFNs.

In order to further clarify those results, we performed a PLA on Panc-1 cells using the myoferlin HPA and the 3C9 MFN1/2 antibodies. This experiment showed 21.3 ± 6.8 proximity dots per cell, indicating a maximal 40 nm distance between myoferlin and MFN1/2 **(Figure 4-3D)**. We next inhibited myoferlin expression using siRNA to confirm the specificity of the PLA signal. Myoferlin silencing suppressed more than 95% of the colocalization signal confirming the specificity of the colocalization **(Figure 4-3E)**.

PLA results were supported in Panc-1 cells by indirect fluorescence resonance energy transfer (FRET) analysis, showing a significant FRET ratio **(Figure 4-5)**. While the FRET ratio was <0.005 in the negative control (using SP1 and GLUT1), it was of 0.5 in the positive control (two secondary antibodies, carrying acceptor or donor fluorochromes, that recognize the same HPA myoferlin primary antibody) and of 0.141 between myoferlin (HPA) and MFN1/2. It is worth

mentioning that the FRET ratio between myoferlin and MFNs was higher at the perinuclear region. This experiment supported the previous results obtained by PLA and immunofluorescence using those antibodies.

We then decided to perform MFN1/2-myoferlin colocalization in three additional PDAC cell lines (BxPC-3, MiaPaCa-2 and PaTu8988T) for which we reported the relative myoferlin and MFN1/2 expression (Figure 4-6). While BxPC-3, MiaPaCa-2 and Panc-1 cell lines are originating from the pancreas itself (primary tumor), Patu8988T were cultured from liver metastasis of a primary pancreatic adenocarcinoma (320,321). With the exception of MiaPaCa-2, all the cell lines were obtained from female patients (320,321). Regarding genetic alterations, BxPC-3 is the only cell line with the absence of mutations in *KRAS*. Panc-1 has a KRAS G12D mutation, while MiaPaCa-2 has a KRAS G12C mutation and PaTu8988T has a KRAS G12V mutation, those last ones being less common than the G12D mutation. BxPC-3, MiaPaCa-2 and Panc-1 are all mutated for *TP53* and *CDKN2A* (320). In addition to these characteristics, the PDAC cell lines used in this study were classified according to their metabolic status. Indeed, while BxPC-3 and Panc-1 cell lines are considered as lipogenic, MiaPaCa-2 and Patu8988T cell lines are considered as glycolytic (see section *Overview of PDAC metabolism*) (57). In these cell lines, correlation coefficients (PCC and SRCC) showed a weaker association (from 0.20 to 0.6 depending on the cell line) than in Panc-1 cell lines. In the BxPC-3 cell line, immunofluorescence staining showed that MFN1/2-myoferlin association was mainly localized at cell periphery (Figure 4-7). In PaTu8988T cell line, the very limited observable cytoplasm area and the low myoferlin expression level made results difficult to interpret.

Since it was difficult to draw conclusions about immunofluorescence analyses, we decided to perform PLA for these additional cell lines. The results obtained by PLA showed less colocalization dots in BxPC-3, MiaPaCa-2, and PaTu8988T than in Panc-1 cells (Figure 4-7). The relative amount of proximity dots appeared to be correlated with myoferlin abundance of each cell line (Figure 4-6). Considering our findings, we then tested whether myoferlin was physically interacting with MFN1/2.

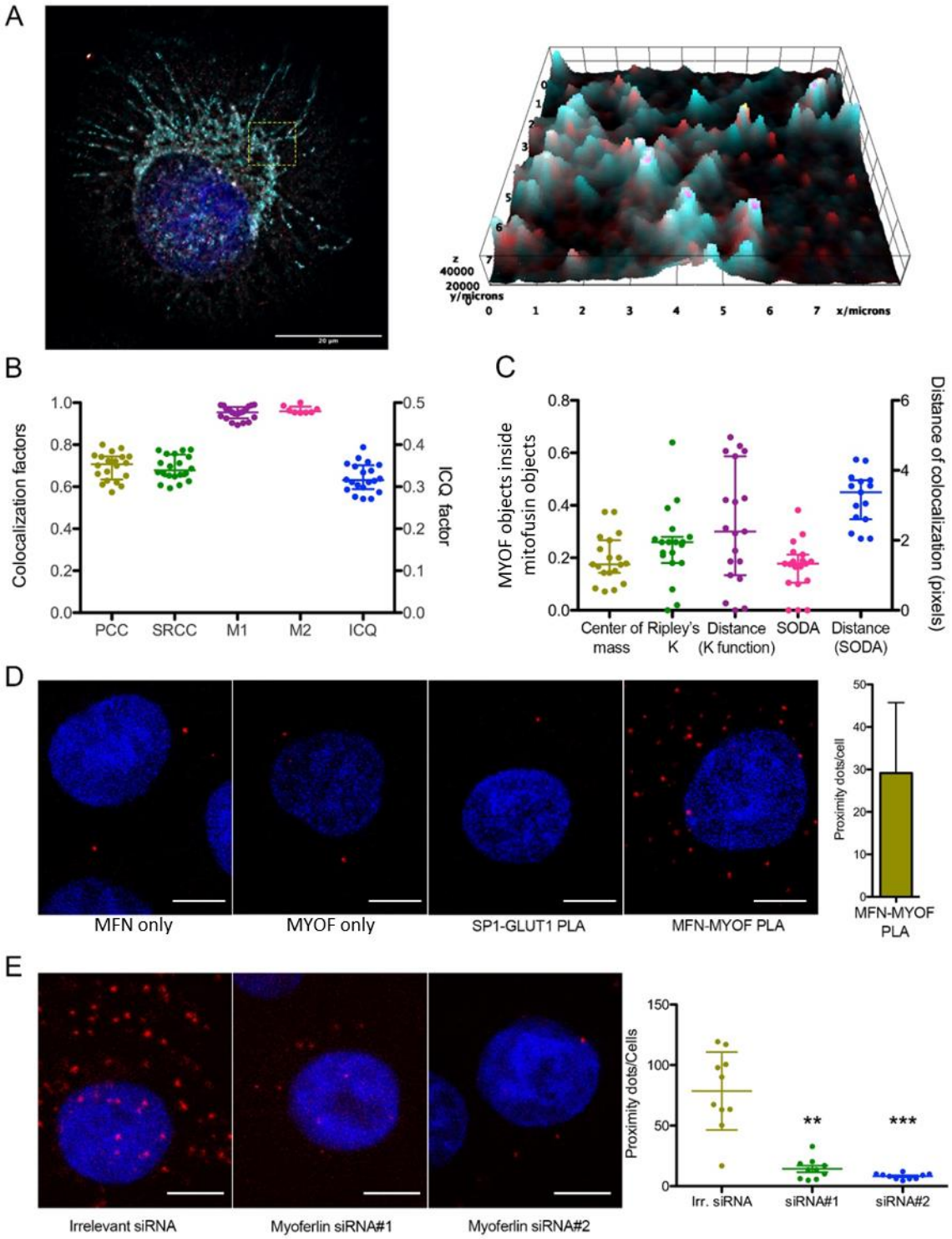

Figure 4-3. Myoferlin colocalizes with mitochondrial fusion machinery. **(A)** Representative deconvoluted confocal image of nuclei (blue), myoferlin (K16—"hot" red scale) and mitofusin-1 (H65—"cold" cyan scale) immunofluorescence. Scale bar = 20 µm. The region surrounded by yellow dashed box was used to generate the 2D intensity profile; **(B)** Pearson (PCC), Spearman rank (SRCC) correlation coefficients, Manders' colocalization coefficients (M1,M2), and intensity correlation quotient (ICQ) were calculated on 20 independent microscopic fields randomly selected; **(C)** percentage of myoferlin-positive objects (N = 7128) with center of mass overlapping mitochondrial object (N = 369), percentage of myoferlin-positive objects colocalizing with mitochondrial objects calculated by fitting of the Ripley's K function or by statistical object distance analysis (SODA). Colocalization distances in pixels were measured in both cases; **(D)** representative images of proximity ligation assay (PLA) between myoferlin (HPA) and mitofusin-1/2 (3C9). Scale bar = 4 µm. Controls were established by using only one of the primary antibodies or by using antibodies against non-interacting proteins (SP1 and

GLUT1); **(E)** representative images of PLA in Panc-1 cells transfected with irrelevant or myoferlin-specific siRNA. Scale bar = 4 µm. MFN1/2-MYOF PLA (N = 10) were quantified using ImageJ software (307). Kruskal–Wallis non-parametric test followed by Dunn's pairwise comparison was performed, ** $p < 0.01$, *** $p < 0.001$. All experiments were performed as three independent biological replicates. The median ±interquartile range is represented.

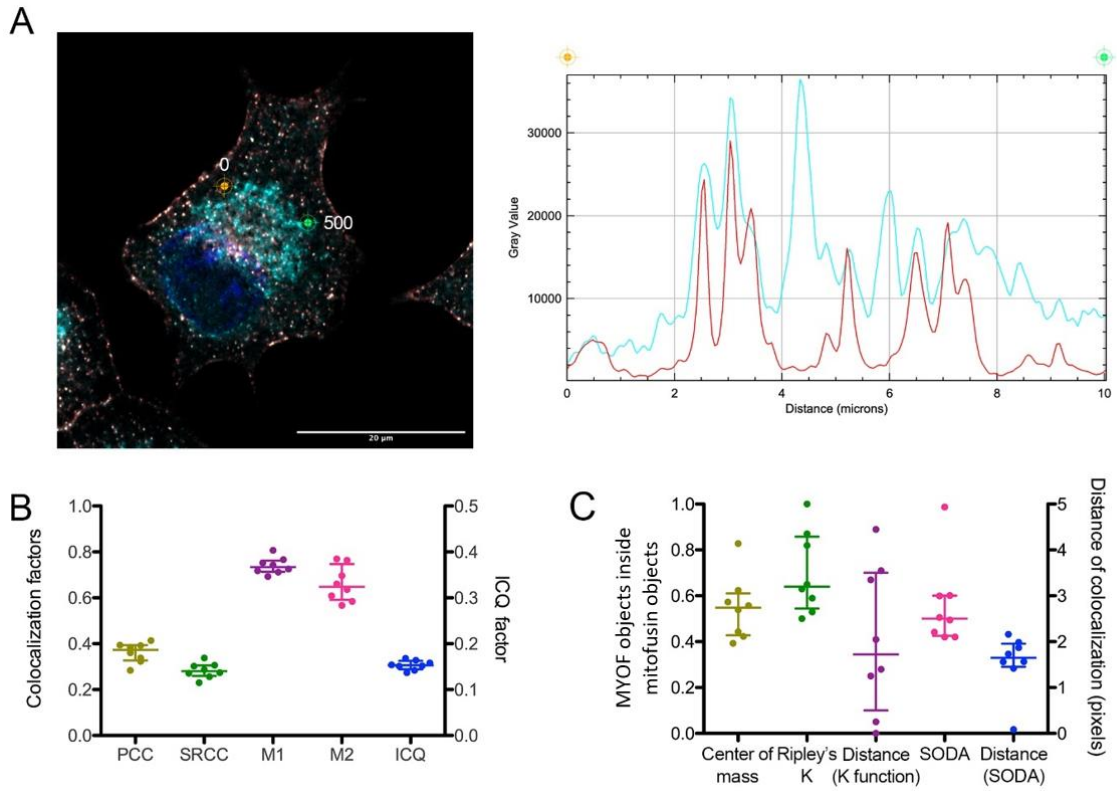

Figure 4-4. Myoferlin colocalizes with mitofusins in Panc-1 cells. **(A)** Deconvoluted confocal image of nuclei (blue), myoferlin (HPA - "hot" red scale), mitofusin-1/2 (3C9 - "cold" cyan scale). Scale bar = 20 µ m. The channel intensity profile was established following the segment between orange (0-pixel position) and green (500-pixel position) cross marks. **(B)** Pearson (PCC), Spearman rank (SRCC) correlation coefficients, Manders' colocalization coefficients (M1, M2), and intensity correlation quotient (ICQ) calculated on 8 independent microscopic fields. **(C)** Percentage of myoferlin-positive objects (N=7128) with center of mass overlapping mitofusin-positive objects (N=369), percentage of myoferlin positive objects colocalizing with mitofusin-positive objects calculated by fitting of the Ripley's K function or by statistical object distance analysis (SODA). Colocalization distances in pixels were measured in both cases. The median ±interquartile range is represented.

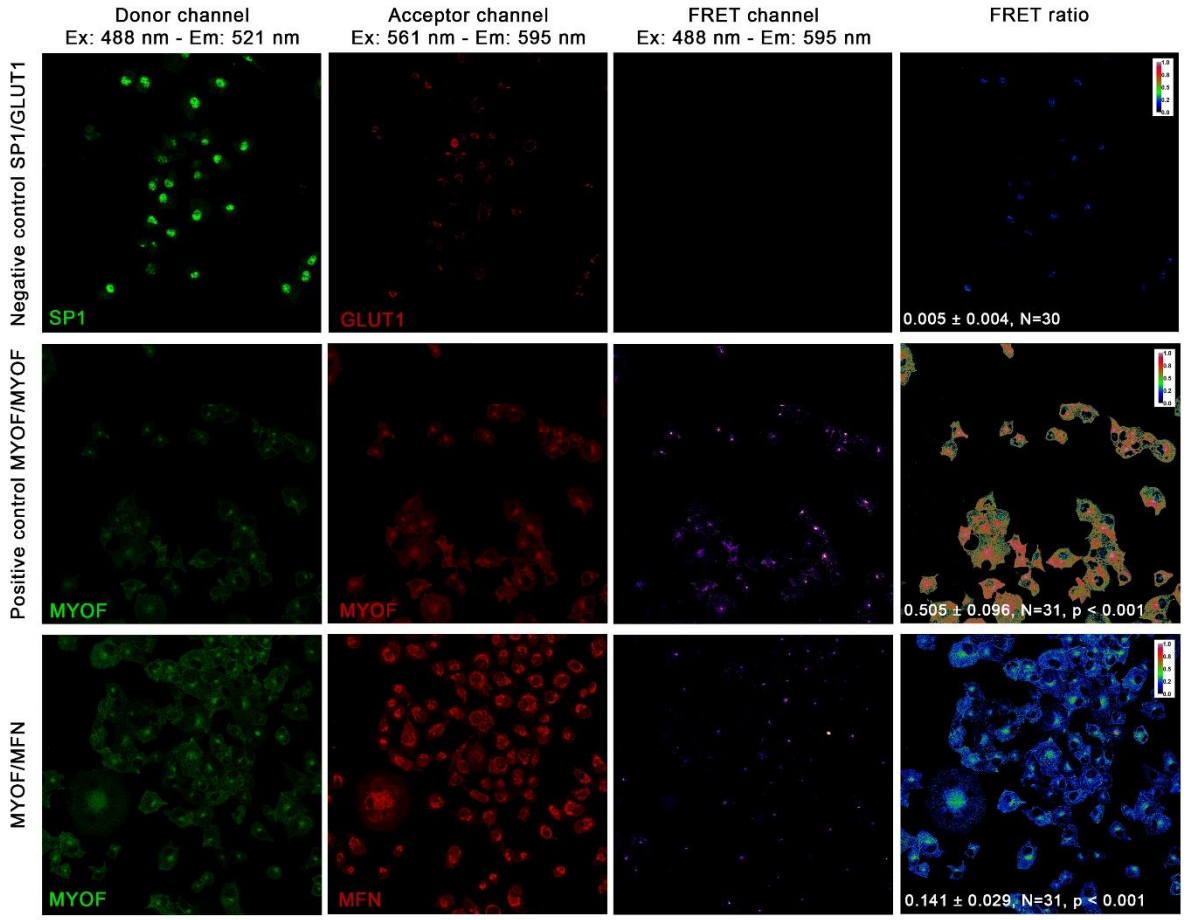

Figure 4-5. Fluorescence resonance energy transfer showing myoferlin and mitofusins proximity in Panc-1 cell line. Confocal images of myoferlin (HPA - green) and mitofusin-1/2 (3C9 - red) immunofluorescence. The fluorescence resonance energy transfer (FRET) channel is represented with "fire" color scale. The FRET ratio is represented with a "rainbow" color scale associated with mean ± standard deviation

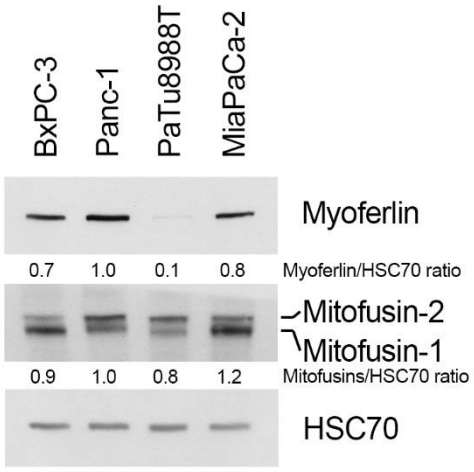

Figure 4-6. Myoferlin and mitofusins abundance in PDAC cell lines. Western blot of 20 µg protein samples from PDAC cell lines. Myoferlin and mitofusins were detected on the same membrane. HSC70 was used as a loading control. The relative quantification was performed using ImageJ software (307).

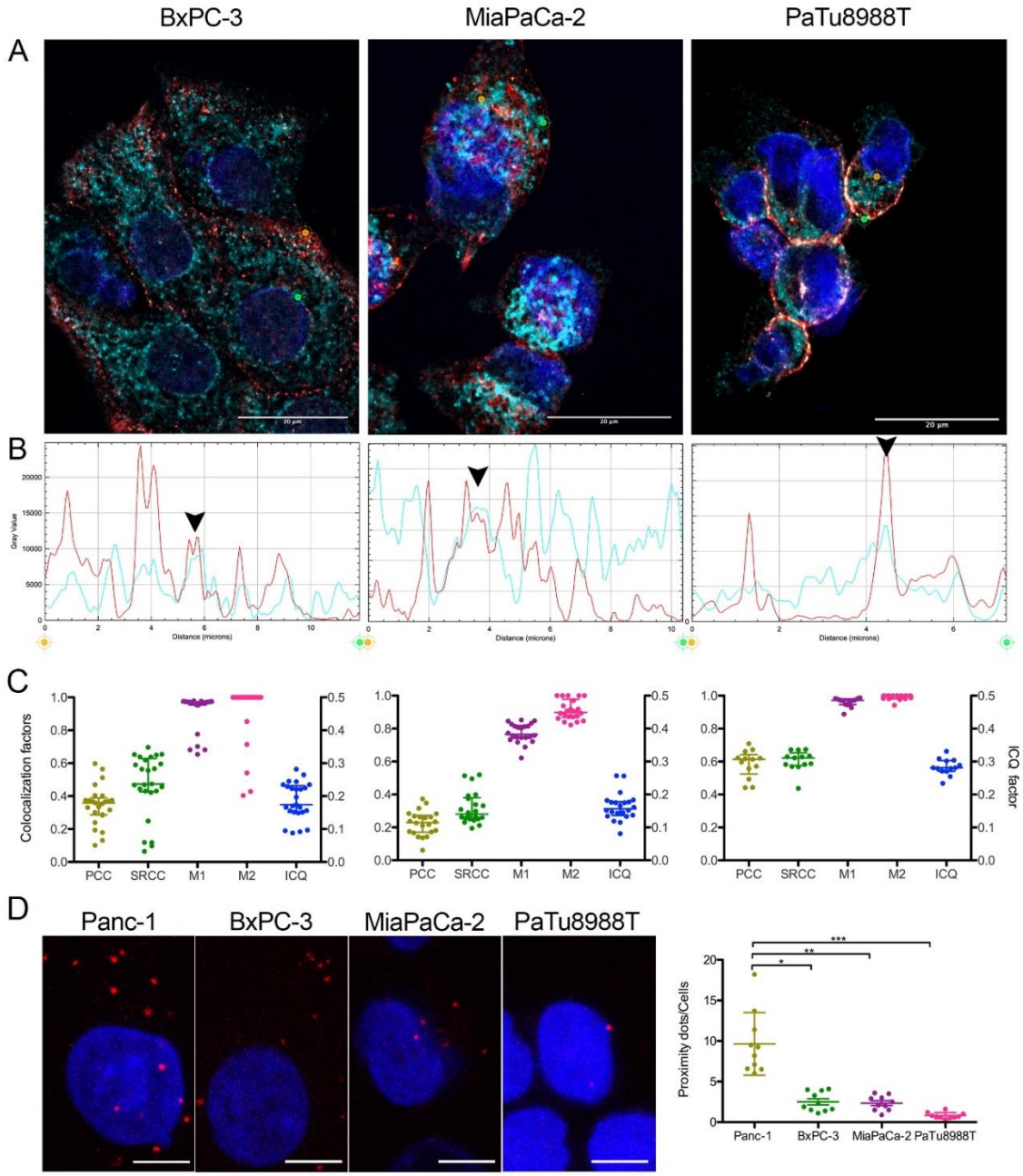

Figure 4-7. Myoferlin colocalizes with MFN1/2 in several pancreas cancer cell lines. **(A)** Representative deconvoluted confocal image of nuclei (blue), myoferlin (HPA—"hot" red scale) and mitofusin-1/2 (3C9—"cold" cyan scale) immunofluorescence of BxPC-3, MiaPaCa-2 and PaTu8988T cell lines. Scale bar = 20 µm. **(B)** The channel intensity profiles were established following the segment between orange and green cross marks. Black arrow heads indicate colocalization spots. **(C)** Pearson (PCC), Spearman rank (SRCC) correlation coefficients, Manders' colocalization coefficients (M1,M2), and intensity correlation quotient (ICQ) were calculated on >13 independent microscopic fields. **(D)** Representative images of MFN1/2-MYOF proximity ligation assay (PLA). Scale bar = 4 µm. MFN1/2-MYOF PLA (N = 10) were quantified using ImageJ software (307). Kruskal–Wallis non-parametric test followed by Dunn's a pairwise comparison was performed, * $p < 0.05$, ** $p < 0.01$, *** $p < 0.001$. All experiments were performed as three independent biological replicates. The median ±interquartile range is represented.

4.1.3. Myoferlin interacts with mitofusins in pancreas cancer cells

We first took advantage of an overexpression model of hemagglutinin (HA)-tagged myoferlin in Panc-1 cells to maximize the myoferlin-MFN1/2 interaction, and performed a co-immunoprecipitation assay. We immunoprecipitated MFN1/2 and showed the co-precipitation of HA-tagged myoferlin (Figure 4-8A).

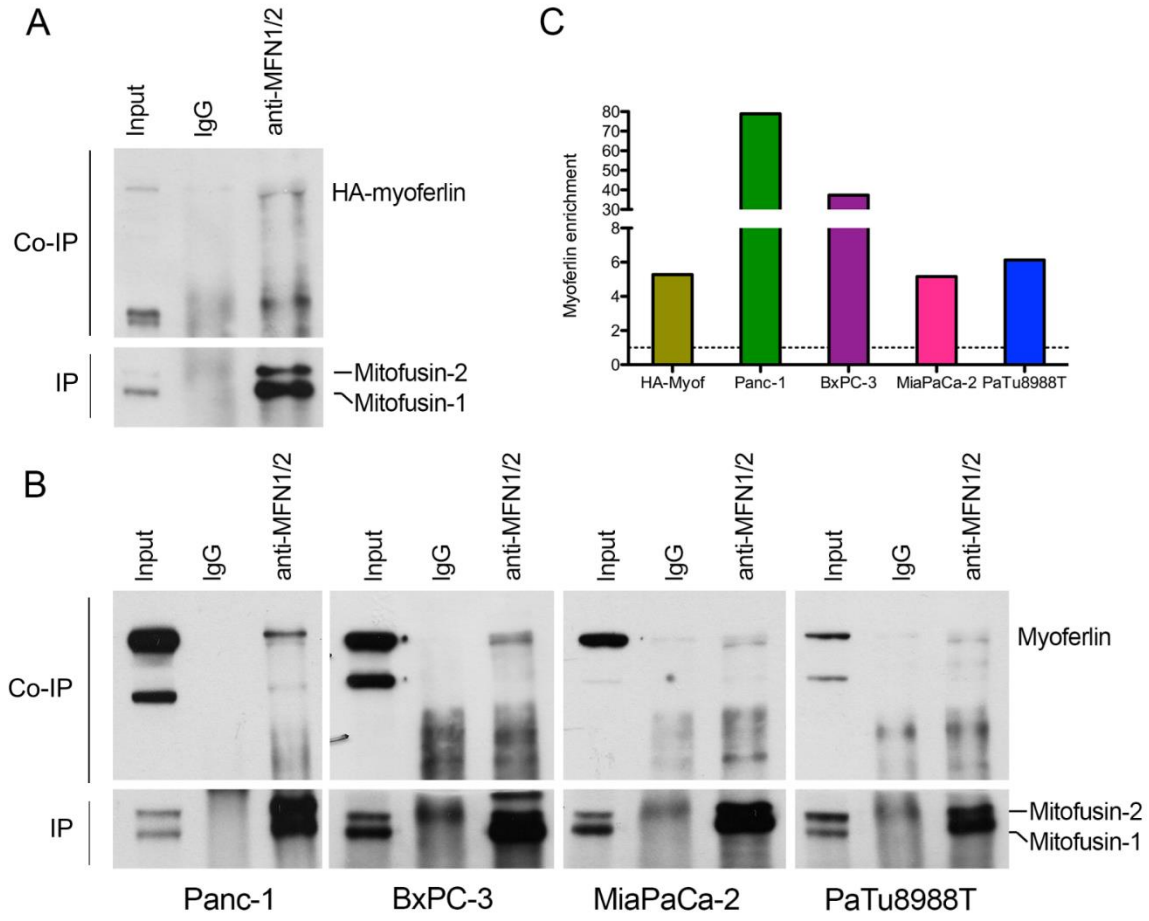

Figure 4-8. Myoferlin interacts with mitofusins in pancreas cancer cell lines. **(A)** Co-immunoprecipitation of mitofusins and HA-tagged myoferlin with an anti-mitofusins antibody. Western blot of protein samples from whole cells (input), IgG control immunoprecipitation (IgG), and mitofusins immunoprecipitation (anti-MFN1/2) of HA-myoferlin transfected Panc-1 cells. HA-myoferlin and mitofusins were detected on the same membrane; **(B)** Co-immunoprecipitation of mitofusins and endogenous myoferlin with an anti-mitofusins antibody. Western blot of protein samples from whole cells, IgG control immunoprecipitation, and mitofusins immunoprecipitation of Panc-1, BxPC-3, MiaPaCa-2, and PaTu8988T cell lines. Myoferlin and mitofusins were detected on the same membrane; **(C)** Myoferlin (or HA-tagged myoferlin) enrichment in anti-MFN1/2 relatively to IgG. The quantification was performed using ImageJ software (307). All experiments were performed as three independent biological replicates.

Then, we decided to confirm the myoferlin-MFN1/2 interaction in endogenous expression systems. We thus performed the same experiment in Panc-1, BxPC-3, MiaPaCa-2 and PaTu8988T cell lines. In all the tested cell lines, myoferlin co-precipitated with MFN1/2 (Figure 4-8B,C) with an abundance in agreement with the previously described myoferlin expression

level (Figure 4-6). In the light of our results, we wondered whether the myoferlin-MFN1/2 interaction also occurred in normal cells.

4.1.4. Myoferlin colocalizes but does not interact with mitofusins in normal cells

Myoferlin expression is supposed to be low in differentiated normal cells. We thus selected subconfluent (90%) murine C2C12 myoblasts, for their known functional expression of myoferlin, and immortalized human pancreatic normal epithelial (HPNE) cell lines with undifferentiated phenotype (246,322).

In both cell lines, the PCC was of ~60%, while Manders' coefficients reached almost 100%. As mentioned in the *Part I: limitations of the study* section, the results regarding correlation/colocalization analyses in this part of the *Results* section should be interpret with caution due to a potential overestimation of coefficients (Figure 4-9C,D). Interestingly, in these cell lines, MFN1/2 immunoprecipitation did not reveal a convincing physical interaction with myoferlin (Figure 4-9E,F) suggesting an interaction specific to cancer cells.

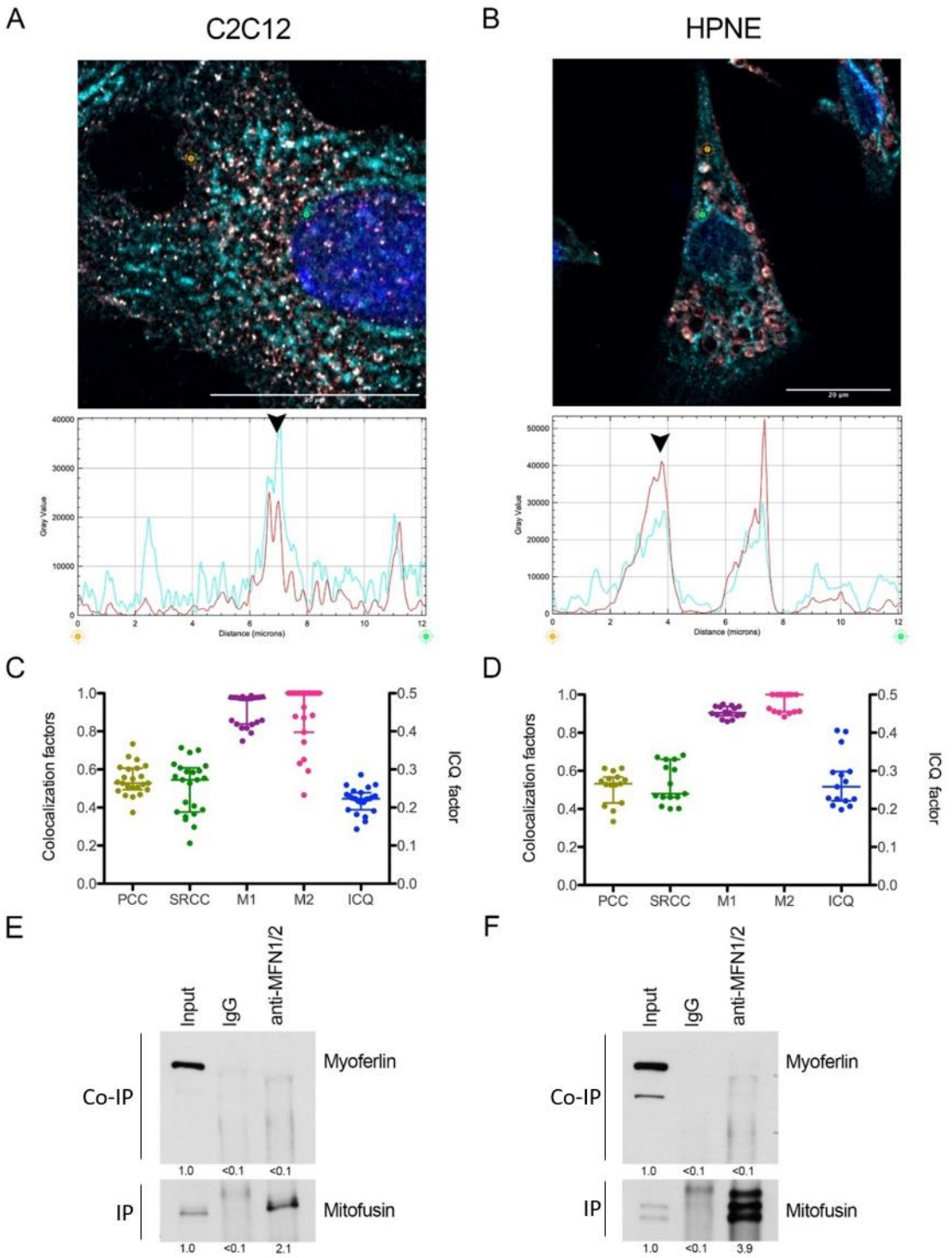

Figure 4-9. Myoferlin colocalizes with mitofusin-1 in normal cell lines. Representative deconvoluted confocal image of nuclei (blue), myoferlin (HPA—"hot" red scale) and mitofusin-1/2 (3C9—"cold" cyan scale) immunofluorescence of **(A)** C2C12 murine myoblast and **(B)** immortalized human pancreatic normal epithelial (HPNE) cell lines. Scale bar = 20 µm. Channel intensity profiles were established following the segment between orange and green cross marks. Black arrow heads indicate colocalization spots. **(C,D)** Pearson (PCC), Spearman rank (SRCC) correlation coefficients, Manders' colocalization coefficients (M1,M2), and intensity correlation quotient (ICQ) were calculated on >15 independent microscopic fields; **(E,F)** Co-immunoprecipitation of mitofusins and endogenous myoferlin with an anti-mitofusin antibody. Western blot of protein samples from whole cells (input), IgG control immunoprecipitation (IgG), and mitofusins immunoprecipitation (anti-MFN1/2) of C2C12 and HPNE cell lines. Myoferlin and mitofusins were detected on the same membrane. The quantification was performed using ImageJ software (307). All experiments were performed as three independent biological replicates. The median ±interquartile range is represented.

4.1.5. Part I: limitations of the study

In this study, we investigated myoferlin localization in relation with mitochondria or MFNs. We mainly used indirect immunofluorescence, PLA and co-immunoprecipitation assays to investigate the potential relationship existing between myoferlin and mitochondria or MFNs. In that regard, our study showed important limitations. Indeed, at that point of our investigations, some choices of antibodies or methodology for the colocalization analyses lead to significant biases. For instance, we mentioned using the myoferlin K-16 antibody from Santa-Cruz Biotechnology. Since the publication of this study, we learned that this antibody was discontinued by the firm. Using this antibody, the staining was of poor quality as shown on Figure 4-1B and Figure 4-3A and did not match the reported myoferlin staining in the literature (242). In addition, it was difficult to obtain a signal using the myoferlin K-16 antibody by western blot. Therefore, results interpretation using this antibody should be made with caution. In part II of the *Results* section, we stopped using this antibody in favor of the myoferlin HPA or D-11 antibodies. We also improved our method for immunofluorescence by changing the blockage and fixation conditions. This improved our immunofluorescence stainings and allowed us to observe myoferlin labeling as reported in the literature (242). Of course, the use of poor-quality antibodies certainly impacted colocalization studies in this part of the *Results* section.

Nevertheless, other concerns regarding those colocalization analyses should be pointed out. First, the methods used for the analyses probably biased the results. The colocalization factors such as Manders' coefficients were probably overestimated due to the inclusion of non-specific signals such as background noise (see *Colocalization studies* for additional details). As shown on Figure 4-7C, almost all the analyzed pictures for Manders' coefficients in BxPC-3 cell line reached 100% of colocalization, which is technically and biologically improbable. The "distance between objects"-based methods, and especially the SODA method, represent robust method for colocalization analyses. Nonetheless, this method requires to define a cell as a ROI. Indeed, a too large ROI can lead to colocalization of objects while they are not. In this study, we used the whole picture as the ROI, which could bias the results towards too large colocalization values (316). Then, some discrepancies emerged between the "colocalization factors" and the "distance between objects"-based methods, making results interpretation difficult. Indeed, the SODA analyses often provided lower percentages of colocalized objects compared to the "colocalization factors" (Figure 4-3C). Finally, the number of analyzed pictures was insufficient

for some analyses, such as the one performed between myoferlin and mitochondria, as shown on Figure 4-2, where only three pictures were used for the SODA analysis.

As a conclusion, in this study, colocalization analyses should be taken with prudence. In the part II of the *Results* section, we aimed at improving the colocalization method to clarify myoferlin presence on mitochondria. We focused mainly on Manders' coefficients, prioritizing quality of analyses over quantity. Even if the colocalization studies for this part of the *Results* section were precarious, we did not re-perform them for myoferlin and MFNs, because myoferlin was in proximity with MFNs using the PLA and because we saw an interaction by co-immunoprecipitation between both proteins.

4.1.6. Part I: conclusions and discussion

In this work, we hypothesized that myoferlin was interacting with proteins involved in mitochondrial fusion (MFNs). We thought that myoferlin was located on the OMM, where it was able to interact with MFNs and mediate fusion. Indeed, some reports showed that myoferlin silencing impacts mitochondrial dynamics and metabolism (47,49).

For the first time, we showed that myoferlin indeed interacts with MFNs. This interaction seems to be specific to PDAC cell lines since we were unable to demonstrate an interaction between those proteins in C2C12 and HPNE cells. We still do not know whether this interaction is direct or involves other proteins. If myoferlin is part of a protein complex including MFNs, it might be of interest to identify proteins within this complex to have a better understanding of myoferlin function related to MFNs. In this context, it might also be interesting to identify whether myoferlin interacts with MFN1, MFN2 or both.

In this study, we were not able to clearly demonstrate myoferlin presence on mitochondria. Indeed, the mitochondrial fraction appeared as containing microsome constituents. Therefore, it was not possible to conclude whether the presence of myoferlin in this fraction was related to its presence on mitochondria or on microsomes. In addition, we performed colocalization/ correlation studies between a 60 kDa mitochondrial protein and myoferlin. Our results showed low percentages of correlation between both proteins. Even though those percentages appeared low, we could not exclude myoferlin presence on mitochondria. In addition, as explained previously (see *Part I: limitations of the study*), interpretations about colocalization/ correlation analyses should be made with caution. Therefore, in order to validate our

hypothesis, further investigations regarding myoferlin localization on mitochondria are required.

If myoferlin is not located on mitochondria, our discovery about its interaction with MFNs might open new insights regarding its function and localization within the cell. Indeed, MFN1 and MFN2 have also been described in MAMs, where they participate to the tethering of ER to mitochondria. If myoferlin interacts with MFNs without being located on mitochondria, it might suggest that myoferlin is located in the ER membrane in association with mitochondria. In the following part of the *Results* section, we aimed at clarifying myoferlin localization in relation to mitochondria and at investigating a potential localization for this protein in MAMs.

PART II: Myoferlin is located in MAMs, where it plays a role in calcium transfer and interacts with IP3R3

4.2. Part II: myoferlin is located in MAMs, where it plays a role in calcium transfer and interacts with IP3R3

As mentioned in Part I of the *Results* section, we found that myoferlin interacts with proteins involved in mitochondrial fusion, the MFNs. We hypothesized that myoferlin interaction with MFNs could modulate mitochondrial fusion. Thus, upon myoferlin silencing, we would obtain a fragmented mitochondrial network as reported in the literature (47). In order to prove this hypothesis, we investigated myoferlin localization in relation to mitochondria. However, our results about myoferlin localization on mitochondria were not fully conclusive. Indeed, we found low percentages of correlation/colocalization between myoferlin and an OMM protein. In addition, as mentioned in the *Part I: limitations of the study* section, the results were probably biased by the way the analyses were performed. We also found myoferlin in mitochondrial fraction obtained by cell fractionation. However, this fraction appeared contaminated by microsomes. Since myoferlin has been reported as being part of the endosomal pathway (242), we could not exclude the possibility that the presence of myoferlin in the mitochondrial fraction was related to the microsomal contamination.

In Part II of the *Results* section, we aimed at clarifying myoferlin presence on mitochondria by improving our methods for colocalization studies and cell fractionation. Since MFNs have also been reported in MAMs (98), where they play a role of tethering, we also aimed at investigating myoferlin presence in those subcellular regions. If myoferlin does not appear to be located on mitochondria, its presence in MAMs could explain the interaction described in the Part I of the *Results* section with MFNs.

4.2.1. Myoferlin is unlikely to be located on mitochondria of PDAC cell lines

In order to clarify whether myoferlin was located or not on mitochondria, we first performed immunofluorescence co-staining on two PDAC cell lines, Panc-1 and MiaPaCa-2. We used a rabbit primary antibody targeting TOM20 to highlight mitochondria, while a mouse antibody was used for myoferlin (D-11). As shown by white arrows on **Figure 4-10**, myoferlin was in proximity with TOM20 in both Panc-1 and MiaPaCa-2 cell lines. However, visual colocalizations (represented by yellow pixels and yellow arrows) between TOM20 and myoferlin were infrequent **(Figure 4-10)**. Pictures at low magnification as well as controls are shown in **Figure 7-1**.

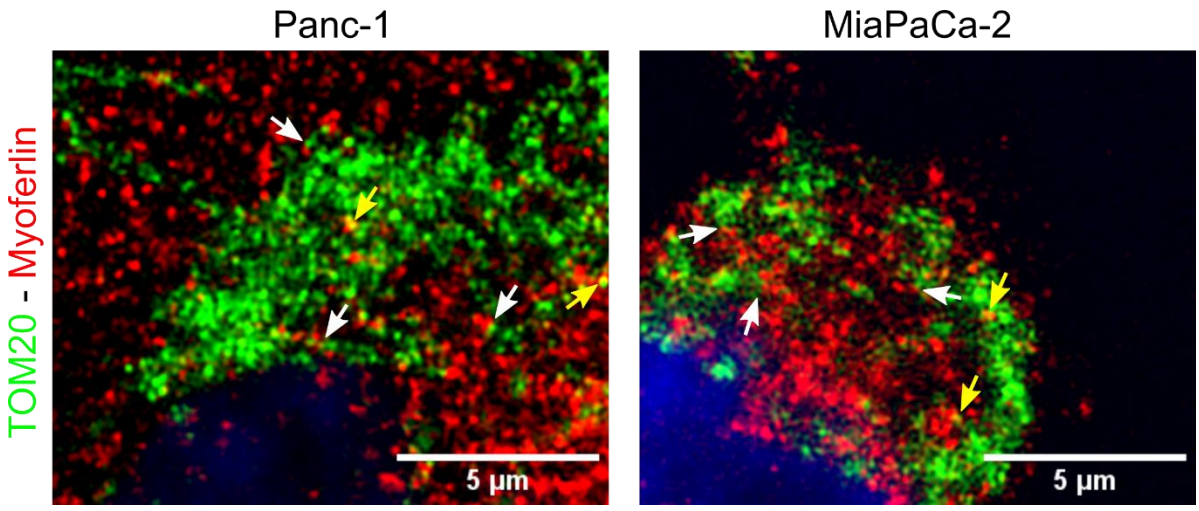

Figure 4-10. Myoferlin is in proximity with TOM20 in Panc-1 and MiaPaCa-2 cell lines. Indirect immunofluorescence, performed on both cell lines, using TOM20 rabbit monoclonal and myoferlin (D-11) mouse monoclonal antibodies, showed proximity between TOM20 and myoferlin (white arrows). Although visible, the colocalizing pixels in yellow were not frequent (yellow arrows). TOM20 is represented in green, while myoferlin is labelled in red. DAPI was used to highlight the nucleus (blue). Confocal pictures were acquired with a high resolution LSM 880 microscope.

Moreover, as highlighted by the white arrows on Figure 4-11, the labeling for myoferlin was weaker in the regions containing mitochondria (identified by TOM20). Even if the labeling of myoferlin and TOM20 intertwined in certain places, myoferlin and TOM20 did not seem to be located in similar subcellular regions.

Because visual assessment of colocalization is often biased by signal intensity, we performed colocalization studies based on Manders' method using ImageJ software (307,313). Compared to the analyses performed in the Part-I of the *Results* section, we refined our analysis procedures. In order to avoid a bias produced by the image background, each cell was defined as a ROI, in which the analysis was performed. In addition, since Manders' method is sensitive to background, we ensured that the thresholds used were representative of the staining. This procedure avoids an overestimation of the colocalization coefficients. Our results showed that the percentage of TOM20 colocalizing with myoferlin (M1) in the Panc-1 cell line was of 12.82 ±5.01%, while in MiaPaCa-2, this percentage was only of 7.70 ±5.61% (Figure 4-12A). Similarly, the percentage of myoferlin colocalizing with TOM20 (M2) was of 7.16 ±3.56% in Panc-1 and 7.66 ±6.32% in MiaPaCa-2 (Figure 4-12A). The descriptive statistics are presented on Table 3.

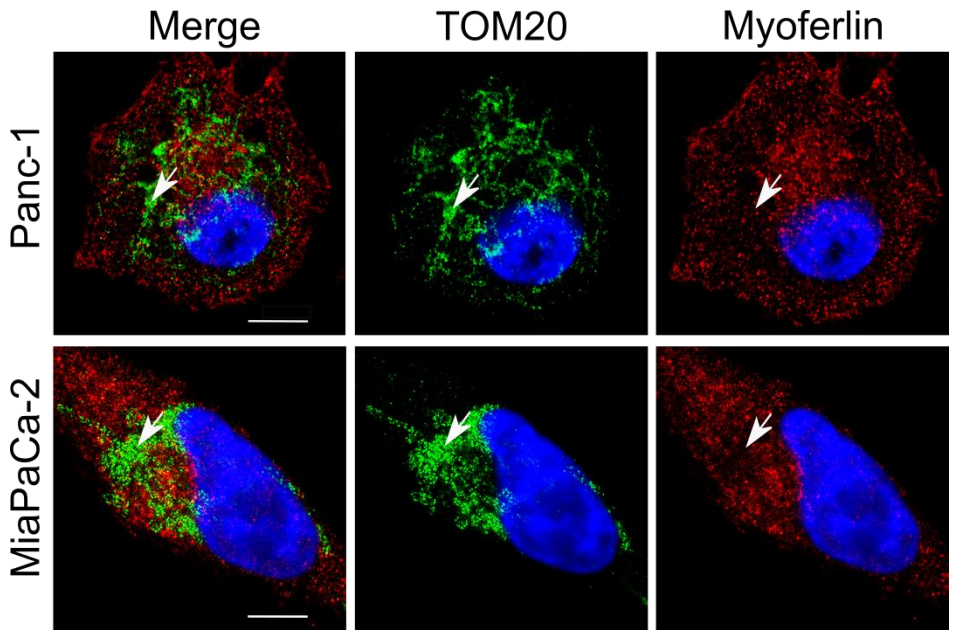

Figure 4-11. Myoferlin and TOM20 co-labeling in Panc-1 and MiaPaCa-2 cell lines. Where the staining for TOM20 appeared condensed in some regions of the cell, the staining intensity for myoferlin was low (white arrows). TOM20 rabbit monoclonal and myoferlin (D-11) mouse monoclonal antibodies were used for this immunofluorescence assay. TOM20 appears in green, myoferlin in red and the nucleus in blue (DAPI). The scale bar represents 8.89 µm in Panc-1 and 5 µm in MiaPaCa-2 cell lines. The confocal pictures were acquired with a high resolution LSM 880 microscope.

Because the percentage of colocalization between both proteins appeared globally low, we decided to randomize the pictures (Figure 4-13A) and to perform the same analysis. The Manders' coefficients from randomized pictures were significantly lower than the one from non-randomized pictures (Figure 4-12A). Indeed, the first colocalization coefficient, M1, was of 5.68 ±1.92% in Panc-1 cell line, while in MiaPaCa-2, this percentage was of 3.66 ±2.33%. Concerning M2, the percentage of colocalization was of 3.28 ±0.93% in Panc-1 and 4.15 ±3.77% in MiaPaCa-2. Nevertheless, despite being statistically significantly lower, the percentage of colocalization of randomized pictures remained close to the one of non-randomized pictures (Panc-1: 12.82% vs 5.68% for M1; 7.16% vs 3.28% for M2. MiaPaCa-2: 7.70% vs 3.65% for M1; 7.66% vs 4.15% for M2) (Table 3). The significant differences observed between randomized and non-randomized pictures might be explained by myoferlin proximity with TOM20 as shown on Figure 4-10, without, however, being localized on mitochondria. At this step of our investigations, myoferlin localization in relation to mitochondria was still unclear.

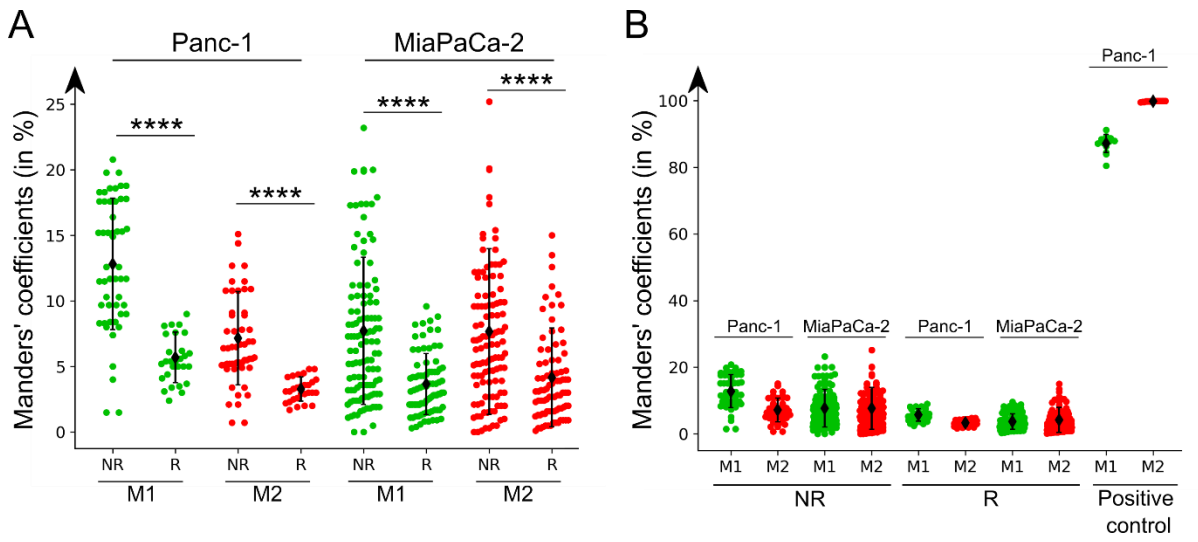

Figure 4-12. Myoferlin and TOM20 poorly colocalize in Panc-1 and MiaPaCa-2 cell lines. **(A)** Colocalization between TOM20 and myoferlin using Manders' method from non-randomized (NR) or randomized (R) pictures. M1 (in green) represents the proportion of TOM20 colocalizing with myoferlin, while M2 (in red) represents the proportion of myoferlin colocalizing with TOM20. **(B)** Same as A, with a comparison with positive control. Regarding the positive control, M1 represents the proportion of pixels (above-background) in channel 1 overlapping the pixels (above-background) in channel 2, and vice versa for M2. TOM20 rabbit monoclonal antibody and myoferlin (D-11) mouse monoclonal antibody were used for the TOM20-myoferlin co-labeling. For the positive control, two secondary antibodies carrying distinct fluorochromes (Alexa Fluor 488 and 546), recognized the same myoferlin rabbit polyclonal primary antibody (HPA). The experiment was performed at least three times (biological replicates), except for the positive control, where the experiment was performed only once. One dot on the graph represents one cell. The non-parametric test of Mann-Whitney was performed for statistical analyses. ****: p-value < 0.0001. Mean ±SD is represented. Descriptive statistics are presented on **Table 3**.

In order to further validate the method used for colocalization and to further demonstrate the low colocalization existing between TOM20 and myoferlin, we used a positive control in Panc-1 cell line, where two secondary antibodies, carrying distinct fluorochromes, recognized the same myoferlin primary antibody (HPA) **(Figure 4-13B)**. Using our method for Manders' coefficients, we found 87.17 ±2.71% of colocalization for M1 (proportion of above-background pixels in channel 1, colocalizing with above-background pixels in channel 2) and 99.82 ±0.09% of colocalization for M2 (proportion of above-background pixels in channel 2 colocalizing with above-background pixels in channel 1), validating the positive control **(Table 3)**. Compared to this control, both randomized and non-randomized pictures for TOM20-myoferlin co-labeling displayed a low percentage of colocalization **(Figure 4-12B)**. Therefore, we concluded that myoferlin and TOM20 were colocalizing at a really low extent with each other, suggesting that myoferlin is close to mitochondria rather than located on this organelle.

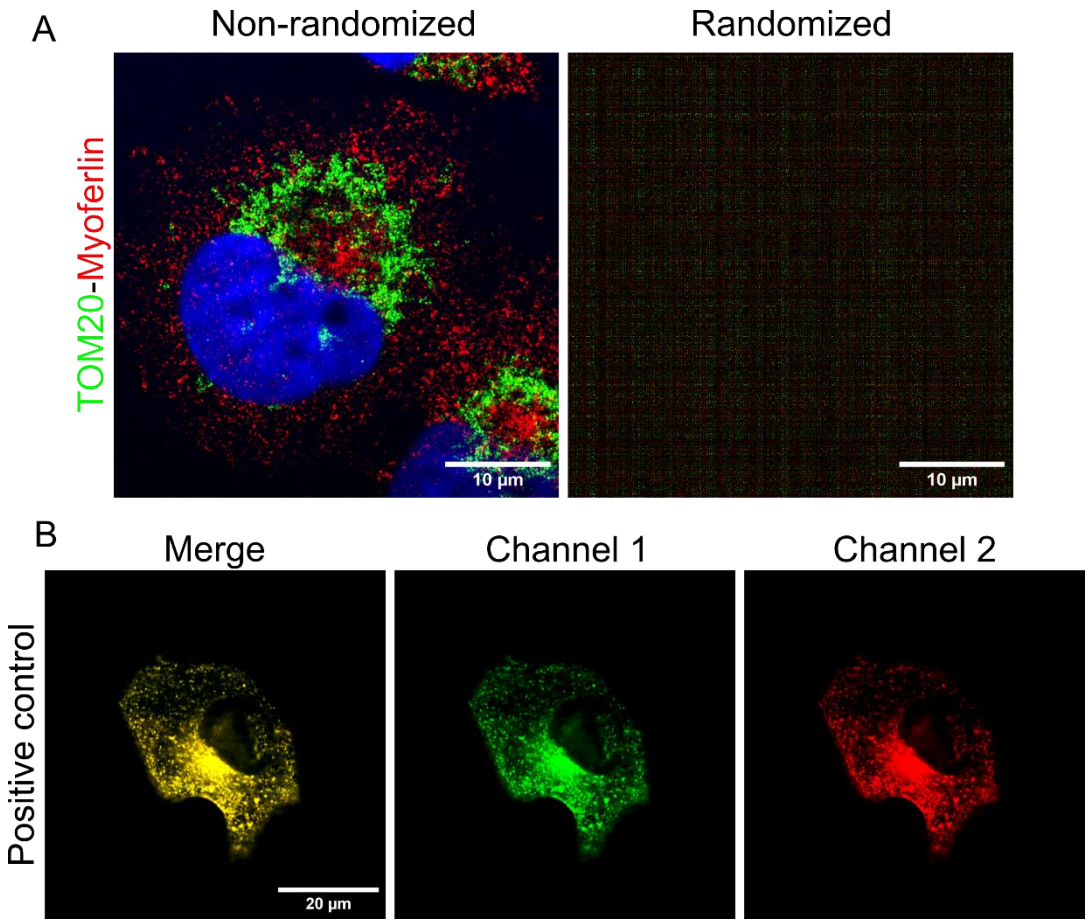

Figure 4-13. Example of pictures for non-randomized, randomized and positive control. **(A)** Non-randomized picture of a Panc-1 cell (on the left) with myoferlin labeling in red, TOM20 labeling in green and the nucleus highlighted in blue (DAPI). The same picture after randomization (on the right). For randomization, the DAPI was excluded. TOM20 rabbit monoclonal and myoferlin (D-11) mouse monoclonal antibodies were used as primary antibodies for the indirect immunofluorescence assay. **(B)** Positive control was performed on Panc-1 cells. Two secondary antibodies carrying distinct fluorochromes (Alexa Fluor 488 and 546), recognized the same myoferlin rabbit polyclonal primary antibody (HPA). Confocal pictures were acquired with a high resolution LSM 880 microscope.

Cell line	Manders' coefficients	Category (NR/R/positive control)	Aver. (%)	SD	SEM	n
Panc-1	M1	NR	12,82	5,01	0,68	55
	M2		7,16	3,56	0,48	55
	M1	R	5,68	1,92	0,38	29
	M2		3,28	0,93	0,17	29
MiaPaCa-2	M1	NR	7,70	5,61	0,52	114
	M2		7,66	6,32	0,59	114
	M1	R	3,65	2,33	0,25	85
	M2		4,15	3,77	0,41	85
Panc-1	M1	Positive control	87,17	2,71	0,68	16
	M2		99,82	0,09	0,02	16

Table 3. Average (Aver.) percentage of colocalization between TOM20 and myoferlin, standard deviation (SD), standard error of mean (SEM), sample size (n) from non-randomized (NR) or randomized (R) pictures regarding M1 or M2 coefficients in Panc-1 or MiaPaCa-2. This table also includes the descriptive statistics for the positive control. M1 represents the proportion of pixels in channel 1 (TOM20 for NR and R pictures or myoferlin for positive control) overlapping the pixels in channel 2 (Myoferlin for NR, R and positive control pictures) and vice versa for M2.

To further validate our observations, we decided to perform a PLA between myoferlin and a 60 kDa protein localized on the OMM (Figure 4-14). This method allows the detection of red dots if the distance between the proteins of interest is less than 40nm. Our results showed no signals for the PLA performed on the MiaPaCa-2 cell line, while only few dots were detected in the Panc-1 cell line (Figure 4-14). In order to validate the PLA results, we performed the experiment without one or both of the primary antibodies. There were no signals in the negative controls, validating antibodies specificity for the PLA (Figure 4-14A).

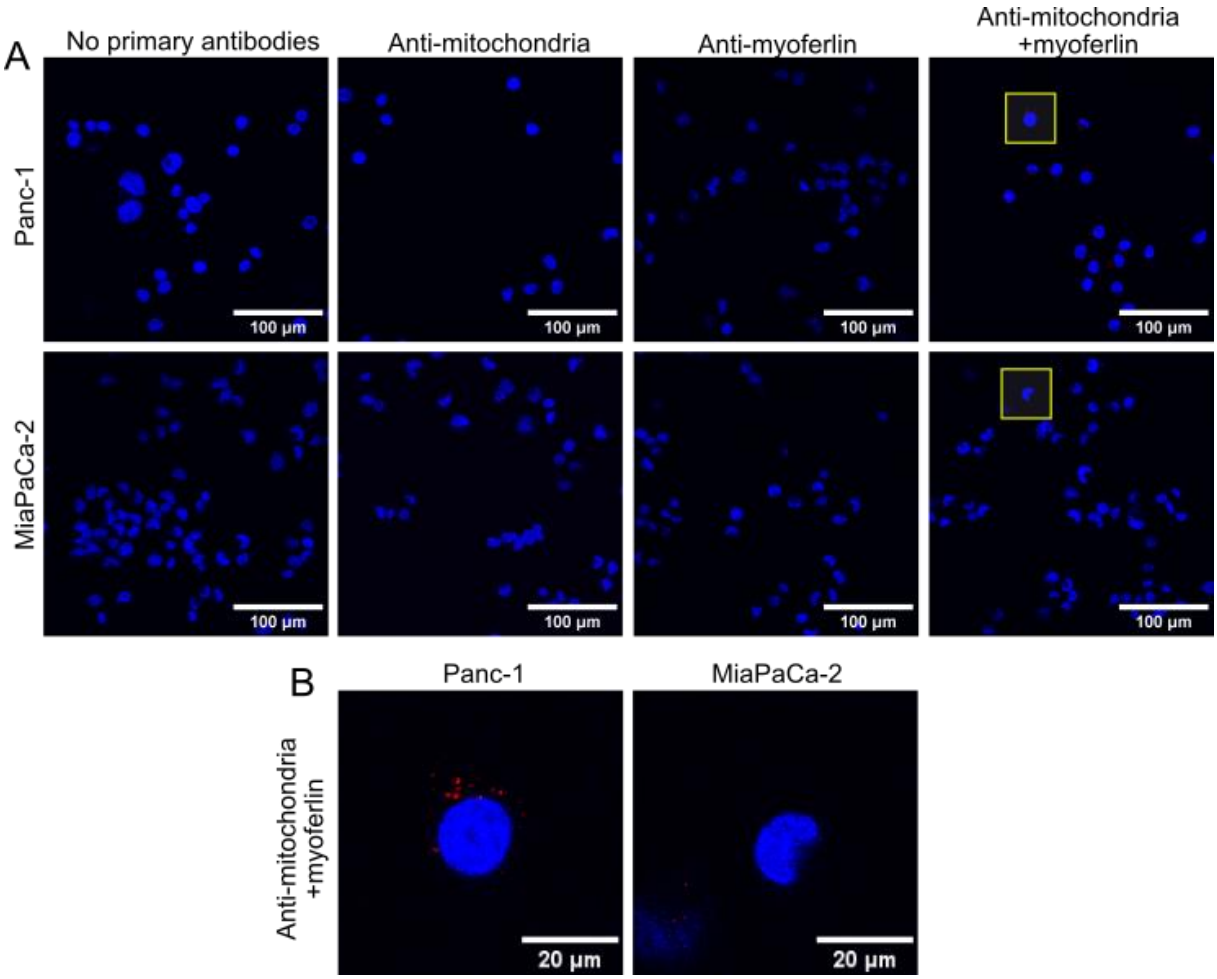

Figure 4-14. PLA between myoferlin and a 60 kDa OMM protein in Panc-1 and MiaPaCa-2 cell lines. **(A)** Representative pictures for the PLA (40X magnification). Regarding negative controls, we performed the PLA without primary antibodies (no primary antibodies), with the primary antibody for the 60 kDa OMM protein only (anti-mitochondria) or with the primary antibody for myoferlin only (anti-myoferlin). Both primary antibodies for the 60 kDa OMM protein and myoferlin were used to assess myoferlin proximity to mitochondria (anti-mitochondria+myoferlin). Yellow squares in the "anti-mitochondria+myoferlin" condition are represented in **(B)** at high magnification. Dots were detected in Panc-1 but not in MiaPaCa-2. Myoferlin rabbit polyclonal primary antibody (HPA) and the 60 kDa OMM protein mouse monoclonal primary antibody were employed for this PLA assay. Pictures were acquired with a confocal Nikon A1R microscope. The experiment was performed twice for both cell lines.

In accordance with previous results obtained by immunofluorescence, the PLA suggests that myoferlin is probably not located on mitochondria. Nevertheless, since we obtained signals for

the PLA in Panc-1 cells, whether myoferlin was located or not on this organelle remained under debate.

Finally, in order to clarify the presence of myoferlin on mitochondria, we isolated this organelle using differential centrifugations and percoll gradient in Panc-1 and MiaPaCa-2 cell lines **(Figure 4-15)**. This allows us to obtain a purer fraction compared to those described in the Part-I of the *Results* section **(Figure 4-1)**. Without surprise, we saw an enrichment of TOM20 in the PM fraction in comparison to the whole cell lysate. The enrichment ratio was about 26 and 35 in Panc-1 and MiaPaCa-2 cell lines, respectively. Calreticulin, a marker of the ER, was almost undetectable in the PM fraction, while significantly present in the CM fraction of both Panc-1 and MiaPaCa-2. Interestingly, myoferlin was not detectable (or at really low extent) in the PM fraction of both cell lines. In addition, myoferlin was enriched in the CM fraction. The enrichment ratio was about 3 in both Panc-1 and MiaPaCa-2 cell lines. Altogether, our results suggest that myoferlin is not located on mitochondria but is rather in proximity with this organelle, explaining the low percentage of colocalization obtained with TOM20 by immunofluorescence and the results obtained by PLA.

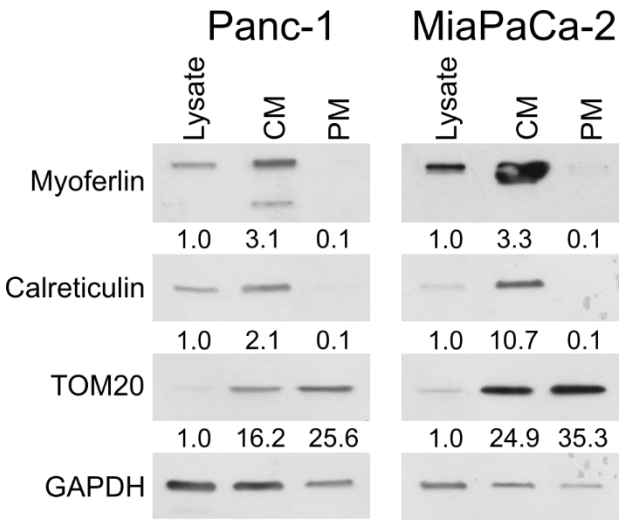

Figure 4-15. Myoferlin is barely present in the purified mitochondrial fraction (PM) of both Panc-1 and MiaPaCa-2 cell lines. Mitochondria were isolated using differential centrifugations and a percoll gradient. Calreticulin was used as an ER marker, while TOM20 was used as a mitochondrial marker. GAPDH was used as a loading control, allowing comparison between cell fractions. The reference used for the quantification of western blots was the lysate. Western blot quantification was performed with ImageJ software (307). For each fraction, 5 µg of proteins were loaded. Those western blots are representative of three biological replicates. CM: crude mitochondria.

4.2.2. Myoferlin is found in MAMs of PDAC cell lines

We previously demonstrated that myoferlin was interacting with MFNs in PDAC cell lines. Nevertheless, since myoferlin was not found in the PM fraction and poorly colocalized with

TOM20, we could not conclude that myoferlin was located on mitochondria, where it would interact with MFNs. Because MFNs have been reported in MAMs, we thought myoferlin may also be located in those subcellular structures (100). This hypothesis is supported by the proximity observed by immunofluorescence between myoferlin and TOM20 (Figure 4-10), as well as the presence of myoferlin in the CM fraction of PDAC cell lines (Figure 4-15).

In order to check whether myoferlin is present in MAMs, we performed a cell fractionation on both Panc-1 and MiaPaCa-2 cell lines using a protocol published by Lewis *et al.* in 2016 (118). We obtained seven fractions: P1 (whole cell lysate), cytosol, microsomes, CM, PM, CMAMs and PMAMs fractions (Figure 4-16). In order to check the quality of the fractions, we estimated the abundance of several markers. As a cytosolic marker, we used vinculin. This protein was enriched in the cytosolic fraction as expected (Panc-1: 2.5-fold and MiaPaCa-2: 4.0-fold) and was barely detected in other fractions. Concerning the ER marker, we used calreticulin, which was found in the microsomal, CM, CMAMs and PMAMs fractions of both cell lines. A faint band for this protein was visible in the PM fraction of Panc-1 cell line, suggesting a minor contamination with ER in the PM fraction. Nevertheless, the results were in accordance with the literature, where calreticulin was found in the microsomes, CM as well as CMAMs and PMAMs fractions (117). It is worth noting that we did not check the quality of the PM fractions by transmission electron microscopy (TEM). This technique is, however, a good way to evaluate the quality of an extraction. In addition to calreticulin, we used S1R as a marker of MAMs. This protein has been described as being enriched in PMAMs fraction of HEK-293 and CHO-K1 cell lines (118). Our results confirmed in PDAC cell lines what was reported in the literature. Indeed, S1R was enriched in the PMAMs fraction, with an enrichment ratio of 88,1 and 7.2 in Panc-1 and MiaPaCa-2 cell lines, respectively. In order to further validate the extracts, we used TOM20 (OMM protein) and COXIV (IMM protein) as mitochondrial markers. As expected, those proteins were enriched in the purified mitochondrial fraction of both Panc-1 and MiaPaCa-2 cell lines, while they were absent from the cytosol and microsome fractions. Those markers were also detected in the CMAMs fraction and were extensively reduced in the PMAMs fraction. Because TOM20 is an OMM protein and COXIV is an IMM protein, we expected to detect higher amounts of TOM20 in the PMAMs fractions than COXIV. Indeed, while the TOM20 abundance relative to the P1 fraction was of 1.5 and 0.6 in the PMAMs fraction of Panc-1 and

MiaPaCa-2 cell lines respectively, it was of 0 for COXIV in both cell lines. Altogether, those markers validated the quality of the extraction.

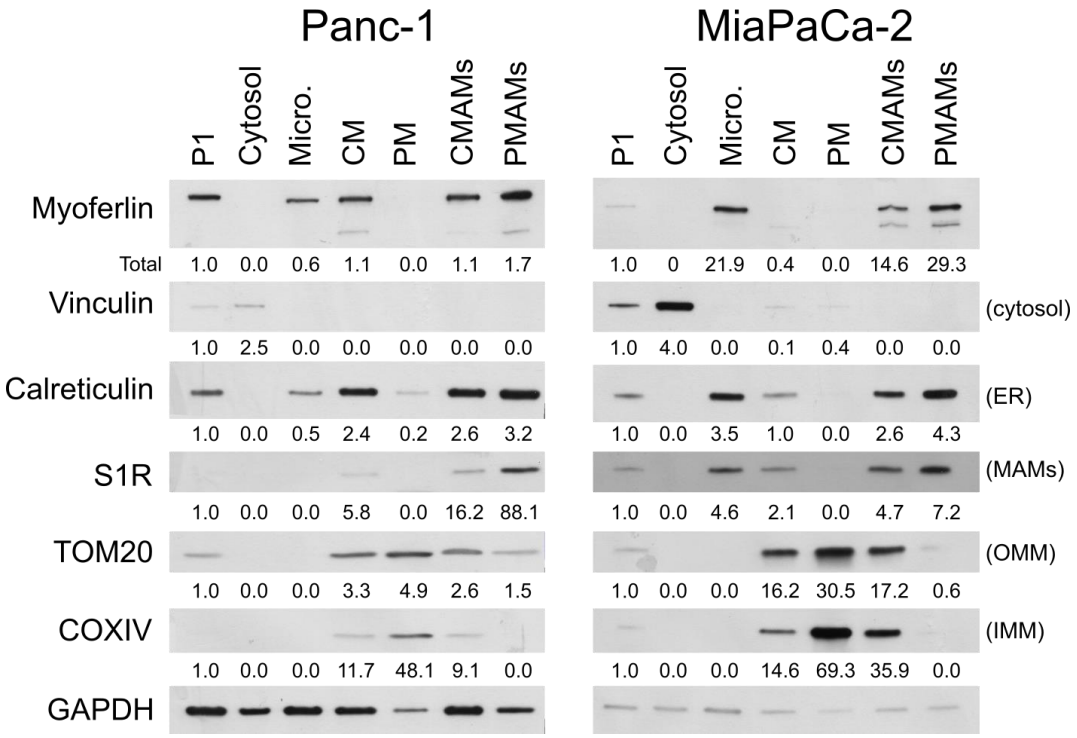

Figure 4-16. Cell fractionation performed on Panc-1 and MiaPaCa-2 cell lines (representative of three biological replicates). Seven fractions were obtained: P1 (whole cell lysate), Cytosol, Micro. (microsomes), CM (crude mitochondria), PM (pure mitochondria), CMAMs (crude MAMs), PMAMs (pure MAMs). Vinculin was used as a cytosolic marker, calreticulin as an ER marker, S1R as a MAMs marker, TOM20 as an OMM maker and COXIV as an IMM marker. GAPDH allows comparison of Panc-1 and MiaPaCa-2 extracts. The western blot quantification was performed with ImageJ software (307). P1 was used as the reference for quantification. For each fraction, 5 µg of proteins were loaded.

Following validation, we evaluated the abundance of myoferlin in the fractions (Figure 4-16). In accordance with the literature, myoferlin was found in the microsomal fraction (242,323). In addition, in accordance with our previous results, myoferlin was absent from the PM fraction, but present in the CMAMs and PMAMs fractions (Figure 4-15 and Figure 4-16). In the PMAMs fraction, myoferlin enrichment ratio was of 1.7 in Panc-1 and 29.3 in MiaPaCa-2. Therefore, our results demonstrated the presence of myoferlin in MAMs, confirming our hypothesis. It is worth noting that myoferlin was not found in the cytosolic fraction. Furthermore, the ~180 kDa myoferlin band, reported as a specific isoform, was clearly enriched in the PMAMs fraction (254).

4.2.3. Myoferlin silencing impacts mitochondrial Ca^{2+} level upon histamine stimulation

Because myoferlin displays a rare structure with multiple calcium-binding C2 domains and impacts mitochondrial metabolism and dynamics upon silencing, we thought this protein could

be involved in Ca^{2+} signaling at MAMs. In order to monitor mitochondrial Ca^{2+} level in an intensiometric manner, we took advantage of the CMV-Mito-R-GECO-1 plasmid (Addgene plasmid #46021) encoding a calmodulin-RFP fusion protein harboring a mitochondrial import signal (306). To validate the mitochondrial localization of the fusion protein, we used a MitoTracker probe to highlight mitochondria in green. As shown on **Figure 4-17A**, in both Panc-1 and MiaPaCa-2, the fusion protein was fully colocalizing with the MitoTracker Green probe (yellow pixels in merge channel). Then, we decided to perform the colocalization analyses using the method previously described for myoferlin and TOM20 (see *Colocalization studies*). This allowed us to test the method in other situations. Our results showed almost 100% of colocalization between the probe and the fusion protein, confirming mitochondrial localization **(Figure 4-17B)**.

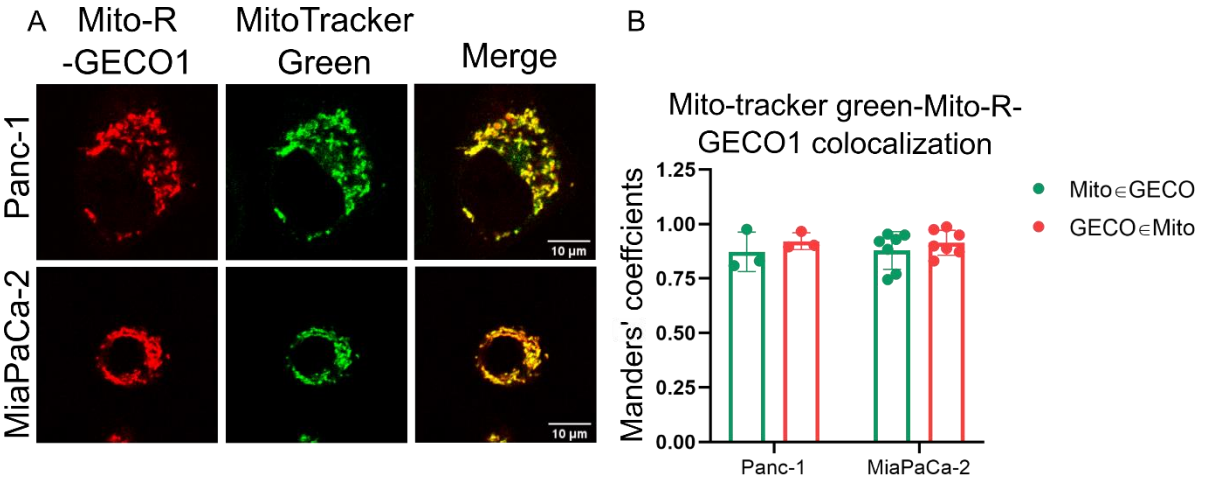

Figure 4-17. Validation of mitochondrial localization for the fusion protein encoded by the CMV-Mito-R-GECO-1 plasmid in Panc-1 and MiaPaCa-2 cell lines. **(A)** The fusion protein appears in red (RFP), while the mitochondrial probe (MitoTracker) is in green. The fusion protein and the MitoTracker green probe are perfectly colocalizing (Merge picture, yellow pixels). **(B)** Colocalization analysis using Manders' method. One dot represents one cell. The Mito ϵ GECO (in green on the graph) represents the proportion of above-threshold pixels for the MitoTracker green probe colocalizing with above-threshold pixels for the CMV-Mito-R-GECO-1 fusion protein. The opposite is represented by the "GECO ϵ Mito" (in red on the graph).

Thanks to PDAC cell lines transfected with CMV-Mito-R-GECO-1 plasmid, we monitored mitochondrial Ca^{2+} level upon histamine stimulation **(Figure 4-18)**. Since cells were in a Ca^{2+} free medium, histamine triggers Ca^{2+} release from ER through IP3Rs, allowing us to monitor Ca^{2+} transfer from ER to mitochondria. In order to evaluate the impact of myoferlin on Ca^{2+} transfer, we silenced the cells for myoferlin using two siRNA (Myof#1 and Myof#2 siRNA). We also used two controls of transfection; a control with no siRNA and one with irrelevant siRNA. Our results showed that upon histamine stimulation, an enhanced fluorescence was visible in the no siRNA and irrelevant conditions for both Panc-1 and MiaPaCa-2 cell lines **(Figure 4-18)**. Interestingly,

in both cell lines, the cells silenced for myoferlin displayed a low increase of fluorescence upon histamine stimulation.

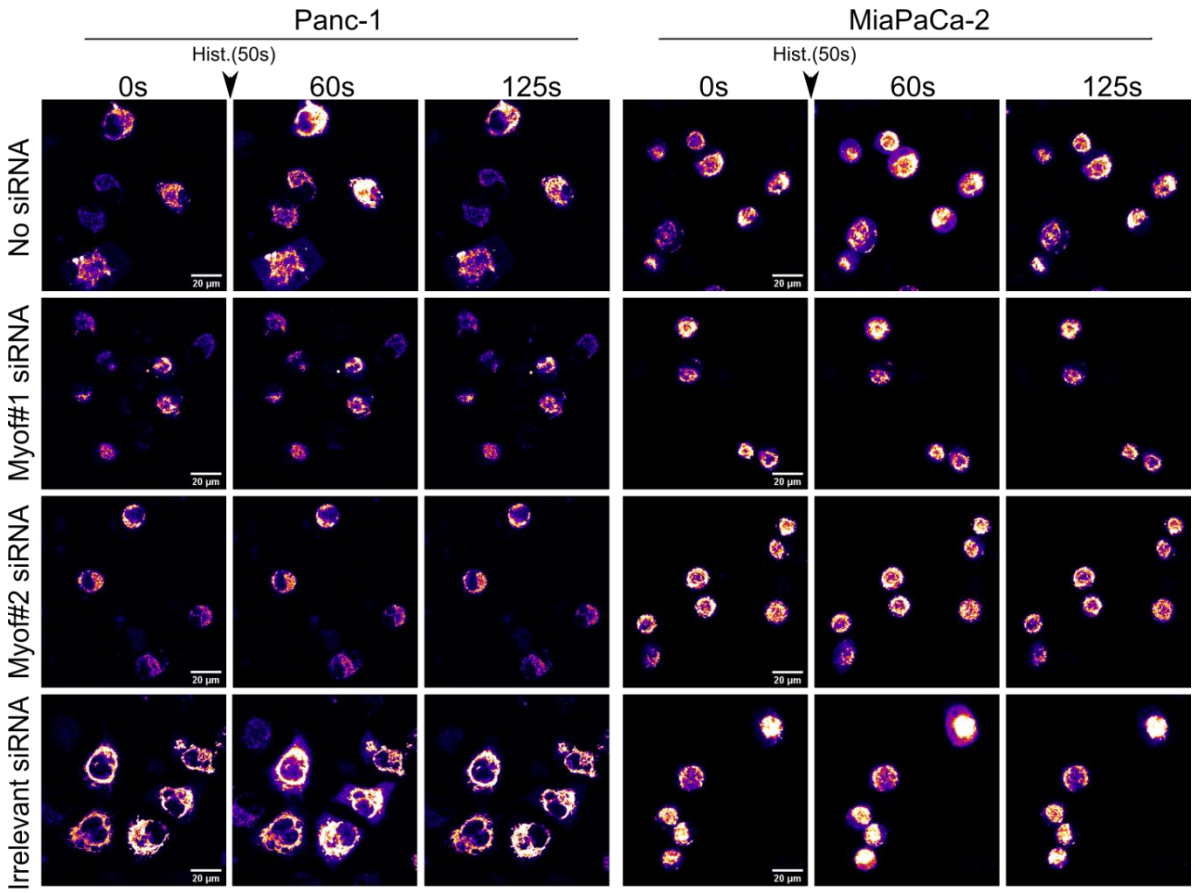

Figure 4-18. Representative pictures of three biological replicates over time of Panc-1 and MiaPaCa-2 cell lines transfected with CMV-Mito-R-GECO-1 plasmid upon histamine stimulation at different time steps (0, 60, 125 seconds). Histamine injection was done after 50 seconds. The cells were silenced for myoferlin using siRNA (Myof#1 and Myof#2 siRNA). Cells transfected with no siRNA or irrelevant siRNA were used as a control of transfection. The experiment was performed in a Ca^{2+}-free medium. The time-lapse (confocal images) was performed with a Nikon A1R microscope.

We performed a quantification for each condition. We monitored fluorescence over time (Fn) for each individual cell and we normalized it to the first frame (F0) of the time-lapse (Fn/F0), which allows comparisons between conditions (Figure 4-19A). The quantifications confirmed the visual observations. Indeed, upon histamine stimulation, the peak of normalized fluorescence was higher in the no siRNA and irrelevant conditions compared to myoferlin siRNA conditions in both cell lines. Peak amplitudes, represented on Figure 4-19B, were significantly lower in cells silenced for myoferlin compared to the irrelevant condition in both Panc-1 and MiaPaCa-2 cell lines.

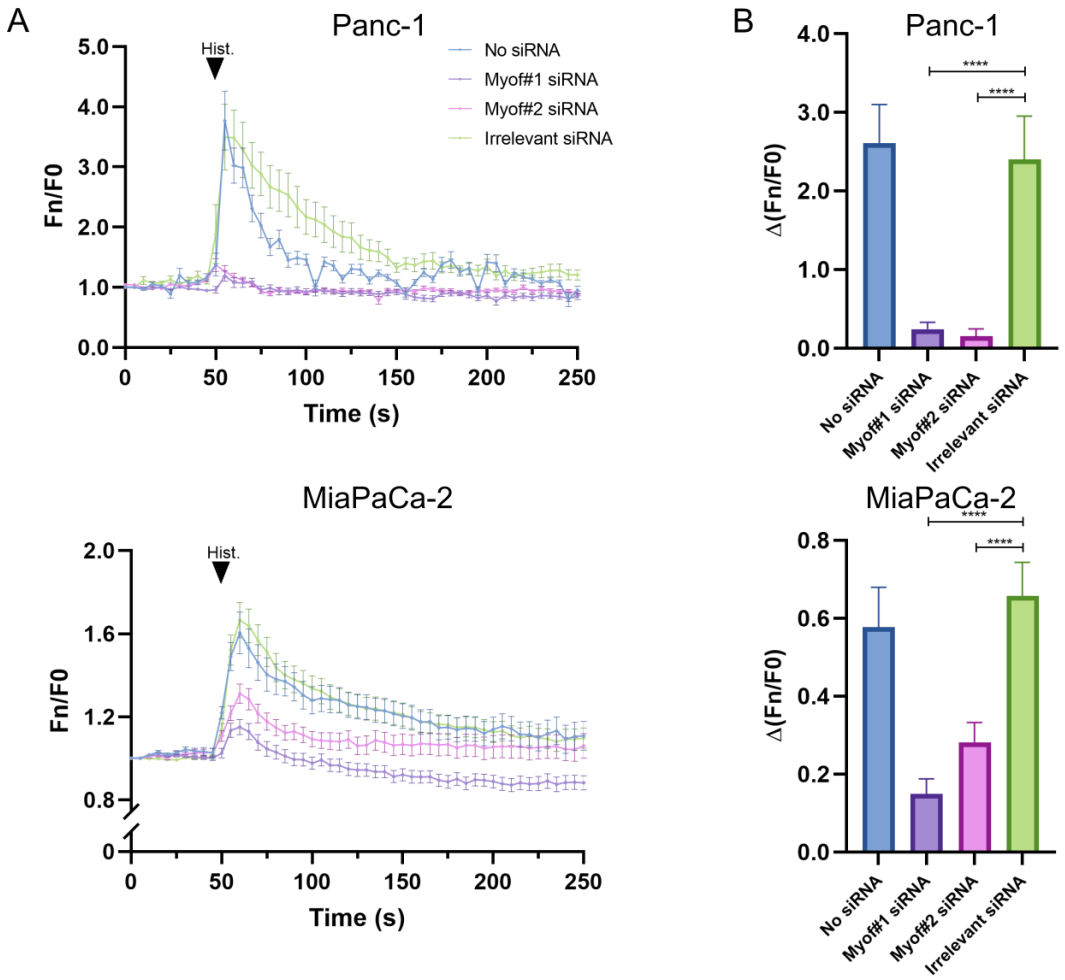

Figure 4-19. Variation of mitochondrial Ca^{2+} level upon histamine stimulation in Panc-1 and MiaPaCa-2 cell lines silenced for myoferlin. **(A)** Panc-1 and MiaPaCa-2 cell lines were first transfected with the CMV-Mito-R-GECO-1 plasmid. Fluorescence was monitored over time in the four conditions (no siRNA, Myof#1 siRNA, Myof#2 siRNA and irrelevant siRNA). After 50 seconds, histamine was injected (arrow). The fluorescence was monitored for each individual cell over time (Fn) and normalized to the fluorescence of the first frame of the time lapse (F0). **(B)** The peak amplitude was the difference between the normalized fluorescence at 60 and 45 seconds for the Panc-1 cell line and 65 and 45 seconds for the MiaPaCa-2 cell line ($\Delta Fn/F0 = (Fn/F0)_{tf} - (Fn/F0)_{ti}$) . The total number of cells for each condition was: n=38 (no siRNA), n=25 (Myof#1 siRNA), n=33 (Myof#2 siRNA) and n=41 (Irrelevant siRNA) for the Panc-1 cell line and n=43 (no siRNA), n=79 (Myof#1 siRNA), n=60 (Myof#2 siRNA) and n=107 (irrelevant siRNA) for the MiaPaCa-2 cell line. Mean ±SEM is represented. The analyses were performed with ImageJ software (307). This experiment encompasses at least three biological replicates for each condition. The test of Tukey was used for statistical analysis. ****: p-value < 0.0001.

It is worth mentioning that upon histamine stimulation, the amplitude of the peak in the no siRNA condition of MiaPaCa-2 was significantly lower (~0.6) than the amplitude of the peak for the same condition in Panc-1 (~2.6) (Figure 4-20). The data presented on Figure 4-20 are from the same experiments as for the one presented on Figure 4-19.

As a conclusion, we demonstrated that upon histamine stimulation, in cells silenced for myoferlin, the peak of fluorescence is significantly reduced compared to control cells, meaning that myoferlin silencing impairs Ca^{2+} transfer to mitochondria.

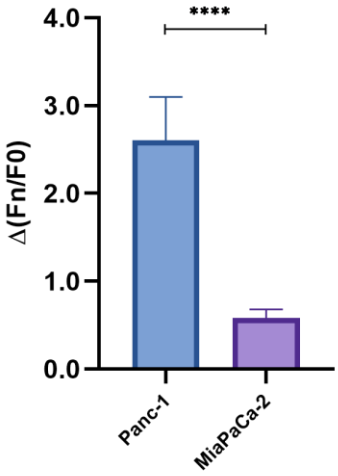

Figure 4-20. Peak amplitude after histamine stimulation in Panc-1 and MiaPaCa-2 cell lines (no siRNA condition). The peak amplitude is the difference between the normalized fluorescence at 60 and 45 seconds for Panc-1 cell line and 65 and 45 seconds for MiaPaCa-2 cell line ($\Delta Fn/F0 = (Fn/F0)_{tf} - (Fn/F0)_{ti}$). The number of cells for each condition was: n = 38 (Panc-1) and n=43 (MiaPaCa-2). Mean ± SEM is represented. A student t-test was performed for statistical analysis. ****: p-value < 0.0001.

4.2.4. Myoferlin silencing does not impair ER integrity

Owing to the known role of ER in Ca^{2+} storage, and since myoferlin has been reported as being part of the secretory pathway, we wanted to ensure that ER integrity is not impaired by myoferlin silencing (242,323). Indeed, an altered ER might not be able to deliver Ca^{2+} to mitochondria. We first evaluated ER morphology upon myoferlin silencing based on TEM images. It is worth noting that the ER is a dynamic structure within the cell, being present under two forms: the rough ER, constituted of flattened sacs and covered by ribosomes and the smooth ER, formed by interconnected tubules. While the rough ER participates to protein synthesis, the smooth ER is involved the synthesis of lipids. A good illustration of the ER dynamics is the one occurring at MAMs, where the surface of the ER in contact with mitochondria is often lacking ribosomes, while the opposite face is often covered by ribosomes. Because of the dynamics and interconnected features, we showed mainly rough ER for illustration.

As shown on Figure 4-21, highlighted by black arrows, no morphological alterations of the ER were visible upon myoferlin silencing in Panc-1 and MiaPaCa-2 cell lines. We saw no enlarged lumen or other abnormalities related to ER.

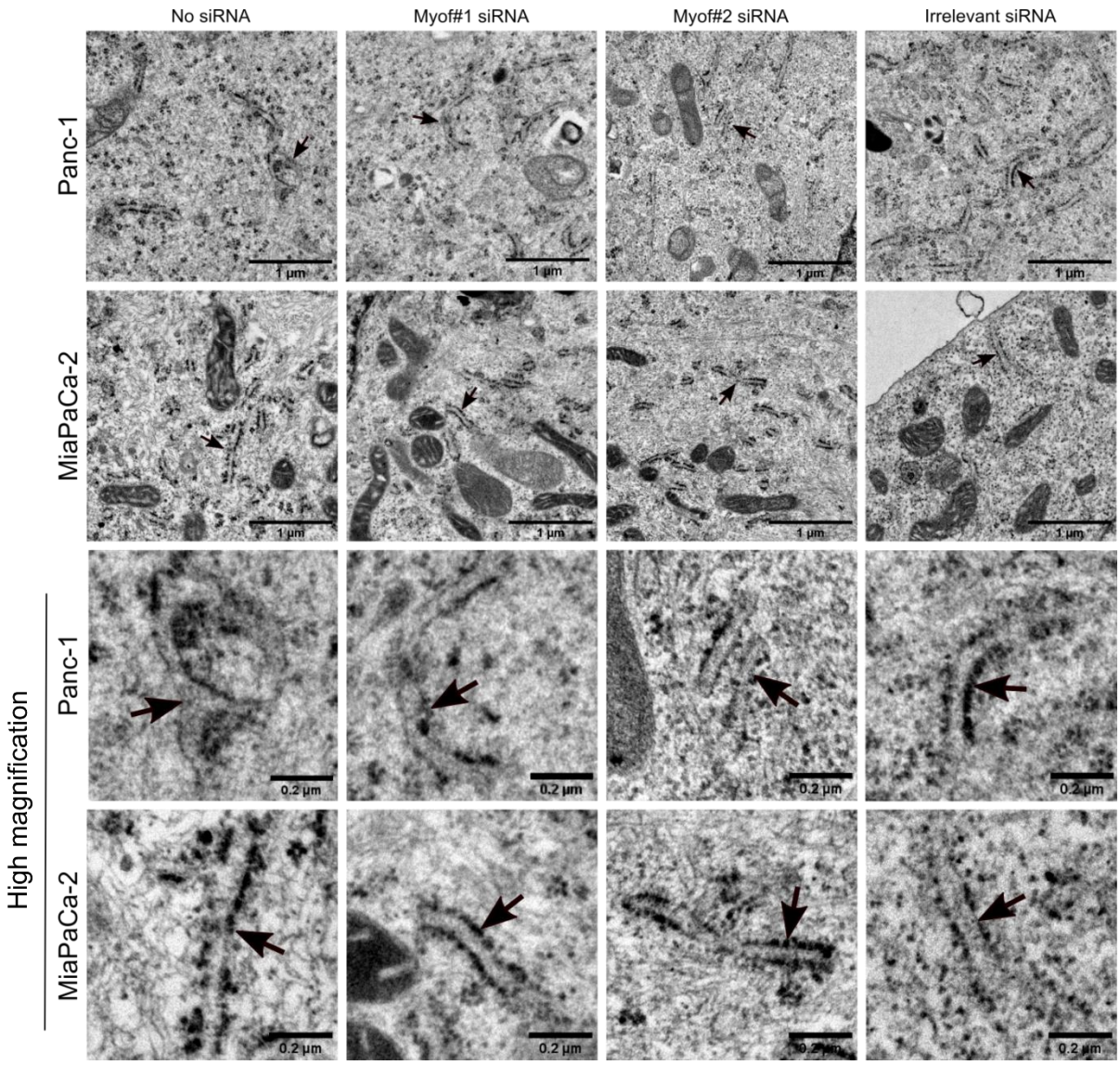

Figure 4-21. TEM images of the ER for the no siRNA, Myof#1, Myof#2 and irrelevant siRNA conditions in Panc-1 and MiaPaCa-2 cell lines. The ER is highlighted by black arrows. For both cell lines, pictures at high magnification of representative ER, in each condition, are shown for better visualization. Scale bar= 1 µm, except for enlarged pictures where scale bar = 0.2 µm.

Additionally, in order to check the ER Ca^{2+} homeostasis, we took advantage of the research field about ER stress. Indeed, alteration of the ER Ca^{2+} stock has been reported to trigger ER stress (208). In response, the cell induces the UPR. Many proteins involved in this response, such as BIP, IRE1, XBP1, PERK, ATF4 or CHOP, are used as markers of the ER stress (207). We expected that upon myoferlin silencing, the ER Ca^{2+} stock might be impaired, explaining the reduced mitochondrial Ca^{2+} level observed upon myoferlin silencing and histamine stimulation. Thus, we decided to silence PDAC cell lines using siRNA targeting myoferlin and to use the UPR markers to monitor a potential ER stress. To validate the selected markers, we used

thapsigargin, a compound able to inhibit the SERCA pump, reducing ER Ca^{2+} concentration over time and inducing ER stress by impairing chaperone activity.

Our results showed that upon 16h of thapsigargin treatment at 1µM in Panc-1 cell line, abundance for UPR markers increased **(Figure 4-22A)**. This increase was also observed upon myoferlin silencing, meaning that myoferlin-silenced cells are still able to activate the UPR when needed. In addition, our results showed no induction of the UPR in myoferlin-silenced cells compared to control cells in Panc-1 and MiaPaCa-2 cell lines **(Figure 4-22B)**. Those results are in accordance with our observations by TEM.

Taken together, those results suggest that upon myoferlin silencing, the ER is not impaired and might be able, regarding Ca^{2+} stock, to deliver Ca^{2+} to mitochondria.

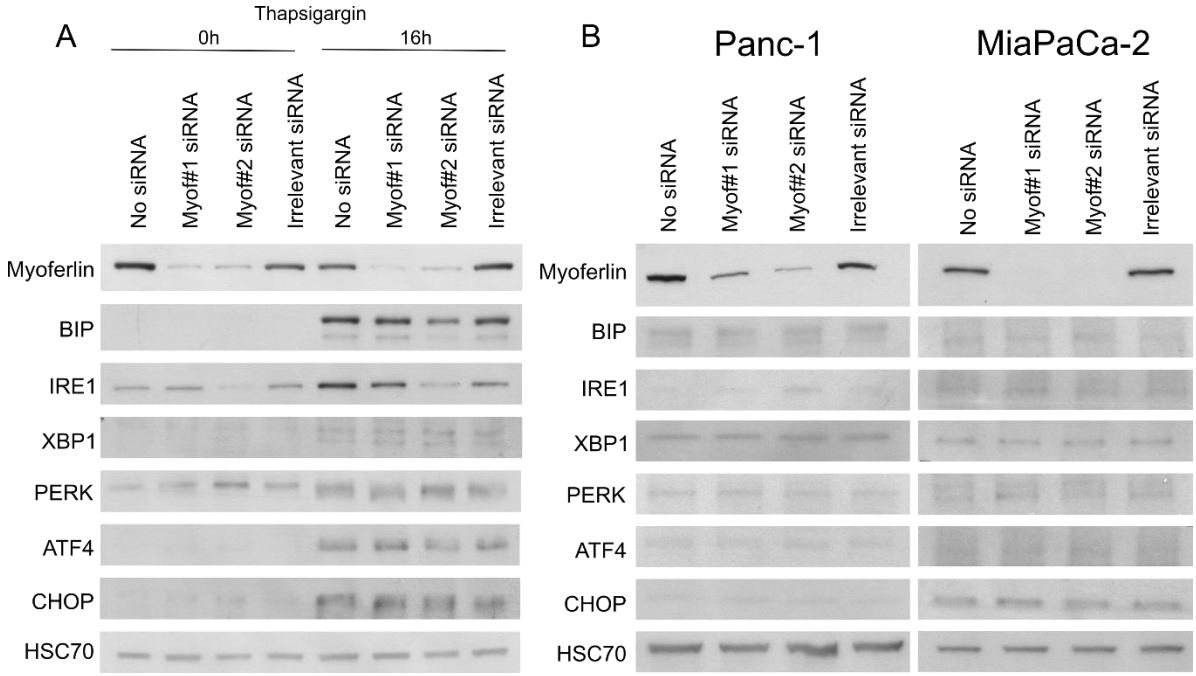

Figure 4-22. ER stress upon myoferlin silencing using UPR markers in Panc-1 and MiaPaCa-2 cell lines. **(A)** Panc-1 cells, transfected with no siRNA, Myof#1 siRNA, Myof#2 siRNA or an irrelevant siRNA, were treated with 1µM thapsigargin for 0h or 16h. Markers of the UPR (BIP, IRE1, XBP1, PERK, ATF4 and CHOP) were checked under those conditions. **(B)** Western blot assessment of the UPR markers upon myoferlin silencing in Panc-1 and MiaPaCa-2 cell lines. HSC70 was used as a loading control. Myoferlin was also assessed to confirm the silencing. Western blots were performed from 20 µg of total proteins. Those western blots are representative of three biological replicates.

4.2.5. Myoferlin silencing does not impact abundance of MAMs proteins related to Ca^{2+} signaling

The reduced Ca^{2+} flow we pointed out upon myoferlin silencing could be related to a modification of the abundance of MAMs proteins. Thus, we performed a western blot on whole cell lysate from Panc-1 and MiaPaCa-2 cell lines. We checked mainly for proteins related to Ca^{2+}

signaling and/or located in MAMs such as IP3R3, VDAC1, MCU, S1R and GRP75 (Figure 4-23). Our results showed no global trends upon myoferlin silencing in both cell lines for MFNs, IP3R3, VDAC1, MCU, S1R and GRP75. It is worth mentioning that we observed a decrease in IP3R3 using the Myof#2 siRNA in Panc-1 cells.

Even if we did not investigate all the proteins related to Ca^{2+} signaling, our results suggest that myoferlin silencing does not impact the abundance of MAMs proteins related to Ca^{2+} signaling.

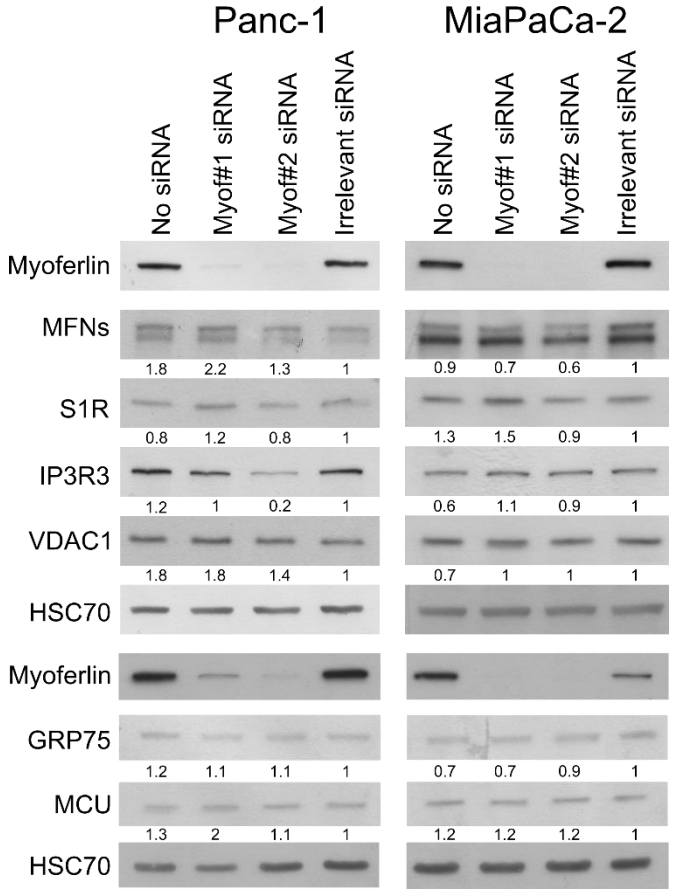

Figure 4-23. Abundance of MAMs-related proteins upon myoferlin silencing in Panc-1 and MiaPaCa-2 cell lines. MFNs, S1R, IP3R3, VDAC1, GRP75 and MCU from whole cell lysate were assessed by western blot. The quantifications were performed with ImageJ software (307). The irrelevant siRNA condition was used as reference for the quantifications. 20 µg of proteins were loaded and HSC70 was used as a loading control. The western blots are representative of at least three biological replicates.

4.2.6. Myoferlin silencing has no impact on ER-Mitochondrial contact sites

Due to its rare structure with multiple C2 domains able to bind Ca^{2+} and phospholipids, we thought that, upon Ca^{2+} release, myoferlin might interact with OMM phospholipids. Therefore, we hypothesized that myoferlin may modulate the physical interactions between ER and mitochondria (Figure 4-24). According to our hypothesis, myoferlin silencing would impair Ca^{2+} signaling by impacting the physical contacts between ER and mitochondria.

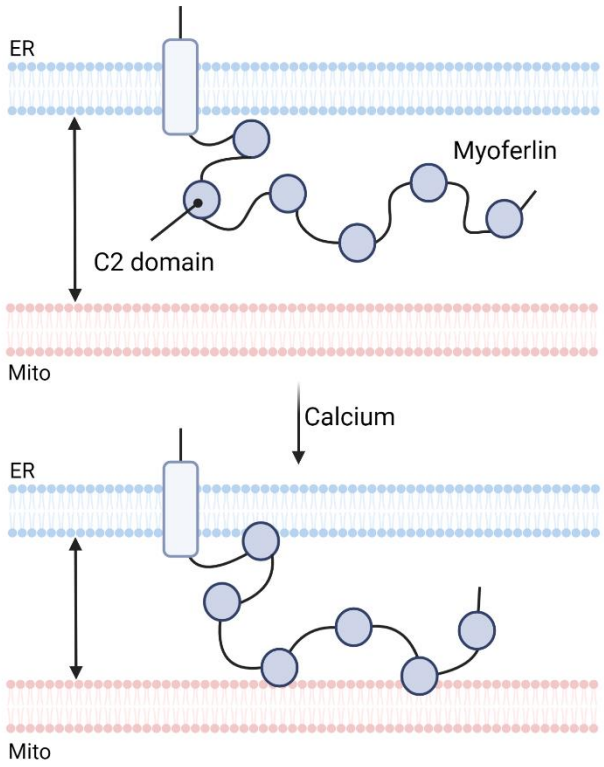

Figure 4-24. Myoferlin may interact with OMM phospholipids thanks to its C2 domains able to bind Ca^{2+}. This would modulate the physical contacts between ER and mitochondria and allow efficient Ca^{2+} transfer between both organelles. The picture was created with BioRender.com.

In order to check our hypothesis, we analyzed TEM images of no siRNA, Myof#1 siRNA, Myof#2 siRNA and irrelevant siRNA conditions on both Panc-1 and MiaPaCa-2 cell lines. TEM images of ER-mitochondria contact sites in the four conditions for both cell lines are represented on Figure 4-25 (highlighted by black arrows). To evaluate the extent of the contact between ER and mitochondria, we referred to the ER-mitochondria contact coefficient (ERMICC), described by Naon *et al.* in 2016 (100). This coefficient relies on three parameters: the length of ER-mitochondria interface (L_{in}), the distance between mitochondria and ER ($Dist_{ER\text{-}M}$) and finally, the mitochondrial perimeter (Per_M) (Figure 4-26).

The ERMICC is defined as followed:

$$ERMICC = \frac{L_{in}}{Per_M * Dist_{ER-M}}$$

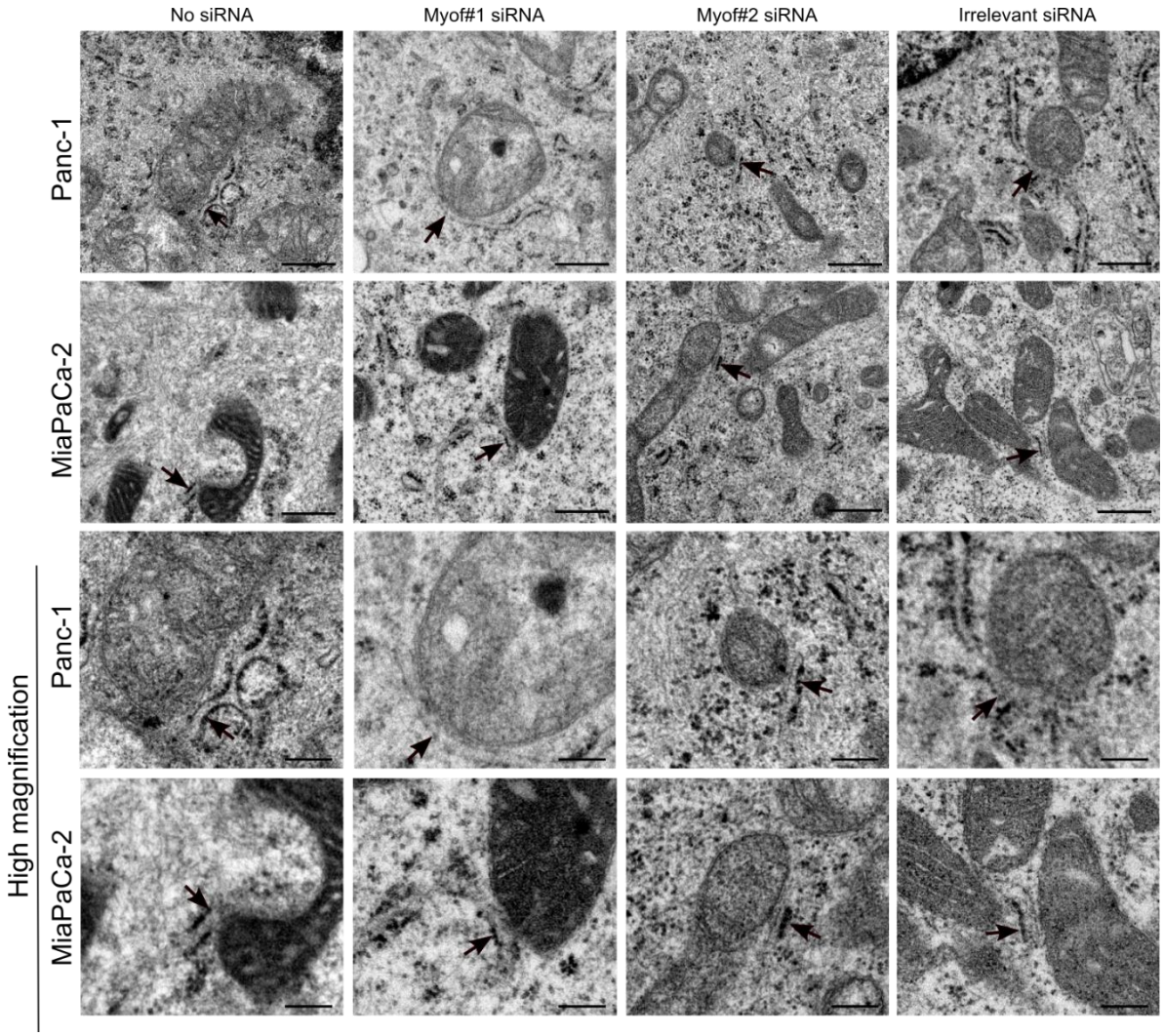

Figure 4-25. TEM pictures representing MAMs in Panc-1 and MiaPaCa-2 cell lines in no , Myof#1, Myof#2 and irrelvant siRNA conditions. MAMs, highlighted by black arrows on the upper pannel of the figure, are shown at high magnification on the lower pannel for better visualization. Scale bar = 5 µm, except for high magnification, where scale bar = 0.2 µm.

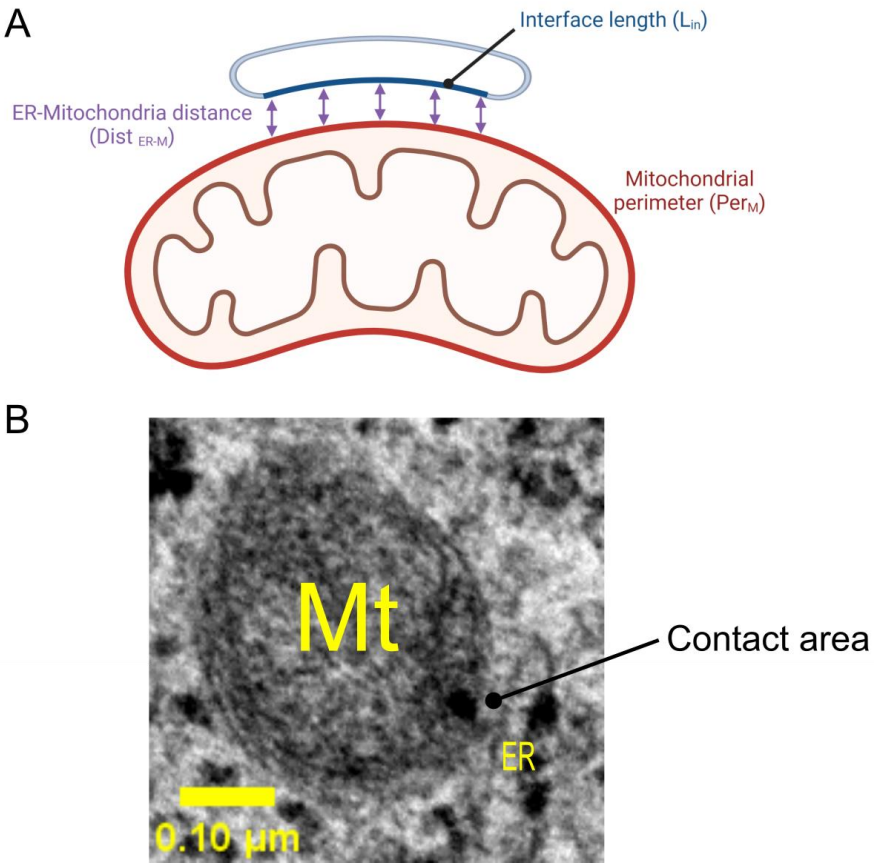

Figure 4-26. Visual description of the ERMICC. **(A)** The coefficient relies on three parameters: the interface length of the ER in contact with mitochondria (blue, L_{in}), the ER-mitochondria distance (double-headed arrows, $Dist_{ER-M}$) and the mitochondrial perimeter (red, Per_M). The picture was created with BioRender.com. **(B)** Picture from TEM showing a contact between ER and mitochondria (Mt).

No significant ERMICC differences were observed in Panc-1 and MiaPaCa-2 cell lines. This means that myoferlin silencing has no impact on the topology of the physical contacts existing between ER and mitochondria **(Figure 4-27)**. In the Panc-1 cell line, we noticed a significantly increased L_{in} only in the Myof#1 siRNA condition compared to the irrelevant condition **(Figure 4-27B)**. However, when divided by Per_M and $Dist_{ER-M}$, the ERMICC was not significantly impacted. We found no statistical differences regarding Per_M and $Dist_{ER-M}$ in myoferlin-silenced cells compared to irrelevant siRNA-transfected Panc-1 cells. For the MiaPaCa-2 cell line, we observed no significant differences upon myoferlin silencing in the Per_M and L_{in} parameters. However, when using Myof#1 siRNA, the $Dist_{ER-M}$ was significantly reduced **(Figure 4-27C)**. Despite this decrease, no significant differences for the ERMICC were observed compared to the irrelevant condition.

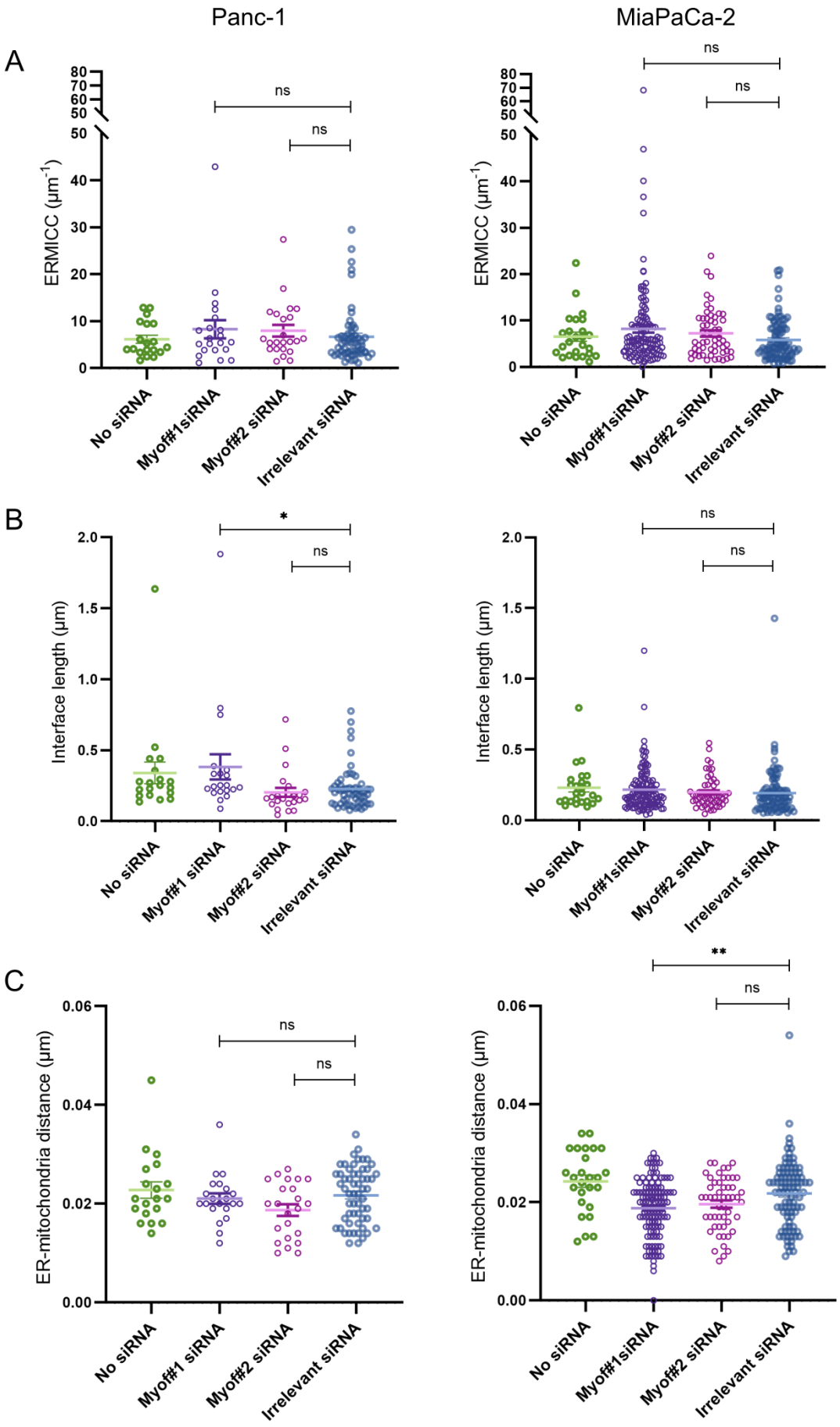
Panc-1
MiaPaCa-2
A
ERMICC (µm-1)
ns
ns
B
Interface length (µm)
*
ns
C
ER-mitochondria distance (µm)
**
No siRNA
Myof#1siRNA
Myof#2 siRNA
Irrelevant siRNA

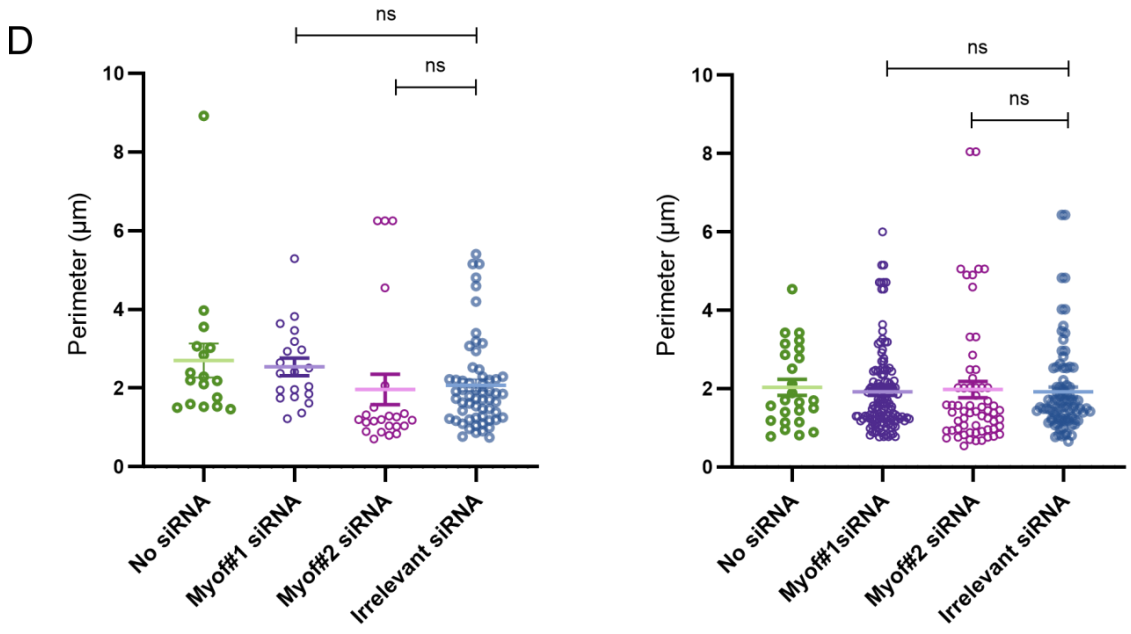

Figure 4-27. Myoferlin silencing does not impact the topology of contacts between ER and mitochondria in Panc-1 and MiaPaCa-2 cell lines. **(A)** Graphs showing the ERMICC value from controls (no and irrelevant siRNA) and myoferlin-silenced cells (Myof#1 and Myof#2 siRNA) in both cell lines. **(B)** Interface length of ER in contact with mitochondria in controls and myoferlin-silenced cells. **(C)** Distance between ER and mitochondria in controls and myoferlin-silenced cells. **(D)** Graphs showing the perimeter of mitochondria in contact with ER in controls and myoferlin-silenced cells. The non-parametric test of Kruskal-Wallis was used for statistical analysis. For the Panc-1 cell line, the number of mitochondria in each condition was: n=298 (16 pictures, irrelevant), n=138 (7 pictures, Myof#1 siRNA), n=122 (5 pictures, Myof#2 siRNA) and n=93 (6 pictures, no siRNA). Regarding the MiaPaCa-2 cell line, the number of mitochondria was: n=210 (10 pictures, irrelevant), n= 224 (9 pictures, Myof#1 siRNA), n=174 (11 pictures, Myof#2 siRNA) and n= 189 (9 pictures, no siRNA). ns = non-significant. *: p-value < 0.05. **: p-value < 0.01. Mean ±SEM is represented.

In addition to the ERMICC, a PLA between VDAC1 and IP3R3, two proteins described in the literature to be involved in Ca^{2+} transfer between ER and mitochondria, has been performed upon myoferlin silencing in both Panc-1 and MiaPaCa-2 cell lines (Figure 4-30). Prior to the PLA, we wanted to confirm the presence of VDAC1 and IP3R3 in MAMs by making a western blot on MAMs extracts for both cell lines (Figure 4-28). As expected, and in accordance with literature (117), VDAC1 was enriched in the PM fraction and IP3R3 was detected in the microsomal fraction. Moreover, VDAC1 and IP3R3 were present in the PMAMs fraction of both cell lines, confirming their presence in MAMs. On a side note, IP3R3 was enriched in the PMAMs fraction of Panc-1, while it was not in MiaPaCa-2. Moreover, the PM fraction for the Panc-1 cell line seemed contaminated by microsomes as suggested by the presence of IP3R3 and myoferlin in this fraction. A fraction of microsomes associated with mitochondria was probably lost in the PM fraction. Therefore, if we had to re-perform this experiment, by limiting the microsome contamination in the PM, we would probably see a higher enrichment of IP3R3 and myoferlin

in the CMAMs and PMAMs fractions. The extract used to assess IP3R3 and VDAC1 in the MiaPaCa-2 cell line was the same as the one presented in Figure 4-16. As explained in the *Cell metabolic profile: is there a relationship with MAMs?* section, the difference observed for IP3R3 abundance in the PMAMs fraction could be explained by the metabolic profile or by the intrinsic characteristics of the cell lines.

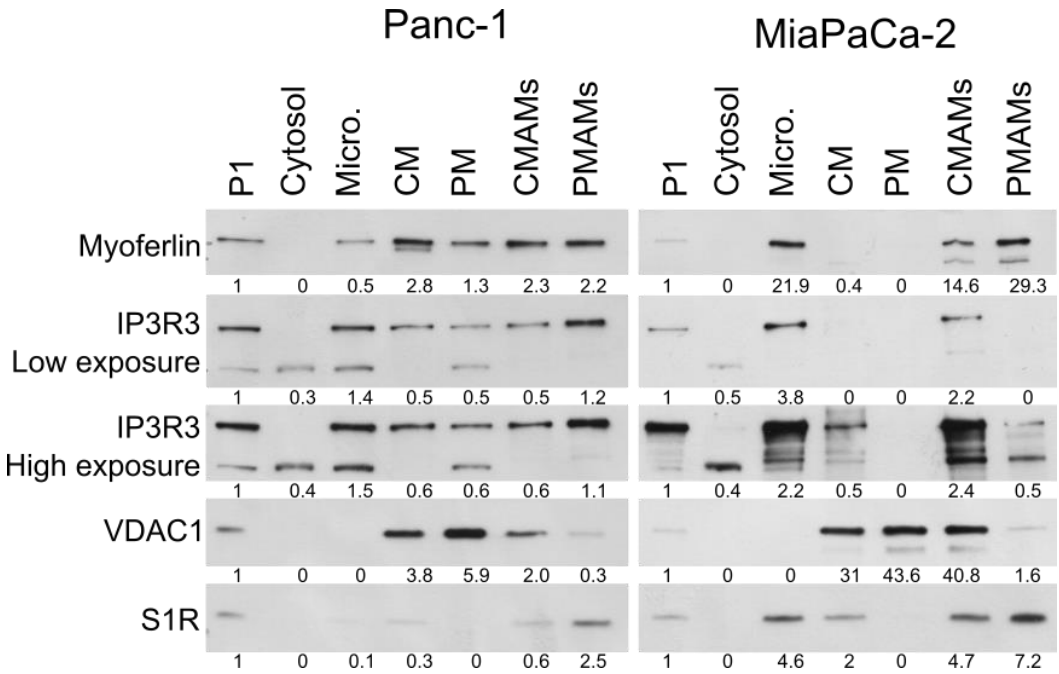

Figure 4-28. Assessment of IP3R3 and VDAC1 in the PMAMs fractions of Panc-1 and MiaPaCa-2 cell lines by western blot. IP3R3 and VDAC1 were assessed from the same extract as the one presented in **Figure 4-16** for MiaPaCa-2. Myoferlin, the protein of interest, and S1R, a marker of MAMs, are also represented. Low and high exposures of IP3R3 are shown. 5 µg of proteins were loaded on the gels for each fraction. P1 (lysate), cytosol, Micro. (microsomes), CM (crude mitochondria), PM (pure mitochondria), CMAMs (crude MAMs), PMAMs (pure MAMs). P1 was used as reference for quantifications (made with ImageJ software (307)). The assessment of myoferlin and S1R was made on at least three biological replicates, while IP3R3 and VDAC1 were only assessed from one biological replicate.

In addition, prior to the PLA, primary antibodies for VDAC1 and IP3R3 were validated for immunofluorescence (Figure 4-29). Indeed, both immunofluorescence and PLA techniques rely on the same principle. If the antibodies display unspecific stainings by immunofluorescence, the signals obtained by PLA could be the consequence of unspecific binding of the primary antibody. Therefore, validating the antibodies prior to the PLA by immunofluorescence ensure us about the specificity of the PLA signals. Even so, using cell lines that do not express the proteins of interest or using siRNA against those proteins would constitute a better guarantee. VDAC1 labeling was detected throughout the cytoplasm and was similar to the one reported in the literature (324). Similarly, IP3R3 was found throughout the cytoplasm. Moreover, it formed clusters in the perinuclear region, which was also described in the literature (325,326).

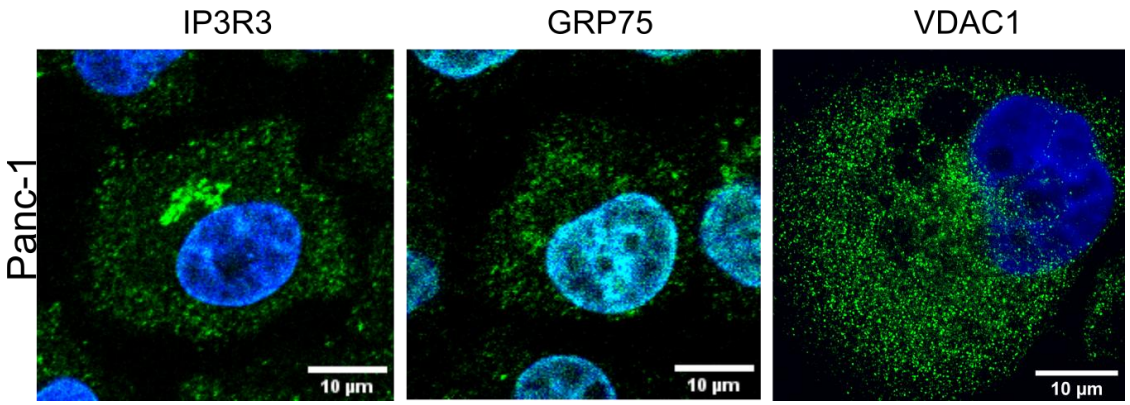

Figure 4-29. Validation of IP3R3, GRP75 and VDAC1 primary antibodies for immunofluorescence in the Panc-1 cell line. IP3R3 and GRP75 pictures were taken with a Nikon A1R confocal microscope, while VDAC1 confocal pictures were acquired with a high resolution LSM 880 microscope.

Since VDAC1 and IP3R3 are supposed to be in proximity to transfer Ca^{2+} from ER to mitochondria (97), we expected to obtain PLA signals. Indeed, in both cell lines, proximity dots were detected (Figure 4-30A). Interestingly, the mean number of dots per cell in the MiaPaCa-2 cell line was encompassed in a range of 10 to 15 dots per cell, while in Panc-1, this range was higher, between 30 and 50 dots per cell. This can be explained by the cell size, MiaPaCa-2 cells being smaller than Panc-1 cells or by the biological differences existing between those cellular models. No significant differences were found in both cell lines regarding the number of dots per cell upon myoferlin silencing, except for the Myof#2 siRNA condition in the Panc-1 cell line, where the number of dots per cell was significantly reduced in comparison to the irrelevant siRNA condition (Figure 4-30B). Controls for the PLA are shown in Figure 7-3.

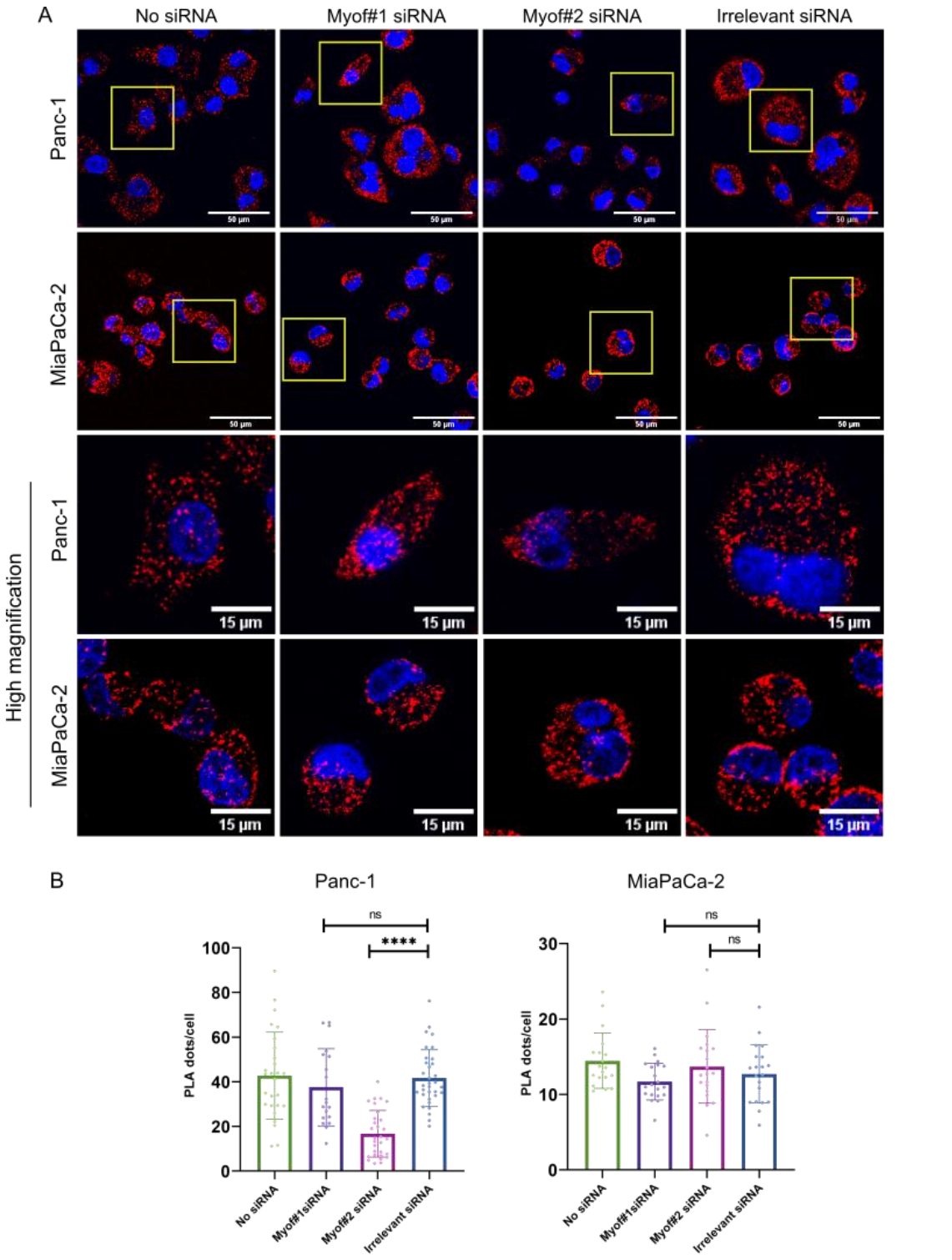

Figure 4-30. PLA between VDAC1 and IP3R3 in Panc-1 and MiaPaCa-2 cell lines. **(A)** Representative pictures for the PLA in no siRNA, Myof#1 siRNA, Myof#2 siRNA and irrelevant siRNA conditions. Strong signals for the PLA were visible in all conditions and for both cell lines **(B)** Quantification of PLA dots per cells in Panc-1 and MiaPaCa-2 cell lines. A dot represents the number of dots/cell/picture. IP3R3 rabbit polyclonal primary and VDAC1 mouse monoclonal primary antibodies were used. The pictures were acquired with a confocal Nikon A1R microscope. The number of pictures, from three independent experiments, analyzed for the PLA in the Panc-1 cell line was: n=33 (irrelevant), n=19 (Myof#1 siRNA), n=30 (Myof#2 siRNA), n=27 (no siRNA). The number of pictures, from three independent experiments, for the PLA in the MiaPaCa-2 cell line was: n=20 (irrelevant), n=20 (Myof#1 siRNA), n=20 (Myof#2 siRNA) and n=19 (no siRNA). The analyses were performed with ImageJ software (307). Mean ±SD is represented. The non-parametric Kruskal-Wallis test was used for statistical analysis. ****: p-value < 0.0001. ns: non-significant.

4.2.7. Myoferlin interacts with IP3R3, a protein involved in Ca^{2+} signaling in MAMs

Since myoferlin silencing does not impacting the abundance of MAMs proteins related to Ca^{2+} signaling, the ERMICC or the proximity between IP3R3 and VDAC1, we thought myoferlin was instead interacting with proteins involved in Ca^{2+} signaling in MAMs.

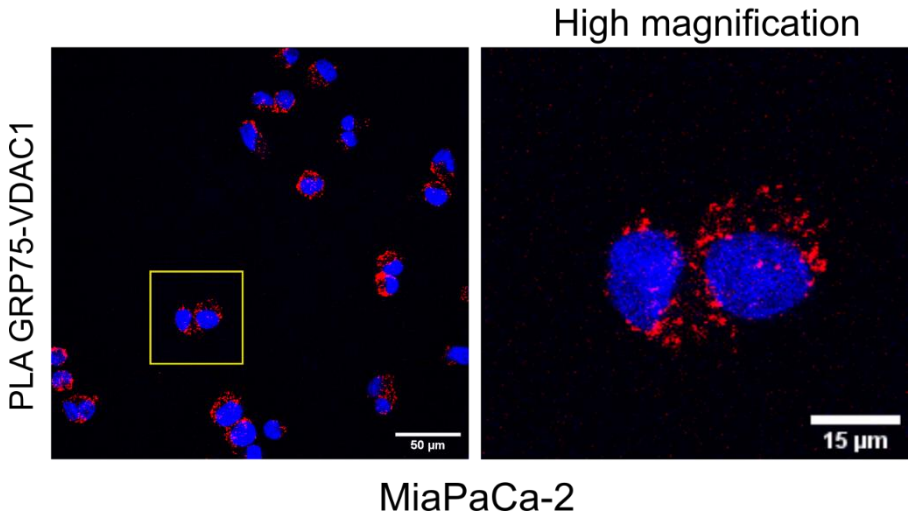

Figure 4-31. PLA between VDAC1 and GRP75 in the MiaPaCa-2 cell line. Representative picture for the PLA (left). The picture on the right represents the yellow square from the left picture at high magnification. Strong signals for the PLA were visible. GRP75 rabbit monoclonal primary antibody and VDAC1 mouse monoclonal primary antibody were used. The pictures were acquired with confocal Nikon A1R microscope.

In order to investigate our hypothesis, we performed a PLA between myoferlin and IP3R3, VDAC1 or GRP75. Before exploring the potential proximity between myoferlin and GRP75, a validation of the GRP75 primary antibody by immunofluorescence was performed. The staining is presented in **Figure 4-29**. It is worth mentioning that GRP75 can be found in the nucleus, mitochondria, cytosol and ER (327). In the literature, IP3Rs and VDAC1 have been described to be in proximity, to ensure efficient Ca^{2+} transfer at MAMs. GRP75 has been reported as a stabilizer of the IP3Rs-VDAC1 axis (97,328). Therefore, to further validate the antibody and confirm GRP75 proximity with IP3R3 or VDAC1, we performed a PLA. Our results showed signals for the PLA between GRP75 and VDAC1 in the MiaPaCa-2 cell line, confirming proximity between both proteins, as described in the literature **(Figure 4-31)** (328). We did not perform the PLA between GRP75 and IP3R3 because the corresponding primary antibodies available at the laboratory were from the same species.

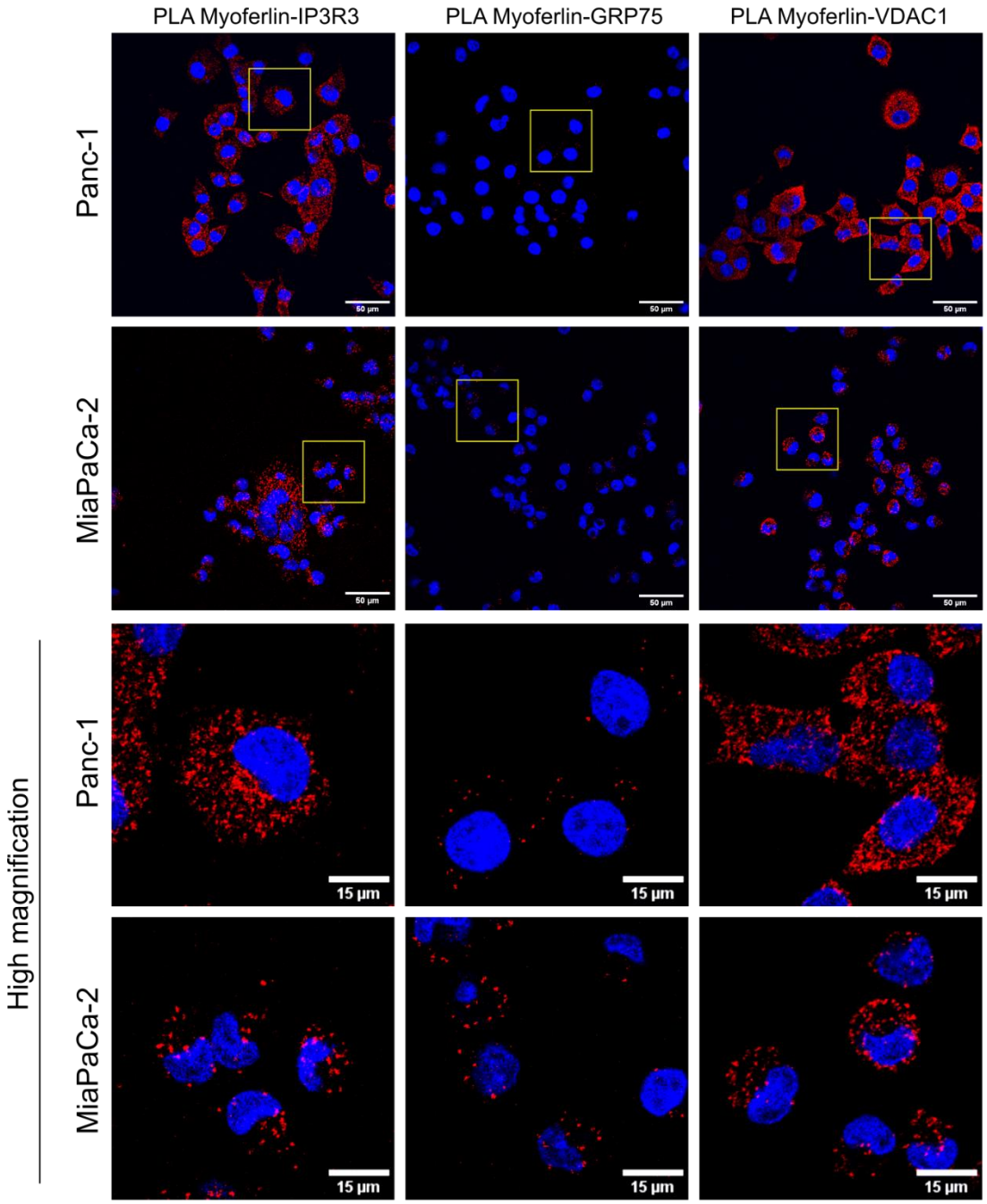

Figure 4-32. PLA between myoferlin and key proteins described in Ca^{2+} signaling at MAMs (IP3R3, GRP75 and VDAC1) in Panc-1 and MiaPaCa-2 cell lines. On the upper panel of the figure, respresentative pictures for the PLA are shown. The lower panel represents high magnification of the yellow squares from the upper panel. The pictures were acquired with Nikon A1R confocal microscope. The scale bar on the upper pannel represents 50 µm, while on the lower panel it represents 15 µm. The pictures are representative of three independent experiments.

Interestingly, a strong signal for the PLA between myoferlin and IP3R3 as well as for myoferlin and VDAC1 was visible (Figure 4-32). Although present, few dots were detected for the PLA between myoferlin and GRP75. Those results demonstrated the proximity existing between myoferlin and key components of Ca^{2+} signaling reported in MAMs. The controls for the PLA are shown in Figure 7-4.

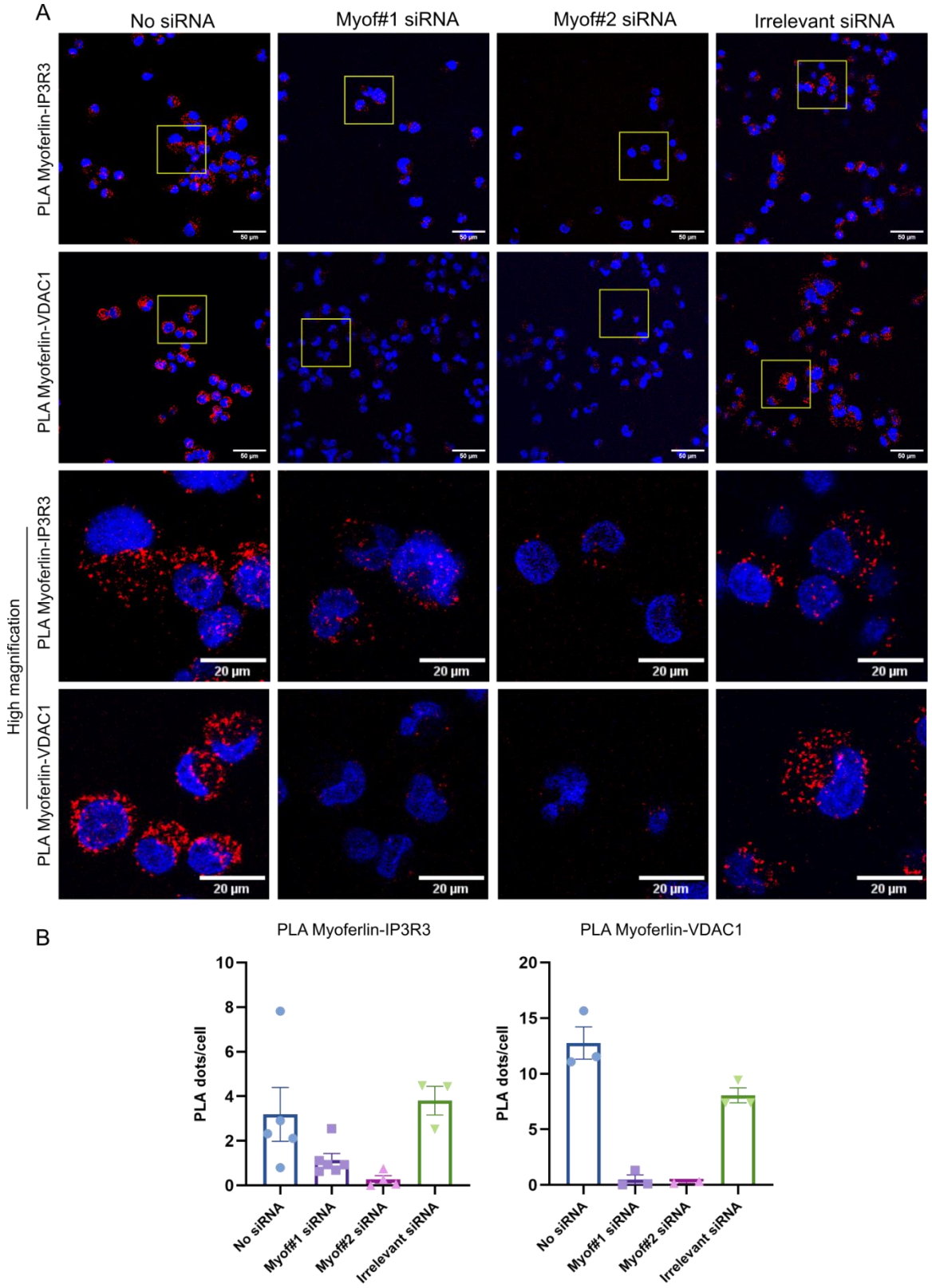

Figure 4-33. PLA between myoferlin and VDAC1 as well as myoferlin and IP3R3 from control or myoferlin-silenced cells. The experiment was performed on the MiaPaCa-2 cell line. **(A)** Representative pictures of PLA for myoferlin-VDAC1 or myoferlin-IP3R3 upon myoferlin silencing or in control cells. Scale bar = 50 µm. **(B)** Quantification of dots/cell/picture for both myoferlin-IP3R3 and myoferlin-VDAC1 PLA. The quantification was performed in myoferlin-silenced and control cells. Pictures were acquired with a Nikon A1R microscope and analyses were performed with ImageJ software (307). This experiment was performed only once.

To ensure that the signals observed for the myoferlin-IP3R3 and myoferlin-VDAC1 PLA were specific, we performed the same experiment upon myoferlin silencing in the MiaPaCa-2 cell line **(Figure 4-33)**. The number of dots per cell was drastically reduced upon silencing, showing that the signal was specific to the proximity of myoferlin with IP3R3 or VDAC1.

Encouraged by those results, we decided to immunoprecipitate IP3R3, VDAC1 and GRP75 from Panc-1 whole cell lysate and to check for co-immunoprecipitation of myoferlin **(Figure 4-34)**. We efficiently immunoprecipitated IP3R3 and, we noticed that myoferlin was co-immunoprecipitated with this protein. Two defined bands were visible in the IP-IP3R3 condition, at the same molecular weight as the uppermost band corresponding to myoferlin in the lysate. It is worth noting that this upper band in fact encompasses several myoferlin isoforms (https://www.uniprot.org/). Therefore, observing two co-immunoprecipitated bands for myoferlin is not surprising. These results prompted us to perform the same experiment on the MiaPaCa-2 cell line. Similarly, we could see two bands for myoferlin as a co-immunoprecipitate of IP3R3 in this cell line **(Figure 4-34)**. However, the bands were barely visible after 30 minutes exposure, while they were already visible after 5 minutes exposure in the Panc-1 cell line. This highlighted once again differences between cell lines, IP3R3 interacting probably to a higher extent with myoferlin in Panc-1 than in MiaPaCa-2. Unfortunately, we were not able to efficiently immunoprecipitate VDAC1 and therefore, we could not conclude for myoferlin co-immunoprecipitation with this protein. In addition, our results showed no co-immunoprecipitation between GRP75 and myoferlin in Panc-1 cells **(Figure 4-34)**.

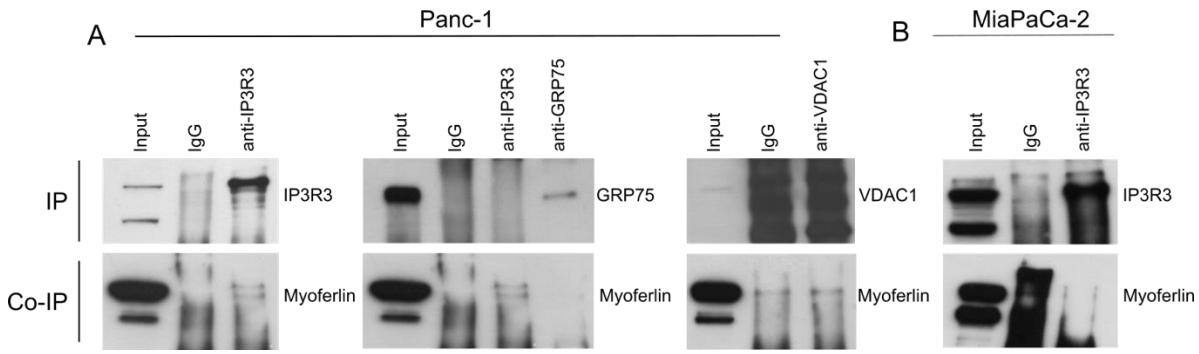

Figure 4-34. Assessement of myoferlin co-immunoprecipitation with key proteins involved in Ca^{2+} signaling at MAMs. **(A)** IP3R3, GRP75 and VDAC1 were immunoprecipitated from the Panc-1 cell line. The immunoprecipitation was checked by western blot. As opposed to VDAC1, IP3R3 as well as GRP75 were efficiently immunoprecipitated. Myoferlin co-immunoprecipitation was assessed by western blot. Myoferlin was successfully co-immunoprecipitated with IP3R3 but not with GRP75. **(B)** Immunoprecipitation of IP3R3 was also performed on the MiaPaCa-2 cell line and myoferlin co-immunoprecipitation was assessed by western blot. The IP3R3-myoferlin co-immunoprecipitation is representative of three independent experiments (in both cell lines), while the IP myoferlin-GRP75 and Myoferlin-VDAC1 are representative of two independent experiments (in Panc-1 cells).

Regarding the results obtained by immunoprecipitation, we were curious about a potential myoferlin-IP3R3 colocalization in the cell. To answer this question, we performed a co-labeling of myoferlin and IP3R3 by indirect immunofluorescence in both Panc-1 and MiaPaCa-2 cell lines (Figure 4-35). As previously mentioned, IP3R3 forms clusters at the perinuclear region of both Panc-1 and MiaPaCa-2 cell lines. In accordance with the literature, myoferlin labeling was found throughout the cytoplasm and the staining was more intense in the perinuclear region (242). Interestingly, myoferlin and the IP3R3 clusters seemed to colocalize in both cell lines. It is worth noting that all the cells did not display IP3R3 clusters at the perinuclear region as highlighted by the white arrows (Figure 4-35A). In this work, we focused our experiments on IP3R3, because historically IP3R3 was described as the most abundant isoform in MAMs (180,181). Nevertheless, other IP3R isoforms are found in MAMs such as IP3R1 (182). Interestingly, myoferlin seemed to colocalize with IP3R1 as shown in Figure 7-5.

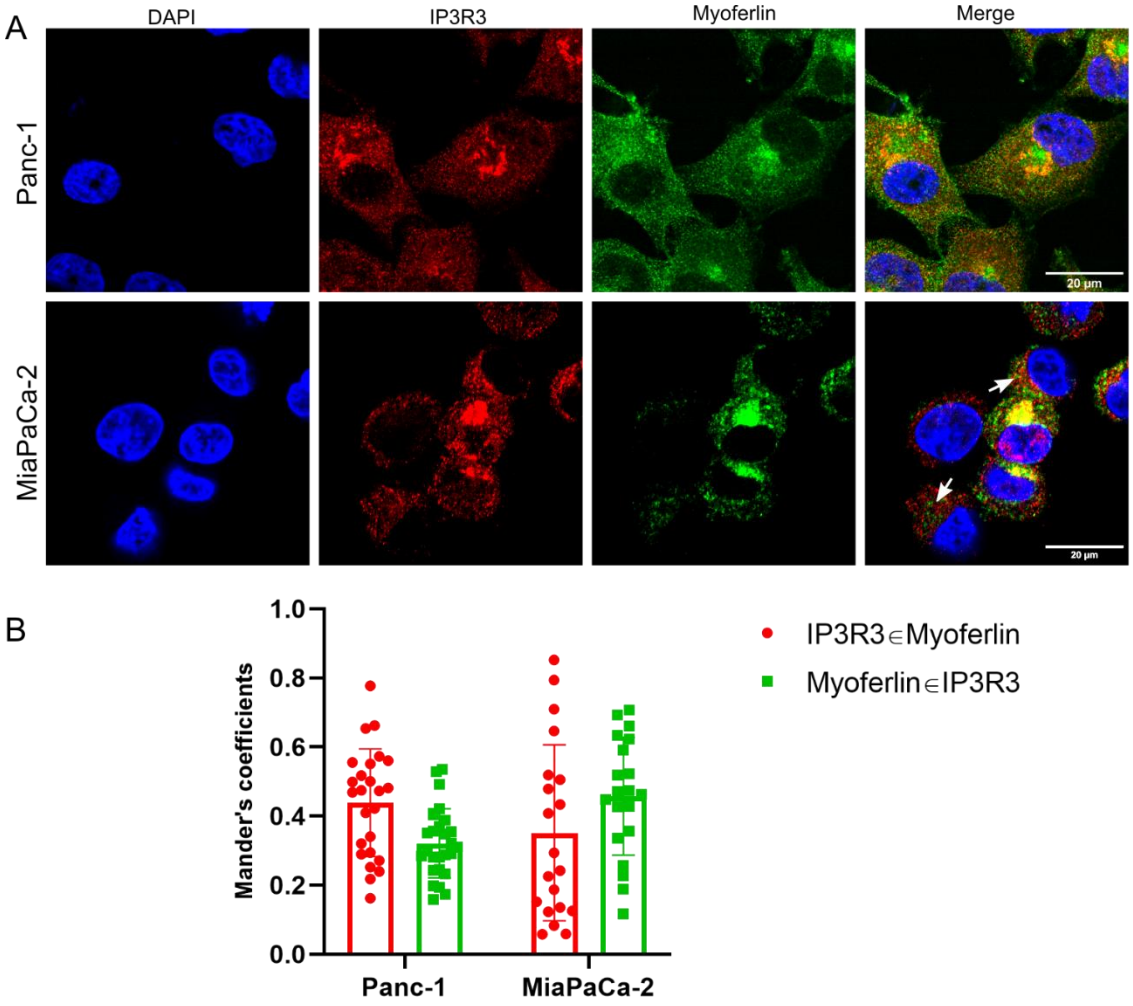

Figure 4-35. Myoferlin and IP3R3 colocalize in Panc-1 and MiaPaCa-2 cell lines. **(A)** IP3R3 forms clusters at the perinuclear region, while myoferlin is abundant in this cell region. On the "Merge pictures", colocalizing pixels are visible in yellow. The white arrows show cells where no IP3R3 clusters were found. IP3R3 rabbit polyclonal antibody and myoferlin (D-11) mouse monoclonal antibody were used. IP3R3 appears in red, myoferlin in green and the nucleus in blue (DAPI). Scale bar represented 20 µm. Confocal pictures were acquired with a high resolution LSM 880 microscope. **(B)** Colocalization analyses using Manders' method on both Panc-1 and MiaPaCa-2 cell lines. "IP3R3 ϵ Myoferlin" (in red on the graph) represents the proportion of above-threshold pixels in channel 1 (IP3R3) colocalizing with above-threshold pixels in channel 2 (Myoferlin) and vice versa for "Myoferlin ϵ IP3R3". Mean ±SD is represented. The number of analyzed cells for the Panc-1 cell line was 27, while 20 cells were analyzed for MiaPaCa-2. The analyses were performed with ImageJ software (307). The pictures are representative of at least two independent experiments.

We then performed colocalization studies using the same method as described previously (see *Colocalization studies*). When using each individual cell as a ROI, our results showed that the proportion of IP3R3 colocalizing with myoferlin (M1) was of 41.21 ±15.38% in Panc-1 and 35.15 ±25.46% in MiaPaCa-2 cell lines (Figure 4-35B). Conversely, the proportion of myoferlin colocalizing with IP3R3 was of 33.01 ±10.88% in Panc-1 and 45.72 ±17.04% in MiaPaCa-2 cell lines (M2). Because myoferlin seemed to colocalize mainly with IP3R3 clusters, we decided to perform colocalization analyses using the clusters as ROI. In addition, we performed the analyses on the whole cell without considering the clusters (Figure 4-36).

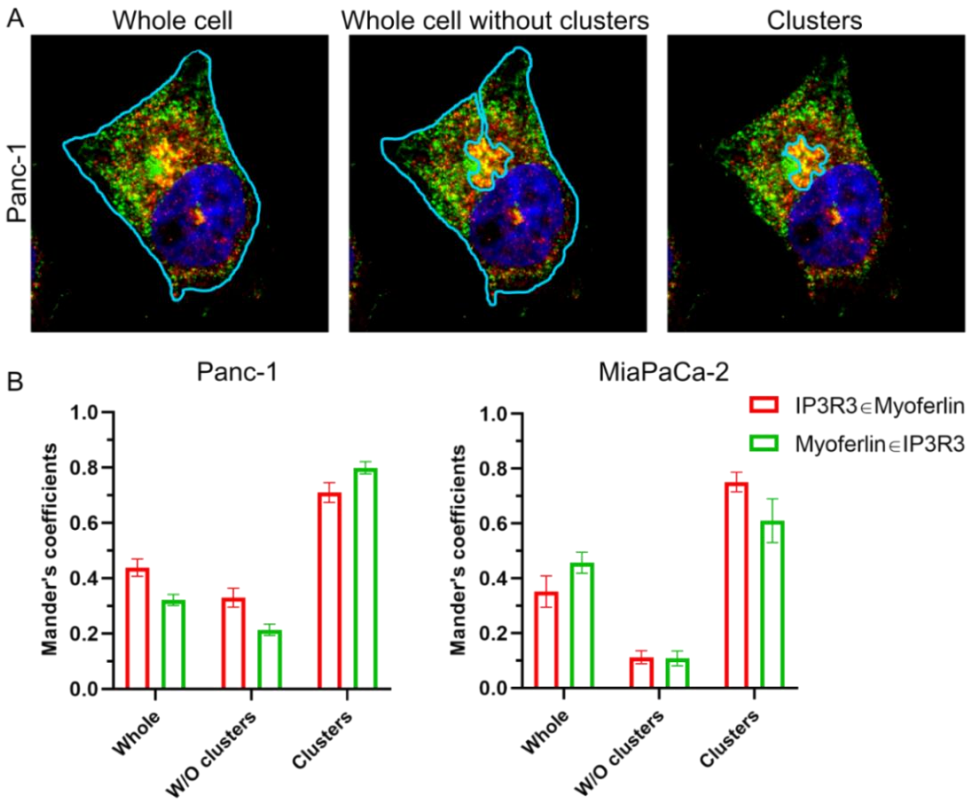

Figure 4-36. Myoferlin strongly colocalizes with IP3R3 clusters. **(A)** Representation of ROI used for colocalization analyses using Manders' method in a Panc-1 cell. The colocalization was performed using the whole cell, the whole cell without clusters or the clusters only as ROI. The pictures were acquired with a high resolution LSM 880 microscope. Myoferlin is represented in green, IP3R3 in red and the nucleus in blue. **(B)** Graphs representing the percentage of colocalization between myoferlin and IP3R3 when the whole cell, the cell without clusters (W/O clusters) or the clusters only were used as ROI. The analyses were perfomed on Panc-1 and MiaPaCa-2 cell lines. "IP3R3 ϵ Myoferlin" (in red on the graph) represents the proportion of above-threshold pixels in channel 1 (IP3R3) colocalizing with above-threshold pixels in channel 2 (Myoferlin) and vice versa for "Myoferlin ϵ IP3R3". The number of analyzed cells for Panc-1 cell line was 27, while 20 cells were analyzed for MiaPaCa-2. Mean ± SEM is represented. The analyses were performed with ImageJ software (234).

Interestingly, when considering the whole cell without clusters for analysis, the percentage of colocalization remained similar to the one performed on the whole cell in the Panc-1 cell line (M1: 41.21 ±15.38% vs 32.90 ±16.10%, M2: 33.01 ±10.88% vs 21.30 ±9.50% with the ROI being the whole cell vs the whole cell without clusters, respectively). This means that myoferlin is also colocalizing with IP3R3 outside the cluster regions in Panc-1 cells. In MiaPaCa-2, the percentage of colocalization outside the clusters dropped drastically from 35.15 ±25.46% to 11.20 ±11.90% for M1 and from 45.72 ±17.04% to 10.80 ±13.60% for M2. Nevertheless, in both cell lines, the percentage of colocalization between IP3R3 and myoferlin increased in the cluster regions. In Panc-1, the percentage of colocalization in the clusters was of 70,90 ±18.9% for M1 and 79,90 ±11.70% for M2, while those percentages were of 75,20 ±14.80% and 61,00 ±30.90% for M1 and M2, respectively, in MiaPaCa-2 (Figure 4-36B).

Finally, in order to prove myoferlin interaction with IP3R3 in MAMs, we decided to immunoprecipitate IP3R3 from Panc-1 MAMs extract and to investigate for a potential myoferlin co-immunoprecipitation. Our results showed that IP3R3 was present and perfectly immunoprecipitated from the PMAMs fraction (Figure 4-37). Interestingly, myoferlin was co-immunoprecipitated with IP3R3 as three individual bands at the same height as the upper band (the most abundant band) corresponding to myoferlin in the input. As overmentioned, this large band encompasses several myoferlin isoforms. Indeed, three myoferlin isoforms have been proposed around 230 kDa: myoferlin isoform 1 (234.709 kDa), isoform 3 (233.324 kDa) and isoform 6 (233.477 kDa). The two lower bands, clearly visible in the input and detected below 230 kDa, may correspond to the isoforms 2 (229.895 kDa) and 5 (179.551 kDa) (https://www.uniprot.org/) (254). Interestingly, we observed two bands at similar molecular weights in the anti-IP3R3 input. The five bands are highlighted by arrows on Figure 4-37. On a side note, signal in the IgG control was found at a molecular weight corresponding to myoferlin. However, as visible on Figure 4-37, this signal was mainly background and no defined bands were discernible.

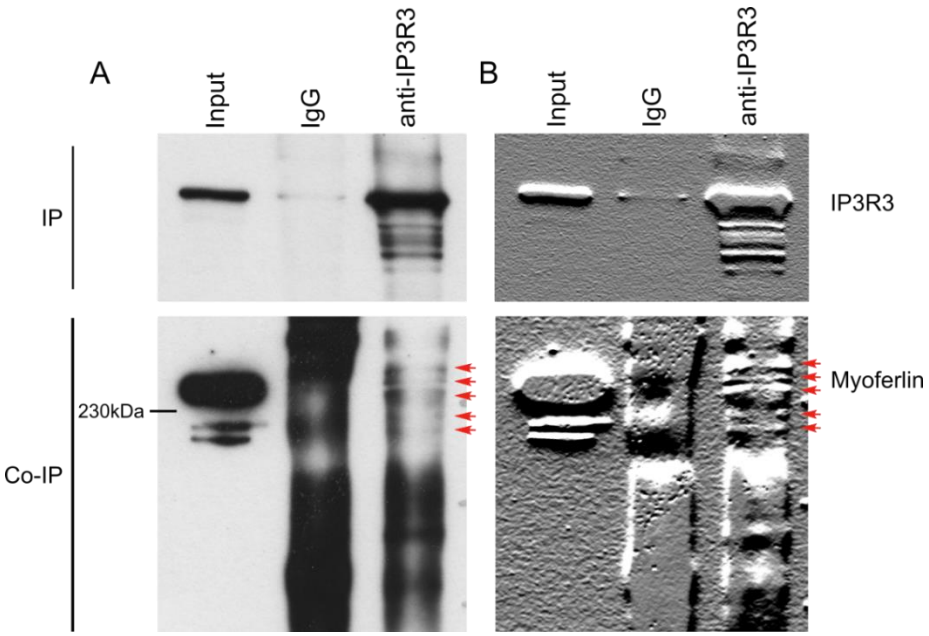

Figure 4-37. Myoferlin co-immunoprecipiates with IP3R3 from Panc-1 PMAMs extract. **(A)** IP3R3 was efficiently immunoprecipitated from PMAMs extract as shown by western blot (IP). Myoferlin co-immunoprecipitation with IP3R3 was checked by western blot (Co-IP). PMAMs extract was used for the input. A rabbit IgG antibody was used for immunoprecipitation as negative control. For IP3R3 immunoprecipitation, the IP3R3 primary antibody was used (Anti-IP3R3). **(B)** Same picture as on the right with a sobel filter applied. The detection was based on bottom edges with a vertical and horizontal radius of 5 pixels. This allows better visualization of bands. This experiment was performed only once.

Altogether, those results demonstrate that myoferlin is in proximity with proteins involved in Ca^{2+} signaling at MAMs. In addition, we were able to prove a physical interaction between

myoferlin and IP3R3. Thanks to the IP performed from MAMs extract, we showed that this interaction occurs, at least in part, in MAMs.

4.2.8. The overall survival of patients with PDAC is correlated with *ITPR3* expression

Our team previously demonstrated that myoferlin expression is correlated to PDAC patients' overall survival (47). Since IP3R3 interacts with myoferlin in PDAC, we next thought to investigate whether *ITPR3* (gene corresponding to IP3R3) expression is also correlated to patients' survival. Indeed, this protein has been associated with many cancers, where it confers metabolic advantages through modulation of Ca^{2+} transfer between ER and mitochondria. Interestingly, we found many publications about *ITPR3* expression in correlation with patients' survival in cancers such as colorectal (216), breast (68), renal (69) and bile duct (70) cancers. However, we found no publications concerning PDAC. Therefore, this prompted us to investigate *ITPR3* expression in PDAC based on the Human Protein Atlas (https://www.proteinatlas.org/) and patients' cohort from the TCGA PanCancer Atlas (n=177). We discovered that *ITPR3* expression is significantly associated with the overall survival (p=0.0067). Indeed, the risk of death in patients with PDAC increases with *ITPR3* expression (HR=2.19; 95% confidence interval= 1.23-3.91) **(Figure 4-38A)**. Surprisingly, expressions of *MYOF* (gene corresponding to myoferlin) and *ITPR3* were significantly correlated (R = 0.74) in those PDAC patients **(Figure 4-38B)**. In addition, we found in the Human Protein Atlas that IP3R3 immunocytochemistry staining is enhanced in PDAC tissues **(Figure 4-38C)**. Those results constitute preliminary data and, of course, further investigations should be conducted. For instance, evaluation of IP3R3 abundance by immunocytochemistry in PDAC should be performed in a larger extent in order to validate the observation.

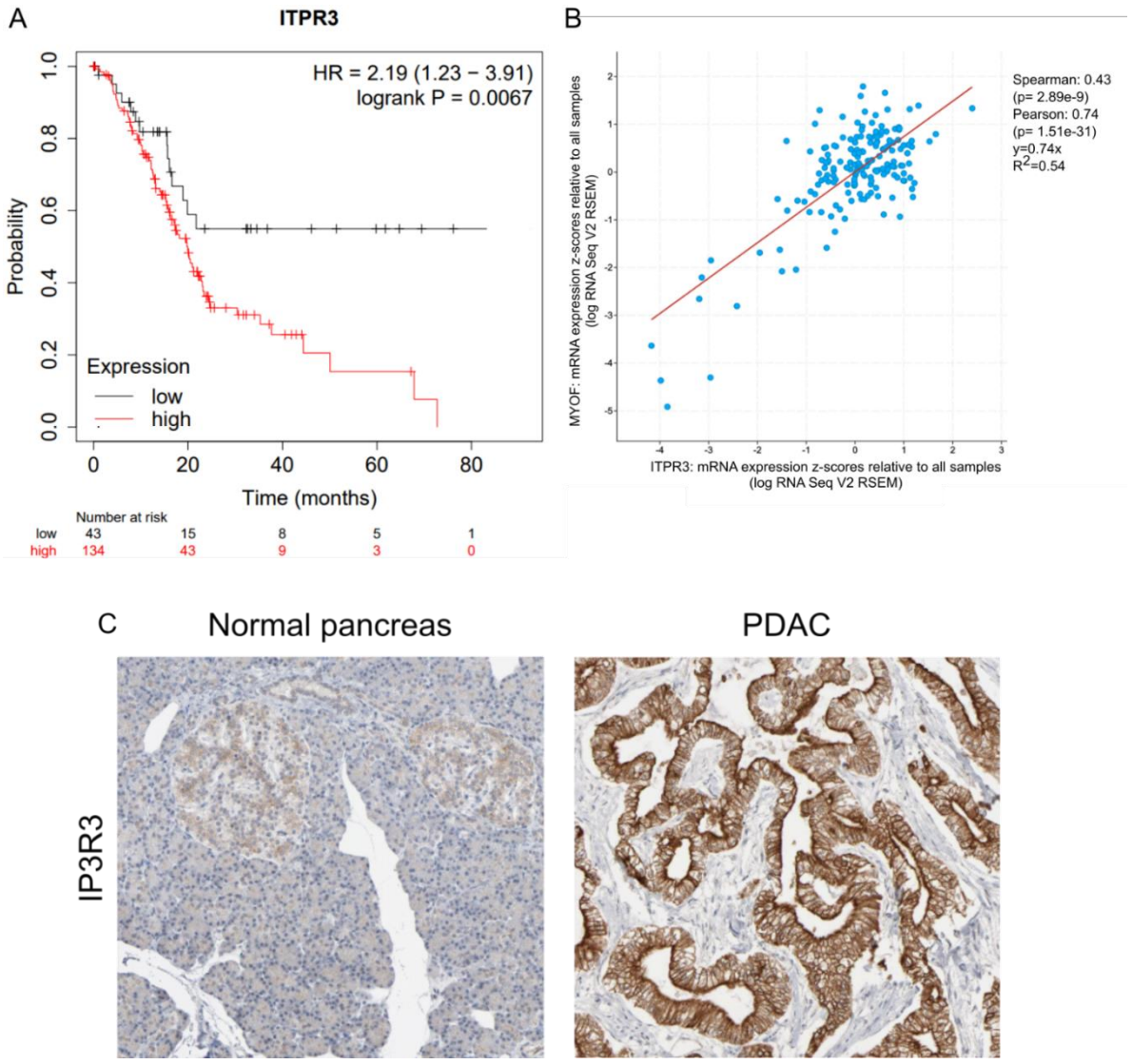

Figure 4-38. (A) Correlation between *ITPR3* expression and overall survival in PDAC patients. TCGA PanCancer Atlas data (http://cancergenome.nih.gov/) were analyzed for overall survival (n=177) according to their *ITPR3* gene expression. Patients with low expression of *ITPR3*, n=43. Patients with high expression of *ITPR3*, n=134. A Kaplan–Meier curve was established thanks to the Kaplan-Meier tool available online (https://kmplot.com) and a log-rank probability was calculated. **(B)** The mRNA expressions of *MYOF* and *ITPR3* were significantly correlated (R = 0.74) in PDAC patients. The data are from the TCGA PanCancer Atlas data (http://cancergenome.nih.gov/) **(C)** IP3R3 staining by immunocytochemistry in non-cancer (left, patient ID 2220) vs PDAC (right, patient ID 2650) tissues. The pictures are from the Human Protein Atlas (https://www.proteinatlas.org/).

4.2.9. Myoferlin expression is significantly correlated to *ITPR3* expression in pancreatic cancer but not in normal pancreas.

In order to further investigate the correlation between both proteins, we performed analyses from a second database, the ARCHS4, which comprises 238,522 human normalized sequencing samples (329). Thanks to the *Correlation AnalyserR* tool developed by Miller *et al.* in 2021, it is possible to assess Pearson's correlation between *MYOF* and every genes of the genome in normal and tumoral conditions (Figure 4-39) (330). The correlations between these genes and

MYOF are sorted in a histogram counting the number of occurrences of values within correlation bins. The red vertical lines represented on Figure 4-39A are the correlation values between *ITPR3* and *MYOF*. In the case of normal pancreas, the correlation value is close to 0 (Pearson's correlation R= 0.058), meaning that the two genes are almost uncorrelated. Conversely, in the pancreatic cancer, the linear correlation coefficient reached 0.612, meaning that both genes are positively correlated in pancreatic cancer. Figure 4-39B details the red lines from Figure 4-39A, where the scatterplot of the expressions of both genes is represented. Figure 4-39C depicts the simultaneous correlation between *ITPR3* and *MYOF* with the same genes. This allows us to assess their possible involvement in common pathways. In pancreatic cancer, we observe that genes correlated to *ITPR3* expression are also correlated to *MYOF* expression (R=0.82), which was not the case in normal pancreas (R=-0.097).

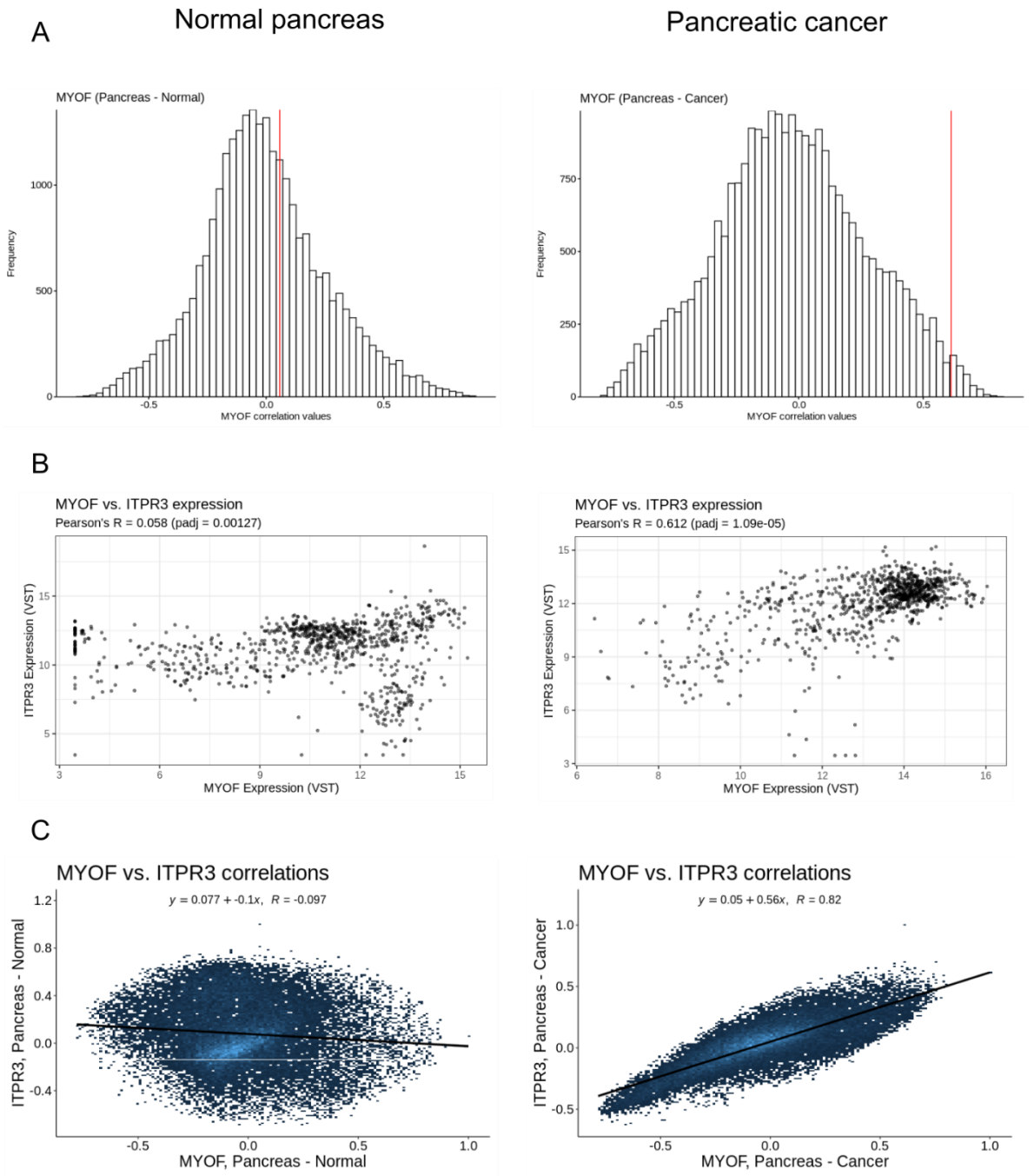

Figure 4-39. Correlation of myoferlin expression with *IT3R3* expression in normal and cancer pancreas, using the ARCHS4 database (276) and the Correlation AnalyserR tool (277). **(A)** Correlations between every genes of the genome and *MYOF* in normal and cancer pancreas are sorted in a histogram counting the number of occurrences of values within correlation bins. The red vertical lines represented are the correlation values between *ITPR3* and *MYOF*. **(B)** Scatterplots of the expressions of *MYOF* and *ITPR3* genes are represented. **(C)** Simultaneous correlation between *ITPR3* and *MYOF* with the same genes, allowing assessement in common pathways.

4.2.10. Investigation of myoferlin silencing on mitochondrial metabolism

We demonstrated above that myoferlin is located in MAMs, where it interacts with IP3R3, a protein involved in Ca^{2+} signaling. Interestingly, we showed that upon myoferlin silencing, Ca^{2+}

transfer between ER and mitochondria is impaired. Indeed, we showed that upon histamine stimulation and myoferlin silencing, the level of Ca^{2+} entering mitochondria is significantly reduced. Knowing that myoferlin silencing has been described in the literature as impacting mitochondrial metabolism and dynamics (47), we thought that the presence of myoferlin in MAMs could influence mitochondrial metabolism through Ca^{2+} signaling. Since Ca^{2+} is a cofactor of several enzymes of the TCA cycle, we decided to perform a WST1 assay to monitor mitochondrial dehydrogenase activity. We expected that myoferlin silencing would reduce their activity. Our results showed that upon myoferlin silencing, the activity of mitochondrial dehydrogenases was not impacted **(Figure 4-40A)**. Because Ca^{2+} is also a cofactor of the PDH phosphatase, we checked for an enhanced phospho-PDH/PDH ratio upon myoferlin silencing. Unfortunately, we observed discrepancy in the ratio between both Myof#1 and Myof#2 siRNA. Indeed, the ratio for the Myof#2 siRNA was equal to 0.3, while it was equal to 0.8 for the Myof#1 siRNA **(Figure 4-40B)**. Despite, the lack of effect of myoferlin depletion on dehydrogenase activity, and in accordance with the literature, we observed a decrease of mitochondrial respiration upon myoferlin silencing **(Figure 4-40C)** (47). This decrease of mitochondrial respiration was not associated with a reduced abundance of mitochondria. Indeed, we saw no variations of the abundance of TOM20 or the OMM 60 kDa proteins upon myoferlin silencing **(Figure 4-40D)** (see also MCU on **Figure 4-23**). Similarly, we checked the abundance of mitochondrial complexes and ATP synthase by western blot. Interestingly, no differences were observed upon myoferlin silencing **(Figure 4-40E)**. Finally, we investigated the level of phospho-AMPK and observed an increased phospho-AMPK/AMPK ratio in the Panc-1 cells transfected with Myof#1 siRNA. Conversely, the ratio was decreased when Myof#2 siRNA was transfected **(Figure 4-40B)**. This discrepancy did not allow us to propose any relationship between the impaired mitochondrial Ca^{2+} level and the mitochondrial metabolism modification. The role of myoferlin in relation to mitochondrial metabolism remains unclear and further investigations should be conducted.

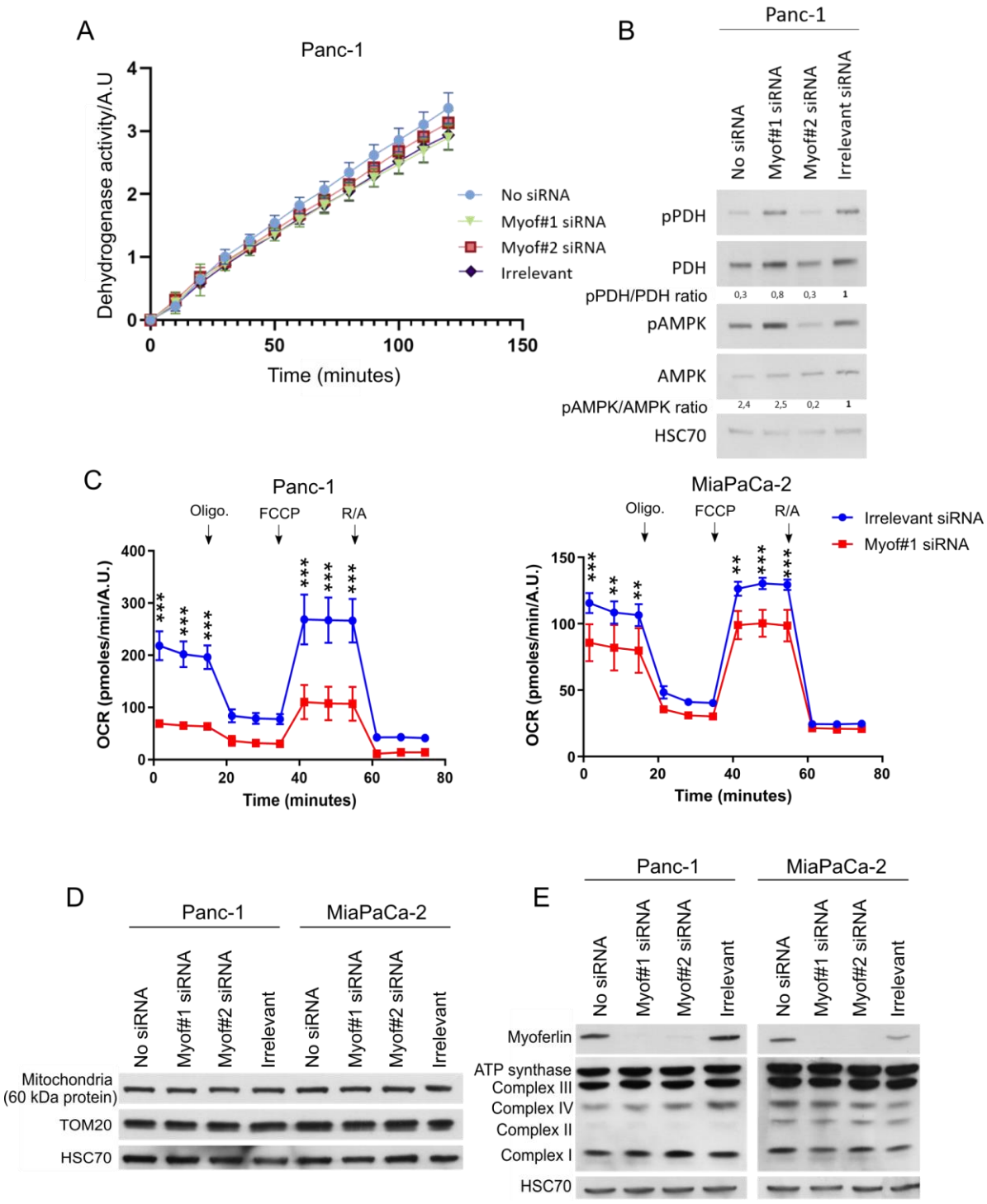

Figure 4-40. Investigation of a potential relationship existing between myoferlin silencing, mitochondrial metabolism and impaired Ca^{2+} transfer to mitochondria. **(A)** Impact of myoferlin silencing on mitochondrial dehydrogenases using a WST-1 assay in Panc-1 cells. This experiment is representative of three independent experiments. **(B)** Phospho-PDH/PDH and phospho-AMPK/AMPK ratios upon myoferlin silencing in Panc-1 cells. The experiment is representative of, at least, three biological replicates. **(C)** Myoferlin silencing decreases mitochondrial oxygen consumption rate (OCR) in Panc-1 and MiaPaCa-2. Oligomycin: Oligo. ; Rotenone/Antimycin A: R/A. This experiment confirms already published data (47). A two-way ANOVA was performed for statistical analyses. ***: p-value < 0.001, **: p-value < 0.01. **(D)** Abundance of TOM20 and a 60 kDa OMM protein upon myoferlin silencing in Panc-1 and MiaPaCa-2 cell lines. **(E)** Abundance of the ATP synthase and mitochondrial complexes upon myoferlin silencing in Panc-1 and MiaPaCa-2 cell lines.

4.2.11. Part II: limitations of the study

In this part of the *Results* section, we improved our procedure for colocalization, focusing on Manders' method (313). We tested our method in various situations: colocalization between TOM20 and myoferlin, between the fusion protein encoded by the CMV-Mito-R-GECO-1 plasmid and the MitoTracker Green probe or between myoferlin and IP3R3. Each time, the percentage of colocalization seemed in adequation with the visual colocalization, demonstrating the strength of our method. For instance, the colocalization between the fusion protein encoded by the CMV-Mito-R-GECO-1 and the MitoTracker Green probe showed almost 100% of colocalization, which was in accordance with the visual colocalization **(Figure 4-17)**. Nevertheless, it is worth mentioning that few cells were analyzed for this experiment since the purpose was to test the method in various situations rather than performing robust colocalization studies. We also used randomized pictures as a negative control **(Figure 4-13)**. Analyses on such a control represent the colocalization in noisy conditions. In the future, it might be interesting to include a biological negative control, using for instance, an IMM protein.

In this study, we performed cell fractionation and we identified myoferlin as being present in the PMAMs fraction of both Panc-1 and MiaPaCa-2 cell lines **(Figure 4-16)**. We used many markers to validate the extracts, such as MAMs, cytosolic, mitochondrial and ER markers. Nevertheless, our interpretation of the results remains limited since we did not check for representative markers of, for instance, the Golgi apparatus or the lysosomes. Indeed, what is the abundance of these markers in ours fractions? Is our PMAMs fraction contaminated by those organelles? Since myoferlin has been described in the Golgi apparatus and the lysosomes of PDAC cell lines, answering those questions could be valuable for the interpretation of the cell fractionation experiments. However, since we used a very similar protocol than the one described in the publication of Vance in 1989, we could expect a minor contamination for the plasma membrane, Golgi apparatus, peroxisomes and lysosomes in our PMAMs fraction (116).

Our results showed that the transfer of Ca^{2+} to mitochondria was impaired upon myoferlin silencing and histamine stimulation **(Figure 4-19)**. In order to understand this phenomenon, we investigated several leads such as the ER integrity or the ERMICC. We finally found an interaction between myoferlin and a key protein involved in Ca^{2+} transfer at MAMs. We think this interaction might be biologically relevant and might contribute to Ca^{2+} transfer at MAMs. Nonetheless, we did not investigate whether the trafficking for the histamine receptors was

impacted by myoferlin silencing. Even if myoferlin silencing was suggested to only impact RTK trafficking, whether histamine receptors are impacted by myoferlin silencing should be investigated (275).

Finally, in this part of the *Results* section, some experiments were performed only once, such as the co-immunoprecipitation of IP3R3 with myoferlin from PMAMs extracts **(Figure 4-37)**. Therefore, even if we believe in those results, especially since we also observed a co-immunoprecipitation for those proteins from whole cell lysates, we should keep in mind that this experiment was performed only once. Similarly, the results relative to the analyses of TEM images for the ERMICC should be taken with caution since the data set was limited and the pictures were representative of MAMs, meaning that they were not taken randomly **(Figure 4-27).**

4.2.12. Part II: conclusions and discussion

In this part of our work, we aimed at clarifying myoferlin localization in relation to mitochondria. We demonstrated that myoferlin was unlikely to be located on this organelle but rather localized in the membranes in contact with mitochondria. In accordance with our findings, proteomic analyses did not detect myoferlin in human mitochondria (331–333). In addition, our results were supported by previous investigations performed in our lab. Indeed, for the purpose of supporting this work and discussion, Pr. Marc Thiry and Dr. Arnaud Blomme generously provided TEM pictures, where myoferlin was labelled by immunogold in breast cancer cell line (MDA-MB-231). As shown on **Figure 4-41**, signals corresponding to myoferlin labeling (yellow arrow) were found next to mitochondria.

In addition to the discovery of myoferlin as a MAMs component, we found that silencing this protein impairs Ca^{2+} transfer to mitochondria. In this context, we highlighted a proximity existing between myoferlin and key proteins involved in Ca^{2+} signaling at MAMs, such as IP3R3, VDAC1 and, to a lower extent, GRP75. Furthermore, by immunoprecipitation of IP3R3 from pure MAMs fraction, we demonstrated a physical interaction of IP3R3 with myoferlin in Panc-1 cell line.

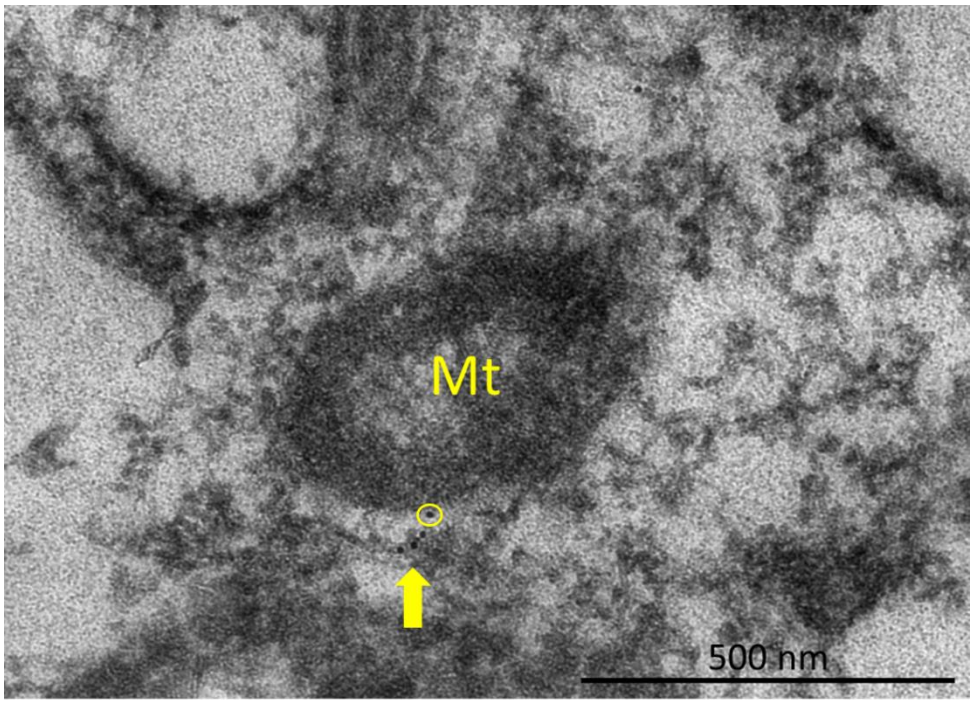

Figure 4-41. TEM picture showing a mitochondrion (Mt) with myoferlin labeling by immunogold in its proximity (showed by yellow arrow) in MDA-MB-231. One dot corresponding to myoferlin labeling is circled in yellow. The picture was provided by the Pr. Marc Thiry and Dr. Arnaud Blomme. The technical details are provided in the article of Blomme *et al.* (2017) (49).

We don't know yet if this interaction is direct or indirect. Nevertheless, we think that myoferlin is probably part of a protein complex located in MAMs that involves proteins related to Ca^{2+} signaling. Indeed, in their article published in 2021, Szczesniak *et al.* identified myoferlin as being part of the interactome of the BCL-2 related ovarian killer (BOK), a protein involved in Ca^{2+} signaling at MAMs (334). This member of the BCL-2 family interacts and protects IP3Rs from degradation (334). In addition, myoferlin has been shown to interact with STAT3, which acts as a gatekeeper for ER-mitochondria Ca^{2+} fluxes (279,335,336). Interestingly, in their study published in 2020, Su *et al*. showed that STAT3 was located in MAMs rather than on mitochondria, in opposition with the previous paradigm (337). Another component of this potential protein complex might be VDAC1. In the literature, myoferlin interaction with VDAC1 has already been reported (338). In addition, in our study, we observed strong signals for the PLA between myoferlin and VDAC1. However, we failed at immunoprecipitating this protein. Therefore, it does not allow us to draw conclusions about the interaction of VDAC1 with myoferlin. Further investigations are needed to understand myoferlin interactome at MAMs. This might provide precious information about myoferlin functions in this subcellular region.

GENERAL CONCLUSION AND DISCUSSION

5. General conclusion and discussion

5.1. Myoferlin localization with respect to mitochondria

Myoferlin has been shown to influence mitochondrial respiration and network in pancreatic and breast cancers (47,49). The mechanism by which myoferlin silencing impacts mitochondrial metabolism and dynamics is still unknown today. However, having a better understanding of myoferlin in cancer biology is essential, especially since myoferlin has been introduced as a potential therapeutic target (45,46). It is now known that, even if mitochondrial respiration is often repressed in cancer cells, it remains perfectly functional and even contributes to cancer progression (51,339). In PDAC, mitochondria have been associated with cancer relapse, cell proliferation, tumor growth and resistance to chemotherapy (61–63,319,339,340). Moreover, mitochondrial-targeting through inhibition of complex I by phenformin or metformin has shown strong anti-tumoral effects in *in vitro* and *in vivo* models of PDAC (341–343). However, the mechanism of action of metformin or phenformin remains controversial and might also be related to mechanisms independent of complex I inhibition (344). Due to the lack of specificity and to associated side effects of these compounds, studying proteins, such as myoferlin, could constitute another approach to target mitochondria in cancer. Indeed, myoferlin targeting has been shown by our team to decrease mitochondrial respiration in PDAC cell lines, inducing a glycolytic switch (47). In addition, PDAC cells displaying a high metastatic potential and a high OXPHOS capacity have increased expression of myoferlin (48). In the literature, no mechanistic explanations have been proposed regarding myoferlin function in a mitochondrial context. However, having a better comprehension of the mechanisms linking this protein to mitochondrial function could provide new insights about safety and efficacy of myoferlin targeting. As a first attempt to understand the mechanisms by which myoferlin influences mitochondria, we aimed at clarifying myoferlin localization in relation to this organelle. Indeed, there are no publications treating this matter. In this work, **we demonstrated that myoferlin is unlikely to be located on mitochondria of PDAC cell lines, but rather in MAMs.** Our findings suggest that myoferlin may influence mitochondrial function thanks to this specific location. Knowing that myoferlin is located in MAMs may open new insights about myoferlin function.

Myoferlin localization in MAMs is supported by the literature. Indeed, several proteomic studies have been performed on MAMs from various tissues and species (95,119–

121,345,346). Six notable reports and their findings are summarized in Table 4. Myoferlin was found in six out of the eight sample types. It was detected in MAMs from human skin fibroblasts, human and rat skeletal muscles, rat heart, human testis and human liver (119–121,345), while myoferlin paralog, dysferlin, was only found in MAMs of human liver as well as human and rat skeletal muscles (119–121). Interestingly, myoferlin and dysferlin were not detectable when the study was performed on mouse samples (95,345). The discrepancy observed between these proteins could be explained by their potential functions in MAMs but also by their expression pattern in various tissues. Further investigations looking at the ferlin family members in MAMs could be of interest, opening new insights about ferlin functions.

Species	Material	Pathology	Myoferlin detection (Yes/No)	Dysferlin detection (Yes/No)	Authors	Date of publication
Human	Skin fibroblasts (culture)	None	Yes	No	Zhang *et al.*(120)	2011
Human	Liver (culture)	Carcinoma vs Non-cancer cells	Yes	Yes	Horner *et al.*(119)	2015
Mouse	Liver	None	No	No	Sala-Vila *et al.* (95)	2016
Human	Skeletal muscle	Type-2 dia-betes	Yes	Yes	Chae *et al.*(346)	2018
Human	Testis	None	Yes	No	Wang *et al.*(345)	2018
Mouse	Testis, brain		No	No		
Rat	Skeletal muscle	None	Yes	Yes	Lu *et al.*(121)	2022
	Heart		Yes	No		

Table 4. Assessment of myoferlin and dysferlin presence from proteomic studies performed on MAMs with different materials and species. The studies are classified by year of publication.

5.2. Myoferlin silencing and calcium transfer at MAMs

Owing to the relationship existing between Ca^{2+} transfer at MAMs and mitochondrial metabolism, we thought that the impact of myoferlin depletion on mitochondrial metabolism could be related to an alteration of Ca^{2+} transfer at MAMs. Interestingly, **our results showed that upon myoferlin silencing, the level of Ca^{2+} entering mitochondria is drastically reduced (Figure 4-19)**. Since myoferlin has been described as being part of the secretory pathway (242), we verified that this reduction was not the result of a loss of ER integrity. Indeed, impaired ER might not be able to deliver properly Ca^{2+} to mitochondria. We found neither impaired ER

morphology nor inducement of ER stress, invalidating this hypothesis (Figure 4-21 and Figure 4-22). Nevertheless, since our results remain indirect, further investigations about ER Ca^{2+} storage using plasmids, such as the CMV-ER-LAR-GECO1 plasmid (306), must be conducted.

To further explore the cause of the reduced Ca^{2+} transfer to mitochondria, we evaluated the abundance of proteins related to Ca^{2+} signaling at MAMs. We found no major variations in the protein abundance upon myoferlin silencing (Figure 4-23). It is worth mentioning that the protein abundance was estimated from whole cell lysate and not MAMs extract, which could bias the results. Indeed, myoferlin silencing might impair protein distribution and abundance at MAMs without impacting global abundance. Despite this limitation, we concluded that myoferlin was not impacting abundance of proteins related to Ca^{2+} signaling at MAMs. In the future, it might be interesting to re-perform this experiment from MAMs extracts and to check whether the protein abundance varies upon myoferlin silencing by western blot or by mass spectrometry.

In this work, the IP3R3-VDAC1 proximity was not altered by myoferlin silencing (Figure 4-30). Since we demonstrated an interaction between myoferlin and IP3R3, those results suggest that myoferlin depletion probably impacts Ca^{2+} transfer at MAMs through the regulation of proteins involved in this process rather than by impacting stability or proximity of the VDAC1-IP3R3 axis. In the future, it would be interesting to identify whether the impaired Ca^{2+} transfer occurs on the ER or on the mitochondria side. Indeed, is it a defect in Ca^{2+} release by ER or in Ca^{2+} uptake by mitochondria, or is it the entire axis which is impacted?

Conducting ultrastructural analyses, we assessed the physical contacts existing between ER and mitochondria. We observed no significant changes for the ERMICC upon myoferlin silencing (Figure 4-27). As mentioned previously, those results should be considered carefully due to the data set used for analyses. Complementary micrometric analyses obtained from a larger data set and provided by Pr. Marc Thiry (Figure 7-2), highlighted a trend upon myoferlin silencing: the ERMICC tends to increase upon myoferlin silencing, which seems in contradiction with our hypothesis. Indeed, based on the literature, we expected that the importance of contacts would be reduced, explaining the decreased mitochondrial Ca^{2+} uptake observed upon myoferlin silencing (82). However, since other factors, like protein interactions, might also influence Ca^{2+} dynamics, the ERMICC is not necessarily correlated with the amplitude of the Ca^{2+} transfer. In addition, since upon myoferlin silencing, less Ca^{2+} is transferred to

mitochondria, a compensatory effect could arise and increase the ERMICC. To date, it is difficult to draw definitive conclusions about the impact of myoferlin silencing on ER-mitochondria contact sites. We are currently in collaboration with Dr.Yamanaka and his team (Nagoya university, Japan) who accepted to provide us their pMAMtracker-green and PMAMtracker-Luc plasmids (124). These will constitute new tools for our lab to study the effect of myoferlin silencing on MAMs. Indeed, those plasmids allow high throughput screening and quantification of MAMs in living cells. In addition, such plasmids are suitable to assess MAMs dynamics over time, which represents an advantage regarding TEM. As a matter of fact, TEM allows powerful visualization of MAMs, even though image analyses are time consuming and cannot be performed in living cells.

5.3. Myoferlin, calcium transfer and mitochondrial metabolism

Since we demonstrated that myoferlin silencing reduces the Ca^{2+} level inside mitochondria upon stimulation, we thought it could impact mitochondrial metabolism (347,348). Thus, we assessed the mitochondrial dehydrogenase activity, AMPK activation and mitochondrial respiration. In accordance with the literature, mitochondrial respiration was reduced upon myoferlin silencing (47). Unfortunately, we observed discrepancies for phospho-AMPK/AMPK and for phospho-PDH/PDH ratios between Myof#1 and #2 siRNA. In addition, we noticed no impact of myoferlin silencing on mitochondrial dehydrogenase activity, which was in contradiction with previously published results **(Figure 4-40)** (47,49). Taken together, **those results do not allow us to draw conclusions about the impact of myoferlin silencing, related to Ca^{2+} signaling, on mitochondrial metabolism**. Nevertheless, as mentioned previously, myoferlin might have more than one function related to MAMs and the effect of myoferlin silencing on mitochondria is probably influenced by other functions of myoferlin in the cell, such as the endosomal trafficking (244,245). In fact, myoferlin silencing might impact diverse pathways, affecting mitochondrial function.

5.4. Myoferlin and mitochondrial dynamics: from the perspective of MAMs

Our results upon myoferlin silencing showed a decrease in mitochondrial Ca^{2+} uptake and mitochondrial respiration **(Figure 4-19 and Figure 4-40)**, which is in accordance with the literature (47,349). Indeed, Ca^{2+} has been described as a cofactor of TCA cycle enzymes, which could explain our previously mentioned results (350). Nevertheless, since Ca^{2+} is involved in

mitochondrial dynamics (351,352), the fragmented network observed upon myoferlin silencing is puzzling (see Figure 7-7 for mitochondrial network upon myoferlin silencing or targeting). Indeed, this feature is often observed upon calcium overload in mitochondria (141). Nevertheless, this discrepancy with the literature might be explained by other potential functions of myoferlin. Indeed, in the present work, we only investigated myoferlin in relation to Ca^{2+} transfer. We should keep in mind that the impact of myoferlin silencing on MAMs is probably more complex and may encompass several phenomena. For instance, we showed that myoferlin interacts with MFNs. However, we do not know yet to which function this interaction might be related to.

It is only in the last few years that interest in MAMs for mitochondrial fusion has emerged. For instance, in their article published in 2020, Abrisch *et al*. showed that ~ 90% of fusion events occur at ER-mitochondria contact sites, involving MFNs (144). They also showed that fusion and fission events can occur at the same MAMs spot, suggesting that both machineries could be concomitantly present. In addition, since they showed that fusion and fission events can occur at the same spot, proteins involved in both machineries may exist. Therefore, perhaps myoferlin plays a role in mitochondrial fusion and/or fission through its interaction with MFNs. In their article, Abrisch *et al.* also discussed a potential protein machinery present in MAMs, able to promote a high membrane curvature, leading to fusion and fission events. They suggested that this machinery would be recruited at MAMs due to the particular lipid composition, similar to plasma membrane lipid rafts. They also mentioned that this potential machinery could be activated by Ca^{2+} to modulate fusion and fission events (144). Interestingly, myoferlin has been shown to be enriched in plasma membrane lipid rafts where it plays a role in vesicular fusion (245,246). In addition, myoferlin displays a rare structure with multiple C2 domains able to bind Ca^{2+} (266). In their study, Marty *et al.* showed that myoferlin is able to actively sculpt phospholipid bilayers (266). This activity is enhanced by the presence of Ca^{2+} and negatively charged phospholipids such as phosphatidylserine. The authors suggested that this capacity to sculpt lipid bilayers could facilitate membrane fusion and fission. Therefore, our discovery about myoferlin presence in MAMs and its interaction with MFNs in PDAC might open new insights about a potential role of myoferlin in mitochondrial dynamics at ER-mitochondria contact sites, through a Ca^{2+}-dependent sculpture of the membranes.

In addition, myoferlin has been reported as being part of a protein complex involving RAB32, a protein described as a MAMs component, playing a role in mitochondrial fission (45). RAB32 prevents mitochondrial fission by phosphorylation of DRP1 and its silencing results in mitochondrial fragmentation and a decreased mitochondrial respiration (45). Myoferlin targeting has been shown to dissociate the RAB32-myoferlin complexes, which has been proposed as a mechanism explaining the impact of myoferlin targeting on mitochondria (45). The relationship/localization between RAB32 and myoferlin remained unclear. However, our work may suggest an interaction between these proteins in MAMs.

5.5. Considerations about other potential functions for myoferlin in MAMs

An observation, reported by our team, is the presence of altered mitochondria upon myoferlin silencing (302). The number of altered mitochondria is higher in myoferlin-silenced cells compared to non-silenced cells (302). Additionally, since we frequently observed contacts between ER and altered mitochondria, it might be interesting to check whether those altered mitochondria display more ER-mitochondria contact sites and whether the ERMICC is increased (Figure 7-6). Indeed, MAMs have been involved in mitophagy (196,198) and it has been recently reported that myoferlin targeting by WJ460 triggers this process (302). Therefore, myoferlin targeting could modulate mitophagy through a modification of its localization or interaction inside MAMs. An approach to study the role of myoferlin in mitophagy regulation would be to induce mitophagy in control or myoferlin-silenced cells and to monitor their capacity to deal with this process. This could constitute a lead to understand the mechanism linking myoferlin to mitophagy in PDAC.

Another interesting concern about a potential function of myoferlin in MAMs is related to its participation to lipid transfer and thus, to mitochondrial membrane integrity. Indeed, it has been reported that lipid transfers are essential for mitochondrial function (183). In 2016, Sala-Vila *et al.* have identified CAV1 to be enriched in MAMs of healthy mouse livers (95). While its absence leads to a mitochondrial fragmented network, similar to the one observed upon myoferlin silencing (Figure 7-7), proteomic studies performed on MAMs extracts from CAV1 knock-out mice showed a reduced amount of proteins involved in steroid metabolism and cholesterol biosynthesis (95). In addition, the absence of CAV1 has been reported to induce an accumulation of cholesterol in mitochondrial membranes, leading to the organelle dysfunction

(192). Interestingly, myoferlin has been shown to colocalize and form a complex with CAV1 in many studies (45,49,244,276,353). In breast cancer, myoferlin silencing impairs caveolin oligomerization and increases the level of free fatty acids, raising questions about myoferlin and lipid homeostasis (49,244). Thus, it would be interesting to establish whether myoferlin interacts with CAV1 in MAMs. Through this interaction, myoferlin might modulate lipid transfer to mitochondria.

5.6. Cell metabolic profile: is there a relationship with MAMs?

During our investigations, we noticed differences between Panc-1 and MiaPaCa-2 cell lines. First, we observed that IP3R3 was enriched in the pure MAMs fraction of Panc-1, while it was not in MiaPaCa-2 **(Figure 4-28)**. Then, we saw that the bands corresponding to myoferlin co-immunoprecipitating with IP3R3 were visible after a longer exposure in MiaPaCa-2 than in Panc-1 cells **(Figure 4-34)**. This difference suggests that a higher amount of IP3R3 was interacting with myoferlin in Panc-1 cell line. Additionally, in Panc-1, **myoferlin colocalized with IP3R3 clusters** but also outside those regions, while in MiaPaCa-2, myoferlin colocalization with IP3R3 drastically dropped outside of the clusters **(Figure 4-36)**. Finally, the peak of fluorescence upon histamine stimulation was significantly lower in MiaPaCa-2 than in Panc-1 cell line **(Figure 4-20)**. The difference observed upon histamine stimulation in both cell lines could be explained by a distinct sensitivity in response to histamine. Indeed, MiaPaCa-2 and Panc-1 cells lines may express distinct levels of histamine receptors. Nonetheless, the overmentioned differences could also be explained by the metabolic profile of those cell lines. Indeed, Panc-1 and MiaPaCa-2 cell lines have been classified according to their metabolic signature (57). For instance, Panc-1 has been classified as a lipogenic cell line, relying mainly on mitochondrial respiration and lipid synthesis (57). On the other hand, MiaPaCa-2 cell line has been reported as glycolytic (57). Thus, the differences observed between both cell lines may be related to their metabolism, MiaPaCa-2 relying less on mitochondria and thus, on MAMs. Therefore, our results could be further extended to additional cell lines belonging to these subtypes.

Since myoferlin has been shown to be overexpressed in a restricted panel of cancers (see *Myoferlin in cancer* section), its interaction with IP3R3 may be specific to these types of cancer or, as we saw for MiaPaCa-2 and Panc-1, to some metabolic profiles (57). Moreover, this

interaction might confer metabolic advantages to cancer cells since both proteins interact and are associated with cancer progression (46,64,302,354) (Figure 4-34 and Figure 4-39).

5.7. Extension to other cancers and non-cancer tissues

Our discoveries were obtained from PDAC cell lines and should be extended on other tumors and on non-cancer tissues. Indeed, in the first part of this work, we did not find an interaction between myoferlin and MFNs in non-cancer cells (Figure 4-8 and Figure 4-9). The confirmation of this cancer-specific interaction, eventually extended to our whole results, could provide clues about a myoferlin specific function in cancers. It is worth mentioning that myoferlin targeting in non-cancer cells such as HPNE had no impact on mitochondrial network, suggesting different mechanisms involved in cancer vs non-cancer cells (302). In this context, knowing that myoferlin was interacting with MFNs only in PDAC cell lines also raises interest.

Additionally, it might be interesting to investigate the presence of myoferlin in MAMs of other cancers and of non-cancer tissues. Indeed, is myoferlin present in MAMs of non-cancer cells? Is it interacting with IP3Rs in those cells and is the interactome similar to the one of cancer cells? Answering those questions might help to understand the physiological functions of myoferlin. For instance, myoferlin has been involved in myoblast differentiation and its expression is dependent on NFAT (240,246,256). Interestingly, IP3R1 has also been involved in myoblast differentiation, where it downregulates NFAT (355). Therefore, a relationship between those two proteins might exist. Furthermore, myoferlin is involved in adipocyte differentiation and maturation. Upon a high fat diet, myoferlin contributes to excessive adipogenesis and obesity, which is accentuated by a decreased energy expenditure (356). Since MAMs have been associated with adipocytes metabolism (167), studying myoferlin and MAMs in this context could be of interest.

5.8. Contributions of other myoferlin localizations within the cell

Myoferlin has been reported on various localizations in the cell such as plasma membrane, late and early endosomes, lysosomes, exosomes, Golgi apparatus and ER (240,242,243,254). Therefore, the proximity observed between myoferlin and VDAC1, IP3R3 or GRP75 could reflect several localizations of myoferlin within the cell (Figure 5-1). For instance, myoferlin has been described on lysosomes of PDAC cell lines (243). Since lysosomes have been shown to be in contact with mitochondria and ER, it is conceivable that those contacts participate to the

observations presented in this work (78,178,357,358). Indeed, it is known that Ca^{2+} transfer also occurs between lysosomes and ER as well as mitochondria (178,357). This transfer involves proteins also found in MAMs such as IP3Rs and VDAC1 (178) **(Figure 5-1)**. Therefore, the presence of myoferlin in other cellular localizations probably contributes to some of our observations.

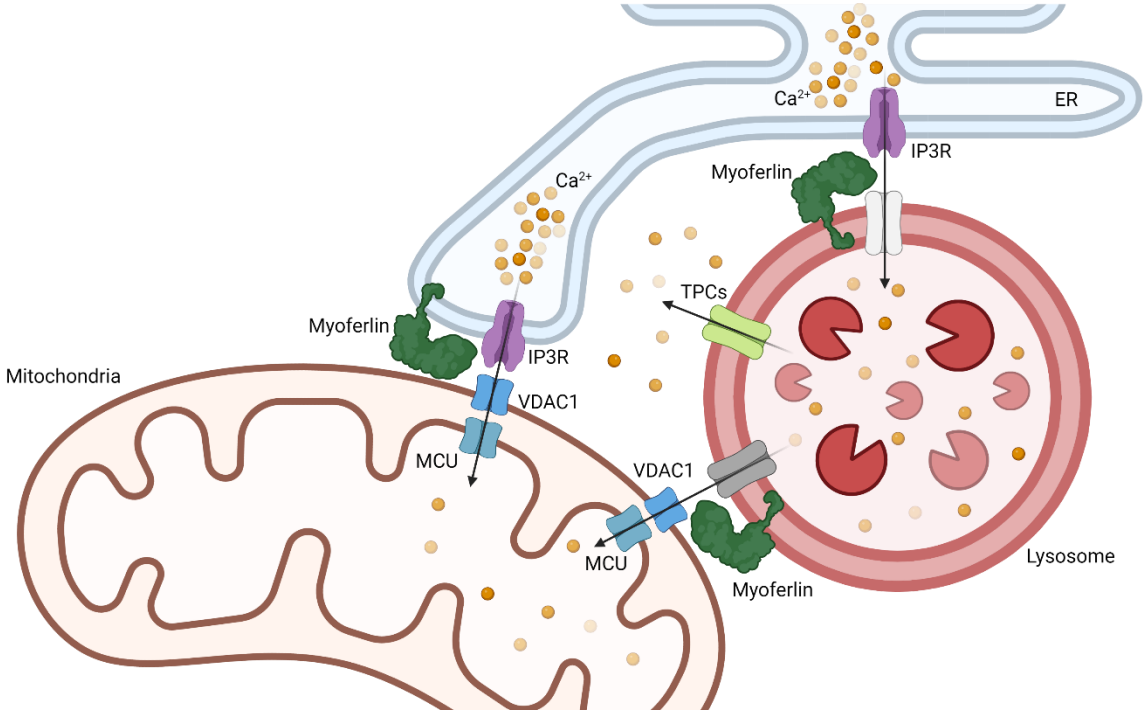

Figure 5-1. The proximity observed between myoferlin and proteins involved in Ca^{2+} transfer, such as VDAC1 or IP3R3 could be explained by other locations for myoferlin within the cell. For instance, lysosomes have been reported to interact with mitochondria and ER, where it participates to Ca^{2+} transfer. This transfer involves proteins such as VDAC1 or IP3Rs. Since myoferlin has been shown to be on lysosomes of PDAC cell lines, the proximity observed between myoferlin and IP3R3 or VDAC1 could be explained, in part, by its localization on lysosomes. This picture is adapted from Castro *et al.* (2021) (178).

Furthermore, we identified myoferlin as colocalizing with IP3R3 clusters in the perinuclear regions **(Figure 4-36)**. A previous report has described IP3Rs cluster formation to increase Ca^{2+} release efficiency (359). Why myoferlin colocalizes with IP3R3 clusters and whether those clusters are part of MAMs remain a mystery. **We showed that myoferlin interacts with IP3R3** in MAMs **(Figure 4-37)**. However, myoferlin may also interact with IP3R3 outside of MAMs, triggering ER Ca^{2+} release. Investigation of myoferlin interaction with other IP3Rs, such as IP3R1, could also be interesting, especially since IP3R1 has been associated with autophagy and cancer progression in PDAC (360). Interestingly, preliminary results show a visual colocalization between myoferlin and IP3R1 at the cell periphery **(Figure 7-5)**.

5.9. Therapeutic perspectives

In combination with other treatments (such as glycolysis inhibitors) and by considering the genetic and metabolic background of the tumor, targeting mitochondria in cancer seems to be a promising therapeutic strategy (341–343). In this context, myoferlin, a protein overexpressed in PDAC compared to normal tissues, where it is barely detectable, has been proposed as a potential therapeutic target (301). Indeed, myoferlin targeting in PDAC has been shown to reduce tumor growth and metastasis in mouse models (301). Even if myoferlin targeting or silencing impacts many functions in the cell such as the receptor trafficking, its influence on mitochondrial metabolism seems to contribute to cancer aggressiveness (48,244). In this study, we found that myoferlin is located in MAMs, where it contributes to Ca^{2+} transfer, probably through its interaction with IP3R3. Of course, further investigations should be performed to clarify the roles of myoferlin in MAMs. Nevertheless, since IP3R3 has been shown to be overexpressed in many cancers and to participate to cancer progression, the development of specific compounds able to dissociate myoferlin-IP3R3 interaction could constitute a clue for future targeted therapies (68,70,216). This would allow targeting of a restricted number of myoferlin functions, with potentially a stronger effect on cancer cells due to the overexpression of both IP3R3 and myoferlin.

References

6. References

1. Leung PS. The Renin-Angiotensin System: Current Research Progress in The Pancreas: The RAS in the Pancreas [Internet]. Dordrecht: Springer Netherlands; 2010 [cited 2022 Sep 14]. (Advances in Experimental Medicine and Biology; vol. 690). Available from: http://link.springer.com/10.1007/978-90-481-9060-7

2. Karpińska M, Czauderna M. Pancreas—Its Functions, Disorders, and Physiological Impact on the Mammals' Organism. Frontiers in Physiology [Internet]. 2022 [cited 2022 Sep 13];13. Available from: https://www.frontiersin.org/articles/10.3389/fphys.2022.807632

3. Ibrahim Abdalla MM. Ghrelin – Physiological Functions and Regulation. Eur Endocrinol. 2015 Aug;11(2):90–5.

4. Mastracci TL, Sussel L. The Endocrine Pancreas: insights into development, differentiation and diabetes. Wiley Interdiscip Rev Membr Transp Signal. 2012;1(5):609–28.

5. Bengtsson A, Andersson R, Ansari D. The actual 5-year survivors of pancreatic ductal adenocarcinoma based on real-world data. Sci Rep. 2020 Oct;10(1):16425.

6. Rawla P, Sunkara T, Gaduputi V. Epidemiology of Pancreatic Cancer: Global Trends, Etiology and Risk Factors. World J Oncol. 2019 Feb;10(1):10–27.

7. Khalaf N, El-Serag HB, Abrams HR, Thrift AP. Burden of Pancreatic Cancer: From Epidemiology to Practice. Clinical Gastroenterology and Hepatology. 2021 May;19(5):876–84.

8. Lambert A, Schwarz L, Borbath I, Henry A, Van Laethem JL, Malka D, et al. An update on treatment options for pancreatic adenocarcinoma. Ther Adv Med Oncol. 2019 Aug;11:1–43.

9. Klein AP. Pancreatic cancer epidemiology: understanding the role of lifestyle and inherited risk factors. Nat Rev Gastroenterol Hepatol. 2021 Jul;18(7):493–502.

10. Hu JX, Zhao CF, Chen WB, Liu QC, Li QW, Lin YY, et al. Pancreatic cancer: A review of epidemiology, trend, and risk factors. World J Gastroenterol. 2021 Jul;27(27):4298–321.

11. Molina-Montes E, Van Hoogstraten L, Gomez-Rubio P, Löhr M, Sharp L, Molero X, et al. Pancreatic Cancer Risk in Relation to Lifetime Smoking Patterns, Tobacco Type, and Dose-Response Relationships. Cancer Epidemiol Biomarkers Prev. 2020 May;29(5):1009–18.

12. Larsson SC, Wolk A. Red and processed meat consumption and risk of pancreatic cancer: meta-analysis of prospective studies. Br J Cancer. 2012 Jan;106(3):603–7.

13. Zheng J, Stuff J, Tang H, Hassan MM, Daniel CR, Li D. Dietary N-nitroso compounds and risk of pancreatic cancer: results from a large case-control study. Carcinogenesis. 2019 Apr;40(2):254–62.

14. Klein AP, Brune KA, Petersen GM, Goggins M, Tersmette AC, Offerhaus GJA, et al. Prospective Risk of Pancreatic Cancer in Familial Pancreatic Cancer Kindreds. Cancer Research. 2004 Apr;64(7):2634–8.

15. Vincent A, Herman J, Schulick R, Hruban RH, Goggins M. Pancreatic cancer. Lancet. 2011 Aug;378(9791):607–20.

16. Orth M, Metzger P, Gerum S, Mayerle J, Schneider G, Belka C, et al. Pancreatic ductal adenocarcinoma: biological hallmarks, current status, and future perspectives of combined modality treatment approaches. Radiation Oncology. 2019 Aug;14(1):141.

17. Malinova A, Veghini L, Real FX, Corbo V. Cell Lineage Infidelity in PDAC Progression and Therapy Resistance. Frontiers in Cell and Developmental Biology. 2021 Dec;9:795251.

18. Daoud AZ, Mulholland EJ, Cole G, McCarthy HO. MicroRNAs in Pancreatic Cancer: biomarkers, prognostic, and therapeutic modulators. BMC Cancer. 2019 Nov;19(1):1130.

19. Buscail L, Bournet B, Cordelier P. Role of oncogenic KRAS in the diagnosis, prognosis and treatment of pancreatic cancer. Nat Rev Gastroenterol Hepatol. 2020 Mar;17(3):153–68.

20. Mao Z, Xiao H, Shen P, Yang Y, Xue J, Yang Y, et al. KRAS(G12D) can be targeted by potent inhibitors via formation of salt bridge. Cell Discov. 2022 Jan 25;8(1):1–14.

21. Wang L, Xie D, Wei D. Pancreatic Acinar-to-Ductal Metaplasia and Pancreatic Cancer. Methods Mol Biol. 2019;1882:299–308.

22. Lee AYL, Dubois CL, Sarai K, Zarei S, Schaeffer DF, Sander M, et al. Cell of origin affects tumour development and phenotype in pancreatic ductal adenocarcinoma. Gut. 2019 Mar;68(3):487–98.

23. Ferreira RMM, Sancho R, Messal HA, Nye E, Spencer-Dene B, Stone RK, et al. Duct- and Acinar-Derived Pancreatic Ductal Adenocarcinomas Show Distinct Tumor Progression and Marker Expression. Cell Rep. 2017 Oct;21(4):966–78.

24. Walter FM, Mills K, Mendonça SC, Abel GA, Basu B, Carroll N, et al. Symptoms and patient factors associated with diagnostic intervals for pancreatic cancer (SYMPTOM pancreatic study): a prospective cohort study. The Lancet Gastroenterology & Hepatology. 2016 Dec;1(4):298–306.

25. Paye A. Manuel oncologique: Cancer du pancrés. CHU de Liège: Institut de cancérologie; 2018 May p. 1–38.

26. Cong L, Liu Q, Zhang R, Cui M, Zhang X, Gao X, et al. Tumor size classification of the 8th edition of TNM staging system is superior to that of the 7th edition in predicting the survival outcome of pancreatic cancer patients after radical resection and adjuvant chemotherapy. Sci Rep. 2018 Jul;8(1):10383.

27. Suto H, Okano K, Oshima M, Ando Y, Takahashi S, Shibata T, et al. The predictors and patterns of the early recurrence of pancreatic ductal adenocarcinoma after pancreatectomy: the influence of pre- and post- operative adjuvant therapy. BMC Surgery. 2019 Dec;19(1):186.

28. Moletta L, Serafini S, Valmasoni M, Pierobon ES, Ponzoni A, Sperti C. Surgery for Recurrent Pancreatic Cancer: Is It Effective? Cancers (Basel). 2019 Jul;11(7):991.

29. Longley DB, Harkin DP, Johnston PG. 5-Fluorouracil: mechanisms of action and clinical strategies. Nat Rev Cancer. 2003 May;3(5):330–8.

30. Fujita K ichi, Kubota Y, Ishida H, Sasaki Y. Irinotecan, a key chemotherapeutic drug for metastatic colorectal cancer. World J Gastroenterol. 2015 Nov 21;21(43):12234–48.

31. Arango D, Wilson AJ, Shi Q, Corner GA, Arañes MJ, Nicholas C, et al. Molecular mechanisms of action and prediction of response to oxaliplatin in colorectal cancer cells. Br J Cancer. 2004 Nov;91(11):1931–46.

32. Weaver BA. How Taxol/paclitaxel kills cancer cells. MBoC. 2014 Sep 15;25(18):2677–81.

33. Plunkett W, Huang P, Xu YZ, Heinemann V, Grunewald R, Gandhi V. Gemcitabine: metabolism, mechanisms of action, and self-potentiation. Semin Oncol. 1995 Aug;22(4 Suppl 11):3–10.

34. de Sousa Cavalcante L, Monteiro G. Gemcitabine: Metabolism and molecular mechanisms of action, sensitivity and chemoresistance in pancreatic cancer. European Journal of Pharmacology. 2014 Oct;741:8–16.

35. Perez EA, Romond EH, Suman VJ, Jeong JH, Sledge G, Geyer CE, et al. Trastuzumab plus adjuvant chemotherapy for human epidermal growth factor receptor 2-positive breast cancer: planned joint analysis of overall survival from NSABP B-31 and NCCTG N9831. J Clin Oncol. 2014 Nov;32(33):3744–52.

36. Gajria D, Chandarlapaty S. HER2-amplified breast cancer: mechanisms of trastuzumab resistance and novel targeted therapies. Expert Rev Anticancer Ther. 2011 Feb;11(2):263–75.

37. Carter J, Tadi P. Erlotinib. In: StatPearls. Treasure Island (FL): StatPearls Publishing; 2022. p. PMID: 32119371.

38. Pao W, Wang TY, Riely GJ, Miller VA, Pan Q, Ladanyi M, et al. KRAS Mutations and Primary Resistance of Lung Adenocarcinomas to Gefitinib or Erlotinib. PLoS Med. 2005 Jan;2(1):e17.

39. Moore MJ, Goldstein D, Hamm J, Figer A, Hecht JR, Gallinger S, et al. Erlotinib plus gemcitabine compared with gemcitabine alone in patients with advanced pancreatic cancer: a phase III trial of the National Cancer Institute of Canada Clinical Trials Group. J Clin Oncol. 2007 May;25(15):1960–6.

40. Hanahan D, Weinberg RA. Hallmarks of Cancer: The Next Generation. Cell. 2011 Mar;144(5):646–74.

41. Li J, Eu JQ, Kong LR, Wang L, Lim YC, Goh BC, et al. Targeting Metabolism in Cancer Cells and the Tumour Microenvironment for Cancer Therapy. Molecules. 2020 Oct;25(20):4831.

42. Ngoi NYL, Eu JQ, Hirpara J, Wang L, Lim JSJ, Lee SC, et al. Targeting Cell Metabolism as Cancer Therapy. Antioxidants & Redox Signaling. 2020 Jan;32(5):285–308.

43. Magaway C, Kim E, Jacinto E. Targeting mTOR and Metabolism in Cancer: Lessons and Innovations. Cells. 2019 Dec;8(12):1584.

44. Turtoi A, Musmeci D, Wang Y, Dumont B, Somja J, Bevilacqua G, et al. Identification of novel accessible proteins bearing diagnostic and therapeutic potential in human pancreatic ductal adenocarcinoma. J Proteome Res. 2011 Sep;10(9):4302–13.

45. He Y, Kan W, Li Y, Hao Y, Huang A, Gu H, et al. A potent and selective small molecule inhibitor of myoferlin attenuates colorectal cancer progression. Clin Transl Med. 2021 Feb;11(2):e289.

46. Zhang T, Li J, He Y, Yang F, Hao Y, Jin W, et al. A small molecule targeting myoferlin exerts promising anti-tumor effects on breast cancer. Nat Commun. 2018 Sep;9(1):3726.

47. Rademaker G, Hennequière V, Brohée L, Nokin MJ, Lovinfosse P, Durieux F, et al. Myoferlin controls mitochondrial structure and activity in pancreatic ductal adenocarcinoma, and affects tumor aggressiveness. Oncogene. 2018 Aug;37(32):4398–412.

48. Rademaker G, Costanza B, Anania S, Agirman F, Maloujahmoum N, Di Valentin E, et al. Myoferlin Contributes to the Metastatic Phenotype of Pancreatic Cancer Cells by Enhancing Their Migratory Capacity through the Control of Oxidative Phosphorylation. Cancers (Basel). 2019 Jun;11(6):853.

49. Blomme A, Costanza B, de Tullio P, Thiry M, Van Simaeys G, Boutry S, et al. Myoferlin regulates cellular lipid metabolism and promotes metastases in triple-negative breast cancer. Oncogene. 2017 Apr;36(15):2116–30.

50. Andersen HB, Ialchina R, Pedersen SF, Czaplinska D. Metabolic reprogramming by driver mutation-tumor microenvironment interplay in pancreatic cancer: new therapeutic targets. Cancer Metastasis Rev. 2021 Dec;40(4):1093–114.

51. DeBerardinis RJ, Chandel NS. We need to talk about the Warburg effect. Nat Metab. 2020 Feb;2(2):127–9.

52. Liberti MV, Locasale JW. The Warburg Effect: How Does it Benefit Cancer Cells? Trends Biochem Sci. 2016 Mar;41(3):211–8.

53. Perillo B, Di Donato M, Pezone A, Di Zazzo E, Giovannelli P, Galasso G, et al. ROS in cancer therapy: the bright side of the moon. Exp Mol Med. 2020 Feb;52(2):192–203.

54. Li JT, Wang YP, Yin M, Lei QY. Metabolism remodeling in pancreatic ductal adenocarcinoma. Cell Stress. 2019 Nov;3(12):361–8.

55. Qin C, Yang G, Yang J, Ren B, Wang H, Chen G, et al. Metabolism of pancreatic cancer: paving the way to better anticancer strategies. Molecular Cancer. 2020 Mar;19(1):50.

56. Menendez JA, Lupu R. Fatty acid synthase and the lipogenic phenotype in cancer pathogenesis. Nat Rev Cancer. 2007 Oct;7(10):763–77.

57. Daemen A, Peterson D, Sahu N, McCord R, Du X, Liu B, et al. Metabolite profiling stratifies pancreatic ductal adenocarcinomas into subtypes with distinct sensitivities to metabolic inhibitors. Proc Natl Acad Sci U S A. 2015 Aug;112(32):4410–7.

58. Kamphorst JJ, Cross JR, Fan J, de Stanchina E, Mathew R, White EP, et al. Hypoxic and Ras-transformed cells support growth by scavenging unsaturated fatty acids from lysophospholipids. Proc Natl Acad Sci U S A. 2013 May;110(22):8882–7.

59. Shi W, Wu H, Liu S, Wu Z, Wu H, Liu J, et al. Progesterone Suppresses Cholesterol Esterification in APP/PS1 mice and a cell model of Alzheimer's Disease. Brain Research Bulletin. 2021 Aug;173:162–73.

60. Ferreira A, Pereira F, Reis C, Oliveira MJ, Sousa MJ, Preto A. Crucial Role of Oncogenic KRAS Mutations in Apoptosis and Autophagy Regulation: Therapeutic Implications. Cells. 2022 Jan;11(14):2183.

61. Hollinshead KER, Parker SJ, Eapen VV, Encarnacion-Rosado J, Sohn A, Oncu T, et al. Respiratory Supercomplexes Promote Mitochondrial Efficiency and Growth in Severely Hypoxic Pancreatic Cancer. Cell Rep. 2020 Oct;33(1):108231.

62. Sancho P, Burgos-Ramos E, Tavera A, Bou Kheir T, Jagust P, Schoenhals M, et al. MYC/PGC-1α Balance Determines the Metabolic Phenotype and Plasticity of Pancreatic Cancer Stem Cells. Cell Metabolism. 2015 Oct;22(4):590–605.

63. Masoud R, Reyes-Castellanos G, Lac S, Garcia J, Dou S, Shintu L, et al. Targeting Mitochondrial Complex I Overcomes Chemoresistance in High OXPHOS Pancreatic Cancer. Cell Rep Med. 2020 Nov;1(8):100143.

64. Morciano G, Marchi S, Morganti C, Sbano L, Bittremieux M, Kerkhofs M, et al. Role of Mitochondria-Associated ER Membranes in Calcium Regulation in Cancer-Specific Settings. Neoplasia. 2018 Apr;20(5):510–23.

65. Bustos G, Ahumada-Castro U, Silva-Pavez E, Puebla A, Lovy A, Cesar Cardenas J. The ER-mitochondria Ca2+ signaling in cancer progression: Fueling the monster. Int Rev Cell Mol Biol. 2021 Apr;363:49–121.

66. Pinton P. Mitochondria-associated membranes (MAMs) and pathologies. Cell Death Dis. 2018 Mar;9(4):1–3.

67. Cardenas C, Müller M, McNeal A, Lovy A, Jaňa F, Bustos G, et al. Selective Vulnerability of Cancer Cells by Inhibition of Ca2+ Transfer from Endoplasmic Reticulum to Mitochondria. Cell Reports. 2016 Apr;15(1):219–20.

68. Foulon A, Rybarczyk P, Jonckheere N, Brabencova E, Sevestre H, Ouadid-Ahidouch H, et al. Inositol (1,4,5)-Trisphosphate Receptors in Invasive Breast Cancer: A New Prognostic Tool? International Journal of Molecular Sciences. 2022 Jan;23(6):2962.

69. Rezuchova I, Hudecova S, Soltysova A, Matuskova M, Durinikova E, Chovancova B, et al. Type 3 inositol 1,4,5-trisphosphate receptor has antiapoptotic and proliferative role in cancer cells. Cell Death Dis. 2019 Feb;10(3):186.

70. Ueasilamongkol P, Khamphaya T, Guerra MT, Rodrigues MA, Gomes DA, Kong Y, et al. Type 3 Inositol 1,4,5-Trisphosphate Receptor Is Increased and Enhances Malignant Properties in Cholangiocarcinoma. Hepatology. 2020 Feb;71(2):583–99.

71. Young MP, Schug ZT, Booth DM, Yule DI, Mikoshiba K, Hajnóczky G, et al. Metabolic adaptation to the chronic loss of Ca2+ signaling induced by KO of IP3 receptors or the mitochondrial Ca2+ uniporter. J Biol Chem. 2022 Jan;298(1):101436.

72. Coku J, Booth DM, Skoda J, Pedrotty MC, Vogel J, Liu K, et al. Reduced ER–mitochondria connectivity promotes neuroblastoma multidrug resistance. The EMBO Journal. 2022 Apr;41(8):108272.

73. Scorrano L, De Matteis MA, Emr S, Giordano F, Hajnóczky G, Kornmann B, et al. Coming together to define membrane contact sites. Nat Commun. 2019 Mar;10(1):1287.

74. Westermann B. The mitochondria-plasma membrane contact site. Curr Opin Cell Biol. 2015 Aug;35:1–6.

75. Montes de Oca Balderas P. Mitochondria–plasma membrane interactions and communication. Journal of Biological Chemistry. 2021 Oct;297(4):101164.

76. Gao P, Yang W, Sun L. Mitochondria-Associated Endoplasmic Reticulum Membranes (MAMs) and Their Prospective Roles in Kidney Disease. Oxidative Medicine and Cellular Longevity. 2020 Sep;2020:3120539.

77. Peng W, Wong YC, Krainc D. Mitochondria-lysosome contacts regulate mitochondrial Ca2+ dynamics via lysosomal TRPML1. PNAS. 2020 Aug;117(32):19266–75.

78. Wong YC, Ysselstein D, Krainc D. Mitochondria–lysosome contacts regulate mitochondrial fission via RAB7 GTP hydrolysis. Nature. 2018 Feb;554(7692):382–6.

79. Fan J, Li X, Issop L, Culty M, Papadopoulos V. ACBD2/ECI2-Mediated Peroxisome-Mitochondria Interactions in Leydig Cell Steroid Biosynthesis. Mol Endocrinol. 2016 Jul;30(7):763–82.

80. Vance JE. MAM (mitochondria-associated membranes) in mammalian cells: Lipids and beyond. Biochimica et Biophysica Acta (BBA) - Molecular and Cell Biology of Lipids. 2014 Apr;1841(4):595–609.

81. Xu L, Wang X, Tong C. Endoplasmic Reticulum–Mitochondria Contact Sites and Neurodegeneration. Frontiers in Cell and Developmental Biology. 2020;8:428.

82. Lim D, Dematteis G, Tapella L, Genazzani AA, Calì T, Brini M, et al. Ca2+ handling at the mitochondria-ER contact sites in neurodegeneration. Cell Calcium. 2021 Sep;98:102453.

83. Giacomello M, Pellegrini L. The coming of age of the mitochondria–ER contact: a matter of thickness. Cell Death Differ. 2016 Sep;23(9):1417–27.

84. Copeland DE, Dalton AJ. An Association between Mitochondria and the Endoplasmic Reticulum in Cells of the Pseudobranch Gland of a Teleost. The Journal of Biophysical and Biochemical Cytology. 1959 May;5(3):393–6.

85. Simoes ICM, Morciano G, Lebiedzinska-Arciszewska M, Aguiari G, Pinton P, Potes Y, et al. The mystery of mitochondria-ER contact sites in physiology and pathology: A cancer perspective. Biochimica et Biophysica Acta (BBA) - Molecular Basis of Disease. 2020 Oct;1866(10):165834.

86. Wilson EL, Metzakopian E. ER-mitochondria contact sites in neurodegeneration: genetic screening approaches to investigate novel disease mechanisms. Cell Death Differ. 2021 Jun;28(6):1804–21.

87. Cooper GM. Mitochondria. The Cell: A Molecular Approach 2nd edition [Internet]. 2000 [cited 2022 Jan 10]; Available from: https://www.ncbi.nlm.nih.gov/books/NBK9896/

88. Lemeshko SV, Lemeshko VV. Energy flux modulation on the outer membrane of mitochondria by metabolically-derived potential. Mol Cell Biochem. 2004 Jan;256(1/2):127–39.

89. Martínez-Reyes I, Chandel NS. Mitochondrial TCA cycle metabolites control physiology and disease. Nat Commun. 2020 Jan 3;11(1):102.

90. Eyenga P, Rey B, Eyenga L, Sheu SS. Regulation of Oxidative Phosphorylation of Liver Mitochondria in Sepsis. Cells. 2022 May 10;11(10):1598.

91. Daumke O, Praefcke GJK. Structural insights into membrane fusion at the endoplasmic reticulum. Proceedings of the National Academy of Sciences. 2011 Feb 8;108(6):2175–6.

92. Schwarz DS, Blower MD. The endoplasmic reticulum: structure, function and response to cellular signaling. Cell Mol Life Sci. 2016 Jan;73(1):79–94.

93. Park SH, Blackstone C. Further assembly required: construction and dynamics of the endoplasmic reticulum network. EMBO reports. 2010 Jul;11(7):515–21.

94. Jacquemyn J, Cascalho A, Goodchild RE. The ins and outs of endoplasmic reticulum-controlled lipid biosynthesis. EMBO Rep. 2017 Nov;18(11):1905–21.

95. Sala-Vila A, Navarro-Lérida I, Sánchez-Alvarez M, Bosch M, Calvo C, López JA, et al. Interplay between hepatic mitochondria-associated membranes, lipid metabolism and caveolin-1 in mice. Scientific Reports. 2016 Jun;6(1):27351.

96. Tubbs E, Rieusset J. Metabolic signaling functions of ER–mitochondria contact sites: role in metabolic diseases. Journal of Molecular Endocrinology. 2017 Feb;58(2):R87–106.

97. Szabadkai G, Bianchi K, Várnai P, De Stefani D, Wieckowski MR, Cavagna D, et al. Chaperone-mediated coupling of endoplasmic reticulum and mitochondrial Ca2+ channels. J Cell Biol. 2006 Dec;175(6):901–11.

98. de Brito OM, Scorrano L. Mitofusin 2 tethers endoplasmic reticulum to mitochondria. Nature. 2008 Dec;456(7222):605–10.

99. Filadi R, Greotti E, Turacchio G, Luini A, Pozzan T, Pizzo P. Mitofusin 2 ablation increases endoplasmic reticulum-mitochondria coupling. Proc Natl Acad Sci U S A. 2015 Apr;112(17):E2174-2181.

100. Naon D, Zaninello M, Giacomello M, Varanita T, Grespi F, Lakshminaranayan S, et al. Critical reappraisal confirms that Mitofusin 2 is an endoplasmic reticulum–mitochondria tether. PNAS. 2016 Oct;113(40):11249–54.

101. De Vos KJ, Mórotz GM, Stoica R, Tudor EL, Lau KF, Ackerley S, et al. VAPB interacts with the mitochondrial protein PTPIP51 to regulate calcium homeostasis. Hum Mol Genet. 2012 Mar 15;21(6):1299–311.

102. Stoica R, De Vos KJ, Paillusson S, Mueller S, Sancho RM, Lau KF, et al. ER–mitochondria associations are regulated by the VAPB–PTPIP51 interaction and are disrupted by ALS/FTD-associated TDP-43. Nat Commun. 2014 Jun 3;5(1):3996.

103. Li C, Li L, Yang M, Zeng L, Sun L. PACS-2: A key regulator of mitochondria-associated membranes (MAMs). Pharmacological Research. 2020 Oct;160:105080.

104. Simmen T, Aslan JE, Blagoveshchenskaya AD, Thomas L, Wan L, Xiang Y, et al. PACS-2 controls endoplasmic reticulum-mitochondria communication and Bid-mediated apoptosis. EMBO J. 2005 Feb;24(4):717–29.

105. Myhill N, Lynes EM, Nanji JA, Blagoveshchenskaya AD, Fei H, Carmine Simmen K, et al. The Subcellular Distribution of Calnexin Is Mediated by PACS-2. Mol Biol Cell. 2008 Jul;19(7):2777–88.

106. Doghman-Bouguerra M, Granatiero V, Sbiera S, Sbiera I, Lacas-Gervais S, Brau F, et al. FATE1 antagonizes calcium- and drug-induced apoptosis by uncoupling ER and mitochondria. EMBO Rep. 2016 Sep;17(9):1264–80.

107. Gall JM, Wang Z, Liesa M, Molina A, Havasi A, Schwartz JH, et al. Role of Mitofusin 2 in the Renal Stress Response. PLOS ONE. 2012 Jan;7(1):31074.

108. Stacchiotti A, Favero G, Lavazza A, Garcia-Gomez R, Monsalve M, Rezzani R. Perspective: Mitochondria-ER Contacts in Metabolic Cellular Stress Assessed by Microscopy. Cells. 2019 Jan;8(1):5.

109. Yang S, Zhou R, Zhang C, He S, Su Z. Mitochondria-Associated Endoplasmic Reticulum Membranes in the Pathogenesis of Type 2 Diabetes Mellitus. Frontiers in Cell and Developmental Biology. 2020 Oct;8:571554.

110. Rizzuto R, Pinton P, Carrington W, Fay FS, Fogarty KE, Lifshitz LM, et al. Close Contacts with the Endoplasmic Reticulum as Determinants of Mitochondrial Ca2+ Responses. Science. 1998 Jun 12;280(5370):1763–6.

111. Rieusset J, Fauconnier J, Paillard M, Belaidi E, Tubbs E, Chauvin MA, et al. Disruption of calcium transfer from ER to mitochondria links alterations of mitochondria-associated ER membrane integrity to hepatic insulin resistance. Diabetologia. 2016 Mar;59(3):614–23.

112. Cardenas C, Lovy A, Silva-Pavez E, Urra F, Mizzoni C, Ahumada-Castro U, et al. Cancer cells with defective oxidative phosphorylation require endoplasmic reticulum–to–mitochondria Ca2+ transfer for survival. Science Signaling. 2020 Jul;13(640):1212.

113. Gómez-Suaga P, Bravo-San Pedro JM, González-Polo RA, Fuentes JM, Niso-Santano M. ER–mitochondria signaling in Parkinson's disease. Cell Death Dis. 2018 Mar;9(3):1–12.

114. Agrawal RR, Montesinos J, Larrea D, Area-Gomez E, Pera M. The silence of the fats: A MAM's story about Alzheimer. Neurobiology of Disease. 2020 Nov;145:105062.

115. López-Molina L, Fernández-Irigoyen J, Cifuentes-Díaz C, Alberch J, Girault JA, Santamaría E, et al. Pyk2 Regulates MAMs and Mitochondrial Dynamics in Hippocampal Neurons. Cells. 2022 Jan;11(5):842.

116. Vance JE. Phospholipid synthesis in a membrane fraction associated with mitochondria. Journal of Biological Chemistry. 1990 May 5;265(13):7248–56.

117. Wieckowski MR, Giorgi C, Lebiedzinska M, Duszynski J, Pinton P. Isolation of mitochondria-associated membranes and mitochondria from animal tissues and cells. Nat Protoc. 2009 Nov;4(11):1582–90.

118. Lewis A, Tsai SY, Su TP. Detection of Isolated Mitochondria-Associated ER Membranes Using the Sigma-1 Receptor. Methods Mol Biol. 2016 Aug;1376:133–40.

119. Horner SM, Wilkins C, Badil S, Iskarpatyoti J, Jr MG. Proteomic Analysis of Mitochondrial-Associated ER Membranes (MAM) during RNA Virus Infection Reveals Dynamic Changes in Protein and Organelle Trafficking. PLOS ONE. 2015 Mar;10(3):0117963.

120. Zhang A, Williamson CD, Wong DS, Bullough MD, Brown KJ, Hathout Y, et al. Quantitative Proteomic Analyses of Human Cytomegalovirus-Induced Restructuring of Endoplasmic Reticulum-Mitochondrial Contacts at Late Times of Infection. Molecular & Cellular Proteomics. 2011 Oct;10(10):M111.009936.

121. Lu X, Gong Y, Hu W, Mao Y, Wang T, Sun Z, et al. Ultrastructural and proteomic profiling of mitochondria-associated endoplasmic reticulum membranes reveal aging signatures in striated muscle. Cell Death Dis. 2022 Apr;13(4):296.

122. D'Eletto M. Transglutaminase Type 2 Regulates ER-Mitochondria Contact Sites by Interacting with GRP75. :21.

123. Cieri D, Vicario M, Giacomello M, Vallese F, Filadi R, Wagner T, et al. SPLICS: a split green fluorescent protein-based contact site sensor for narrow and wide heterotypic organelle juxtaposition. Cell Death Differ. 2018 Jun;25(6):1131–45.

124. Sakai S, Watanabe S, Komine O, Sobue A, Yamanaka K. Novel reporters of mitochondria-associated membranes (MAM), MAMtrackers, demonstrate MAM disruption as a common pathological feature in amyotrophic lateral sclerosis. The FASEB Journal. 2021 May;35(7):21688.

125. Tubbs E, Rieusset J. Study of Endoplasmic Reticulum and Mitochondria Interactions by In Situ Proximity Ligation Assay in Fixed Cells. J Vis Exp. 2016 Dec 10;(118):54899.

126. Hajnóczky G, Robb-Gaspers LD, Seitz MB, Thomas AP. Decoding of cytosolic calcium oscillations in the mitochondria. Cell. 1995 Aug;82(3):415–24.

127. John Peter AT, Petrungaro C, Peter M, Kornmann B. METALIC reveals interorganelle lipid flux in live cells by enzymatic mass tagging. Nat Cell Biol. 2022 Jun;24(6):996–1004.

128. Tilokani L, Nagashima S, Paupe V, Prudent J. Mitochondrial dynamics: overview of molecular mechanisms. Essays Biochem. 2018 Jul;62(3):341–60.

129. Rossignol R, Gilkerson R, Aggeler R, Yamagata K, Remington SJ, Capaldi RA. Energy Substrate Modulates Mitochondrial Structure and Oxidative Capacity in Cancer Cells. Cancer Res. 2004 Feb;64(3):985–93.

130. Liesa M, Shirihai OS. Mitochondrial dynamics in the regulation of nutrient utilization and energy expenditure. Cell Metab. 2013 Apr;17(4):491–506.

131. Zemirli N, Morel E, Molino D. Mitochondrial Dynamics in Basal and Stressful Conditions. Int J Mol Sci. 2018 Feb;19(2):564.

132. Simula L, Campello S. Monitoring the Mitochondrial Dynamics in Mammalian Cells | Springer Nature Experiments. In: Methods in Molecular Biology. Palmeira, C., Moreno, A. (eds) Mitochondrial Bioenergetics. New York: Humana Press; 2018.

133. Pernas L, Scorrano L. Mito-Morphosis: Mitochondrial Fusion, Fission, and Cristae Remodeling as Key Mediators of Cellular Function. Annu Rev Physiol. 2016;78:505–31.

134. Ishihara N, Eura Y, Mihara K. Mitofusin 1 and 2 play distinct roles in mitochondrial fusion reactions via GTPase activity. J Cell Sci. 2004 Dec;117(26):6535–46.

135. Casellas-Díaz S, Larramona-Arcas R, Riqué-Pujol G, Tena-Morraja P, Müller-Sánchez C, Segarra-Mondejar M, et al. Mfn2 localization in the ER is necessary for its bioenergetic function and neuritic development. EMBO Rep. 2021 Sep;22(9):51954.

136. Pagliuso A, Cossart P, Stavru F. The ever-growing complexity of the mitochondrial fission machinery. Cell Mol Life Sci. 2018 Feb;75(3):355–74.

137. Lee JE, Westrate LM, Wu H, Page C, Voeltz GK. Multiple dynamin family members collaborate to drive mitochondrial division. Nature. 2016 Dec;540(7631):139–43.

138. Durieux AC, Prudhon B, Guicheney P, Bitoun M. Dynamin 2 and human diseases. J Mol Med (Berl). 2010 Apr;88(4):339–50.

139. Kamerkar SC, Kraus F, Sharpe AJ, Pucadyil TJ, Ryan MT. Dynamin-related protein 1 has membrane constricting and severing abilities sufficient for mitochondrial and peroxisomal fission. Nat Commun. 2018 Dec 7;9(1):5239.

140. Fonseca TB, Sánchez-Guerrero Á, Milosevic I, Raimundo N. Mitochondrial fission requires DRP1 but not dynamins. Nature. 2019 Jun;570(7761):E34–42.

141. Chakrabarti R, Ji WK, Stan RV, de Juan Sanz J, Ryan TA, Higgs HN. INF2-mediated actin polymerization at the ER stimulates mitochondrial calcium uptake, inner membrane constriction, and division. Journal of Cell Biology. 2018 Jan;217(1):251–68.

142. Ohshima Y, Takata N, Suzuki-Karasaki M, Yoshida Y, Tokuhashi Y, Suzuki-Karasaki Y. Disrupting mitochondrial Ca2+ homeostasis causes tumor-selective TRAIL sensitization through mitochondrial network abnormalities. International Journal of Oncology. 2017 Oct;51(4):1146–58.

143. Romero-Garcia S, Prado-Garcia H. Mitochondrial calcium: Transport and modulation of cellular processes in homeostasis and cancer (Review). International Journal of Oncology. 2019 Apr;54(4):1155–67.

144. Abrisch RG, Gumbin SC, Wisniewski BT, Lackner LL, Voeltz GK. Fission and fusion machineries converge at ER contact sites to regulate mitochondrial morphology. Journal of Cell Biology. 2020 Feb;219(4):201911122.

145. D'Arcy MS. Cell death: a review of the major forms of apoptosis, necrosis and autophagy. Cell Biol Int. 2019 Jun;43(6):582–92.

146. Hongmei Z. Extrinsic and Intrinsic Apoptosis Signal Pathway Review. In: Apoptosis and medecine. Tobias M. Ntuli. London: IntechOpen; 2012.

147. Brenner C, Grimm S. The permeability transition pore complex in cancer cell death. Oncogene. 2006 Aug;25(34):4744–56.

148. Seol DW, Jeong SY. The role of mitochondria in apoptosis. BMB Reports. 2008 Jan;41(1):11–22.

149. Bouchier-Hayes L, Lartigue L, Newmeyer DD. Mitochondria: pharmacological manipulation of cell death. J Clin Invest. 2005 Oct;115(10):2640–7.

150. Paillard M, Tubbs E, Thiebaut PA, Gomez L, Fauconnier J, Crola Da Silva C, et al. Depressing Mitochondria-Reticulum Interactions Protects Cardiomyocytes From Lethal Hypoxia-Reoxygenation Injury. Circulation. 2013 Oct;128(14):1555–65.

151. Marchi S, Rimessi A, Giorgi C, Baldini C, Ferroni L, Rizzuto R, et al. Akt kinase reducing endoplasmic reticulum Ca2+ release protects cells from Ca2+-dependent apoptotic stimuli. Biochemical and Biophysical Research Communications. 2008 Oct;375(4):501–5.

152. Frank S, Gaume B, Bergmann-Leitner ES, Leitner WW, Robert EG, Catez F, et al. The role of dynamin-related protein 1, a mediator of mitochondrial fission, in apoptosis. Dev Cell. 2001 Oct;1(4):515–25.

153. Parone PA, James DI, Da Cruz S, Mattenberger Y, Donzé O, Barja F, et al. Inhibiting the mitochondrial fission machinery does not prevent Bax/Bak-dependent apoptosis. Mol Cell Biol. 2006 Oct;26(20):7397–408.

154. Giorgi C, Danese A, Missiroli S, Patergnani S, Pinton P. Calcium Dynamics as a Machine for Decoding Signals. Trends in Cell Biology. 2018 Apr;28(4):258–73.

155. Bagur R, Hajnóczky G. Intracellular Ca2+ sensing: role in calcium homeostasis and signaling. Mol Cell. 2017 Jun;66(6):780–8.

156. Santo-Domingo J, Demaurex N. Calcium uptake mechanisms of mitochondria. Biochimica et Biophysica Acta (BBA) - Bioenergetics. 2010 Jun;1797(6):907–12.

157. Park MK, Ashby MC, Erdemli G, Petersen OH, Tepikin AV. Perinuclear, perigranular and sub-plasmalemmal mitochondria have distinct functions in the regulation of cellular calcium transport. EMBO J. 2001 Apr;20(8):1863–74.

158. Chen X, Egly C, Riley AM, Li W, Tewson P, Hughes TE, et al. PKC-dependent Phosphorylation of the H1 Histamine Receptor Modulates TRPC6 Activity. Cells. 2014 Jun;3(2):247–57.

159. Rizzuto R, Brini M, Murgia M, Pozzan T. Microdomains with high Ca2+ close to IP3-sensitive channels that are sensed by neighboring mitochondria. Science. 1993 Oct;262(5134):744–7.

160. Sander P, Gudermann T, Schredelseker J. A Calcium Guard in the Outer Membrane: Is VDAC a Regulated Gatekeeper of Mitochondrial Calcium Uptake? International Journal of Molecular Sciences. 2021 Jan;22(2):946.

161. Xu H, Guan N, Ren YL, Wei QJ, Tao YH, Yang GS, et al. IP3R-Grp75-VDAC1-MCU calcium regulation axis antagonists protect podocytes from apoptosis and decrease proteinuria in an Adriamycin nephropathy rat model. BMC Nephrology. 2018 Jun;19(1):140.

162. Cárdenas C, Miller RA, Smith I, Bui T, Molgó J, Müller M, et al. Essential regulation of cell bioenergetics by constitutive InsP3 receptor Ca2+ transfer to mitochondria. Cell. 2010 Jul;142(2):270–83.

163. Denton RM. Regulation of mitochondrial dehydrogenases by calcium ions. Biochimica et Biophysica Acta (BBA) - Bioenergetics. 2009 Nov;1787(11):1309–16.

164. Jouaville LS, Pinton P, Bastianutto C, Rutter GA, Rizzuto R. Regulation of mitochondrial ATP synthesis by calcium: Evidence for a long-term metabolic priming. Proc Natl Acad Sci U S A. 1999 Nov;96(24):13807–12.

165. Rutter GA, Midgley PJ, Denton RM. Regulation of the pyruvate dehydrogenase complex by Ca2+ within toluene-permeabilized heart mitochondria. Biochim Biophys Acta. 1989 Dec;1014(3):263–70.

166. Zhou J, Dhakal K, Yi J. Mitochondrial Ca2+ uptake in skeletal muscle health and disease. Sci China Life Sci. 2016 Aug;59(8):770–6.

167. Combot Y, Salo VT, Chadeuf G, Hölttä M, Ven K, Pulli I, et al. Seipin localizes at endoplasmic-reticulum-mitochondria contact sites to control mitochondrial calcium import and metabolism in adipocytes. Cell Reports. 2022 Jan;38(2):110213.

168. Ding L, Yang X, Tian H, Liang J, Zhang F, Wang G, et al. Seipin regulates lipid homeostasis by ensuring calcium-dependent mitochondrial metabolism. EMBO J. 2018 Sep 3;37(17):e97572.

169. Camara AKS, Zhou Y, Wen PC, Tajkhorshid E, Kwok WM. Mitochondrial VDAC1: A Key Gatekeeper as Potential Therapeutic Target. Frontiers in Physiology. 2017 Jun;8:460.

170. Rosencrans WM, Rajendran M, Bezrukov SM, Rostovtseva TK. VDAC regulation of mitochondrial calcium flux: From channel biophysics to disease. Cell Calcium. 2021 Mar;94:102356.

171. De Stefani D, Bononi A, Romagnoli A, Messina A, De Pinto V, Pinton P, et al. VDAC1 selectively transfers apoptotic Ca2+ signals to mitochondria. Cell Death Differ. 2012 Feb;19(2):267–73.

172. Pallafacchina G, Zanin S, Rizzuto R. From the Identification to the Dissection of the Physiological Role of the Mitochondrial Calcium Uniporter: An Ongoing Story. Biomolecules. 2021 Jun;11(6):786.

173. Paupe V, Prudent J. New insights into the role of mitochondrial calcium homeostasis in cell migration. Biochem Biophys Res Commun. 2018 May;500(1):75–86.

174. Boyman L, Lederer WJ. How the mitochondrial calcium uniporter complex (MCUcx) works. PNAS. 2020 Sep;117(37):22634–6.

175. Patron M, Raffaello A, Granatiero V, Tosatto A, Merli G, De Stefani D, et al. The Mitochondrial Calcium Uniporter (MCU): Molecular Identity and Physiological Roles. Journal of Biological Chemistry. 2013 Apr;288(15):10750–8.

176. Quan X, Nguyen TT, Choi SK, Xu S, Das R, Cha SK, et al. Essential Role of Mitochondrial Ca2+ Uniporter in the Generation of Mitochondrial pH Gradient and Metabolism-Secretion Coupling in Insulin-releasing Cells. J Biol Chem. 2015 Feb;290(7):4086–96.

177. Prole DL, Taylor CW. Structure and Function of IP3 Receptors. Cold Spring Harb Perspect Biol. 2019 Apr;11(4):35063.

178. Ahumada-Castro U, Bustos G, Silva-Pavez E, Puebla-Huerta A, Lovy A, Cárdenas C. In the Right Place at the Right Time: Regulation of Cell Metabolism by IP3R-Mediated Inter-Organelle Ca2+ Fluxes. Front Cell Dev Biol. 2021 Mar;9:629522.

179. Pinton P, Pozzan T, Rizzuto R. The Golgi apparatus is an inositol 1,4,5-trisphosphate-sensitive Ca2+ store, with functional properties distinct from those of the endoplasmic reticulum. EMBO J. 1998 Sep;17(18):5298–308.

180. Pedriali G, Rimessi A, Sbano L, Giorgi C, Wieckowski MR, Previati M, et al. Regulation of Endoplasmic Reticulum–Mitochondria Ca2+ Transfer and Its Importance for Anti-Cancer Therapies. Frontiers in Oncology. 2017 Aug;7:180.

181. Mendes CCP, Gomes DA, Thompson M, Souto NC, Goes TS, Goes AM, et al. The Type III Inositol 1,4,5-Trisphosphate Receptor Preferentially Transmits Apoptotic Ca2+ Signals into Mitochondria *. Journal of Biological Chemistry. 2005 Dec;280(49):40892–900.

182. Bartok A, Weaver D, Golenár T, Nichtova Z, Katona M, Bánsághi S, et al. IP3 receptor isoforms differently regulate ER-mitochondrial contacts and local calcium transfer. Nat Commun. 2019 Aug;10(1):3726.

183. Sassano ML, van Vliet AR, Agostinis P. Mitochondria-Associated Membranes As Networking Platforms and Regulators of Cancer Cell Fate. Front Oncol. 2017 Aug;7:174.

184. Popov LD. Mitochondrial-derived vesicles: Recent insights. Journal of Cellular and Molecular Medicine. 2022;26(12):3323–8.

185. Galmes R, Houcine A, van Vliet AR, Agostinis P, Jackson CL, Giordano F. ORP5/ORP8 localize to endoplasmic reticulum–mitochondria contacts and are involved in mitochondrial function. EMBO Rep. 2016 Jun;17(6):800–10.

186. Dudek J. Role of Cardiolipin in Mitochondrial Signaling Pathways. Frontiers in Cell and Developmental Biology. 2017 Sep;5:90.

187. Luan Y, Luan Y, Yuan RX, Feng Q, Chen X, Yang Y. Structure and Function of Mitochondria-Associated Endoplasmic Reticulum Membranes (MAMs) and Their Role in Cardiovascular Diseases. Oxidative Medicine and Cellular Longevity. 2021 Jul;2021:4578809.

188. Miller WL. Steroid hormone synthesis in mitochondria. Molecular and Cellular Endocrinology. 2013 Oct;379(1):62–73.

189. Annunziata I, Sano R, d'Azzo A. Mitochondria-associated ER membranes (MAMs) and lysosomal storage diseases. Cell Death & Disease. 2018 Feb;9(3):1–16.

190. Zhemkov V, Geva M, Hayden MR, Bezprozvanny I. Sigma-1 Receptor (S1R) Interaction with Cholesterol: Mechanisms of S1R Activation and Its Role in Neurodegenerative Diseases. Int J Mol Sci. 2021 Apr;22(8):4082.

191. Simón L, Campos A, Leyton L, Quest AFG. Caveolin-1 function at the plasma membrane and in intracellular compartments in cancer. Cancer Metastasis Rev. 2020 May;39(2):435–53.

192. Bosch M, Marí M, Gross SP, Fernández-Checa JC, Pol A. Mitochondrial Cholesterol: A Connection Between Caveolin, Metabolism, and Disease. Traffic. 2011 Aug;12(11):1483–9.

193. Mizushima N. Autophagy: process and function. Genes Dev. 2007 Feb;21(22):2861–73.

194. Piffoux M, Eriau E, Cassier PA. Autophagy as a therapeutic target in pancreatic cancer. Br J Cancer. 2021 Jan;124(2):333–44.

195. Sun L, Hu L, Cogdell D, Lu L, Gao C, Tian W, et al. MIR506 induces autophagy-related cell death in pancreatic cancer cells by targeting the STAT3 pathway. Autophagy. 2017 Apr;13(4):703–14.

196. Yang M, Li C, Yang S, Xiao Y, Xiong X, Chen W, et al. Mitochondria-Associated ER Membranes – The Origin Site of Autophagy. Front Cell Dev Biol. 2020 Jul;8:595.

197. Rabinowitz JD, White E. Autophagy and Metabolism. Science. 2010 Dec 3;330(6009):1344–8.

198. Hamasaki M, Furuta N, Matsuda A, Nezu A, Yamamoto A, Fujita N, et al. Autophagosomes form at ER-mitochondria contact sites. Nature. 2013 Mar;495(7441):389–93.

199. Xian H, Yang Q, Xiao L, Shen HM, Liou YC. STX17 dynamically regulated by Fis1 induces mitophagy via hierarchical macroautophagic mechanism. Nat Commun. 2019 May;10(1):2059.

200. Gelmetti V, De Rosa P, Torosantucci L, Marini ES, Romagnoli A, Di Rienzo M, et al. PINK1 and BECN1 relocalize at mitochondria-associated membranes during mitophagy and promote ER-mitochondria tethering and autophagosome formation. Autophagy. 2017 Feb;13(4):654–69.

201. Herrera-Cruz MS, Yap MC, Tahbaz N, Phillips K, Thomas L, Thomas G, et al. Rab32 uses its effector reticulon 3L to trigger autophagic degradation of mitochondria-associated membrane (MAM) proteins. Biology Direct. 2021 Nov;16(1):22.

202. Rizzuto R, De Stefani D, Raffaello A, Mammucari C. Mitochondria as sensors and regulators of calcium signalling. Nature Reviews Molecular Cell Biology. 2012 Sep;13(9):566–78.

203. Missiroli S, Patergnani S, Caroccia N, Pedriali G, Perrone M, Previati M, et al. Mitochondria-associated membranes (MAMs) and inflammation. Cell Death Dis. 2018 Feb;9(3):1–14.

204. Zhou R, Yazdi AS, Menu P, Tschopp J. A role for mitochondria in NLRP3 inflammasome activation. Nature. 2011 Jan;469(7329):221–5.

205. Horner SM, Liu HM, Park HS, Briley J, Gale M. Mitochondrial-associated endoplasmic reticulum membranes (MAM) form innate immune synapses and are targeted by hepatitis C virus. Proc Natl Acad Sci U S A. 2011 Aug;108(35):14590–5.

206. Vazquez C, Horner SM. MAVS Coordination of Antiviral Innate Immunity. Journal of Virology. 2015 Jul;89(14):6974–7.

207. Adams CJ, Kopp MC, Larburu N, Nowak PR, Ali MMU. Structure and Molecular Mechanism of ER Stress Signaling by the Unfolded Protein Response Signal Activator IRE1. Frontiers in Molecular Biosciences. 2019 Mar;6:11.

208. Mekahli D, Bultynck G, Parys JB, De Smedt H, Missiaen L. Endoplasmic-Reticulum Calcium Depletion and Disease. Cold Spring Harb Perspect Biol. 2011 Jun;3(6):004317.

209. Rozpędek W, Pytel D, Mucha B, Leszczyńska H, Diehl JA, Majsterek I. The Role of the PERK/eIF2α/ATF4/CHOP Signaling Pathway in Tumor Progression During Endoplasmic Reticulum Stress. Curr Mol Med. 2016;16(6):533–44.

210. Goloubinoff P, Sassi AS, Fauvet B, Barducci A, De Los Rios P. Chaperones convert the energy from ATP into the nonequilibrium stabilization of native proteins. Nat Chem Biol. 2018 Apr;14(4):388–95.

211. Bravo R, Vicencio JM, Parra V, Troncoso R, Munoz JP, Bui M, et al. Increased ER-mitochondrial coupling promotes mitochondrial respiration and bioenergetics during early phases of ER stress. J Cell Sci. 2011 Jul;124(Pt 13):2143–52.

212. Hayashi T, Su TP. Sigma-1 receptor chaperones at the ER-mitochondrion interface regulate Ca(2+) signaling and cell survival. Cell. 2007 Nov;131(3):596–610.

213. Hou S, Wang L, Zhang G. Mitofusin-2 regulates inflammation-mediated mouse neuroblastoma N2a cells dysfunction and endoplasmic reticulum stress via the Yap-Hippo pathway. J Physiol Sci. 2019 Sep;69(5):697–709.

214. Ngoh GA, Papanicolaou KN, Walsh K. Loss of mitofusin 2 promotes endoplasmic reticulum stress. J Biol Chem. 2012 Jun;287(24):20321–32.

215. Carreras-Sureda A, Jaña F, Urra H, Durand S, Mortenson DE, Sagredo A, et al. Non-canonical function of IRE1α determines mitochondria-associated endoplasmic reticulum composition to control calcium transfer and bioenergetics. Nat Cell Biol. 2019 Jun;21(6):755–67.

216. Shibao K, Fiedler MJ, Nagata J, Minagawa N, Hirata K, Nakayama Y, et al. The type III inositol 1,4,5-trisphosphate receptor is associated with aggressiveness of colorectal carcinoma. Cell Calcium. 2010 Dec;48(6):315–23.

217. Pierro C, Cook SJ, Foets TCF, Bootman MD, Roderick HL. Oncogenic K-Ras suppresses IP_3-dependent Ca^{2+} release through remodelling of the isoform composition of IP_3Rs and ER luminal Ca^{2+} levels in colorectal cancer cell lines. J Cell Sci. 2014 Apr;127(Pt 7):1607–19.

218. Liao C, Zhang Y, Fan C, Herring LE, Liu J, Locasale JW, et al. Identification of BBOX1 as a Therapeutic Target in Triple-Negative Breast Cancer. Cancer Discovery. 2020 Nov;10(11):1706–21.

219. Singh A, Chagtoo M, Tiwari S, George N, Chakravarti B, Khan S, et al. Inhibition of Inositol 1, 4, 5-Trisphosphate Receptor Induce Breast Cancer Cell Death Through Deregulated Autophagy and Cellular Bioenergetics. Journal of Cellular Biochemistry. 2017 Jan;118(8):2333–46.

220. Zhong F, Harr MW, Bultynck G, Monaco G, Parys JB, De Smedt H, et al. Induction of Ca2+-driven apoptosis in chronic lymphocytic leukemia cells by peptide-mediated disruption of Bcl-2–IP3 receptor interaction. Blood. 2011 Mar;117(10):2924–34.

221. Bononi A, Bonora M, Marchi S, Missiroli S, Poletti F, Giorgi C, et al. Identification of PTEN at the ER and MAMs and its regulation of Ca2+ signaling and apoptosis in a protein phosphatase-dependent manner. Cell Death Differ. 2013 Dec;20(12):1631–43.

222. Kuchay S, Giorgi C, Simoneschi D, Pagan J, Missiroli S, Saraf A, et al. PTEN counteracts FBXL2 to promote IP3R3- and Ca2+-mediated apoptosis limiting tumour growth. Nature. 2017 Jun 22;546(7659):554–8.

223. Heslop KA, Milesi V, Maldonado EN. VDAC Modulation of Cancer Metabolism: Advances and Therapeutic Challenges. Frontiers in Physiology. 2021 Sep;12:742839.

224. Arif T, Vasilkovsky L, Refaely Y, Konson A, Shoshan-Barmatz V. Silencing VDAC1 Expression by siRNA Inhibits Cancer Cell Proliferation and Tumor Growth In Vivo. Molecular Therapy - Nucleic Acids. 2014 Jan;3:159.

225. Monaco G, Decrock E, Arbel N, van Vliet AR, La Rovere RM, De Smedt H, et al. The BH4 Domain of Anti-apoptotic Bcl-XL, but Not That of the Related Bcl-2, Limits the Voltage-dependent Anion Channel 1 (VDAC1)-mediated Transfer of Pro-apoptotic Ca2+ Signals to Mitochondria. Journal of Biological Chemistry. 2015 Apr;290(14):9150–61.

226. Fouqué A, Lepvrier E, Debure L, Gouriou Y, Malleter M, Delcroix V, et al. The apoptotic members CD95, BclxL, and Bcl-2 cooperate to promote cell migration by inducing Ca2+ flux from the endoplasmic reticulum to mitochondria. Cell Death Differ. 2016 Oct;23(10):1702–16.

227. Arbel N, Ben-Hail D, Shoshan-Barmatz V. Mediation of the Antiapoptotic Activity of Bcl-xL Protein upon Interaction with VDAC1 Protein. Journal of Biological Chemistry. 2012 Jun;287(27):23152–61.

228. Huang H, Shah K, Bradbury NA, Li C, White C. Mcl-1 promotes lung cancer cell migration by directly interacting with VDAC to increase mitochondrial Ca2+ uptake and reactive oxygen species generation. Cell Death Dis. 2014 Oct;5(10):1482–1482.

229. Tossato. The mitochondrial calcium uniporter regulates breast cancer progression via HIF-1α. EMBO Molecular Medicine. 2016 May;8(5):569–85.

230. Liu Y, Jin M, Wang Y, Zhu J, Tan R, Zhao J, et al. MCU-induced mitochondrial calcium uptake promotes mitochondrial biogenesis and colorectal cancer growth. Sig Transduct Target Ther. 2020 May;5(1):1–13.

231. Wang X, Li Y, Li Z, Lin S, Wang H, Sun J, et al. Mitochondrial calcium uniporter drives metastasis and confers a targetable cystine dependency in pancreatic cancer. Cancer Res. 2022 Apr;82(12):2254–68.

232. Johri A, Chandra A. Connection Lost, MAM: Errors in ER–Mitochondria Connections in Neurodegenerative Diseases. Brain Sciences. 2021 Nov;11(11):1437.

233. Yu W, Jin H, Huang Y. Mitochondria-associated membranes (MAMs): a potential therapeutic target for treating Alzheimer's disease. Clinical Science. 2021 Jan 6;135(1):109–26.

234. Völgyi K, Badics K, Sialana FJ, Gulyássy P, Udvari EB, Kis V, et al. Early Presymptomatic Changes in the Proteome of Mitochondria-Associated Membrane in the APP/PS1 Mouse Model of Alzheimer's Disease. Mol Neurobiol. 2018 Oct;55(10):7839–57.

235. Eysert F, Kinoshita PF, Mary A, Vaillant-Beuchot L, Checler F, Chami M. Molecular Dysfunctions of Mitochondria-Associated Membranes (MAMs) in Alzheimer's Disease. International Journal of Molecular Sciences. 2020 Jan;21(24):9521.

236. Beaulant A, Dia M, Pillot B, Chauvin MA, Ji-cao J, Durand C, et al. Endoplasmic reticulum-mitochondria miscommunication is an early and causal trigger of hepatic insulin resistance and steatosis. Journal of Hepatology. 2022 Sep;77(3):710–22.

237. Tubbs E, Theurey P, Vial G, Bendridi N, Bravard A, Chauvin MA, et al. Mitochondria-Associated Endoplasmic Reticulum Membrane (MAM) Integrity Is Required for Insulin Signaling and Is Implicated in Hepatic Insulin Resistance. Diabetes. 2014 Sep 15;63(10):3279–94.

238. Gan KX, Wang C, Chen JH, Zhu CJ, Song GY. Mitofusin-2 ameliorates high-fat diet-induced insulin resistance in liver of rats. World Journal of Gastroenterology. 2013 Mar 14;19(10):1572–81.

239. Sebastián D, Hernández-Alvarez MI, Segalés J, Sorianello E, Muñoz JP, Sala D, et al. Mitofusin 2 (Mfn2) links mitochondrial and endoplasmic reticulum function with insulin signaling and is essential for normal glucose homeostasis. Proceedings of the National Academy of Sciences. 2012 Apr 3;109(14):5523–8.

240. Davis DB, Delmonte AJ, Ly CT, McNally EM. Myoferlin, a candidate gene and potential modifier of muscular dystrophy. Hum Mol Genet. 2000 Jan;9(2):217–26.

241. Davis DB, Doherty KR, Delmonte AJ, McNally EM. Calcium-sensitive phospholipid binding properties of normal and mutant ferlin C2 domains. J Biol Chem. 2002 Jun;277(25):22883–8.

242. Redpath GMI, Sophocleous RA, Turnbull L, Whitchurch CB, Cooper ST. Ferlins Show Tissue-Specific Expression and Segregate as Plasma Membrane/Late Endosomal or Trans-Golgi/Recycling Ferlins. Traffic. 2016 Mar;17(3):245–66.

243. Gupta S, Yano J, Htwe HH, Shin HR, Cakir Z, Ituarte T, et al. Lysosomal retargeting of Myoferlin mitigates membrane stress to enable pancreatic cancer growth. Nature Cell Biology. 2021 Mar;23(3):232–42.

244. Turtoi A, Blomme A, Bellahcène A, Gilles C, Hennequière V, Peixoto P, et al. Myoferlin is a key regulator of EGFR activity in breast cancer. Cancer Res. 2013 Sep;73(17):5438–48.

245. Doherty KR, Demonbreun AR, Wallace GQ, Cave A, Posey AD, Heretis K, et al. The endocytic recycling protein EHD2 interacts with myoferlin to regulate myoblast fusion. J Biol Chem. 2008 Jul;283(29):20252–60.

246. Doherty KR, Cave A, Davis DB, Delmonte AJ, Posey A, Earley JU, et al. Normal myoblast fusion requires myoferlin. Development. 2005 Dec;132(24):5565–75.

247. Eisenberg MC, Kim Y, Li R, Ackerman WE, Kniss DA, Friedman A. Mechanistic modeling of the effects of myoferlin on tumor cell invasion. Proc Natl Acad Sci U S A. 2011 Dec;108(50):20078–83.

248. Posey AD, Demonbreun A, McNally EM. Ferlin proteins in myoblast fusion and muscle growth. Curr Top Dev Biol. 2011 Jun;96:203–30.

249. Yasunaga S, Grati M, Chardenoux S, Smith TN, Friedman TB, Lalwani AK, et al. OTOF encodes multiple long and short isoforms: genetic evidence that the long ones underlie recessive deafness DFNB9. Am J Hum Genet. 2000 Sep;67(3):591–600.

250. Kiselev A, Vaz R, Knyazeva A, Sergushichev A, Dmitrieva R, Khudiakov A, et al. Truncating Variant in Myof Gene Is Associated With Limb-Girdle Type Muscular Dystrophy and Cardiomyopathy. Frontiers in Genetics. 2019 Jun;10:608.

251. Ariano A, D'Apolito M, Bova M, Bellanti F, Loffredo S, D'Andrea G, et al. A myoferlin gain-of-function variant associates with a new type of hereditary angioedema. Allergy. 2020 Jun;75(11):2989–92.

252. Achanzar WE, Ward S. A nematode gene required for sperm vesicle fusion. J Cell Sci. 1997 May;110 (Pt 9):1073–81.

253. Choi B, Ahmed Z, Riazuddin S, Bhinder M, Shahzad M, Husnain T, et al. Identities and frequencies of mutations of the otoferlin gene (OTOF) causing DFNB9 deafness in Pakistan. Clinical Genetics. 2009;75(3):237–43.

254. Blomme A, Fahmy K, Peulen O, Costanza B, Fontaine M, Struman I, et al. Myoferlin is a novel exosomal protein and functional regulator of cancer-derived exosomes. Oncotarget. 2016 Dec;7(50):83669–83.

255. Kumar B, Brown NV, Swanson BJ, Schmitt AC, Old M, Ozer E, et al. High expression of myoferlin is associated with poor outcome in oropharyngeal squamous cell carcinoma patients and is inversely associated with HPV-status. Oncotarget. 2016 Apr;7(14):18665–77.

256. Demonbreun AR, Lapidos KA, Heretis K, Levin S, Dale R, Pytel P, et al. Myoferlin regulation by NFAT in muscle injury, regeneration and repair. J Cell Sci. 2010 Jul;123(Pt 14):2413–22.

257. Hermanns C, Hampl V, Holzer K, Aigner A, Penkava J, Frank N, et al. The novel MKL target gene myoferlin modulates expansion and senescence of hepatocellular carcinoma. Oncogene. 2017 Jun;36(24):3464–76.

258. Bulankina AV, Thoms S. Functions of Vertebrate Ferlins. Cells. 2020 Mar;9(3):534.

259. Lek A, Evesson FJ, Sutton RB, North KN, Cooper ST. Ferlins: regulators of vesicle fusion for auditory neurotransmission, receptor trafficking and membrane repair. Traffic. 2012 Feb;13(2):185–94.

260. Corbalan-Garcia S, Gómez-Fernández JC. Signaling through C2 domains: More than one lipid target. Biochimica et Biophysica Acta (BBA) - Biomembranes. 2014 Jun;1838(6):1536–47.

261. Zhang D, Aravind L. Identification of novel families and classification of the C2 domain superfamily elucidate the origin and evolution of membrane targeting activities in eukaryotes. Gene. 2010 Dec;469(1):18–30.

262. Nalefski EA, Falke JJ. The C2 domain calcium-binding motif: Structural and functional diversity. Protein Science. 1996 Sep;5(12):2375–90.

263. Shin OH, Han W, Wang Y, Südhof TC. Evolutionarily Conserved Multiple C2 Domain Proteins with Two Transmembrane Regions (MCTPs) and Unusual Ca2+ Binding Properties. Journal of Biological Chemistry. 2005 Jan;280(2):1641–51.

264. Min SW, Chang WP, Südhof TC. E-Syts, a family of membranous Ca2+-sensor proteins with multiple C2 domains. Proceedings of the National Academy of Sciences. 2007 Mar;104(10):3823–8.

265. Washington NL, Ward S. FER-1 regulates Ca2+-mediated membrane fusion during C. elegans spermatogenesis. Journal of Cell Science. 2006 Jun;119(12):2552–62.

266. Marty NJ, Holman CL, Abdullah N, Johnson CP. The C2 domains of otoferlin, dysferlin, and myoferlin alter the packing of lipid bilayers. Biochemistry. 2013 Aug;52(33):5585–92.

267. Harsini FM, Chebrolu S, Fuson KL, White MA, Rice AM, Sutton RB. FerA is a Membrane-Associating Four-Helix Bundle Domain in the Ferlin Family of Membrane-Fusion Proteins. Sci Rep. 2018 Jul;8(1):10949.

268. Morrée A de, Hensbergen PJ, Haagen HHHBM van, Dragan I, Deelder AM, Hoen PAC 't, et al. Proteomic Analysis of the Dysferlin Protein Complex Unveils Its Importance for Sarcolemmal Maintenance and Integrity. PLOS ONE. 2010 Nov;5(11):13854.

269. Przybylski RJ, Szigeti V, Davidheiser S, Kirby AC. Calcium regulation of skeletal myogenesis. II. Extracellular and cell surface effects. Cell Calcium. 1994 Feb;15(2):132–42.

270. Demonbreun AR, Posey AD, Heretis K, Swaggart KA, Earley JU, Pytel P, et al. Myoferlin is required for insulin-like growth factor response and muscle growth. FASEB J. 2010 Apr;24(4):1284–95.

271. Redpath GMI, Woolger N, Piper AK, Lemckert FA, Lek A, Greer PA, et al. Calpain cleavage within dysferlin exon 40a releases a synaptotagmin-like module for membrane repair. Molecular biology of the cell. 2014 Jan;25(19):3037–48.

272. O'Connor V, Lee AG. Synaptic vesicle fusion and synaptotagmin: 2B or not 2B? Nat Neurosci. 2002 Sep;5(9):823–4.

273. Bernatchez PN, Acevedo L, Fernandez-Hernando C, Murata T, Chalouni C, Kim J, et al. Myoferlin regulates vascular endothelial growth factor receptor-2 stability and function. J Biol Chem. 2007 Oct;282(42):30745–53.

274. Sharma A, Yu C, Leung C, Trane A, Lau M, Utokaparch S, et al. A new role for the muscle repair protein dysferlin in endothelial cell adhesion and angiogenesis. Arterioscler Thromb Vasc Biol. 2010 Nov;30(11):2196–204.

275. Yu C, Sharma A, Trane A, Utokaparch S, Leung C, Bernatchez P. Myoferlin gene silencing decreases Tie-2 expression in vitro and angiogenesis in vivo. Vascul Pharmacol. 2011 Jul;55(1–3):26–33.

276. Bernatchez PN, Sharma A, Kodaman P, Sessa WC. Myoferlin is critical for endocytosis in endothelial cells. Am J Physiol Cell Physiol. 2009 Sep;297(3):C484-492.

277. Iacobuzio-Donahue CA, Maitra A, Shen-Ong GL, van Heek T, Ashfaq R, Meyer R, et al. Discovery of Novel Tumor Markers of Pancreatic Cancer using Global Gene Expression Technology. The American Journal of Pathology. 2002 Apr;160(4):1239–49.

278. Amatschek S, Koenig U, Auer H, Steinlein P, Pacher M, Gruenfelder A, et al. Tissue-Wide Expression Profiling Using cDNA Subtraction and Microarrays to Identify Tumor-Specific Genes. Cancer Research. 2004 Feb;64(3):844–56.

279. Yadav A, Kumar B, Lang JC, Teknos TN, Kumar P. A muscle-specific protein "myoferlin" modulates IL-6/STAT3 signaling by chaperoning activated STAT3 to nucleus. Oncogene. 2017 Nov;36(46):6374–82.

280. Wang WS, Liu XH, Liu LX, Lou WH, Jin DY, Yang PY, et al. iTRAQ-based quantitative proteomics reveals myoferlin as a novel prognostic predictor in pancreatic adenocarcinoma. J Proteomics. 2013 Oct;91:453–65.

281. Adam PJ, Boyd R, Tyson KL, Fletcher GC, Stamps A, Hudson L, et al. Comprehensive Proteomic Analysis of Breast Cancer Cell Membranes Reveals Unique Proteins with Potential Roles in Clinical Cancer. Journal of Biological Chemistry. 2003 Feb;278(8):6482–9.

282. Leung C, Yu C, Lin MI, Tognon C, Bernatchez P. Expression of myoferlin in human and murine carcinoma tumors: role in membrane repair, cell proliferation, and tumorigenesis. Am J Pathol. 2013 May;182(5):1900–9.

283. Song DH, Ko GH, Lee JH, Lee JS, Lee GW, Kim HC, et al. Myoferlin expression in non-small cell lung cancer: Prognostic role and correlation with VEGFR-2 expression. Oncol Lett. 2016 Feb;11(2):998–1006.

284. Koh HM, An HJ, Ko GH, Lee JH, Lee JS, Kim DC, et al. Identification of Myoferlin Expression for Prediction of Subsequent Primary Malignancy in Patients With Clear Cell Renal Cell Carcinoma. In Vivo. 2019 Jul;33(4):1103–8.

285. Kim MH, Song DH, Ko GH, Lee JH, Kim DC, Yang JW, et al. Myoferlin Expression and Its Correlation with FIGO Histologic Grading in Early-Stage Endometrioid Carcinoma. J Pathol Transl Med. 2018 Mar;52(2):93–7.

286. Li R, Ackerman WE, Mihai C, Volakis LI, Ghadiali S, Kniss DA. Myoferlin depletion in breast cancer cells promotes mesenchymal to epithelial shape change and stalls invasion. PLoS One. 2012;7(6):39766.

287. Volakis LI, Li R, Ackerman WE, Mihai C, Bechel M, Summerfield TL, et al. Loss of myoferlin redirects breast cancer cell motility towards collective migration. PLoS One. 2014;9(2):86110.

288. Blackstone BN, Li R, Ackerman WE, Ghadiali SN, Powell HM, Kniss DA. Myoferlin depletion elevates focal adhesion kinase and paxillin phosphorylation and enhances cell-matrix adhesion in breast cancer cells. Am J Physiol Cell Physiol. 2015 Apr;308(8):642–9.

289. Barnhouse VR, Weist JL, Shukla VC, Ghadiali SN, Kniss DA, Leight JL. Myoferlin regulates epithelial cancer cell plasticity and migration through autocrine TGF-β1 signaling. Oncotarget. 2018 Apr;9(27):19209–22.

290. Zhang W, Zhou P, Meng A, Zhang R, Zhou Y. Down-regulating Myoferlin inhibits the vasculogenic mimicry of melanoma via decreasing MMP-2 and inducing mesenchymal-to-epithelial transition. J Cell Mol Med. 2018 Mar;22(3):1743–54.

291. Örtegren U, Aboulaich N, Öst A, Strålfors P. A new role for caveolae as metabolic platforms. Trends in Endocrinology & Metabolism. 2007 Nov;18(9):344–9.

292. Piper AK, Ross SE, Redpath GM, Lemckert FA, Woolger N, Bournazos A, et al. Enzymatic cleavage of myoferlin releases a dual C2-domain module linked to ERK signalling. Cell Signal. 2017 May;33:30–40.

293. Qian T, Liu C, Ding Y, Guo C, Cai R, Wang X, et al. PINCH-1 interacts with myoferlin to promote breast cancer progression and metastasis. Oncogene. 2020 Mar;39(10):2069–87.

294. Li M, Peng F, Wang G, Liang X, Shao M, Chen Z, et al. Coupling of Cell Surface Biotinylation and SILAC-Based Quantitative Proteomics Identified Myoferlin as a Potential Therapeutic Target for Nasopharyngeal Carcinoma Metastasis. Front Cell Dev Biol. 2021 Jun;9:621810.

295. Harada K, Sakamoto N, Ukai S, Yamamoto Y, Pham QT, Taniyama D, et al. Establishment of oxaliplatin-resistant gastric cancer organoids: importance of myoferlin in the acquisition of oxaliplatin resistance. Gastric Cancer. 2021 Jul;

296. Rademaker G, Costanza B, Bellier J, Herfs M, Peiffer R, Agirman F, et al. Human colon cancer cells highly express myoferlin to maintain a fit mitochondrial network and escape p53-driven apoptosis. Oncogenesis. 2019 Mar;8(3):1–13.

297. Pi R, Chen Y, Du Y, Dong S. Comprehensive Analysis of Myoferlin in Human Pancreatic Cancer via Bioinformatics. BioMed Research International. 2021 Dec;2021:2602322.

298. Fahmy K, Gonzalez A, Arafa M, Peixoto P, Bellahcène A, Turtoi A, et al. Myoferlin plays a key role in VEGFA secretion and impacts tumor-associated angiogenesis in human pancreas cancer. Int J Cancer. 2016 Feb;138(3):652–63.

299. Porporato PE, Payen VL, Pérez-Escuredo J, De Saedeleer CJ, Danhier P, Copetti T, et al. A mitochondrial switch promotes tumor metastasis. Cell Rep. 2014 Aug;8(3):754–66.

300. LeBleu VS, O'Connell JT, Gonzalez Herrera KN, Wikman H, Pantel K, Haigis MC, et al. PGC-1α mediates mitochondrial biogenesis and oxidative phosphorylation in cancer cells to promote metastasis. Nat Cell Biol. 2014 Oct;16(10):992–1003.

301. Li Y, He Y, Shao T, Pei H, Guo W, Mi D, et al. Modification and Biological Evaluation of a Series of 1,5-Diaryl-1,2,4-triazole Compounds as Novel Agents against Pancreatic Cancer Metastasis through Targeting Myoferlin. J Med Chem. 2019 May;62(10):4949–66.

302. Rademaker G, Boumahd Y, Peiffer R, Anania S, Wissocq T, Liégeois M, et al. Myoferlin targeting triggers mitophagy and primes ferroptosis in pancreatic cancer cells. Redox Biology. 2022 Jul;53:102324.

303. Inoue M, Wakayama Y, Kojima H, Shibuya S, Jimi T, Oniki H, et al. Expression of myoferlin in skeletal muscles of patients with dysferlinopathy. Tohoku J Exp Med. 2006 Jun;209(2):109–16.

304. Leung C, Shaheen F, Bernatchez P, Hackett TL. Expression of myoferlin in human airway epithelium and its role in cell adhesion and zonula occludens-1 expression. PLoS One. 2012;7(7):40478.

305. Lippi G, Mattiuzzi C. The global burden of pancreatic cancer. Arch Med Sci. 2020 May;16(4):820–4.

306. Wu J, Liu L, Matsuda T, Zhao Y, Rebane A, Drobizhev M, et al. Improved orange and red Ca^{2}± indicators and photophysical considerations for optogenetic applications. ACS Chem Neurosci. 2013 Jun;4(6):963–72.

307. Schindelin J, Arganda-Carreras I, Frise E, Kaynig V, Longair M, Pietzsch T, et al. Fiji: an open-source platform for biological-image analysis. Nat Methods. 2012 Jul;9(7):676–82.

308. Stauffer W, Sheng H, Lim HN. EzColocalization: An ImageJ plugin for visualizing and measuring colocalization in cells and organisms. Sci Rep. 2018 Oct;8(1):15764.

309. de Chaumont F, Dallongeville S, Chenouard N, Hervé N, Pop S, Provoost T, et al. Icy: an open bioimage informatics platform for extended reproducible research. Nat Methods. 2012 Jul;9(7):690–6.

310. Pearson K. Determination of the Coefficient of Correlation. Science. 1909;30(757):23–5.

311. Schober P, Boer C, Schwarte LA. Correlation Coefficients: Appropriate Use and Interpretation. Anesth Analg. 2018 May;126(5):1763–8.

312. Spearman C. The proof and measurement of association between two things. By C. Spearman, 1904. Am J Psychol. 1987 Fall-Winter;100(3–4):441–71.

313. Manders EMM, Verbeek FJ, Aten JA. Measurement of co-localization of objects in dual-colour confocal images. Journal of Microscopy. 1993;169(3):375–82.

314. Li Q, Lau A, Morris TJ, Guo L, Fordyce CB, Stanley EF. A syntaxin 1, Galpha(o), and N-type calcium channel complex at a presynaptic nerve terminal: analysis by quantitative immunocolocalization. J Neurosci. 2004 Apr 21;24(16):4070–81.

315. Lagache T, Sauvonnet N, Danglot L, Olivo-Marin JC. Statistical analysis of molecule colocalization in bioimaging. Cytometry Part A. 2015;87(6):568–79.

316. Lagache T, Grassart A, Dallongeville S, Faklaris O, Sauvonnet N, Dufour A, et al. Mapping molecular assemblies with fluorescence microscopy and object-based spatial statistics. Nat Commun. 2018 Dec;9(1):698.

317. Bolte S, Cordelières FP. A guided tour into subcellular colocalization analysis in light microscopy. J Microsc. 2006 Dec;224(Pt 3):213–32.

318. Guala D, Bernhem K, Blal HA, Jans D, Lundberg E, Brismar H, et al. Experimental validation of predicted cancer genes using FRET. Methods Appl Fluoresc. 2018 Apr;6(3):035007.

319. Viale A, Pettazzoni P, Lyssiotis CA, Ying H, Sánchez N, Marchesini M, et al. Oncogene ablation-resistant pancreatic cancer cells depend on mitochondrial function. Nature. 2014 Oct;514(7524):628–32.

320. Deer EL, Gonzalez-Hernandez J, Coursen JD, Shea JE, Ngatia J, Scaife CL, et al. Phenotype and Genotype of Pancreatic Cancer Cell Lines. Pancreas. 2010 May;39(4):425–35.

321. Elsässer HP, Lehr U, Agricola B, Kern HF. Establishment and characterisation of two cell lines with different grade of differentiation derived from one primary human pancreatic adenocarcinoma. Virchows Arch B Cell Pathol Incl Mol Pathol. 1992;61(5):295–306.

322. Lee KM, Nguyen C, Ulrich AB, Pour PM, Ouellette MM. Immortalization with telomerase of the Nestin-positive cells of the human pancreas. Biochemical and Biophysical Research Communications. 2003 Feb;301(4):1038–44.

323. Bakir H. Studies on muscular dystrophy associated genes. Durham University; 2007.

324. Elinder F, Akanda N, Tofighi R, Shimizu S, Tsujimoto Y, Orrenius S, et al. Opening of plasma membrane voltage-dependent anion channels (VDAC) precedes caspase activation in neuronal apoptosis induced by toxic stimuli. Cell death and differentiation. 2005 Sep;12:1134–40.

325. Okeke E. Epithelial-mesenchymal transition, translocation of Ca2+ signalling complexes and regulation of migration in pancreatic cancer cells. University of Liverpool; 2015.

326. Okeke E, Parker T, Dingsdale H, Concannon M, Awais M, Voronina S, et al. Epithelial-mesenchymal transition, IP3 receptors and ER-PM junctions: translocation of Ca2+ signalling complexes and regulation of migration. Biochem J. 2016 Mar;473(6):757–67.

327. Dhamad AE, Greene E, Sales M, Nguyen P, Beer L, Liyanage R, et al. 75-kDa glucose-regulated protein (GRP75) is a novel molecular signature for heat stress response in avian species. American Journal of Physiology-Cell Physiology. 2020 Feb;318(2):C289–303.

328. Yuan M, Gong M, He J, Xie B, Zhang Z, Meng L, et al. IP3R1/GRP75/VDAC1 complex mediates endoplasmic reticulum stress-mitochondrial oxidative stress in diabetic atrial remodeling. Redox Biology. 2022 Jun;52:102289.

329. Lachmann A, Torre D, Keenan AB, Jagodnik KM, Lee HJ, Wang L, et al. Massive mining of publicly available RNA-seq data from human and mouse. Nat Commun. 2018 Apr 10;9(1):1366.

330. Miller HE, Bishop AJR. Correlation AnalyzeR: functional predictions from gene co-expression correlations. BMC Bioinformatics. 2021 Apr 20;22(1):206.

331. Morgenstern M, Peikert CD, Lübbert P, Suppanz I, Klemm C, Alka O, et al. Quantitative high-confidence human mitochondrial proteome and its dynamics in cellular context. Cell Metabolism. 2021 Dec;33(12):2464–83.

332. Forner F, Foster LJ, Campanaro S, Valle G, Mann M. Quantitative proteomic comparison of rat mitochondria from muscle, heart, and liver. Mol Cell Proteomics. 2006 Apr;5(4):608–19.

333. Rath S, Sharma R, Gupta R, Ast T, Chan C, Durham TJ, et al. MitoCarta3.0: an updated mitochondrial proteome now with sub-organelle localization and pathway annotations. Nucleic Acids Research. 2021 Jan;49(D1):D1541–7.

334. Szczesniak LM, Bonzerato CG, Wojcikiewicz RJH. Identification of the Bok Interactome Using Proximity Labeling. Frontiers in Cell and Developmental Biology. 2021 May;9:689951.

335. Avalle L, Poli V. Nucleus, Mitochondrion, or Reticulum? STAT3 à La Carte. International Journal of Molecular Sciences. 2018 Sep;19(9):2820.

336. Avalle L, Camporeale A, Morciano G, Caroccia N, Ghetti E, Orecchia V, et al. STAT3 localizes to the ER, acting as a gatekeeper for ER-mitochondrion Ca2+ fluxes and apoptotic responses. Cell Death Differ. 2019 May;26(5):932–42.

337. Su Y, Huang X, Huang Z, Huang T, Xu Y, Yi C. STAT3 Localizes in Mitochondria-Associated ER Membranes Instead of in Mitochondria. Frontiers in Cell and Developmental Biology. 2020 Apr;8:274.

338. Moutaoufik MT, Malty R, Amin S, Zhang Q, Phanse S, Gagarinova A, et al. Rewiring of the Human Mitochondrial Interactome during Neuronal Reprogramming Reveals Regulators of the Respirasome and Neurogenesis. iScience. 2019 Sep;19:1114–32.

339. Reyes-Castellanos G, Masoud R, Carrier A. Mitochondrial Metabolism in PDAC: From Better Knowledge to New Targeting Strategies. Biomedicines. 2020 Aug;8(8):270.

340. Kovalenko I, Glasauer A, Schöckel L, Sauter DRP, Ehrmann A, Sohler F, et al. Identification of KCa3.1 Channel as a Novel Regulator of Oxidative Phosphorylation in a Subset of Pancreatic Carcinoma Cell Lines. PLOS ONE. 2016 Aug;11(8):160658.

341. Karnevi E, Said K, Andersson R, Rosendahl AH. Metformin-mediated growth inhibition involves suppression of the IGF-I receptor signalling pathway in human pancreatic cancer cells. BMC Cancer. 2013 May;13:235.

342. Rajeshkumar NV, Yabuuchi S, Pai SG, De Oliveira E, Kamphorst JJ, Rabinowitz JD, et al. Treatment of Pancreatic Cancer Patient-Derived Xenograft Panel with Metabolic Inhibitors Reveals Efficacy of Phenformin. Clin Cancer Res. 2017 Sep;23(18):5639–47.

343. Kisfalvi K, Moro A, Sinnett-Smith J, Eibl G, Rozengurt E. Metformin inhibits the growth of human pancreatic cancer xenografts. Pancreas. 2013 Jul;42(5):781–5.

344. Rena G, Hardie DG, Pearson ER. The mechanisms of action of metformin. Diabetologia. 2017;60(9):1577–85.

345. Wang X, Wen Y, Dong J, Cao C, Yuan S. Systematic In-Depth Proteomic Analysis of Mitochondria-Associated Endoplasmic Reticulum Membranes in Mouse and Human Testes. PROTEOMICS. 2018 Jul;18(14):1700478.

346. Chae S, Kim SJ, Do Koo Y, Lee JH, Kim H, Ahn BY, et al. A mitochondrial proteome profile indicative of type 2 diabetes mellitus in skeletal muscles. Exp Mol Med. 2018 Sep;50(9):1–14.

347. Patergnani S, Suski JM, Agnoletto C, Bononi A, Bonora M, De Marchi E, et al. Calcium signaling around Mitochondria Associated Membranes (MAMs). Cell Commun Signal. 2011 Sep;9:19.

348. Ivanova H, Kerkhofs M, Rovere RML, Bultynck G. Endoplasmic reticulum-mitochondrial Ca2+ fluxes underlying cancer cell survival. Frontiers in Oncology. 2017 May;7:70.

349. Tarasov AI, Griffiths EJ, Rutter GA. Regulation of ATP production by mitochondrial Ca2+. Cell Calcium. 2012 Jul;52(1):28–35.

350. Wan B, LaNoue KF, Cheung JY, Scaduto RC. Regulation of Citric Acid Cycle by Calcium. Journal of Biological Chemistry. 1989 Aug;264(23):13430–9.

351. Hom J, Yu T, Yoon Y, Porter G, Sheu SS. Regulation of mitochondrial fission by intracellular Ca2+ in rat ventricular myocytes. Biochim Biophys Acta. 2010;1797(6–7):913–21.

352. Romero-Garcia S, Prado-Garcia H. Mitochondrial calcium: Transport and modulation of cellular processes in homeostasis and cancer (Review). International Journal of Oncology. 2019 Apr;54(4):1155–67.

353. Zhu W, Zhou B, Zhao C, Ba Z, Xu H, Yan X, et al. Myoferlin, a multifunctional protein in normal cells, has novel and key roles in various cancers. J Cell Mol Med. 2019 Nov;23(11):7180–9.

354. Bustos G, Ahumada-Castro U, Silva-Pavez E, Puebla A, Lovy A, Cesar Cardenas J. The ER-mitochondria Ca2+ signaling in cancer progression: Fueling the monster. Int Rev Cell Mol Biol. 2021 Apr;363:49–121.

355. Antigny F, Konig S, Bernheim L, Frieden M. Inositol 1,4,5 trisphosphate receptor 1 is a key player of human myoblast differentiation. Cell Calcium. 2014 Dec;56(6):513–21.

356. Nozato Y, Takami Y, Yamamoto K, Nagasawa M, Nozato S, Imaizumi Y, et al. Novel properties of myoferlin in glucose metabolism via pathways involving modulation of adipose functions. FASEB J. 2020 Feb;34(2):2792–811.

357. Peng W, Wong YC, Krainc D. Mitochondria-lysosome contacts regulate mitochondrial Ca2+ dynamics via lysosomal TRPML1. Proceedings of the National Academy of Sciences. 2020 Aug;117(32):19266–75.

358. Atakpa P, Thillaiappan NB, Mataragka S, Prole DL, Taylor CW. IP3 Receptors Preferentially Associate with ER-Lysosome Contact Sites and Selectively Deliver Ca2+ to Lysosomes. Cell Reports. 2018 Dec;25(11):3180–93.

359. Sun MY, Geyer M, Komarova YA. IP3 receptor signaling and endothelial barrier function. Cell Mol Life Sci. 2017 Nov;74(22):4189–207.

360. Kania E, Roest G, Vervliet T, Parys JB, Bultynck G. IP3 Receptor-Mediated Calcium Signaling and Its Role in Autophagy in Cancer. Front Oncol. 2017 Jul;7:140.

Supplemental figures

7. Supplemental figures

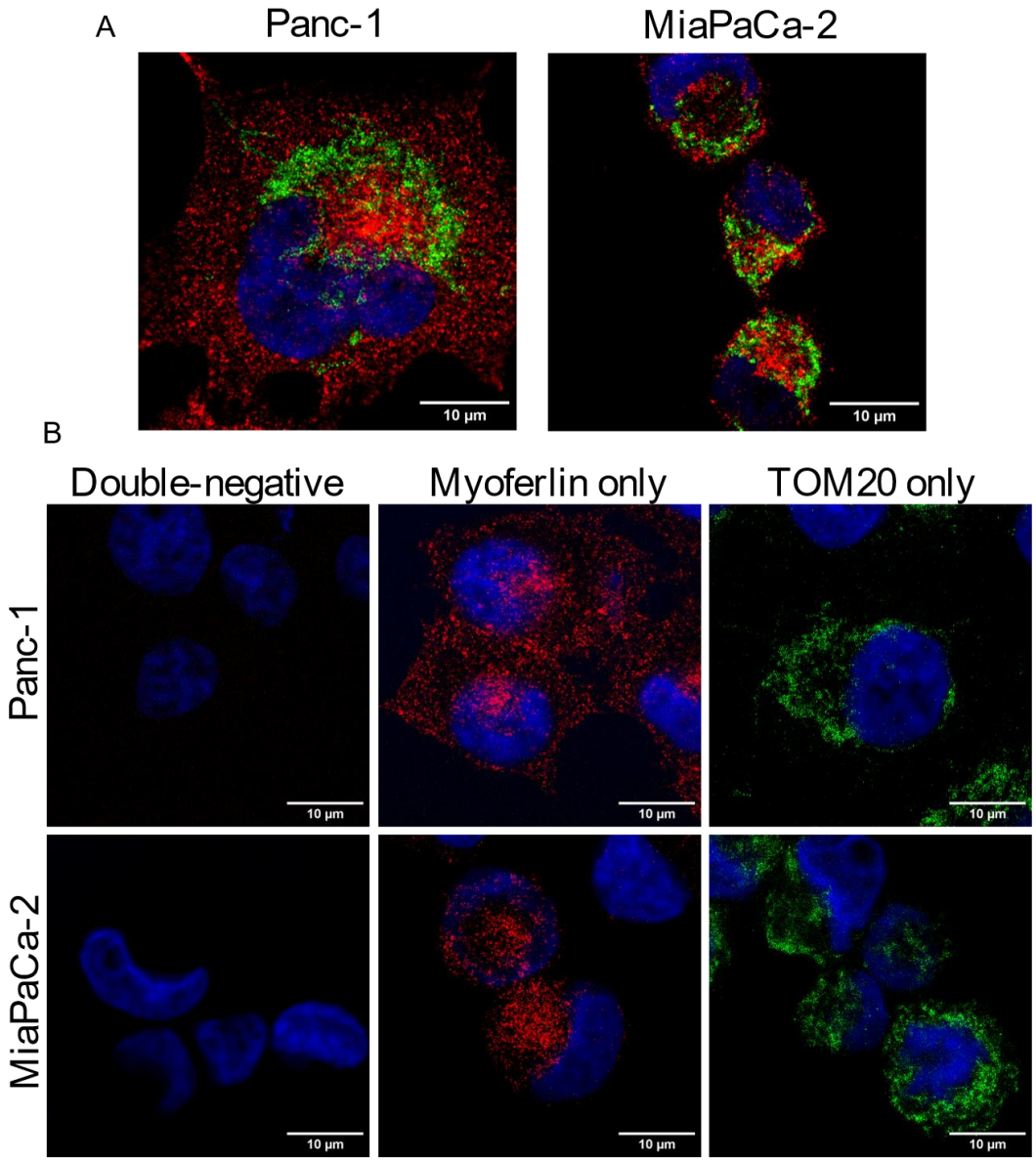

Figure 7-1. **(A)** Pictures at low magnification of myoferlin-TOM20 co-staining in Panc-1 and MiaPaCa-2 cell lines. **(B)** Controls for the myoferlin-TOM20 co-staining. No primary antibodies (double-negative control), myoferlin-only primary antibody or TOM20-only primary antibody were used as negative controls in the presence of secondary antibodies. The negative controls were performed on both Panc-1 and MiaPaCa-2 cell lines

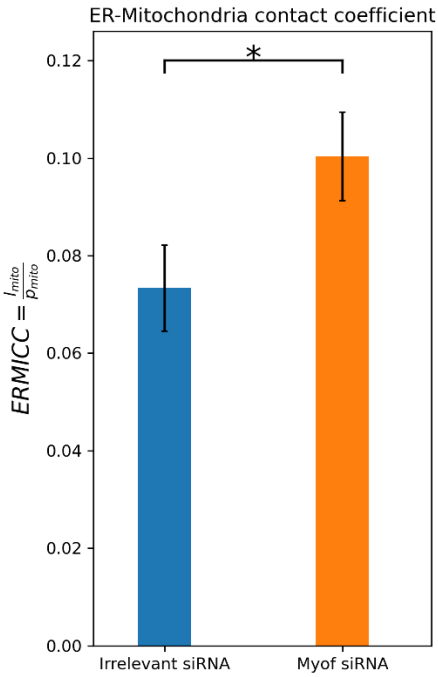

Figure 7-2. ERMICC coeffecient for the irrelevant and Myof#1 siRNA conditions in Panc-1 cells. In myoferlin-silenced cells, the ERMICC was significantly increased. The analyses were made on 24 (555 mitochondria) and 31 (857 mitochondria) images for the irrelevant and Myof#1 siRNA conditions, respectively. The $Dist_{ER\text{-}M}$ was not taken into consideration for the ERMICC. Nevertheless, contacts were considered when less than 30nm seperated ER and mitochondria. P-value = 0.026. For statistical analysis, the test of Mann-Whitney was performed. Mean ± SEM is shown. The analyses were performed by Pr. Marc Thiry.

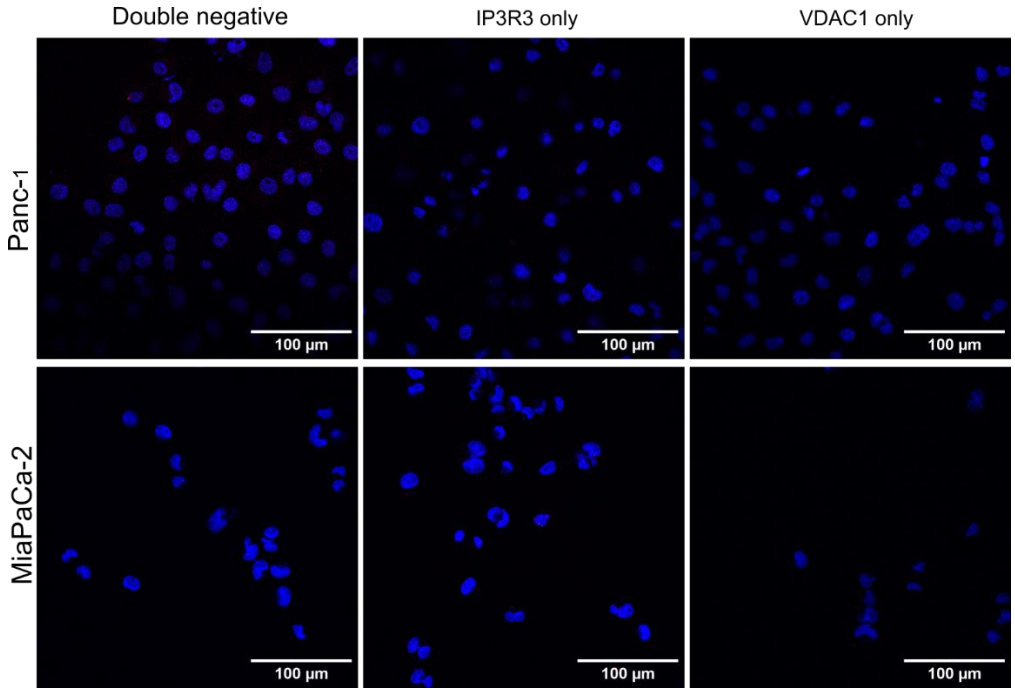

Figure 7-3. Negative controls for the PLA between IP3R3 and VDAC1 in Panc-1 and MiaPaCa-2 cell lines. No primary antibodies (double-negative control), IP3R3-only primary antibody or VDAC1-only primary antibody were used as negative controls in the presence of secondary antibodies.

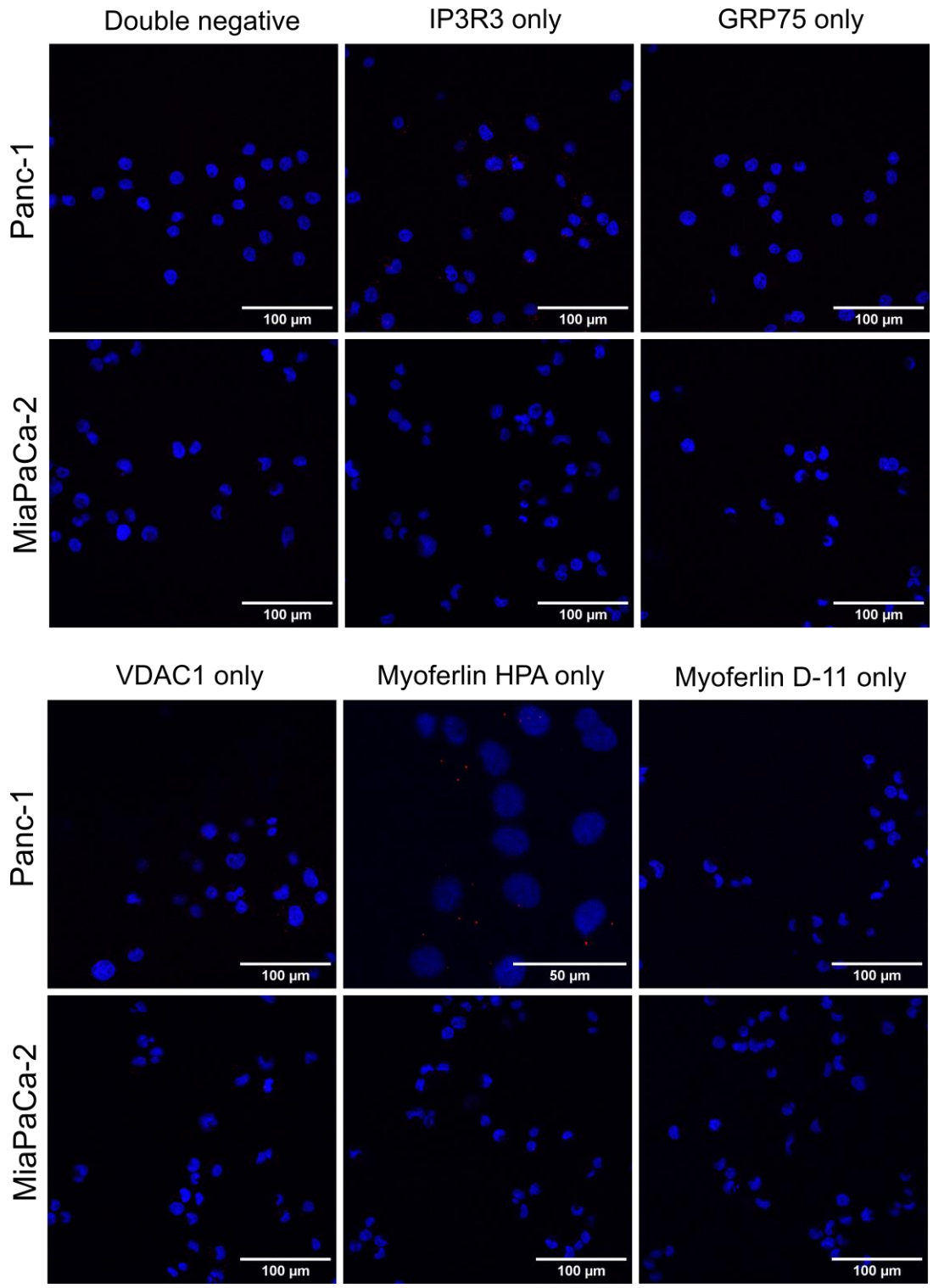

Figure 7-4. Negative controls for the PLA between myoferlin and IP3R3, GRP75 or VDAC1 in Panc-1 and MiaPaCa-2 cell lines. No primary antibodies (double-negative control), IP3R3-only primary antibody, GRP75-only primary antibody, VDAC1-only primary antibody or myoferlin (D-11 or HPA, depending on species compatibility)-only primary antibody were used as negative controls in the presence of secondary antibodies.For the Myoferlin HPA-only negative control in Panc-1, the picture was taken at higher magnification.

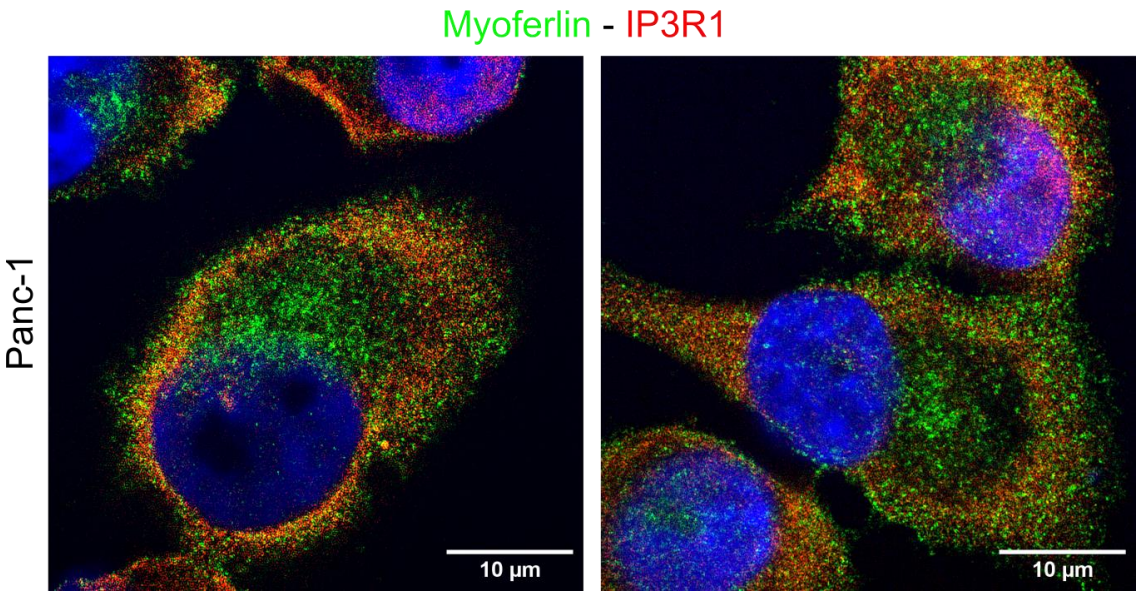

Figure 7-5. Myoferlin-IP3R1 co-staining in the Panc-1 cell line. As described in the literature, in Panc-1 cells, IP3R1 staining appears at the cell periphery in isolated cell (326). Interestingly, myoferlin seemed to colocalize with IP3R1 at cell periphery.

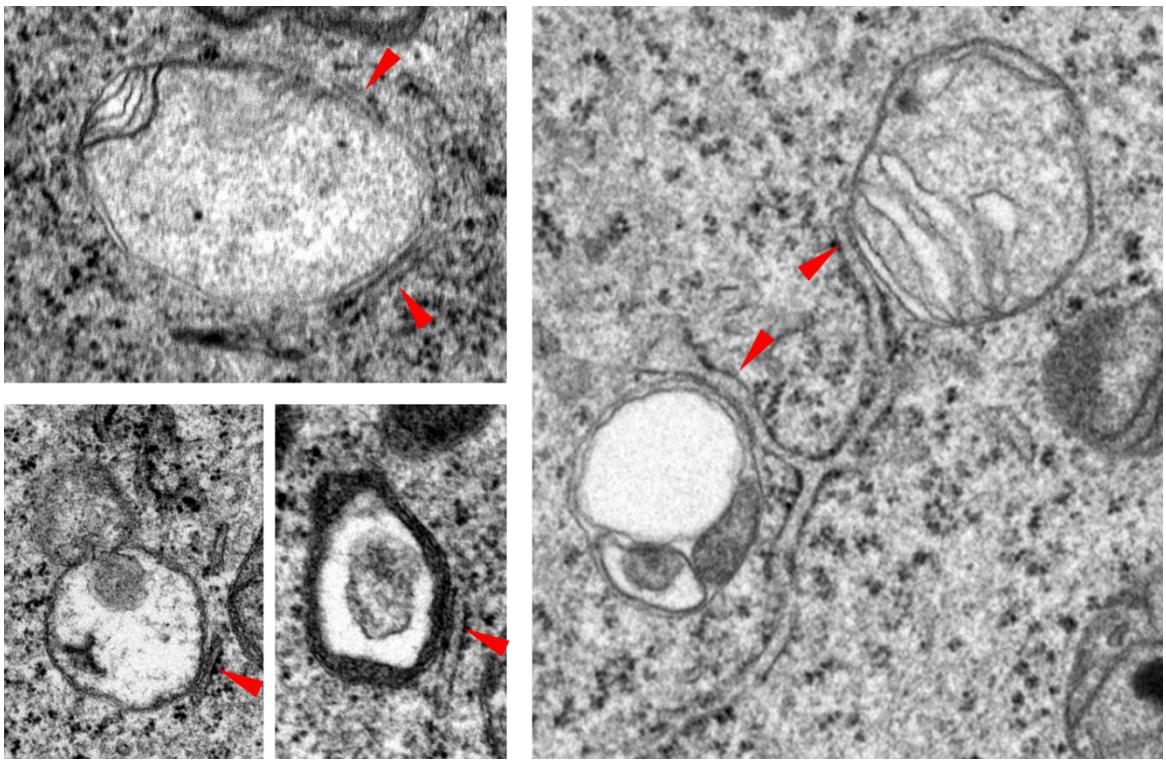

Figure 7-6. TEM pictures of altered mitochondria in contact with ER upon myoferlin silencing. The contacts are highlighted by red arrows. Those pictures were provided by Pr. Marc Thiry.

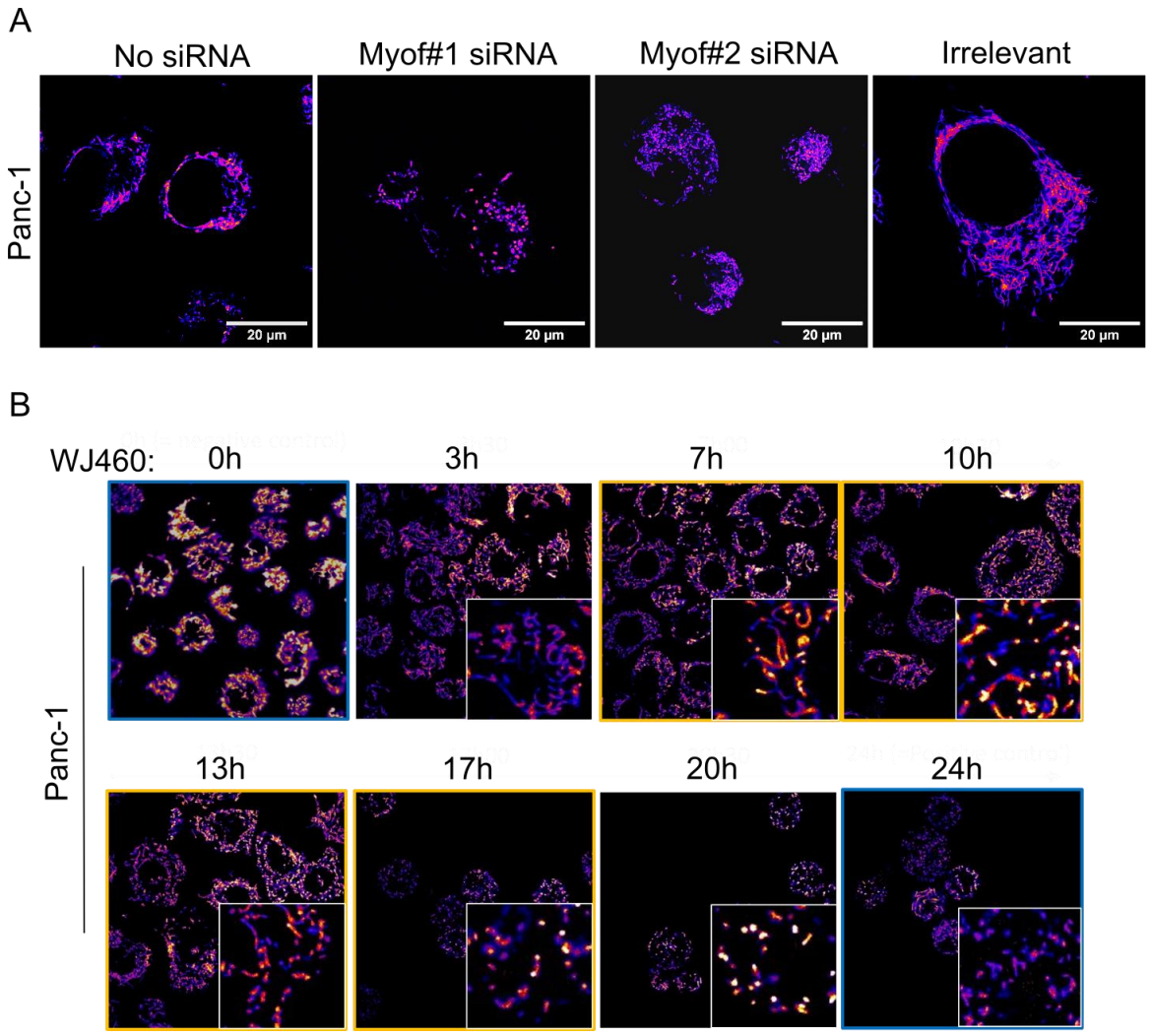

Figure 7-7. Mitochondrial network in Panc-1 cells upon myoferlin silencing or targeting using WJ460. **(A)** Mitochondrial network in Panc-1 in the no siRNA, Myof#1 siRNA, Myof#2 siRNA or irrelevant siRNA conditions using TMRE. **(B)** Effect of WJ460 on the mitochondrial network in Panc-1 cell over time (from 0h to 24h of treatment). TMRE was used for mitochondrial visualization and was used as previously described (302)

Associated publications

Publications

Articles accepted in peer reviewed journal

Rademaker, G.* , Boumahd, Y.* , Peiffer, R., Anania, S., Wissocq, T., Liégeois, M., Luis, G., Sounni, N. E., Agirman, F., Maloujahmoum, N., De Tullio, P., Thiry, M., Bellahcene, A., Castronovo, V., & Peulen, O. (July 2022). Myoferlin targeting triggers mitophagy and primes ferroptosis in pancreatic cancer cells. *Redox Biology, 53*, 102324. doi:10.1016/j.redox.2022.102324
https://hdl.handle.net/2268/289926
Peer Reviewed verified by ORBi

Charavet, C., Van hede, D., Anania, S., MAES, N., Albert, A., & LAMBERT, F. (2022). One-stage versus two-stage piezocision-assisted orthodontic tooth movement: A preclinical study based on Nano-CT and RT-PCR analyses. *Journal of Stomatology, Oral and Maxillofacial Surgery*. doi:10.1016/j.jormas.2022.03.010
https://hdl.handle.net/2268/291953
Peer Reviewed verified by ORBi

Van hede, D., Liang, B., Anania, S., Barzegari, M., Verlée, B., Nolens, G., Pirson, J., Geris, L.* , & LAMBERT, F.*. (2021). 3D-Printed Synthetic Hydroxyapatite Scaffold With In Silico Optimized Macrostructure Enhances Bone Formation In Vivo. *Advanced Functional Materials*. doi:10.1002/adfm.202105002
https://hdl.handle.net/2268/264038
Peer Reviewed verified by ORBi

The COVID-19 Host Genetics Initiative, Gazon, H., JUSZCZAK, D., FADEUR, M., CAMBY, S., MEURIS, C., THYS, M., JACQUES, J., HENKET, M., BEGUIN, Y., Rahmouni, S., Lebrun, M., MOUTSCHEN, M., Misset, B., DARCIS, G., GUIOT, J., AZARZAR, S., DELLOT, P., GOFFLOT, S., & HUYNEN, P. (Other coll.). (2021). Mapping the human genetic architecture of COVID-19. *Nature, 600*, 472-477. doi:10.1038/s41586-021-03767-x
https://hdl.handle.net/2268/260539
Peer Reviewed verified by ORBi

Anania, S., Peiffer, R., Rademaker, G., Hego, A., Thiry, M., Deldicque, L., Francaux, M., Maloujahmoum, N., Agirman, F., Bellahcene, A., Castronovo, V., & Peulen, O. (21 June 2020). Myoferlin is a yet unknown interactor of the mitochondrial dynamics' machinery in pancreas cancer cells. *Cancers, 12* (6), 1643. doi:10.3390/cancers12061643
https://hdl.handle.net/2268/248664
Peer Reviewed verified by ORBi

Peulen, O., Rademaker, G., Anania, S., Turtoi, A., Bellahcene, A., & Castronovo, V. (August 2019). Ferlin overview: from membrane to cancer biology. *Cells, 8*, 954. doi:10.3390/cells8090954
https://hdl.handle.net/2268/238793
Peer Reviewed verified by ORBi

Rademaker, G., Costanza, B., Anania, S., Agirman, F., Maloujahmoum, N., Di Valentin, E., Goval, J.-J., Bellahcene, A., Castronovo, V., & Peulen, O. (June 2019). Myoferlin contributes to the metastatic phenotype of pancreatic cancer cells by enhancing their migratory capacity through the control of oxidative phosphorylation. *Cancers, 11* (6). doi:10.3390/cancers11060853
https://hdl.handle.net/2268/236926
Peer Reviewed verified by ORBi

CHARAVET, C., Van hede, D., Anania, S., MAES, N., & LAMBERT, F. (2019). Multilevel biological responses following piezocision to accelerate orthodontic tooth movement: A study in rats. *Journal of the World Federation of Orthodontists*. doi:10.1016/j.ejwf.2019.07.002
https://hdl.handle.net/2268/241316
Peer Reviewed verified by ORBi

cancers

MDPI

Article

Myoferlin Is a Yet Unknown Interactor of the Mitochondrial Dynamics' Machinery in Pancreas Cancer Cells

Sandy Anania [1,2], Raphaël Peiffer [1,2], Gilles Rademaker [1,2], Alexandre Hego [3], Marc Thiry [4], Louise Deldicque [5], Marc Francaux [5], Naïma Maloujahmoum [1], Ferman Agirman [1], Akeila Bellahcène [1], Vincent Castronovo [1] and Olivier Peulen [1,2,*]

1 Metastasis Research Laboratory (MRL), GIGA-Cancer, Pathology Institute B23, University of Liège, B-4000 Liège, Belgium; sandy.anania@uliege.be (S.A.); r.peiffer@student.uliege.be (R.P.); g.rademaker@uliege.be (G.R.); naima.maloujahmoum@uliege.be (N.M.); f.agirman@uliege.be (F.A.); a.bellahcene@uliege.be (A.B.); vcastronovo@uliege.be (V.C.)
2 Center for Interdisciplinary Research on Medicines (CIRM), Pathology Institute B23, University of Liège, B-4000 Liège, Belgium
3 Imaging Facilities, GIGA-Research, GIGA-Institute B36, University of Liège, B-4000 Liège, Belgium; alexandre.hego@uliege.be
4 Laboratory of Cellular and Tissular Biology, GIGA-Neurosciences, Cell Biology L3, University of Liège, B-4000 Liège, Belgium; mthiry@uliege.be
5 Institute of Neuroscience, Université catholique de Louvain, B-1348 Louvain-la-Neuve, Belgium; louise.deldicque@uclouvain.be (L.D.); marc.francaux@uclouvain.be (M.F.)
* Correspondence: olivier.peulen@uliege.be

Received: 19 May 2020; Accepted: 19 June 2020; Published: 21 June 2020

Abstract: Pancreas ductal adenocarcinoma is one of the deadliest cancers where surgery remains the main survival factor. Mitochondria were described to be involved in tumor aggressiveness in several cancer types including pancreas cancer. We have previously reported that myoferlin controls mitochondrial structure and function, and demonstrated that myoferlin depletion disturbs the mitochondrial dynamics culminating in a mitochondrial fission. In order to unravel the mechanism underlying this observation, we explored the myoferlin localization in pancreatic cancer cells and showed a colocalization with the mitochondrial dynamic machinery element: mitofusin. This colocalization was confirmed in several pancreas cancer cell lines and in normal cell lines as well. Moreover, in pancreas cancer cell lines, it appeared that myoferlin interacted with mitofusin. These discoveries open-up new research avenues aiming at modulating mitofusin function in pancreas cancer.

Keywords: myoferlin; mitochondria; mitofusin; pancreas cancer

1. Introduction

Pancreas ductal adenocarcinoma (PDAC) is one of the deadliest diseases with a 5-year survival lower than 10%. In PDAC, mitochondria activity was described to be involved in tumor relapse [1] and in metastatic dissemination [2]. Mitochondria are highly dynamic structures oscillating from a branched network to individual organelles according to the metabolic needs or mitochondrial damages. This oscillation, referred as mitochondrial dynamics, was tightly linked to PDAC aggressiveness. Indeed, it was shown that increasing mitochondrial fusion suppressed oxidative phosphorylation (OXPHOS), promoted mitophagy, and improved median survival in PDAC mice models significantly [3]. Conversely, we previously showed in PDAC cell lines that a mitochondrial fission was associated with

OXPHOS decrease, and enhanced autophagy [4]. Interestingly, in a mice model, a lower metastatic potential of PDAC cells was associated with a reduced OXPHOS [2]. Consequently, it appeared more important to disturb mitochondrial dynamics rather than to specifically inhibit fusion or fission [5]. Fusion or fission machineries are composed of a limited, but still growing, number of proteins among which the most studied are dynamin-related protein 1 (DRP1), optic atrophy 1 (OPA1), and mitofusins (MFN) 1 and 2 [6,7]. Post-translational modifications of these enzymes participate in the fine-tuning of mitochondrial dynamics. As an example, the initial step of fission is the recruitment of DRP1 at the mitochondrial surface, regulated by the phosphorylation ratio between serine 616 (S616) and S637. The S616 phosphorylation is a fission activator while the S637 one is a fission inhibitor [8].

Myoferlin is a ferlin family member protein, mainly known for its physiological function in membrane fusion, and its expression level was correlated with poor survival in several cancer types including PDAC [9]. Previously, our laboratory pointed to myoferlin as a potential biomarker in PDAC [10], where it is involved in essential membrane processes such as exocytosis and exosome production [11,12]. Using small interfering RNA (siRNA), we demonstrated that myoferlin depletion drives the cell toward mitochondrial fission, suggesting that this protein may act as a potential regulator of mitochondrial dynamics [4,13]. However, despite several advances, the mechanism of action of myoferlin remains largely unsolved. Interestingly, a myoferlin paralog, encoded by the dysferlin_v1 alternate transcript, was discovered to harbor a mitochondrial importation signal [14]. Moreover, a recent proteomic study undertaken in mice revealed that myoferlin could be present in mitochondria [15]. This discovery prompted us to further investigate the putative participation of myoferlin to the mitochondrial dynamics' machinery. For the first time, we revealed that myoferlin interacts with mitofusins, and might contribute to their mitochondrial fusion activities [16].

2. Results

2.1. Endogenous Myoferlin Is Present in Mitochondrial Crude Extract and Colocalized Partly with Mitochondria

Previously, we showed that myoferlin silencing impaired mitochondrial network in Panc-1 cells [4]. Thus, we decided to use the same cell line to investigate the potential mitochondrial localization of endogenous myoferlin (Figure 1A). Using differential centrifugation steps, we prepared a mitochondrial crude extract. The abundance of a mitochondrial-specific 60 kDa protein (clone 113-1) [17] indicated a 4.7-fold enrichment factor in comparison to whole cell extract. Interestingly, the mitochondrial crude extract contained several myoferlin isoforms with a 1.6-fold increase compared to the whole cell extract. Even if its relative abundance decreased by 30%, GRP78 was still detectable in the mitochondrial crude extract indicating either a microsomal contamination or a GRP78 mitochondrial localization [18]. These encouraging results prompted us to perform an immunofluorescence staining to explore myoferlin localization inside Panc-1 cells. For this purpose, we used a goat polyclonal myoferlin antibody (K-16). As previously reported [19], myoferlin staining appeared as a punctuated signal spread all over the cytoplasm but with a higher density close to plasma membrane (Figure 1B). Correlative colocalization analysis of deconvoluted images revealed a partial colocalization between myoferlin and mitochondrial signals (Figure 1C). While linear correlation coefficients (PCC and SRCC) showed only a weak association (~0.20), Manders' colocalization coefficients (M1 and M2) indicated an intermediate colocalization (>0.50). M1 describes the proportion of myoferlin pixels co-occurring with mitochondrial pixels, and vice-versa for M2. Several myoferlin-positive structures were identified in contact with mitochondria (Figure 1D,E). Interestingly, some myoferlin staining was located between mitochondrial sections close to each other and considered as potential mitochondrial fusion sites (Figure 1D,E). Myoferlin and mitochondrial colocalization was confirmed by "distance between objects"-based methods (Figure 1F). These methods showed >5% of the myoferlin-positive objects (N = 4286) were colocalized with a mitochondrial-object (N = 459) with a mean distance of 2 pixels, ranging from 0 to 5 pixels.

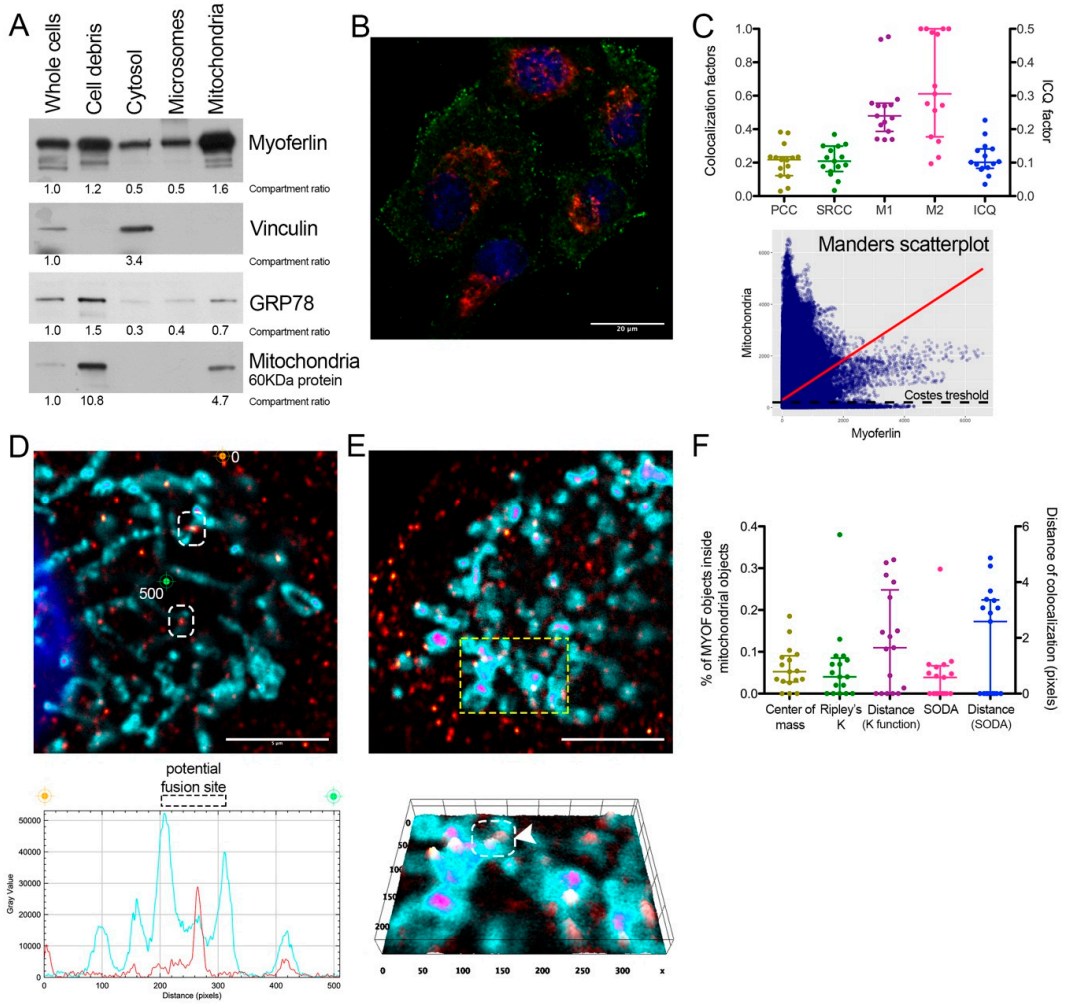

Figure 1. Myoferlin was colocalized with mitochondria in Panc-1 cells. (**A**) Western blot of 6 µg protein samples from whole Panc-1 cells and several cellular compartments isolated from Panc-1 cells. Myoferlin, vinculin, GRP78, and a 60 kDa mitochondrial protein were detected on the same membrane. Compartment relative quantification was performed using ImageJ; (**B**) representative confocal image of nuclei (blue), myoferlin (K-16—green) and mitochondria (113-1—red) immunofluorescence. Scale bar = 20 µm; (**C**) Pearson (PCC), Spearman rank (SRCC) correlation coefficients, Manders' colocalization coefficients (M1,M2), and intensity correlation quotient (ICQ) calculated on 17 independent microscopic fields. Manders scatterplot, associated with its linear regression (red line), shows the correlation between the intensity of each pixels in each channel. (**D**,**E**) Deconvoluted confocal image of nuclei (blue), myoferlin (K-16—"hot" red scale), mitochondria (113-1—"cold" cyan scale). Scale bar = 5 µm. Regions surrounded by white dashed boxes are putative mitochondrial fusion sites. (**D**) Channel intensity profile was established following the segment between orange (0-pixel position) and green (500-pixel position) cross marks; (**E**) The region surrounded by a yellow dashed box was used to generate the 2D intensity profile. Regions surrounded by white dashed box and marked by white arrow head is a putative mitochondrial fusion site; (**F**) percentage of myoferlin-positive objects (N = 4286) with the center of a mass overlapping mitochondrial object (N = 459), a percentage of myoferlin-positive object colocalizing mitochondrial object calculated by fitting of the Ripley's K function or by statistical object distance analysis (SODA). Colocalization distances in pixels were measured in both cases. All experiments were performed as three independent biological replicates.

Immunofluorescence results were confirmed using an additional myoferlin polyclonal antibody raised in rabbits (Figure S1).

2.2. Endogenous Myoferlin Colocalized with Mitochondrial Fusion Machinery in Pancreas Cancer Cell Lines

Owing to the known function of myoferlin in membrane fusion, we thought to evaluate the colocalization of myoferlin with a component of the fusion machinery: mitofusins. We thus performed immunofluorescence using myoferlin antibody (K-16) and MFN1 antibody (H-65). In Panc-1 cells, myoferlin was mainly associated with MFN1 in the perinuclear region (Figure 2A). Linear correlation coefficients (Figure 2B) showed a strong association between stainings. "Distance between objects"-based methods (Figure 2C) revealed that 20% to 30% of the myoferlin-positive objects (N = 7128) were colocalized with a MFN1-positive object (N = 369) with a mean distance of 3 pixels, ranging from 0 to 5 pixels. These results were confirmed by using an additional myoferlin antibody raised in rabbit and a MFN1/2 polyclonal antibody (3C9) raised in mouse (Figure S2). In order to confirm these results, we performed a proximity ligation assay on Panc-1 cells. This experiment showed 21.3 ± 6.8 proximity dots per cell, indicating a maximal 40 nm distance between myoferlin and MFN1/2 (Figure 2D). We next inhibited myoferlin expression using siRNA to confirm the specificity of the proximity ligation assay signal. Myoferlin silencing suppressed more than 95% of the colocalization signal confirming the specificity of the colocalization (Figure 2E). Proximity ligation assay results were confirmed in Panc-1 cells by indirect fluorescence resonance energy transfer analysis showing a significant FRET ratio (Figure S3).

We then decided to confirm MFN1/2-myoferlin colocalization in three additional PDAC cell lines (BxPC-3, MiaPaCa-2 and PaTu8988T) for which we reported the relative myoferlin and MFN1/2 expression (Figure S4). In every evaluated cell line, a colocalization was identified mainly thanks to Manders' colocalization coefficients (M1, M2) (Figure 3A–C). In these cell lines, linear correlation coefficients (PCC and SRCC) showed a weaker association (from 0.20 to 0.6 depending of the cell line) than in Panc-1 cell lines. In the BxPC-3 cell line, immunofluorescence staining showed that MFN1/2-myoferlin association was mainly localized at cell periphery (Figure 3A—left panel). In a PaTu8988T cell line, even if colocalization coefficients were sound, the very limited observable cytoplasm area and the low myoferlin expression level made results difficult to interpret. Consistent with the immunofluorescence results, proximity ligation assay showed less colocalization dots in BxPC-3, MiaPaCa-2, and PaTu8988T than in Panc-1 cells (Figure 3D). The relative amount of proximity dots appeared to be correlated with myoferlin abundance of each cell line. Considering our findings, we then tested whether myoferlin was physically interacting with MFN1/2.

2.3. Myoferlin Interacts with Mitofusins in Pancreas Cancer Cells

We first took advantage of an overexpression model of hemagglutinin (HA)-tagged myoferlin in Panc-1 cells to maximize the myoferlin-MFN1/2 interaction, and performed a coimmunoprecipitation assay. We immunoprecipitated MFN1/2 and showed the coprecipitation of HA-tagged myoferlin (Figure 4A). Encouraged by this unforeseen result, we decided to confirm the myoferlin-MFN1/2 interaction in endogenous expression systems. We thus performed the same experiment in Panc-1, BxPC-3, MiaPaCa-2 and PaTu8988T cell lines. In all cell lines tested, myoferlin coprecipitated with MFN1/2 (Figure 4B,4C) with an abundance in agreement with the previously described myoferlin expression level (Figure S4). In the light of our results, we wondered if the myoferlin-MFN1/2 interaction occurred in normal cells.

2.4. Myoferlin Colocalizes but Does Not Interact with Mitofusins in Normal Cells

Myoferlin expression is supposed to be low in differentiated normal cells. We thus selected subconfluent (90%) murine C2C12 myoblasts for their known functional expression of myoferlin [20] and immortalized human pancreatic normal epithelial (HPNE) cell lines with undifferentiated phenotype [21]. Immunofluorescence revealed a colocalization between myoferlin and MFN1/2 (Figure 5A–D). However, in these cell lines, MFN1/2 immunoprecipitation did not reveal a convincing physical interaction with myoferlin (Figure 5E,F) suggesting an interaction specific to cancer cells.

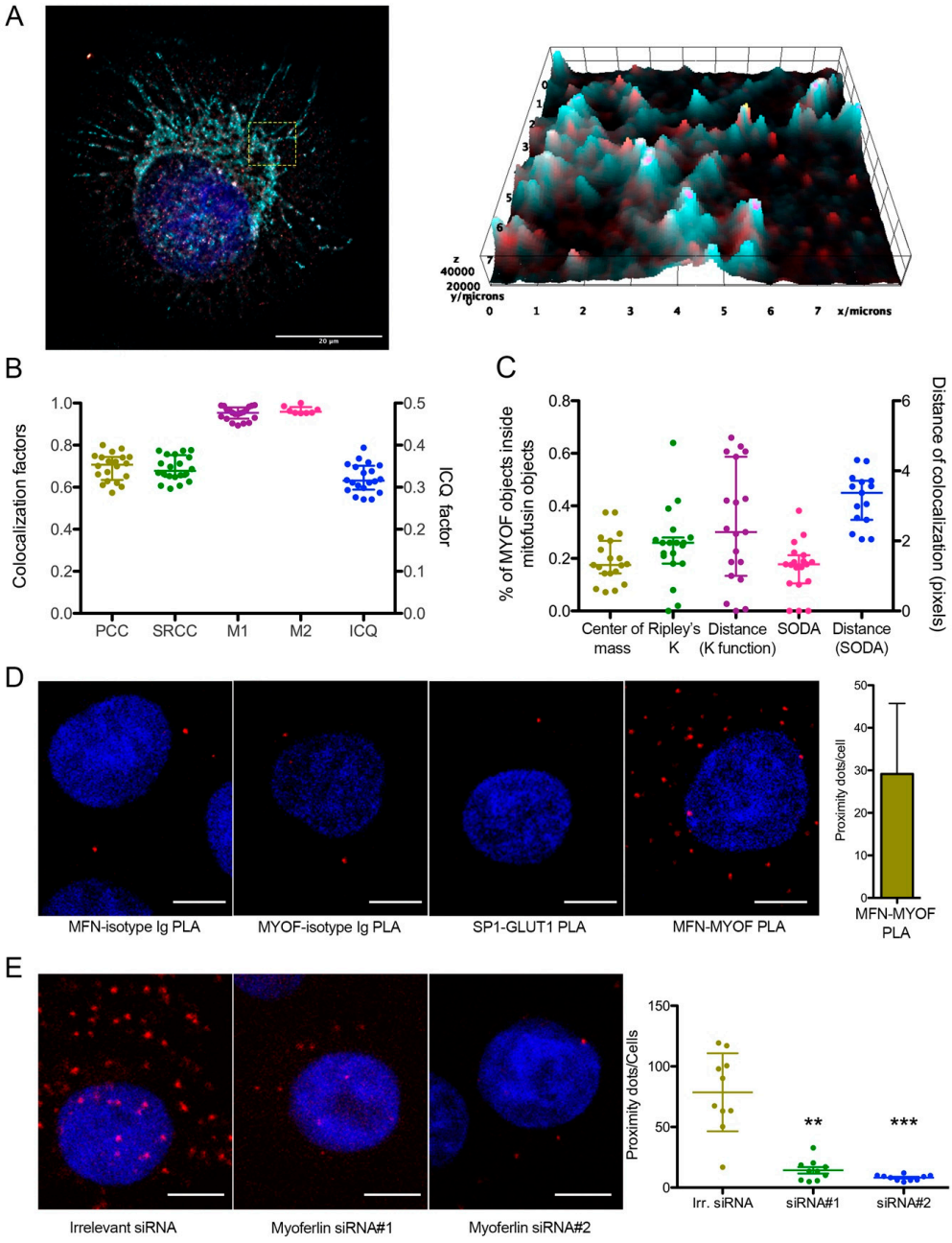

Figure 2. Myoferlin was colocalized with mitochondrial fusion machinery. (**A**) Representative deconvoluted confocal image of nuclei (blue), myoferlin (K16—"hot" red scale) and mitofusin-1 (H65—"cold" cyan scale) immunofluorescence. Scale bar = 20 µm. Region surrounded by yellow dashed box was used to generate the 2D intensity profile; (**B**) Pearson (PCC), Spearman rank (SRCC) correlation coefficients, Manders' colocalization coefficients (M1,M2), and intensity correlation quotient (ICQ) were calculated on 20 independent microscopic fields randomly selected; (**C**) percentage of myoferlin-positive objects (N = 7128) with center of mass overlapping mitochondrial object (N = 369), percentage of myoferlin-positive object colocalizing mitochondrial object calculated by fitting of the Ripley's K function or by statistical object distance analysis (SODA). Colocalization distances in pixels were measured in both cases; (**D**) representative images of proximity ligation assay (PLA) between myoferlin (HPA) and mitofusin-1/2 (3C9). Scale bar = 4 µm. Controls were established by substitution of antibodies by control isotypes or by using antibodies against non-interacting proteins (SP1 and GLUT1); (**E**) representative images of PLA in Panc-1 cells transfected with irrelevant or myoferlin-specific siRNA. Scale bar = 4 µm. MFN1/2-MYOF PLA (N = 10) were quantified using ImageJ. Kruskal–Wallis non-parametric test followed by Dunn's pairwise comparison was performed, ** $p < 0.01$, *** $p < 0.001$. All experiments were performed as three independent biological replicates.

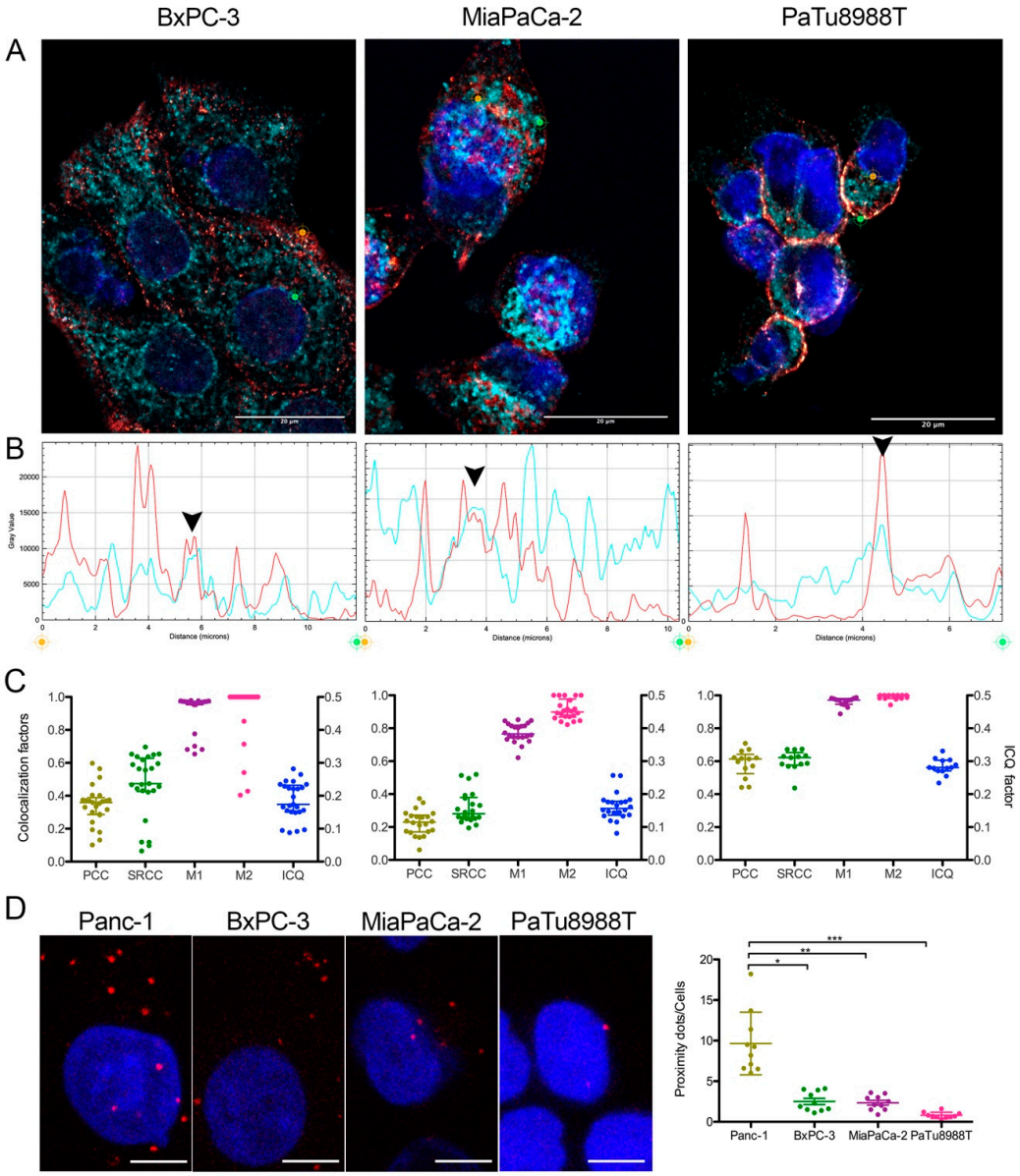

Figure 3. Myoferlin was colocalized with MFN1/2 in several pancreas cancer cell lines. (**A**) representative deconvoluted confocal image of nuclei (blue), myoferlin (HPA—"hot" red scale) and mitofusin-1/2 (3C9—"cold" cyan scale) immunofluorescence of BxPC-3, MiaPaCa-2 and PaTu8988T cell lines. Scale bar = 20 μm. (**B**) Channel intensity profiles were established following the segment between orange and green cross marks. Black arrow heads indicate colocalization spots. (**C**) Pearson (PCC), Spearman rank (SRCC) correlation coefficients, Manders' colocalization coefficients (M1,M2), and intensity correlation quotient (ICQ) were calculated on >13 independent microscopic fields. (**D**) Representatives images of MFN1/2-MYOF proximity ligation assay (PLA). Scale bar = 4 μm. MFN1/2-MYOF PLA (N = 10) were quantified using ImageJ. Kruskal–Wallis non-parametric test followed by Dunn's a pairwise comparison was performed, * $p < 0.05$, ** $p < 0.01$, *** $p < 0.001$. All experiments were performed as three independent biological replicates.

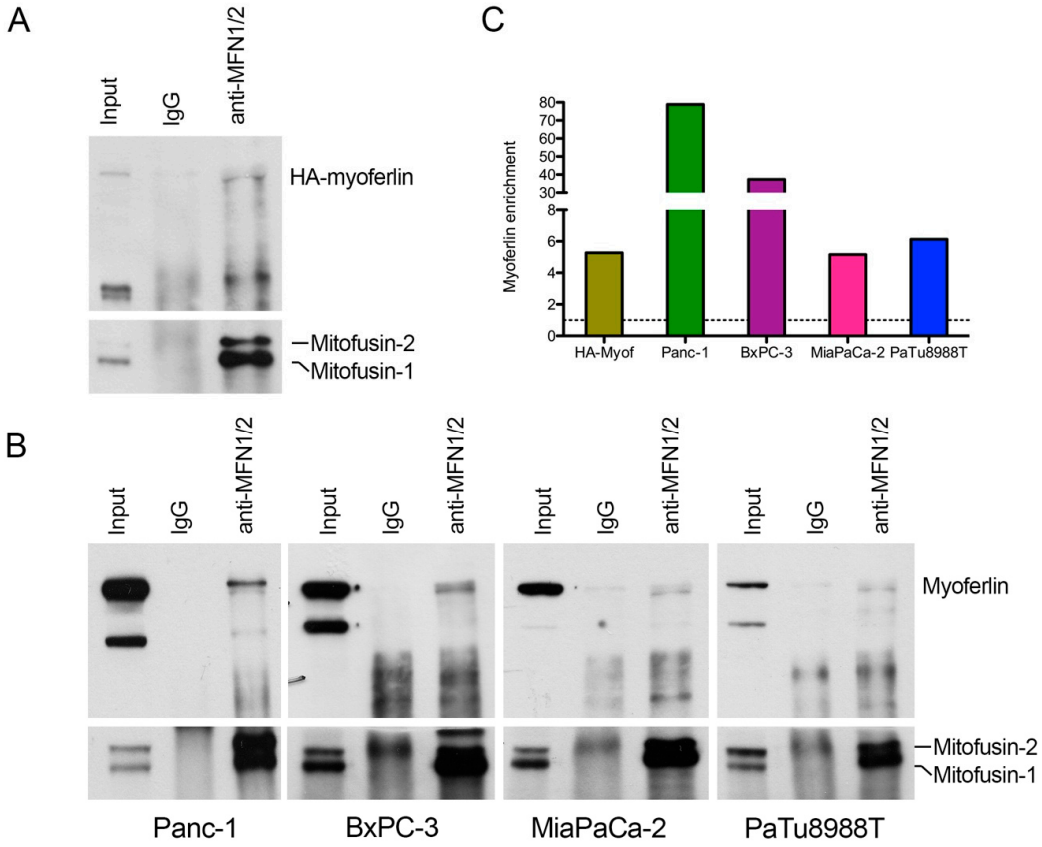

Figure 4. Myoferlin interacts with mitofusins in pancreas cancer cell lines. (**A**) coimmunoprecipitation of mitofusins and HA-tagged myoferlin with an anti-mitofusin antibody. Western blot of protein samples from whole cells (input), IgG control immunoprecipitation (IgG), and mitofusins immunoprecipitation (anti-MFN1/2) of HA-myoferlin transfected Panc-1 cells. HA-myoferlin and mitofusins were detected on the same membrane; (**B**) coimmunoprecipitation of mitofusins and endogenous myoferlin with an anti-mitofusin antibody. Western blot of protein samples from whole cells, IgG control immunoprecipitation, and mitofusins immunoprecipitation of Panc-1, BxPC-3, MiaPaCa-2, and PaTu8988T cell lines. Myoferlin and mitofusins were detected on the same membrane; (**C**) myoferlin (or HA-tagged myoferlin) enrichment in anti-MFN1/2 relatively to IgG. Quantification was performed using ImageJ. All experiments were performed as three independent biological replicates.

2.5. Mitochondrial Impact of Myoferlin Depletion in Pancreas Cancer Cells

In order to illustrate the functional role of myoferlin in mitochondria of pancreas cancer cells, we investigated mitochondrial network, mitochondrial ultrastructure and oxygen consumption rate (OCR) in myoferlin-depleted Panc-1 cells. Tetramethylrhodamine ethyl ester (TMRE) staining showed a mitochondrial swelling and a disruption of the mitochondrial network upon myoferlin silencing (Figure 6A). In Panc-1 cells transfected with irrelevant siRNA, ultrastructural analysis revealed elongated or circular mitochondrial sections with homogeneous matrix and well-defined cristae (Figure 6B). When Panc-1 cells were transfected with myoferlin siRNA, mitochondrial matrix appeared condensed with less abundant cristae. Oxygen consumption rate, reflecting electron transport chain activity, was significantly decreased by myoferlin silencing in Panc-1 cells (Figure 6C).

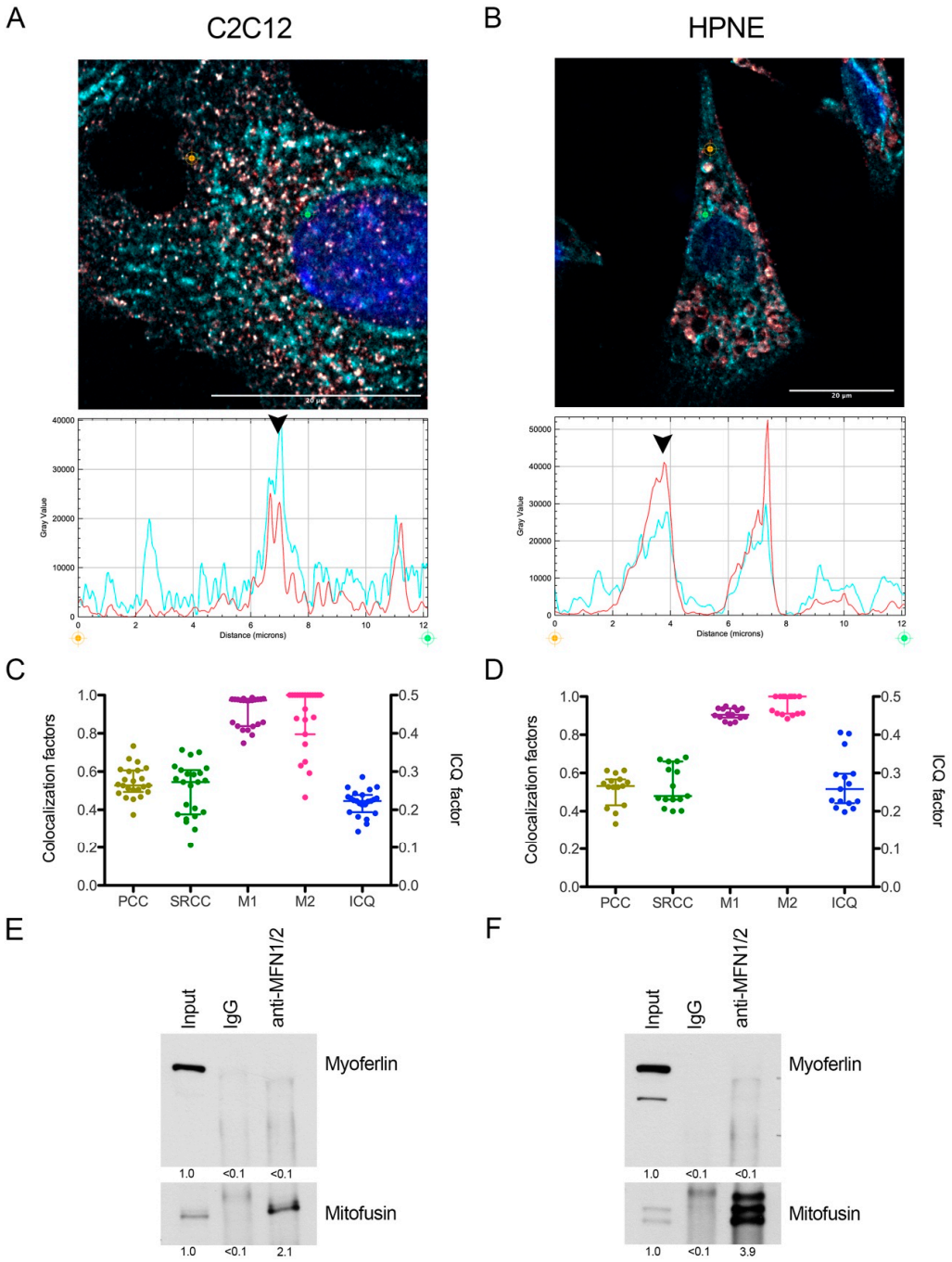

Figure 5. Myoferlin was colocalized with mitofusin-1 in normal cell lines. Representative deconvoluted confocal image of nuclei (blue), myoferlin (HPA—"hot" red scale) and mitofusin-1/2 (3C9—"cold" cyan scale) immunofluorescence of (**A**) C2C12 murine myoblast and (**B**) immortalized human pancreatic normal epithelial (HPNE) cell lines. Scale bar = 20 µm. Channel intensity profiles were established following the segment between orange and green cross marks. Black arrow heads indicate colocalization spots. (**C**,**D**) Pearson (PCC), Spearman rank (SRCC) correlation coefficients, Manders' colocalization coefficients (M1,M2), and intensity correlation quotient (ICQ) were calculated on >15 independent microscopic fields; (**E**,**F**) coimmunoprecipitation of mitofusins and endogenous myoferlin with an anti-mitofusin antibody. Western blot of protein samples from whole cells (input), IgG control immunoprecipitation (IgG), and mitofusins immunoprecipitation (anti-MFN1/2) of C2C12 and HPNE cell lines. Myoferlin and mitofusins were detected on the same membrane. Quantification was performed using ImageJ. All experiments were performed as three independent biological replicates.

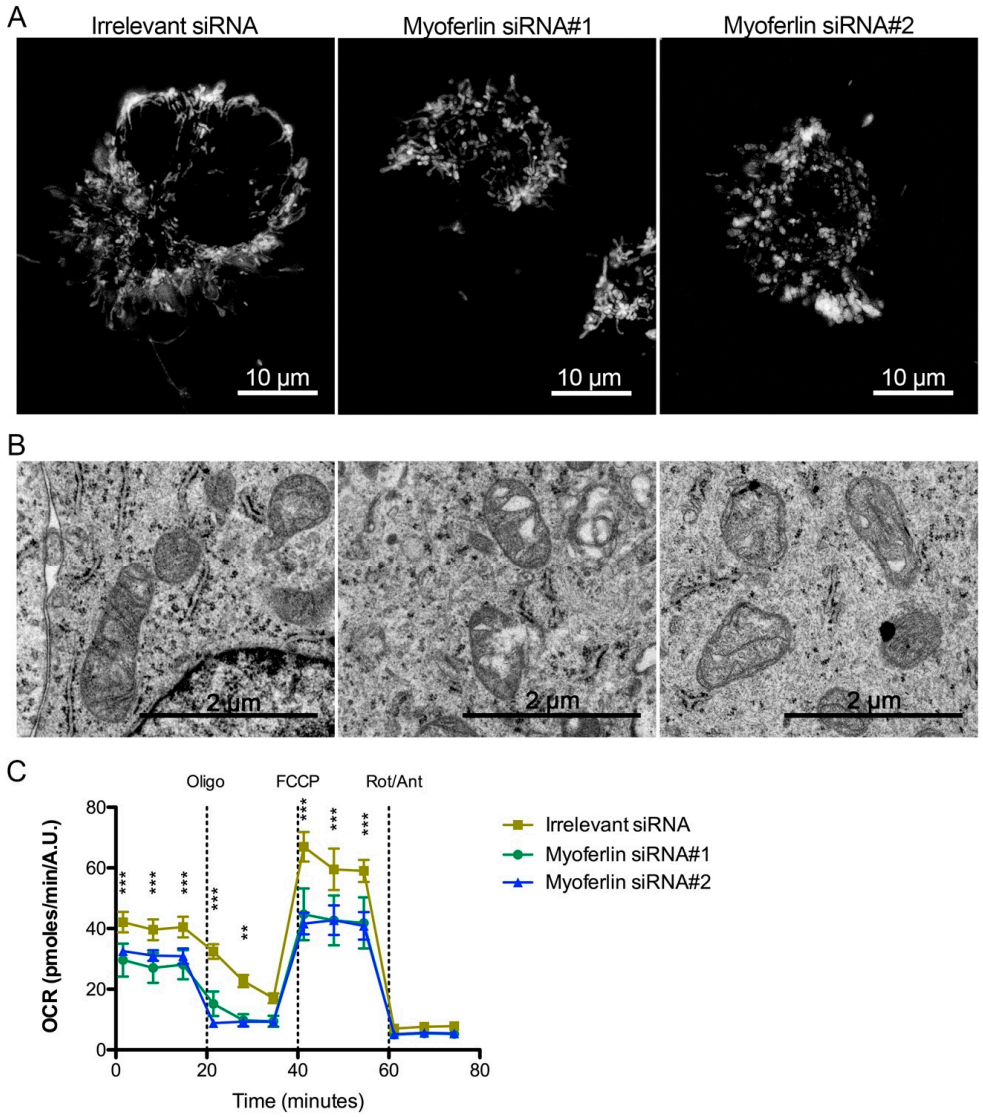

Figure 6. Mitochondrial impact of myoferlin deletion in pancreas cancer cells. (**A**) Mitochondria were stained with tetramethylrhodamine ethyl ester (1 nM TMRE) in Panc-1 living cells depleted for myoferlin. (**B**) Panc-1 cells depleted for myoferlin were fixed with glutaraldehyde and observed under transmission electron microscope. (**C**) Kinetic oxygen consumption rate (OCR) response of Panc-1 cells to oligomycin (oligo, 1 µM), FCCP (1.0 µM), rotenone, and antimycin A mix (Rot/Ant, 0.5 µM each). Each data point represents mean ± SD of technical replicates. All experiments were performed as three independent biological replicates. *** $p < 0.001$, ** $p < 0.01$.

3. Discussion

Myoferlin is a member of the ferlin family, mainly known for its function in myoblast membrane fusion and membrane reparation. Thanks to its multiple C2 domains, myoferlin participates in the tethering of vesicles to membranes and to the calcium sensing. An extensive and excellent review has been recently published on the functions of ferlins in vertebrates [22]. Myoferlin expression is increased in a large panel of cancer cells and tumors, where most of the studies described its role in the recycling of membrane receptors (EGFR, IGFR, . . .). Its participation in signaling pathways explains why its depletion leads to a decrease of cell growth or migration [9,23].

Mitochondrial dynamics is closely related to human diseases such as Charcot–Marie–Tooth disease type 2A and optic atrophy. In cancer, an increasing body of literature links mitochondrial fusion/fission to cancer cell metabolism [24,25]. Apparently discordant results concerning functional impact of

mitochondrial fusion/fission [2–4] suggest that disturbing mitochondrial dynamics is more important than specifically inhibiting fusion or fission [5].

A specific isoform of dysferlin, the closest myoferlin homolog [26], is encoded by the dysferlin_v1 alternate transcript and harbors a mitochondrial importation signal suggesting a mitochondrial localization [14]. Indeed, dysferlin was reported to interact with mitochondrial ATP synthase coupling factor 6 in HUVEC cells [27], ATP synthase subunits, and several other mitochondrial proteins in myoblasts [14]. Surprisingly, patients with dysferlinopathies caused by mutations in DYSF genes present frequently mitochondrial complex I and IV deficiencies [28]. Myoferlin was localized in several cell compartments including plasma membrane and endoplasmic reticulum [19]. However, a recent proteomic study revealed that mouse myoferlin could be present in mitochondria isolated from normal tissues [15]. For the first time, our results showed that myoferlin colocalizes and interacts with mitofusins, key proteins in mitochondrial fusion [29]. Of course, our results did not allow for excluding an indirect interaction between myoferlin and mitofusin. Interestingly, mitofusin-2 is a member of the dynamin-like GTPase superfamily and harbors a proline-rich domain [30] when myoferlin contains a SH3 domain [31] controlling protein-protein interactions through proline-rich domains. It is worth noting that a myoferlin colocalization with rab7 GTPase was reported in late endosomes [19], and a direct interaction was suggested in an exogenous expression system [32]. Myoferlin exhibits several additional domains (FerB, FerI, Ferlin C, DysF) with an unidentified function [9], opening new possibilities for its interaction with mitochondrial mitofusins, including mitofusin-1. Based on the idea that myoferlin participates functionally in the highly responsive mitochondrial dynamics through an interaction with mitofusin, this interaction should be quickly reversed, excluding probably covalent interactions. However, we do believe that this interaction has to be stable to keep mitochondria in the desired states. In this hypothesis, myoferlin could be considered as a functional interactor of mitofusins in the mitochondrial fusion (Figure 7—model A).

Endoplasmic reticulum (ER)-mitochondrial contacts were extensively studied, allowing the identification of mitochondria-associated ER membranes (MAM) working as a platform for Ca2+ transfer, lipid synthesis, and metabolism [33]. Noticeably, mitochondrial fission spatially occurs at sites of proximity to the ER [34].

Mitofusin-2 is enriched in MAM where it has been proposed to control the stability of the organelle's interaction by homotypic and heterocomplex interaction with mitochondrial mitofusins [35]. However, an alternative model for MFN2-mediated ER-mitochondria tethering was proposed. In this model, MFN2 acts as a negative modulator of ER-mitochondria interaction, sequestering a still unknown tethering subunit [36]. Our results do not exclude an interaction of myoferlin with MFN2 on the ER. In the context of the alternative model describing the ER-mitochondria interaction, we hypothesize that myoferlin participates to the sequestration of MFN2, avoiding the stabilization of the ER-mitochondria contact needed for mitochondrial fission (Figure 7—model B).

As it stands for now, our findings clearly demonstrate a physical interaction between myoferlin and mitofusins in pancreas cancer cells. However, several points need to be clarified in the future. Among them, the identification of myoferlin and mitofusin isoforms interacting together seems to be a priority. The nature of the interaction also remains to be elucidated. Is it a direct or an indirect interaction? What are the protein domains involved? In vivo studies have to be considered, first to further validate the potential of myoferlin as a therapeutic target, and then to confirm the biological relevance of the myoferlin–mitofusin interaction. These discoveries will open up new research avenues aiming at modulating mitofusin function or targeting myoferlin to fight pancreas cancer. In this perspective, interrogating TCGA data with OncoLNC engine (http://www.oncolnc.org), it is noteworthy that mitofusin-1 (Cox coefficient = 0.353, $p = 0.004$) and myoferlin expression (Cox coefficient = 0.561, $p < 0.001$) [4,9] are both correlated with a poor overall survival in PDAC. Furthermore, Wang and coworkers reported a significant correlation between overall survival of PDAC patients and myoferlin abundance in resected tumors [37]. Myoferlin involvement in PDAC progression could go beyond cancer cell biology. Indeed, PDAC is generally considered as a "cold" immune environment probably

with the participation of the Wnt/β-catenin pathway. Restoration of anti-PDAC immunity, especially in invasive tumors, remains a valid strategy [38]. In this context, we previously reported myoferlin as a negative regulator of autophagy in PDAC [4]. Additionally, a recent report pointed at myoferlin in muscle development as an indirect regulator of Wnt/β-catenin pathway by a protection of Dishevelled-2 against autophagy. The autophagy induced by myoferlin silencing could be considered as a way to promote disheveled degradation and to switch off Wnt signaling [39]. PDAC aggressiveness is due to its late diagnosis but also to its ability to acquire resistance to treatment, a process in which a Smad2/3-independent TGF-β autocrine loop [40] is involved. Interestingly, myoferlin was previously reported to regulate the TGF-β autocrine loop in breast cancer cells [41], and Smad2, a downstream transducer, was recently reported as a mitofusin interactor in mitochondrial fusion [42]. These findings raise the question of a potential interaction between mitofusin, smad2, and myoferlin and of their relevance as therapeutic target.

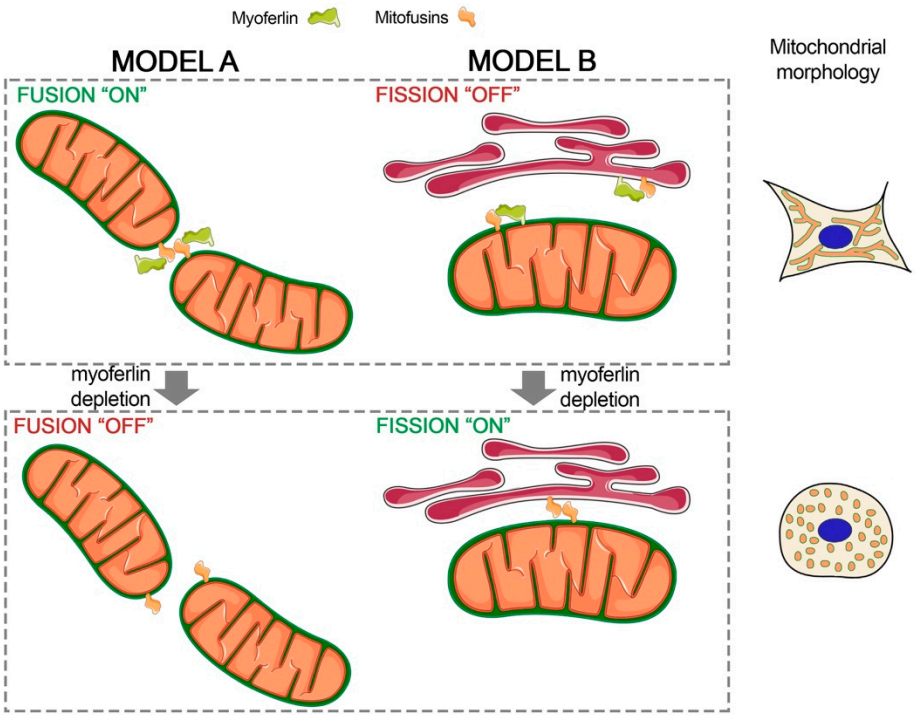

Figure 7. Proposed models for myoferlin involvement in mitochondrial dynamics. Model A describes the functional interaction between mitofusins and myoferlin. Myoferlin interacts with mitofusin and participates, as a positive regulator, to mitochondrial fusion. Myoferlin depletion reduces efficiency or inhibits the mitofusin-mediated mitochondrial fusion. Model B depicts the mitofusin sequestration by myoferlin impairing the ER-mitochondria tethering and subsequent fission. Myoferlin silencing results in the stabilization of the ER-mitochondria tethering by mitofusin interaction allowing ER wrapping and DRP1 recruitment. Designed with Servier Medical Art (https://smart.servier.com) licensed under a Creative Commons Attribution 3.0 Unported License.

4. Materials and Methods

4.1. Cells and Chemicals

PaTu8988T (ACC162) were purchased from the Leibniz-Institute (DSMZ, Braunschweig, Germany) while HPNE (CRL- 4023) and C2C12 (CRL-1772) were purchased from the American Type Culture Collection (ATCC, Manassas, VA, USA). Panc-1 (CRL-1469), BxPC-3 (CRL-1687) and MiaPaCa-2 (CRL-1420) were generous gifts from, respectively, Prof. Muller and Burtea (NMR Laboratory, University of Mons, Belgium), Prof. Bikfalvi (Inserm U1029, Bordeaux, France) and Prof. De Wever (Laboratory of Experimental Cancer Research, University of Gent, Belgium). All cell lines were

recently authenticated using STR profiling (DSMZ, Braunschweig, Germany). Antibodies against hemagglutinin (HA, 3724S), and GLUT1 (12939) were from Cell Signaling (Danvers, MA, USA). Vinculin (sc-25336), Myoferlin K-16 (sc-51367), MFN1 (H-65, sc-50330), SP1 (sc-17824), and HSC70 (sc-7298) antibodies were purchased from Santa-Cruz (Dallas, TX, USA). GRP78 (MAB4846) and mitochondria (Clone 113-1, MAB1273) antibodies were obtained from Millipore (Burlington, MA, USA). Myoferlin polyclonal antibody (identified here under as HPA - HPA014245) and MFN1/2 antibody (clone 3C9, ab57602) were respectively from Sigma (Bornem, Belgium) and Abcam (Cambridge, UK). All reagents were purchased from Sigma (Bornem, Belgium) unless mentioned otherwise.

4.2. Cell Culture

Panc-1 cells were cultured in Dulbecco's modified Eagle's medium (DMEM, Lonza, Basel, Switzerland) supplemented with 10% fetal bovine serum (FBS). Miapaca-2 and C2C12 were maintained in DMEM supplemented with 10% FBS, 1 mM sodium pyruvate and 4 mM L-glutamine. PaTu8988T were cultured in DMEM supplemented with 5% FBS, 5% horse serum, and 2 mM L-glutamine. BxPC-3 were maintained in RPMI1640 supplemented with 10% FBS, 1 mM sodium pyruvate, 10 mM HEPES, and 2.5 g/L of glucose. HPNE required a medium composed of 75% DMEM, 25% M3 Base (Incell Corp, San Antonio, TX, USA), 2.5% FBS, 0.01% epidermal growth factor, 2 mM L-glutamine, and 1 g/L of glucose. The cells were cultured in a humidified 5% CO2 incubator at 37 °C and were used between passage 1 and passage 10. The cells were monthly tested for mycoplasma.

4.3. Small Interfering RNA Transfection

Cells were transfected with 20nM siRNA using calcium phosphate. Medium was replaced 16 h after transfection, media replacement was considered as time 0. All experiments were performed 48 h after treatment. Myof#1-5′ CCCUGUCUGGAAUGAGAUUUU 3′ and Myof#2-5′ CUGAAGAGCUGUGCAUUATT 3′ siRNA were used to target myoferlin while the irrelevant siRNA-5′ CUUACGCUGAGUACUUCGAUU 3′ was used as transfection control. All siRNA were purchased from Eurogentec (Liège, Belgium).

4.4. Plasmid Preparation and Transfection

pCDNA3.1-Myoferlin HA [43], a plasmid encoding for human myoferlin cDNA with a C-terminal HA-tag was a gift from William Sessa (plasmid #22443; http://n2t.net/addgene:22443; RRID:Addgene_22443, Addgene, Watertown, MA, USA). The plasmid was amplified in DH5alpha bacteria cultured in classical LB medium, supplemented with ampicillin (100 μg/mL), overnight at 37 °C in an agitating incubator (200 rpm). Plasmid purification was performed using the PureYieldTM Plasmid Maxiprep System (A2393) from Promega (Fitchburg, WI, USA). Panc-1 cells were transiently transfected with 1 μg of plasmid using 2.5 μL Lipofectamine 2000 (Invitrogen, Carlsbad, CA, USA) as reported by the manufacturer's recommendation. Medium was replaced 4 h after transfection. In order to select transfected cells, antibiotic pressure using G-418 solution was maintained at a concentration of 200 μg/mL.

4.5. Western Blotting

Protein samples were solubilized in 1% sodium dodecyl sulfate (SDS) supplemented with phosphatase and protease inhibitors. Bicinchoninic acid (BCA) protein assay kit (Thermo Scientific, Waltham, MA, USA) was used for protein quantification. Proteins were denatured in Laemmli's buffer during 5 min at 99 °C. Samples were loaded on sodium dodecyl sulfate polyacrylamide gel for migration and were transferred on a PVDF membrane during 90 min at room temperature (RT) or overnight at 4 °C. Membranes were blocked for 1 h according to antibody manufacturers' instructions. Then, they were incubated overnight at 4 °C with primary antibodies (dilution 1:1000) and probed with corresponding secondary antibodies linked to horseradish peroxidase (dilution 1:3000) for 1 h at RT. Revelation was performed using chemiluminescent reagents (ECL Western blotting substrate,

Thermo Scientific, Waltham, MA, USA). Quantification was performed using densitometric analysis and immunoblots were normalized with HSC70 using ImageJ software.

4.6. Immunofluorescence

Cells (6×10^4) were seeded on sterilized glass coverslips. After 24 h, cells were washed once with PBS and fixed with ice-cold methanol-acetone (4:1) during 10 min. Then, cells were washed twice with PBS and were blocked in 2% bovine serum albumin diluted in PBS for 30 min. After blocking, coverslips were incubated during 2 h with primary antibodies (dilution 1:100 in BSA-PBS) at RT in a humidified chamber. This step was followed by three washes in 2% BSA-PBS. Coverslips were then incubated with corresponding Alexa Fluor 488 or Alexa Fluor 546 conjugated secondary antibodies (Invitrogen, Molecular Probes, Carlsbad, CA, USA) in a humidified chamber for 45 min (dilution 1:1000 in BSA-PBS). Nuclei counterstaining was performed using hoechst DNA probe (0.01 g/L, Calbiochem, San Diego, CA, USA). Observation fields were selected randomly and pictures were acquired using an A1R confocal microscope (Nikon, Yokohama, Japan).

4.7. Colocalization Studies

Immunofluorescence images were deconvoluted using online NIS-elements tool (Nikon). Colocalization analysis were first performed, without selection of regions of interest, using correlation methods: Pearson coefficient correlation (PCC), Spearman's rank correlation coefficient (SRCC), Manders' colocalization coefficients (M1 and M2), and intensity correlation quotient (ICQ), thanks to EzColocalization [44] ImageJ plugin. Background was automatically identified according to the Costes method. Then, we used "distance between objects"-based methods: distance analysis (centers of mass of channel 1 objects inside channel 2 masks), parametric analysis of the Ripley's K function, and non-parametric Ripley's analysis (SODA), thanks to colocalization studio plugin in Icy software [45]. A 5-pixel maximal limit was used as a threshold.

4.8. Proximity Ligation Assay

Duolink PLA kit (Sigma, Bornem, Belgium) was used according to the manufacturer's instructions. In order to detect the proximity between myoferlin and mitofusins, rabbit anti-myoferlin (HPA) and mouse anti-MFN1/2 (3C9) primary antibodies were used (dilution 1:75). Oligonucleotides conjugated secondary antibodies were provided by the kit allowing detection of a red signal if less than 40 nm separates both proteins of interest. Observation fields were selected randomly and pictures were acquired using an A1R confocal microscope. In each microscopic field, proximity dots were counted using ImageJ and divided by the number of nuclei.

4.9. Fluorescence Resonance Energy Transfer

All samples were proceeded as described in Immunofluorescence section. Alexa Fluor 488-conjugated secondary antibody was selected as the donor fluorophore while Alexa Fluor 546-conjugated secondary antibody was selected as the acceptor (Invitrogen, Molecular Probes, Carlsbad, CA, USA). As a positive control, two secondary antibodies were used, both targeting rabbit anti-myoferlin (HPA) primary antibody, and carrying acceptor or donor fluorophore. Finally, as a negative biological control, proteins from distinct compartments, the nuclear factor SP1 and the plasma membrane transporter GLUT1 were selected. Images were acquired with a LSM880 Airyscan Elyra Microscope (Zeiss, Oberkochen, Germany).

4.10. Co-Immunoprecipitation

Proteins were extracted using non-denaturing buffer containing Tris-HCl pH 8 (20 mM), NaCl (137 mM), NP40 (1%), EDTA (2 mM), and supplemented with protease inhibitors. Following extraction, proteins were incubated under rotation at 4 °C during 30 min and were centrifuged at 14000× g for

15 min at 4 °C to eliminate cell debris. 5 µg of MFN1/2 or isotype IgG control (Thermo Scientific, Waltham, MA, USA) antibodies were incubated overnight with 500 µg of the protein extract. Then, protein A/G magnetic beads (Thermo Scientific, Waltham, MA, USA) were added and incubated at 4 °C under rotation for 2 h. After three washes with a low salt buffer containing SDS (0.1%), Triton X-100 (1%), EDTA (2 mM), Tris-HCl pH 8 (20 mM) and NaCl (150 mM), and one wash of high salt buffer composed of SDS (0.1%), Triton X-100 (1%), EDTA (2 mM), Tris-HCl pH 8 (20 mM), and NaCl (450 mM), proteins were eluted from magnetic beads using Laemmli's buffer and then processed for Western blotting.

4.11. Mitochondrial Enrichment

Mitochondrial isolation kit (Qiagen, Hilden, Germany) was used according to the manufacturer's instructions. Briefly, 2×10^7 washed cells were suspended in lysis buffer in order to disrupt plasma membrane. After centrifugation (1000× *g*, 10 min, 4 °C), the supernatant contained cytosolic proteins while the pellet was composed of intact mitochondria, endoplasmic reticulum, and other compartmentalized organelles. The pellet was suspended in disruption buffer and homogenized in a potter with a glass pestle (15X). After centrifugation (1000× *g*, 10 min, 4 °C), nuclei, cell debris, and unbroken cells were pelleted while the microsomes and mitochondria were contained in the supernatant. The supernatant was then centrifuged (6000× g, 10 min, 4 °C) and the obtained pellet was resuspended in mitochondrial purification buffer. The mitochondrial suspension was pipetted on density gradient layers. After centrifugation (14,000× *g*, 10 min, 4 °C), mitochondria were pelleted and harvested. All fractions were processed for further Western blotting experiments.

4.12. TMRE Mitochondrial Staining

Tetramethylrhodamine ethyl ester (TMRE) was used to visualize mitochondria in living Panc-1 cells. siRNA-transfected cells were seeded in 8-well slides (IBIDI, Munich, Germany) at low confluence. Staining was performed for 15 min at 37 °C with TMRE (1 nM). Images were acquired by epifluorescence microscopy as Z-stacks with an A1R microscope.

4.13. Ultrastructural Analysis

Panc-1 cells were fixed for 90 min at room temperature with glutaraldehyde (2.5%) in a Sörensen phosphate buffer (0.1 M, pH 7.4) and post-fixed for 30 min with 2% osmium tetroxide. Embedding and observation were performed as previously described [12].

4.14. Oxygen Consumption Rate Analysis

Oxygen consumption rates were measured with a Seahorse XFp extracellular flux analyzer (Agilent, Santa Clara, CA, USA). siRNA-transfected Panc-1 cells were seeded (13000 cells per well) in XFp mini-plates and allowed to attach overnight. For mitochondrial OCR analysis, cells were kept in unbuffered serum-free DMEM (Basal DMEM, Agilent) supplemented with pyruvate (1 mM), glutamine (2 mM), glucose (10 mM), pH 7.4 at 37 °C, and ambient CO2 for 1 h before the assay. During the assay, cells were successively stressed with oligomycin (1 µM), FCCP (1.0 µM), and rotenone/antimycin A (0.5 µM each) mix. Results were normalized according to the cell number evaluated by Hoechst (2 µg/mL) incorporation after cold methanol/acetone fixation.

4.15. Statistical Analysis

Results were presented as individual scatter-plots together with median and interquartile range. Two-sided statistical analysis was performed using non-parametric analysis of variance. Groups were compared by Dunn's *t* test, and $p < 0.05$ was considered as statically significant.

5. Conclusions

The disruption of the mitochondrial network is associated with a significant inhibition of cell proliferation and migration in pancreas cancer cells. The discovery of a mitofusin–myoferlin interaction in PDAC cell lines opens up new research avenues aiming at modulating mitofusin function in pancreas cancer.

Supplementary Materials: The following are available online at http://www.mdpi.com/2072-6694/12/6/1643/s1, Figure S1: Myoferlin was colocalized with mitochondria in Panc-1 cells, Figure S2: Myoferlin was colocalized with mitofusins in Panc-1 cells, Figure S3: Fluorescence resonance energy transfer showing myoferlin and mitofusins proximity in Panc-1 cell line, Figure S4: Myoferlin and mitofusins abundance in PDAC cell lines. All full western blot figures were included in the supplementary materials.

Author Contributions: Conceptualization, O.P. and S.A.; methodology, A.H.; investigation, S.A., R.P., G.R., N.M., F.A., and M.T.; resources, L.D. and M.F.; writing—original draft preparation, O.P. and S.A.; writing—review and editing, O.P.; supervision, O.P.; funding acquisition, O.P., A.B., and V.C. All authors have read and agreed to the published version of the manuscript.

Funding: This research was funded by Fondation Léon-Fredericq and by University of Liège "Fonds spéciaux – credits sectoriels". S.A. is supported by a "Fonds pour la formation à la Recherche dans l'Industrie et l'Agriculture » (FRIA) grant. A.B. is a Research Director (Fonds de la Recherche Scientifique—FNRS).

Acknowledgments: The authors acknowledge Sandra Ormenese (GIGA-imaging platform, ULiège) and Patricia Piscicelli (Laboratory of Cellular and Tissular Biology) for her respective experimental support.

Conflicts of Interest: The authors declare no conflict of interest. The funders had no role in the design of the study; in the collection, analyses, or interpretation of data; in the writing of the manuscript, or in the decision to publish the results.

References

1. Viale, A.; Pettazzoni, P.; Lyssiotis, C.A.; Ying, H.; Sánchez, N.; Marchesini, M.; Carugo, A.; Green, T.; Seth, S.; Giuliani, V.; et al. Oncogene ablation-resistant pancreatic cancer cells depend on mitochondrial function. *Nature* **2014**, *514*, 628–632. [CrossRef] [PubMed]
2. Rademaker, G.; Costanza, B.; Anania, S.; Agirman, F.; Maloujahmoum, N.; Valentin, E.D.; Goval, J.J.; Bellahcène, A.; Castronovo, V.; Peulen, O.J. Myoferlin Contributes to the Metastatic Phenotype of Pancreatic Cancer Cells by Enhancing Their Migratory Capacity through the Control of Oxidative Phosphorylation. *Cancers* **2019**, *11*, 853. [CrossRef] [PubMed]
3. Yu, M.; Nguyen, N.D.; Huang, Y.; Lin, D.; Fujimoto, T.N.; Molkentine, J.M.; Deorukhkar, A.; Kang, Y.; Lucas, F.A.S.; Fernandes, C.J.; et al. Mitochondrial fusion exploits a therapeutic vulnerability of pancreatic cancer. *JCI Insight* **2019**, *5*. [CrossRef] [PubMed]
4. Rademaker, G.; Hennequière, V.; Brohée, L.; Nokin, M.-J.; Lovinfosse, P.; Durieux, F.; Gofflot, S.; Bellier, J.; Costanza, B.; Herfs, M.; et al. Myoferlin controls mitochondrial structure and activity in pancreatic ductal adenocarcinoma, and affects tumor aggressiveness. *Oncogene* **2018**, *66*, 1–15. [CrossRef]
5. Anderson, G.R.; Wardell, S.E.; Cakir, M.; Yip, C.; Ahn, Y.; Ali, M.; Yllanes, A.P.; Chao, C.A.; McDonnell, D.P.; Wood, K.C. Dysregulation of mitochondrial dynamics proteins are a targetable feature of human tumors. *Nat. Commun.* **2018**, *9*, 1677. [CrossRef]
6. Dorn, G.W. Evolving Concepts of Mitochondrial Dynamics. *Annu. Rev. Physiol.* **2018**, *81*, 1–17. [CrossRef]
7. Pagliuso, A.; Cossart, P.; Stavru, F. The ever-growing complexity of the mitochondrial fission machinery. *Cell. Mol. Life Sci.* **2017**, *75*, 355–374. [CrossRef]
8. Tilokani, L.; Nagashima, S.; Paupe, V.; Prudent, J. Mitochondrial dynamics: Overview of molecular mechanisms. *Essays Biochem.* **2018**, *62*, 341–360. [CrossRef]
9. Peulen, O.; Rademaker, G.; Anania, S.; Turtoi, A.; Bellahcène, A.; Castronovo, V. Ferlin Overview: From Membrane to Cancer Biology. *Cells* **2019**, *8*, 954. [CrossRef]
10. Turtoi, A.; Musmeci, D.; Wang, Y.; Dumont, B.; Somja, J.; Bevilacqua, G.; Pauw, E.D.; Delvenne, P.; Castronovo, V. Identification of novel accessible proteins bearing diagnostic and therapeutic potential in human pancreatic ductal adenocarcinoma. *J. Proteome Res.* **2011**, *10*, 4302–4313. [CrossRef]

11. Blomme, A.; Fahmy, K.; Peulen, O.J.; Costanza, B.; Fontaine, M.; Struman, I.; Baiwir, D.; Pauw, E.D.; Thiry, M.; Bellahcène, A.; et al. Myoferlin is a novel exosomal protein and functional regulator of cancer-derived exosomes. *Oncotarget* **2016**, *7*, 83669–83683. [CrossRef] [PubMed]
12. Fahmy, K.; Gonzalez, A.; Arafa, M.; Peixoto, P.; Bellahcène, A.; Turtoi, A.; Delvenne, P.; Thiry, M.; Castronovo, V.; Peulen, O.J. Myoferlin plays a key role in VEGFA secretion and impacts tumor-associated angiogenesis in human pancreas cancer. *Int. J. Cancer* **2016**, *138*, 652–663. [CrossRef] [PubMed]
13. Rademaker, G.; Costanza, B.; Bellier, J.; Herfs, M.; Peiffer, R.; Agirman, F.; Maloujahmoum, N.; Habraken, Y.; Delvenne, P.; Bellahcène, A.; et al. Human colon cancer cells highly express myoferlin to maintain a fit mitochondrial network and escape p53-driven apoptosis. *Oncogenesis* **2019**, *8*, 21. [CrossRef] [PubMed]
14. de Morrée, A.; Hensbergen, P.J.; van Haagen, H.H.H.B.M.; Dragan, I.; Deelder, A.M.; Hoen, P.A.C.t.; Frants, R.R.; Maarel, S.M. van der Proteomic analysis of the dysferlin protein complex unveils its importance for sarcolemmal maintenance and integrity. *PLoS ONE* **2010**, *5*, e13854. [CrossRef] [PubMed]
15. Williams, E.G.; Wu, Y.; Ryu, D.; Kim, J.Y.; Lan, J.; Hasan, M.; Wolski, W.; Jha, P.; Halter, C.; Auwerx, J.; et al. Quantifying and Localizing the Mitochondrial Proteome Across Five Tissues in A Mouse Population. *Mol. Cell. Proteom.* **2018**, *17*, 1766–1777. [CrossRef]
16. Cao, Y.-L.; Meng, S.; Chen, Y.; Feng, J.-X.; Gu, D.-D.; Yu, B.; Li, Y.-J.; Yang, J.-Y.; Liao, S.; Chan, D.C.; et al. MFN1 structures reveal nucleotide-triggered dimerization critical for mitochondrial fusion. *Nature* **2017**, *542*, 372–376. [CrossRef]
17. Cowan, D.B.; Yao, R.; Thedsanamoorthy, J.K.; Zurakowski, D.; del Nido, P.J.; McCully, J.D. Transit and integration of extracellular mitochondria in human heart cells. *Sci. Rep.* **2017**, *7*, 17450. [CrossRef]
18. Sun, F.-C.; Wei, S.; Li, C.-W.; Chang, Y.-S.; Chao, C.-C.; Lai, Y.-K. Localization of GRP78 to mitochondria under the unfolded protein response. *Biochem. J.* **2006**, *396*, 31–39. [CrossRef]
19. Redpath, G.M.I.; Sophocleous, R.A.; Turnbull, L.; Whitchurch, C.B.; Cooper, S.T. Ferlins Show Tissue-Specific Expression and Segregate as Plasma Membrane/Late Endosomal or Trans-Golgi/Recycling Ferlins. *Traffic* **2016**, *17*, 245–266. [CrossRef]
20. Doherty, K.R.; Cave, A.; Davis, D.B.; Delmonte, A.J.; Posey, A.; Earley, J.U.; Hadhazy, M.; McNally, E.M. Normal myoblast fusion requires myoferlin. *Development* **2005**, *132*, 5565–5575. [CrossRef]
21. Lee, K.M.; Nguyen, C.; Ulrich, A.B.; Pour, P.M.; Ouellette, M.M. Immortalization with telomerase of the Nestin-positive cells of the human pancreas. *Biochem. Biophys. Res. Commun.* **2003**, *301*, 1038–1044. [CrossRef]
22. Bulankina, A.; Thoms, S. Functions of Vertebrate Ferlins. *Cells* **2020**, *9*, 534. [CrossRef] [PubMed]
23. Dong, Y.; Kang, H.; Liu, H.; Wang, J.; Guo, Q.; Song, C.; Sun, Y.; Zhang, Y.; Zhang, H.; Zhang, Z.; et al. Myoferlin, a Membrane Protein with Emerging Oncogenic Roles. *BioMed Res. Int.* **2019**, 7365913. [CrossRef] [PubMed]
24. Chen, H.; Chan, D.C. Mitochondrial Dynamics in Regulating the Unique Phenotypes of Cancer and Stem Cells. *Cell Metab.* **2017**, *26*, 39–48. [CrossRef]
25. Chan, D.C. Mitochondrial Dynamics and Its Involvement in Disease. *Annu. Rev. Pathol.* **2019**, *15*, 235–259. [CrossRef]
26. Britton, S.; Freeman, T.; Vafiadaki, E.; Keers, S.; Harrison, R.; Bushby, K.; Bashir, R. The third human FER-1-like protein is highly similar to dysferlin. *Genomics* **2000**, *68*, 313–321. [CrossRef]
27. Leung, C.; Utokaparch, S.; Sharma, A.; Yu, C.; Abraham, T.; Borchers, C.; Bernatchez, P. Proteomic identification of dysferlin-interacting protein complexes in human vascular endothelium. *Biochem. Biophys. Res. Commun.* **2011**, *415*, 263–269. [CrossRef]
28. Vincent, A.E.; Rosa, H.S.; Alston, C.L.; Grady, J.P.; Rygiel, K.A.; Rocha, M.C.; Barresi, R.; Taylor, R.W.; Turnbull, D.M. Dysferlin mutations and mitochondrial dysfunction. *Neuromuscul. Disord.* **2016**, *26*, 782–788. [CrossRef]
29. Chen, H.; Detmer, S.A.; Ewald, A.J.; Griffin, E.E.; Fraser, S.E.; Chan, D.C. Mitofusins Mfn1 and Mfn2 coordinately regulate mitochondrial fusion and are essential for embryonic development. *J. Cell Biol.* **2003**, *160*, 189–200. [CrossRef]
30. Filadi, R.; Greotti, E.; Pizzo, P. Highlighting the endoplasmic reticulum-mitochondria connection: Focus on Mitofusin 2. *Pharmacol. Res.* **2018**, *128*, 42–51. [CrossRef]
31. Davis, D.B.; Delmonte, A.J.; Ly, C.T.; McNally, E.M. Myoferlin, a candidate gene and potential modifier of muscular dystrophy. *Hum. Mol. Genet.* **2000**, *9*, 217–226. [CrossRef]

32. Zhang, T.; Jingjie, L.; He, Y.; Yang, F.; Hao, Y.; Jin, W.; Wu, J.; Sun, Z.; Li, Y.; Chen, Y.; et al. A small molecule targeting myoferlin exerts promising anti-tumor effects on breast cancer. *Nat. Commun.* **2018**, *9*, 3726. [CrossRef]
33. Doghman-Bouguerra, M.; Lalli, E. ER-mitochondria interactions: Both strength and weakness within cancer cells. *Biochim. Biophys. Acta Mol. Cell. Res.* **2019**, *1866*, 650–662. [CrossRef] [PubMed]
34. Friedman, J.R.; Lackner, L.L.; West, M.; DiBenedetto, J.R.; Nunnari, J.; Voeltz, G.K. ER tubules mark sites of mitochondrial division. *Science* **2011**, *334*, 358–362. [CrossRef] [PubMed]
35. de Brito, O.M.; Scorrano, L. Mitofusin 2 tethers endoplasmic reticulum to mitochondria. *Nature* **2008**, *456*, 605–610. [CrossRef] [PubMed]
36. Filadi, R.; Greotti, E.; Turacchio, G.; Luini, A.; Pozzan, T.; Pizzo, P. Mitofusin 2 ablation increases endoplasmic reticulum-mitochondria coupling. *Proc. Natl. Acad. Sci. USA* **2015**, *112*, E2174–E2181. [CrossRef] [PubMed]
37. Wang, W.; Liu, X.; Liu, L.; Lou, W.; Jin, D.; Yang, P.; Wang, X. ITRAQ-based quantitative proteomics reveals myoferlin as a novel prognostic predictor in pancreatic adenocarcinoma. *J. Proteomics.* **2013**, *91*, 453–465. [CrossRef]
38. Argentiero, A.; Summa, S.; Fonte, R.; Iacobazzi, R.; Porcelli, L.; Vià, M.; Brunetti, O.; Azzariti, A.; Silvestris, N.; Solimando, A. Gene Expression Comparison between the Lymph Node-Positive and -Negative Reveals a Peculiar Immune Microenvironment Signature and a Theranostic Role for WNT Targeting in Pancreatic Ductal Adenocarcinoma: A Pilot Study. *Cancers* **2019**, *11*, 942. [CrossRef]
39. Gao, C.; Cao, W.; Bao, L.; Zuo, W.; Xie, G.; Cai, T.; Fu, W.; Zhang, J.; Wu, W.; Zhang, X.; et al. Autophagy negatively regulates Wnt signalling by promoting Dishevelled degradation. *Nat. Cell Biol.* **2010**, *12*, 781–790. [CrossRef]
40. Porcelli, L.; Iacobazzi, R.; Fonte, R.; Serratì, S.; Intini, A.; Solimando, A.; Brunetti, O.; Calabrese, A.; Leonetti, F.; Azzariti, A.; et al. CAFs and TGF-β Signaling Activation by Mast Cells Contribute to Resistance to Gemcitabine/Nabpaclitaxel in Pancreatic Cancer. *Cancers* **2019**, *11*, 330. [CrossRef]
41. Barnhouse, V.; Weist, J.; Shukla, V.; Ghadiali, S.; Kniss, D.; Leight, J. Myoferlin regulates epithelial cancer cell plasticity and migration through autocrine TGF-β1 signaling. *Oncotarget* **2018**, *9*, 19209–19222. [CrossRef] [PubMed]
42. Kumar, S.; Pan, C.; Shah, N.; Wheeler, S.; Hoyt, K.; Hempel, N.; Mythreye, K.; Lee, N. Activation of Mitofusin2 by Smad2-RIN1 Complex during Mitochondrial Fusion. *Mol. Cell* **2016**, *62*, 520–531. [CrossRef] [PubMed]
43. Bernatchez, P.N.; Acevedo, L.; Fernandez-Hernando, C.; Murata, T.; Chalouni, C.; Kim, J.; Erdjument-Bromage, H.; Shah, V.; Gratton, J.-P.; McNally, E.M.; et al. Myoferlin regulates vascular endothelial growth factor receptor-2 stability and function. *J. Biol. Chem.* **2007**, *282*, 30745–30753. [CrossRef] [PubMed]
44. Stauffer, W.; Sheng, H.; Lim, H.N. EzColocalization: An ImageJ plugin for visualizing and measuring colocalization in cells and organisms. *Sci. Rep.* **2018**, *8*, 15764. [CrossRef]
45. de Chaumont, F.; Dallongeville, S.; Chenouard, N.; Hervé, N.; Pop, S.; Provoost, T.; Meas-Yedid, V.; Pankajakshan, P.; Lecomte, T.; Montagner, Y.L.; et al. Icy: An open bioimage informatics platform for extended reproducible research. *Nat. Methods* **2012**, *9*, 690–696. [CrossRef]

cells

MDPI

Review

Ferlin Overview: From Membrane to Cancer Biology

Olivier Peulen [1,*], Gilles Rademaker [1], Sandy Anania [1], Andrei Turtoi [2,3,4], Akeila Bellahcène [1] and Vincent Castronovo [1]

1 Metastasis Research Laboratory, Giga Cancer, University of Liège, B4000 Liège, Belgium
2 Tumor Microenvironment Laboratory, Institut de Recherche en Cancérologie de Montpellier, INSERM U1194, 34000 Montpellier, France
3 Institut du Cancer de Montpeiller, 34000 Montpellier, France
4 Université de Montpellier, 34000 Montpellier, France
* Correspondence: olivier.peulen@uliege.be; Tel.: +32-4-366-37-92

Received: 8 August 2019; Accepted: 21 August 2019; Published: 22 August 2019

Abstract: In mammal myocytes, endothelial cells and inner ear cells, ferlins are proteins involved in membrane processes such as fusion, recycling, endo- and exocytosis. They harbour several C2 domains allowing their interaction with phospholipids. The expression of several Ferlin genes was described as altered in several tumoural tissues. Intriguingly, beyond a simple alteration, myoferlin, otoferlin and Fer1L4 expressions were negatively correlated with patient survival in some cancer types. Therefore, it can be assumed that membrane biology is of extreme importance for cell survival and signalling, making Ferlin proteins core machinery indispensable for cancer cell adaptation to hostile environments. The evidences suggest that myoferlin, when overexpressed, enhances cancer cell proliferation, migration and metabolism by affecting various aspects of membrane biology. Targeting myoferlin using pharmacological compounds, gene transfer technology, or interfering RNA is now considered as an emerging therapeutic strategy.

Keywords: ferlin; myoferlin; dysferlin; otoferlin; C2 domain; plasma membrane

1. Introduction

Ferlin is a family of proteins involved in vesicle fusions. To date, more than 760 articles in Pubmed refer to one of its members. Most of these publications are related to muscle biology, while less than 50 are directly related to cancer. However, the emerging idea of targeting plasma membranes [1] and the discovery of a significant correlation between Ferlin gene expression and cancer patient survival, brings attention to cancer. This review focused attention on the roles of these proteins, first in a healthy context, then in cancer.

During the maturation of spermatids to motile spermatozoa in *Caenorhabditis elegans* worm, large vesicles called membranous organelles fuse with the spermatid plasma membrane. This step requires a functional FER-1 protein encoded by the fer-1 gene (*fertilization defective-1*) [2]. When FER-1 was identified and sequenced, no other known proteins had strong resemblance to it. Subsequently, homologs were found by sequence similarity in mammals, forming a family of similar proteins now called ferlins. In humans, a first *C. elegans* fer-1 homolog gene was discovered and the protein encoded by this gene was named dysferlin [3]. Shortly after, a second human FER-1-Like gene was identified. The product of the gene was named otoferlin [4]. The human EST database mining revealed a dysferlin paralog called myoferlin [5,6]. Three new members joined the ferlin gene family: FER1L4, a pseudogene; FER1L5; and FER1L6. The main features of ferlins are summarized in Table 1.

Table 1. Short description of *C. elegans* and human ferlin genes and proteins.

Protein Name (Uniprot Number)	Gene Name	Chromosome Mapping	Main Protein Size
Sperm vesicle fusion protein FER-1 (Q17388)	fer-1		2034 AA (235 KDa)
Dysferlin (O75923)	Fer1-Like 1 Fer1L1	2p13.2	2080 AA (237 KDa)
Otoferlin (Q9HC10)	Fer1-Like Fer1L2	2p23.3	1997 AA (227 KDa)
Myoferlin (Q9NZM1)	Fer1-Like 3 Fer1L3	10q23.33	2061 AA (230 KDa)
FER1L4 (A9Z1Z3)	Fer1-Like 4 Fer1L4	20q11.22	pseudogene
FER1L5 (A0AVI2)	Fer1-Like 5 Fer1L5	2q11.2	2057 AA (238 KDa)
FER1L6 (Q2WGJ9)	Fer1-Like 6 Fer1L6	8q24.13	1857 AA (209 KDa)

The dysferlin mutations were involved in Limb-Girdle muscular dystrophy 2B (LGMD2B), a autosomal recessive degenerative myopathy, and in Miyoshi muscular dystrophy 1 (MMD1), a late-onset muscular dystrophy [3,7]. The otoferlin mutations were described in the non-syndromic prelingual deafness (DFNB9) and in the auditory neuropathy autosomal recessive 1 (AUNB1) [4,8,9]. Nowadays, myoferlin and the 3 last members of the ferlin family are still not linked to human genetic diseases. However, myoferlin was proposed as a modifier protein for muscular dystrophy phenotype [5] and studies of myoferlin-null mice demonstrated impaired myoblast fusion and myofiber formation during muscle development and regeneration [10]. More recently, a truncated variant of myoferlin was associated with Limb-Girdle type muscular dystrophy and cardiomyopathy [11]. Here under, this review discusses that ferlins, mainly myoferlin, are involved in neoplastic diseases and are potential therapeutic targets.

2. Genomic Organization of Ferlin Gene Family

Ferlin genomic organization has not been extensively investigated. Nonetheless, valuable information was obtained from sequencing and subsequent gene annotation (www.ensembl.org). In *C. elegans*, fer-1 gene is approximately 8.6 kb in length and composed of 21 exons [2]. In humans, dysferlin gene (DYSF) is composed of 55 exons [12], and encodes 19 splice variant transcripts. Otoferlin gene (OTOF) contains 47 exons and encodes 7 splice variants. One of them is retaining an intronic sequence from other locus and is not coding for protein. An alternate splicing results in a neuronal-specific domain for otoferlin, regulated by the inclusion of exon 47 [8]. Myoferlin gene (MYOF), is composed of 54 exons and encodes for 9 splice variants. Four of them are not translated to protein and the shortest retains an intronic sequence. Myoferlin promoter includes several consensus-binding sites, such as for Myc, MEF2, CEBP, Sp1, AP1, and NFAT. The latter is able to bind endogenous NFATc1 and NFATc3 [13]. FER1L5 encodes 7 splice variants obtained by the arrangement of 53 exons. Five transcripts are known to encode proteins when the 2 shortest are retaining intronic sequences and do not encode protein. FER1L6 gene is composed of 41 exons and encodes a unique transcript. The main features of ferlin genes are summarized in Table 2.

Table 2. Short description of *C. elegans* and human ferlin genes and transcripts.

Gene Name	Gene Length	Number of Exons	Transcript Size	Number of Variants
Fer-1	8.6 kb	21	6.2 kb	3
Fer1-Like 1 Fer1L1 (DYSF)	233 kb	55	0.5–6.7 kb	19
Fer1-Like 2 Fer1L2 (OTOF)	121 kb	47	0.5–7.2 kb	7
Fer1-Like 3 Fer1L3 (MYOF)	180 kb	54	0.4–6.7 kb	9
Fer1-Like 4 Fer1L4	48 kb	43	0.2–5.9 kb	13
Fer1-Like 5 Fer1L5	64 kb	53	3.5–6.5 kb	7
Fer1-Like 6 Fer1L6	278 kb	41	6 kb	1

3. Ferlin's Structure and Localization

Caenorrhabditis elegans FER-1 is a large protein rich in charged residues. Charged amino acids are distributed throughout the whole protein length such that no particularly acidic or basic domains are observed. The hydrophobicity plot described a 35 amino acid long hydrophobic region at the C-terminal end [2]. To the authors' knowledge, it has never been experimentally demonstrated. Similarity studies suggest that this region might be a transmembrane domain. FER-1 sequence analysis with Pfam protein families database [14] revealed the existence of 4 C2 domains and several other domains.

Ferlins are proteins harboring multi-C2 domains. These structural domains are ~130 amino acid long independently folded modules found in several eukaryotic proteins. They were identified in classical Protein Kinase C (PKC) as the second conserved domain out of four. The typical C2 domain is composed of a beta-sandwich made of 8 beta-strands coordinating calcium ions, participating to their ability to bind phospholipids (for review [15]). However, some C2 domains have lost their capacity to bind calcium but still bind membranes [16]. A large variety of proteins containing C2 domains have been identified, and most of them are involved in membrane biology, such as vesicular transport (synaptotagmin), GTPase regulation (Ras GTPase activating protein) or lipid modification (phospholipase C) (for review [17]).

Human ferlin proteins harbour 5 to 7 C2 domains as described in the Pfam database (Figure 1A). According to this database, in humans, 342 proteins harbour C2 domains. However, the occurrence of multiple tandem C2 domains is uncommon. Only three vertebrate protein families contain more than two C2 domains: The multiple C2 domain and transmembrane region proteins (MCTP) [18], the E-Syt (extended synaptotagmins) [19], and the ferlins. The typical feature of a C2 domain is its ability to interact with two or three calcium ions. The prototype of this domain is the C2A contained in PKC that binds phospholipids in a calcium-dependent manner. Several other distinct C2 domain subtypes, e.g. those found in PI3K and in PTEN, do not have calcium binding abilities and instead specialize in protein-protein interactions [16,17]. In classical Ca^{2+}-binding C2 domains, 5 aspartate residues are involved in the ion binding [20]. Clustal omega alignment of ferlin C2 domains with PKC and synaptotagmin I C2 domains revealed that the 5 Ca^{2+}-binding aspartic acids were conserved or substituted by a glutamic acid in the C2E and C2F domains of all human paralogs (Figure 1B). The aspartic acid to glutamic acid substitution is considered as highly conservative and observed in some non-ferlin Ca^{2+}-binding C2 domains [21]. Some ferlins showed more C2 domains with Ca^{2+}-binding potential, e.g. dysferlin and myoferlin C2C and C2D, otoferlin C2D and fer1L6 C2D [22]. The phylogenic tree created by neighbour-joining of a Clustal omega alignment of C2 domain sequences shows that a C2 domain is more similar to others at a similar position in ortholog proteins than it is to the other C2 domains within the same protein [23]. A Clustal omega alignment reveals an evolutionary

distribution of the ferlin proteins into two main subgroups (Figure 1C): The type 1 ferlins containing a DysF domain and the type-2 ferlins without the DysF domain [22]. This domain is present in yeast peroxisomal proteins where its established function is to regulate the peroxisome size and number [24]. In mammals, despite the fact that its solution structure was resolved [25] and that many pathogenic point mutations occur in this region [26,27], the function of this domain remains unknown.

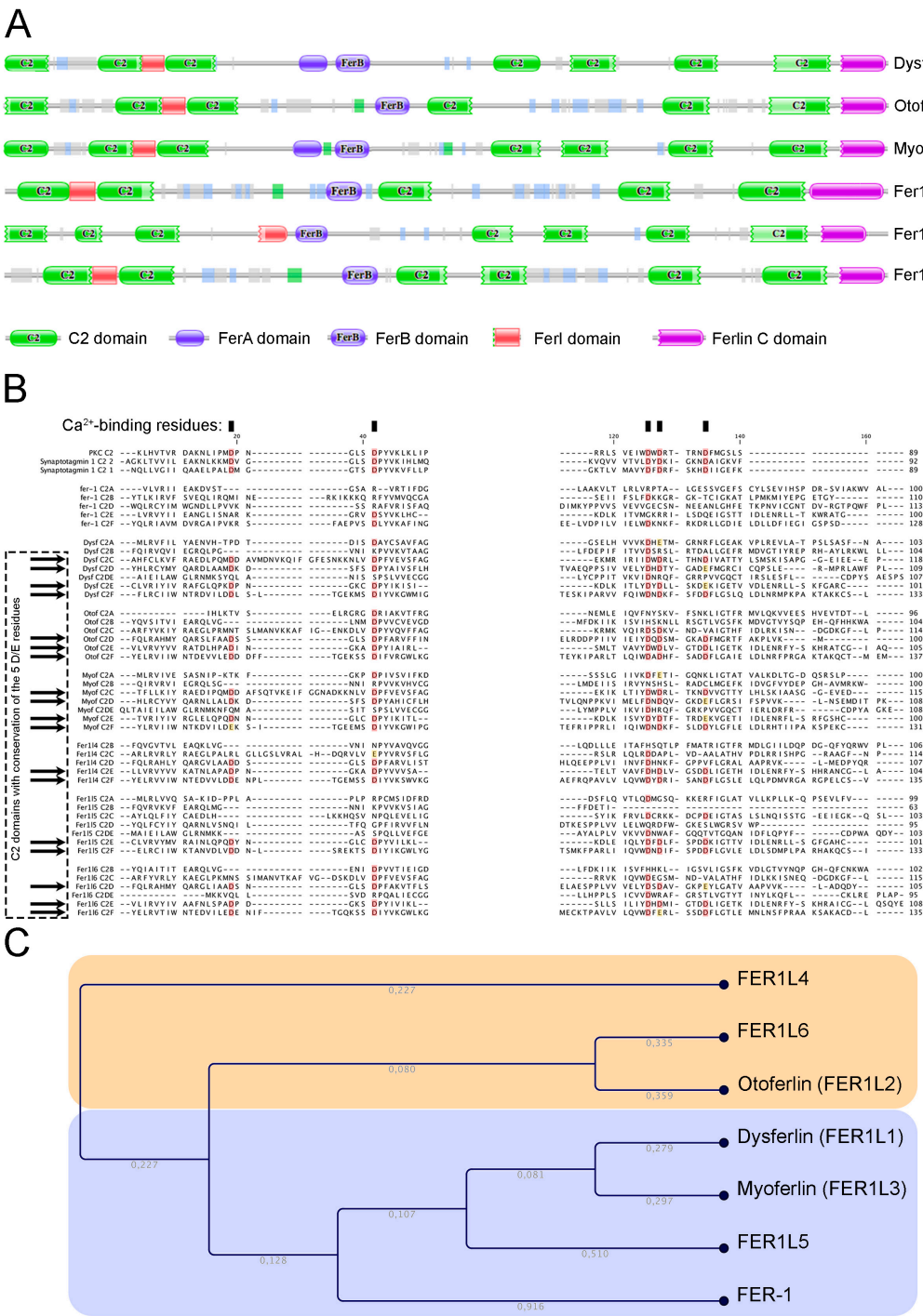

Figure 1. Structure and phylogenic relation of ferlin proteins. (**A**) Schematic structure of FER-1 human homologs as produced by Pfam protein families' database. (**B**) Clustal omega multiple alignment of ferlin C2 domains. Conserved Ca^{2+}-binding site are highlighted in red (aspartic acid—D) or yellow (glutamic acid—E). (**C**) Cladogram of clustal omega alignment indicating type 1 ferlins in blue and type 2 ferlins in yellow. The branch length is indicated in grey.

Immunodetection of a myoferlin-haemagglutinin fusion protein in non-permeabilised COS-7 cells confirmed the presence of the C-terminal domain of the protein in the extracellular compartment [28], supporting the functionality of the putative trans-membrane region. The sublocalisation of ferlins was further studied, indicating robust membrane localisation for dysferlin, myoferlin and Fer1L6 while only low levels of otoferlin were at the plasma membrane and Fer1L5 was intracellular. Dysferlin and myoferlin were localised within the endo-lysosomal pathway accumulating in late endosomes and in recycling compartment. GFP-myoferlin fusion protein revealed that myoferlin was colocalized with lysosomal markers in NIH3T3 cells [29]. Otoferlin has been shown to move from the trans-Golgi network to the plasma membrane and inversely. Fer1L5 was cytosolic while Fer1L6 was detected in a specific sub-compartment of the trans-Golgi network compartment [30].

4. Ferlin's Interactions with Phospholipids

Ferlins are regarded as intrinsic membrane proteins through their putative transmembrane region. However, they can also interact with membranes by other domains. Experimentally, myoferlin C2A was the single C2 domain able to bind to phospholipid vesicles. A significant presence of the negatively charged phosphatidylserine (PS) was required for this interaction. Myoferlin C2A binding to PS-containing vesicles did not occur with calcium concentration similar to the one observed in the basal physiological condition (0.1 μM). Indeed, the half-maximal binding was observed at 1 μM [31], suggesting that the C2A domain is involved in specific processes inside the cell requiring Ca^{2+} release from intracellular stock, like in Ca^{2+}-regulated exocytosis. When cells are stimulated by various means, including depolarization and ligand binding, the cytosolic Ca^{2+} concentration increases to the concentration up to 1 μM or more [32], similar to the one required by myoferlin C2A domain to bind lipids. It appears that dysferlin C2A domain has the same binding properties as myoferlin C2A domain. However, its half-maximal lipid binding was higher (4.5 μM) [31]. A recent publication confirmed that myoferlin and dysferlin C2A domains exhibit different Ca^{2+} affinities. However, they describe myoferlin C2A domain with a lower Ca^{2+} affinity than the dysferlin homolog C2 domain, and a marginal binding of myoferlin C2A domain to phospholipid mixture containing PS [33]. The binding of dysferlin C2A to PS was confirmed and extended to several phosphoinositide monophosphates in a Ca^{2+}-dependent fashion. Therrien et al. observed that all remaining dysferlin C2 domains were able to bind to PS but independently of Ca^{2+} [34]. The laurdan fluorescence emission experiments suggest that dysferlin and myoferlin contribute to increase the lipid order in lipid vesicles. The magnitude of this observation was calcium-enhanced and C2 domains within both N- and C-termini of ferlins influenced lipid packing. The experiments conducted with individual recombinant ferlin's C2A-C domains demonstrated that all of them are able to increase lipid order [35].

The authors described in the first part of this review the conservation of the 5 Ca^{2+}-binding aspartate residues in the C2D-F domains of otoferlin making them putative Ca^{2+}-binding sites. In addition to its C2D-F domains, otoferlin is also able to bind Ca^{2+} via its C2B and C2C domains [36]. Despite the fact that C2A domain from otoferlin does not possess all five aspartate residues, its ability to bind Ca^{2+} is still under debate. Therrien and colleagues showed that otoferlin C2A domain can bind PS in a Ca^{2+}-dependent fashion, suggesting an interaction with this ion [34]. This interaction was confirmed by a direct measure of otoferlin-binding to liposomes in the presence of Ca^{2+} (1 mM). Moreover, C2A-C domains seem to bind lipids also under calcium free conditions [36]. At the opposite, a spectroscopy analysis indicates that otoferlin C2A domain is unable to coordinate Ca^{2+} ion [37].

Floatation assays were unable to confirm the interaction between otoferlin C2A and lipids. This may be due to the presence of a shorter membrane-interacting loop at the top of the domain [37]. As for dysferlin and myoferlin, otoferlin increases lipid order in vesicles. However, its C2A does not participate to the phenomenon [35].

Ferlin proteins contain also a FerA domain recently described as a four-helix bundle fold with its own Ca^{2+}-dependent phospholipid-binding activity [38].

5. Ferlin's Main Functions in Non-Neoplastic Cells and Tissues

5.1. In Mammal Muscle Cells

Dysferlin and myoferlin have a specific temporal pattern of expression in an in vitro model of muscle development. Myoferlin was highly expressed in myoblasts that have elongated prior to fusion to syncytial myotubes. After fusion, myoferlin expression was decreased. The dysferlin expression increased concomitantly with the fusion and maturation of myotubes [31]. A proteomic analysis revealed the interacting partners of dysferlin during muscle differentiation [39]. It appeared that the number of partners decreases during the differentiation process, while the core-set of partners is large (115 proteins). Surprisingly, the dysferlin homolog myoferlin was consistently co-immunoprecipitated with dysferlin. The gene ontology analysis of the core-set proteins indicates that the highest ranked clusters are related to vesicle trafficking. In the C2C12 myoblast model, immunoprecipitation experiments showed that myoferlin interacts with the Eps15 Homology Domain 2 (EHD2) apparently through a NPF (asparagine-proline-phenylalanine) motif in its C2B domain [40]. EHD2 has been implicated in endocytic recycling. It was inferred that the interaction between EHD2 and myoferlin might indirectly regulate disassembly or reorganization of the cytoskeleton that accompanies myoblast fusion.

Dysferlin-null mice develop a slowly progressive muscular dystrophy with a loss of plasma membrane integrity. The presence of a stable and functional dystrophin–glycoprotein complex (DGC), involved in muscle injury-susceptibility when altered, suggests that dysferlin has a role in sarcolemma repair process. This was confirmed in dysferlin-null mice by a markedly delayed membrane resealing, even in the presence of Ca^{2+} [41]. Pharmacological experiments conducted in skeletal muscles demonstrated that dysferlin modulates smooth reticulum Ca^{2+} release and that in its absence injuries cause an increased ryanodine receptor (RyR1)-mediated Ca^{2+} leak from the smooth reticulum into the cytoplasm [42]. In the SJL/J mice model of dysferlinopathy, annexin-1 and -2 co-precipitate with muscle dysferlin and co-localise at sarcolemma in an injury-dependent manner [43]. An immunofluorescence analysis of mitochondrial respiratory chain complexes in the muscles from the patients with dysferlinopathy revealed complex I- and complex IV-deficient myofibers [44]. This report is particularly interesting in light of the dysferlin_v1 alternate transcript discovered in skeletal muscle [45] and harboring a mitochondrial importation signal [39].

Intriguingly, at the site of membrane injury, only the C-terminal extremity of dysferlin was immunodetected. It was reported than dysferlin was cleaved by calpain [46], one of its interacting proteins [39]. The cleavage generate a C-terminal fragment called mini-dysferlin$_{C72}$ bearing two cytoplasmic C2 domains anchored by a transmembrane domain [46]. Myoferlin expression is also up regulated in damaged myofibers and in surrounding mononuclear muscle and inflammatory cells [13]. As it was observed for dysferlin, myoferlin can be cleaved by calpain to produce a mini-myoferlin module composed of the C2E and C2F domains [47].

Membrane repair requires the accumulation and fusion of vesicles with each other and with plasma membrane at the disruption point. A role for dysferlin and myoferlin in these processes is consistent with the presence of several C2 domains and with their homology with FER-1 having a role in vesicle fusion. Moreover, mini-dysferlin and mini-myoferlin bear structural resemblance to synaptotagmin, a well-known actor in synaptic vesicle fusion with the presynaptic membrane [48].

In mouse skeletal muscle, myoferlin was found at the nuclear and plasma membrane [5]. It is highly expressed in myoblasts before their fusion to myotubes [10,31] and found to be highly concentrated at the site of apposed myoblast and myotube membranes, and at site of contact between two myotubes [10]. Myoblast fusion requires a Ca^{2+} concentration increase to 1.4 µM [49], similar to the one reported for myoferlin C2A binding to phospholipids [31]. Myoferlin-null mice myoblasts show impaired fusion in vitro, producing mice with smaller muscles and smaller myofibers in vivo [10]. All together, these observations support a role for myoferlin in the maturation of myotubes and the formation of large myotubes that arise from the fusion of myoblasts to multinucleated myotubes.

Interestingly, myoferlin-null mice are unresponsive to IGF-1 for the myoblast fusion to the pre-existing myofibers. Mechanistic experiments indicate a defect in IGF-1 internalization and a redirection of the IGF1R to the lysosomal degradation pathway instead of recycling. As expected, myoferlin-null myoblasts lacked the IGF1-induced increase in AKT and MAPK activity downstream to IGFR [50].

The defects in myoblast fusion and muscle repair observed in myoferlin-null mice are reminiscent of what was reported in muscle lacking nuclear factor of activated T-cells (NFAT). Demonbreun and colleagues suggested that in injured myofibers, the membrane damages induce an intracellular increase of Ca^{2+} concentration producing a calcineurin-dependent NFAT activation and subsequent translocation to the nucleus. The activated NFAT can therefore bind to its response element on the myoferlin promoter [13].

Using HeLa and HEK293T cell lines overexpressing ADAM-12, it was discovered that myoferlin was one of the ten most abundant interacting partners of ADAM-12 [51]. Though this was discovered in an artificial overexpressing model using cancer cells, it can be considered as pertinent in the context of muscle cell repair. Indeed, ADAM-12 is a marker of skeletal muscle regeneration interacting with the actin-binding protein α-actinin-2 in the context of myoblast fusion [52].

The differentiating myoblast C2C12 expressed Fer1L5 at the protein level with an expression pattern similar to dysferlin throughout myoblast differentiation. Fer1L5 shares with myoferlin a NPF motif in its C2B domain. As in myoferlin, this motif was described as interacting with EHD2, but also with EHD1 [53].

5.2. In mammal Inner Ear Cells

In adult mouse cochlea, otoferlin gene expression is limited to inner hair cells (IHC) [4]. In these cells, the strongest immunostaining of otoferlin was associated with the basolateral region, where the afferent synaptic contacts are located, suggesting that otoferlin is a component of the IHC presynaptic machinery. Ultrastructural observations confirmed the association of otoferlin with the synaptic vesicles. It appears that otoferlin is not necessary for the synapse formation [54], but rather regulates the Ca^{2+}-induced synaptic vesicle exocytosis [36].

At molecular level, otoferlin interacts with plasma membrane t-SNARE (*soluble N-ethylmaleimide-sensitive-factor attachment protein receptor)* proteins (syntaxin 1 and SNAP-25) in a Ca^{2+}-dependent manner [54]. Supporting this discovery, both t-SNARE proteins are known to interact with synaptotagmin I, a C2 domain harbouring protein, in the context of the classical synaptic vesicles docking [55,56]. It was reported that otoferlin relies on C2F domain for its Ca^{2+}-dependent interaction with t-SNARE [57–59]. However, others suggest a Ca^{2+}-dependent interaction through the C2C, C2D, C2E and C2F domains and a Ca^{2+}-independent interaction via the C2A and C2B domains. The SNARE-mediated membrane fusion was reconstituted with proteoliposomes. This assay indicates that in presence of Ca^{2+}, otoferlin accelerates the fusion process [36], suggesting that otoferlin operates as a calcium-sensor for SNARE-mediated membrane fusion.

5.3. In Mammal Endothelial Cells

Bernatchez and colleagues reported that dysferlin and myoferlin are abundant in caveolae-enriched membrane microdomains/lipid rafts (CEM/LR) isolated from human endothelial cells and are highly expressed in mouse blood vessels [28,60]. As observed for dysferlin in muscle cells, myoferlin regulates the endothelial cell membrane resealing after physical damage. In endothelial cells, myoferlin silencing reduced or abolished the ERK-1/2, JNK or PLCγ phosphorylation by VEGF, resulting from a loss of VEGFR-2 stabilization at the membrane. Indeed, myoferlin silencing caused an increase in VEGFR2 polyubiquitination, which leads to its degradation [28]. In contrast to what was observed in myoferlin-silenced endothelial cells, dysferlin gene silencing decrease neither VEGFR2 expression nor its downstream signalling. However, dysferlin-siRNA treated endothelial cells showed a near-complete inhibition of proliferation when they were sub-confluent. The proliferation decrease

seems to be due to an impaired attachment rather than to cell death, as supported by adhesion assays and PECAM-1 poly-ubiquitination that leads to its degradation. Co-immunoprecipitation and co-localisation experiments support the formation of a molecular complex between dysferlin and PECAM-1. This PECAM-1 degradation leads, in dysferlin-null mice, to a blunted VEGF-induced angiogenesis [60]. Another angiogenic tyrosine kinase receptor Tie-2 (tyrosine kinase with Ig and epidermal growth factor homology domains-2) is significantly less expressed at the plasma membrane when myoferlin is silenced in endothelial cells [61]. In this case, it appears that proteasomal degradation plays a minor role in the down regulation of the receptor. Strikingly, G-protein coupled receptors (GCPR) were unaffected by the decrease of myoferlin expression, suggesting a selective effect on receptor tyrosine kinases (RTK).

It was also reported that in endothelial cells, myoferlin is required for an efficient clathrin and caveolae/raft-dependent endocytosis, is co-localized with Dynamin-2 protein [62] and that the FASL-induced lysosome fusion to plasma membrane is mediated by dysferlin C2A domain [63].

5.4. Other Mammal's Cells

Dysferlin and myoferlin are expressed in both basal and ciliated airway epithelial cells from healthy human lungs [64]. In the airway epithelial cell line (16HBE), dysferlin and myoferlin were immuno-detected at the plasma membrane, Golgi membrane and in cytoplasm but not in the nuclei. The silencing of myoferlin in these cells induces the loss of zonula occludens (ZO)-1, inducing apoptosis [64].

Myoferlin was also detected in exosomes from human eye trabecular meshwork cells [65] and in phagocytes where it participates to the fusion between lysosomes and the plasma membrane, thus promoting the release of lysosomal contents [29].

The Fer1L5 gene expression was largely restricted to the pancreas, where it was alternatively spliced by removing exon 51 [30].

6. Ferlins in Cancer, Potential Targets to Kill Cancer

It is clear from the data above that ferlins are consistently involved in membrane processes requiring membrane fusion, including endocytosis, exocytosis, membrane repair, recycling and remodelling. Membrane processes are of extreme importance for cell survival and signalling, making them core machinery for cancer cell adaptation to hostile environments.

Considering that ferlins have been only scarcely investigated in cancer, the authors next sought to mine publicly available databases and gain information regarding ferlin's expression or mutation in tumors. Using the FireBrowse gene expression viewer (firebrowse.org), The Cancer Genome Atlas (TCGA) RNAseq data of all ferlin's genes in neoplastic tissues were investigated in order to obtain a differential expression in comparison to their normal counterparts. It appears that all ferlin genes are modulated in several cancer types. Myoferlin and fer1l4 genes are more frequently up regulated than down regulated, while dysferlin, fer1l5, and fer1l6 are more frequently down regulated (Figure 2).

Experimentally, a myoferlin gene was discovered as highly expressed in several tumour tissues including the pancreas [66,67], breast [68], kidneys [68], and head and neck squamous cell carcinoma (HNSCC) [69]. This expression was confirmed at a protein level in tumour tissue and/or cell lines from the pancreas [70–73], breast [74,75], lungs [75], melanoma [75], hepatocellular carcinoma [76], HNSCC [77], clear cell renal carcinoma [78,79], and endometroid carcinoma [80]. Myoferlin was also detected at a protein level in microvesicles/exosomes derived from several cancer cells including the bladder [81], colon [82–85], ovary [86], prostate [87], breast and pancreas, where it plays a role in vesicle fusion with the recipient endothelial cells [88].

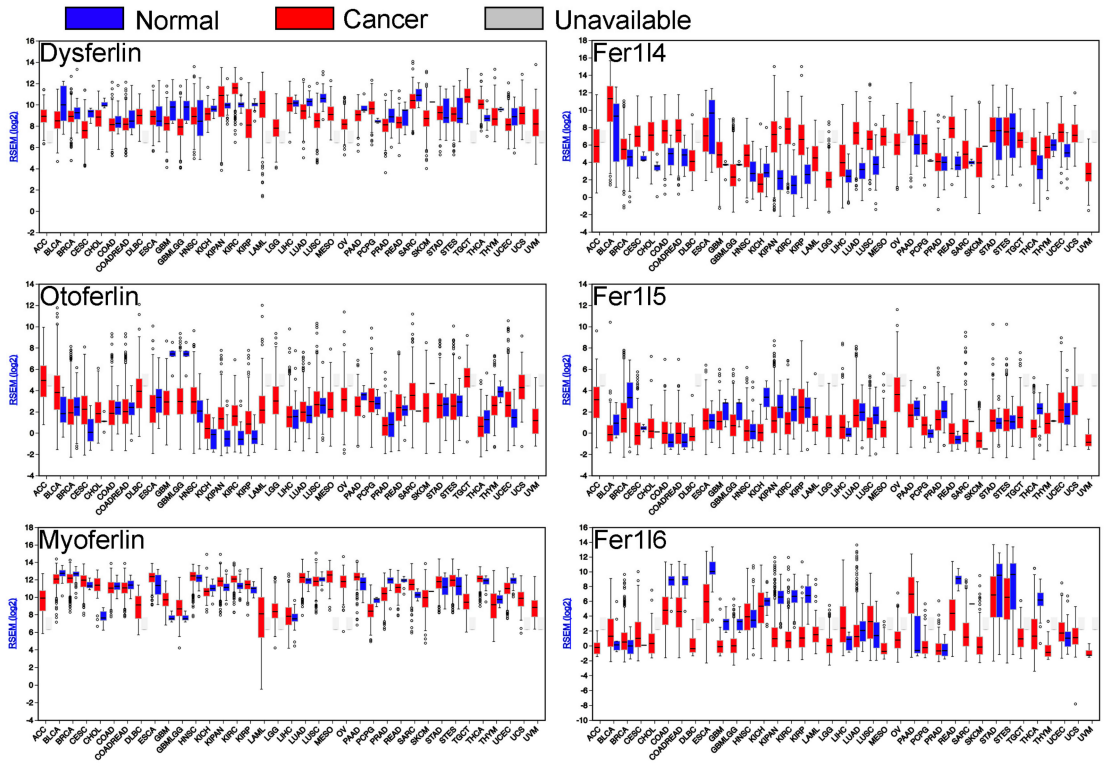

Figure 2. Ferlin gene expression in several cancers (red) and their normal counterparts (blue). Cancer tissues from adrenocortical carcinoma (ACC), bladder urothelial carcinoma (BLCA), breast invasive carcinoma (BRCA), cervical squamous cell carcinoma and endocervical adenocarcinoma (CESC), cholangiocarcinoma (CHOL), colon adenocarcinoma (COAD), colorectal adenocarcinoma (COADREAD), lymphoid neoplasm diffuse large B-cell lymphoma (DLBC), esophageal carcinoma (ESCA), glioblastoma multiforme (GBM), glioma (GBMLGG), head and neck squamous cell carcinoma (HNSC), kidney chromophobe (KICH), pan-kidney cohort (KIPAN), kidney renal clear cell carcinoma (KIRC), kidney renal papillary cell carcinoma (KIRP), acute myeloid leukemia (LAML), brain lower grade glioma (LGG), liver hepatocellular carcinoma (LIHC), lung adenocarcinoma (LUAD), lung squamous cell carcinoma (LUBC), mesothelioma (MESO), ovarian serous cystadenocarcinoma (OV), pancreatic adenocarcinoma (PAAD), pheochromocytoma and paraganglioma (PCPG), prostate adenocarcinoma (PRAD), rectum adenocarcinoma (READ), sarcoma (SARC), skin cutaneous melanoma (SKCM), stomach adenocarcinoma (STAD), stomach and esophageal carcinoma (STES), testicular germ cell tumours (TGCT), thyroid carcinoma (THCA), thymoma (THYM), uterine corpus endometrial carcinoma (UCEC), uterine carcinosarcoma (UCS), uveal melanoma (UVM).

This review then explored the mutations occurring in ferlin genes in tumours using Tumorportal (http://www.tumorportal.org) [89]. Several mutations were reported in ferlin genes in a few cancer types. However, none of them were considered as significant. Survival was also analysed (Table 3) using a pan-cancer method available online (OncoLnc–http://www.oncolnc.org) and combining mRNAs, miRNAs, and lncRNAs expression [90]. Noticeably, otoferlin expression was strongly significantly correlated with survival in renal clear cell carcinoma (KIRC–$p < 10^{-5}$); myoferlin expression was strongly significantly correlated with survival in brain lower grade glioma (LGG–$p < 10^{-4}$) and pancreatic adenocarcinoma (PAAD–$p < 10^{-4}$), and Fer1l4 expression was strongly significantly correlated with survival in bladder urothelial carcinoma (BLCA–$p < 10^{-5}$) and kidney renal clear cell carcinoma (KIRC–$p < 10^{-5}$). The 5 more significant correlations between ferlin's expression and the overall survival were represented as Kaplan-Meier curves with their associated log-rank p-value (Figure 3).

Table 3. Survival analysis by a Cox regression.

Positive Association			Negative Association		
Cohort	**Cox Coefficient**	**p-Value**	**Cohort**	**Cox Coefficient**	**p-Value**
DYSF EXPRESSION					
CESC	0.266	$4.20e^{-02}$	SARC	−0.277	$1.00e^{-02}$
STAD	0.171	$4.80e^{-02}$	KIRC	−0.220	$1.00e^{-02}$
OTOF EXPRESSION					
KIRC	**0.377**	**$1.50e^{-06}$**	BLCA	−0.275	$4.50e^{-04}$
KIRP	0.413	$4.90e^{-03}$	SKCM	−0.169	$1.40e^{-02}$
MYOF EXPRESSION					
LGG	**0.441**	**$1.40e^{-05}$**	SKCM	−0.163	$1.90e^{-02}$
PAAD	**0.561**	**$1.70e^{-05}$**			
LAML	0.215	$4.70e^{-02}$			
FER1L4 EXPRESSION					
KIRC	**0.356**	**$5.20e^{-06}$**	**BLCA**	**−0.383**	**$2.90e^{-06}$**
KIRP	0.492	$1.10e^{-03}$	SKCM	−0.225	$1.10e^{-03}$
LGG	0.244	$4.00e^{-03}$			
FER1L5 EXPRESSION					
LUAD	−0.199	$1.30e^{-02}$			
FER1L6 EXPRESSION					
KIRC	−0.160	$4.80e^{-02}$			
READ	−0.401	$4.90e^{-02}$			

Ferlin gene expression from cohorts with cancer was submitted to a survival analysis with a Cox regression. The red rows indicate a negative Cox coefficient, the green rows indicate positive Cox coefficient. The bold p-values were considered as highly significant ($p < 10^{-4}$). Bladder urothelial carcinoma (BLCA), cervical squamous cell carcinoma and endocervical adenocarcinoma (CESC), kidney renal clear cell carcinoma (KIRC), kidney renal papillary cell carcinoma (KIRP), acute myeloid leukemia (LAML), brain lower grade glioma (LGG), lung adenocarcinoma (LUAD), pancreatic adenocarcinoma (PAAD), rectum adenocarcinoma (READ), sarcoma (SARC), skin cutaneous melanoma (SKCM), stomach adenocarcinoma (STAD).

Interestingly, a recent publication points out specific single nucleotide polymorphisms in dysferlin genes as significantly associated with pancreas cancer patient survival [91]. Mining the TCGA database, a high Fer1L4 expression was reported as a predictor of a poor prognosis in glioma [92,93] and as an oncogenic driver in several human cancers [94]. However, several other publications pointed it out as a predictor of good prognosis in osteosarcoma [95], gastric cancer [96], endometrial carcinoma [97].

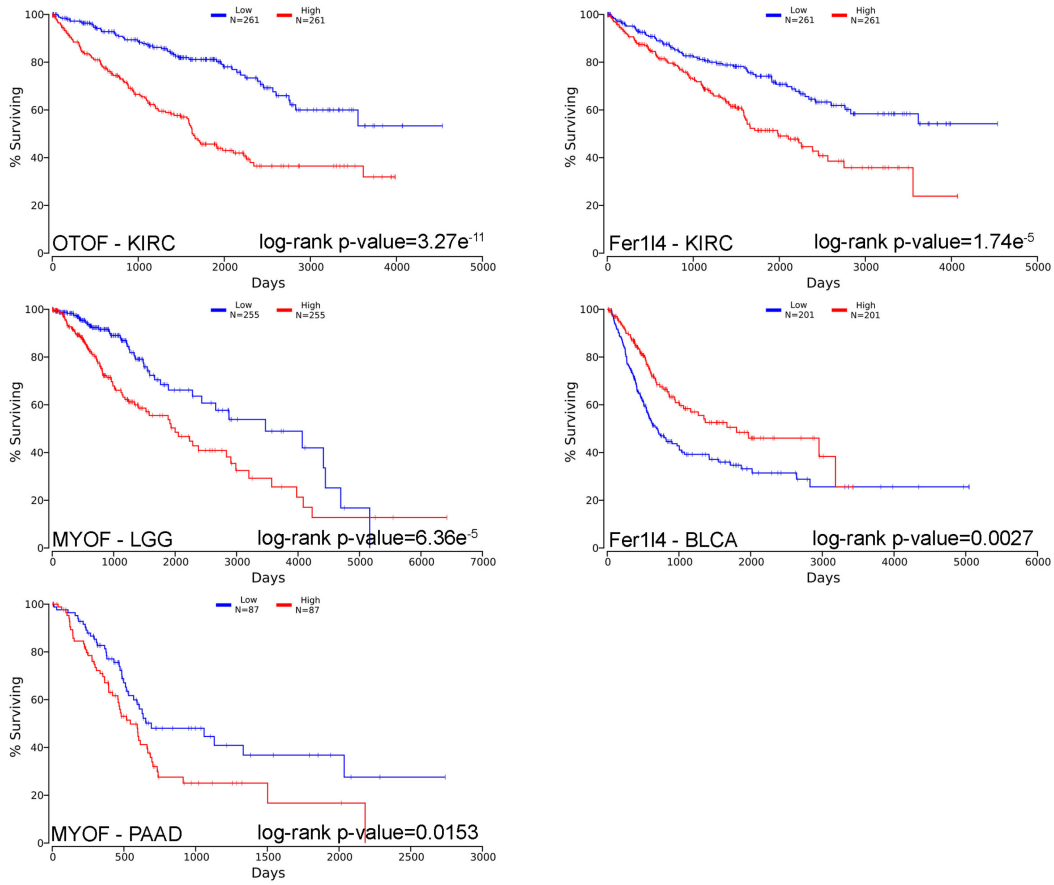

Figure 3. Kaplan-Meier survival curves of patient cohorts with different cancer types. Ferlin gene expression was segregated in low (blue) and high (red) expression according to median in kidney renal clear cell carcinoma (KIRC), brain lower grade glioma (LGG), bladder urothelial carcinoma (BLCA), and pancreatic adenocarcinoma (PAAD).

6.1. Breast Cancer and Melanoma

A mathematical model was proposed to examine the role of myoferlin in cancer cell invasion. This model confirms the experimental observation of decreased invasion of the myoferlin-null breast MDA-MB-231 cell line, and predicts that the pro-invasion effect of myoferlin may be in large partly mediated by MMPs [98]. The model was further validated in vitro suggesting a mesenchymal to epithelial transition (MET) when myoferlin was knockdown [99,100]. Using the same cell model, Blackstone and colleagues showed that myoferlin depletion increased cell adhesion to PET substrate by enhancing focal adhesion kinase (FAK) and its associated protein paxillin (PAX) phosphorylation [101]. Interestingly, myoferlin was reported as regulating the cell migration through a TGF-β1 autocrine loop [102]. Recently, related results were reported in melanoma [103]. Myoferlin expression was first correlated with vasculogenic mimicry (VM) in patients, then its in vitro depletion in A375 cell line impaired VM, migration, and invasion by decreasing MMP-2 production.

Several evidences, obtained from normal endothelial cells, indicate that myoferlin is involved in RTKs recycling (see above). Our group showed that MDA-MB-231 and -468 cells depleted for myoferlin were unable to migrate and to undergo EMT upon EGF stimulation. The authors discovered that myoferlin depletion altered the EGFR fate after ligand binding, most probably by inhibiting the non-clathrin mediated endocytosis [104]. Unexpectedly, myoferlin seemed to be physically associated with lysosomal fraction in MCF-7 cells [105], supporting its involvement in the membrane receptor recycling.

The co-localisation of myoferlin with caveolin-1 [104], the main component of caveolae considered as a metabolic hub [106] prompted our group to investigate the implication of myoferlin in energy metabolism.

In this context, the authors showed in triple-negative breast cancer cells that myoferlin-silencing produces an accumulation of monounsaturated fatty acids (C16:1). Its depletion further decreased oxygen consumption switching the cell metabolism toward glycolysis [107]. This was the first report of the role of myoferlin in mitochondrial function and cell metabolism. A recent report describing the link between dysferlin mutations and mitochondrial respiratory complexes in muscular dysferlinopathy emerged (see above) [44]. It is also intriguing that dysferlin_v1 alternate transcript discovered in skeletal muscle [45] harbours a mitochondrial importation signal [39].

Several breast cancer cell lines and tissues showed a calpain-independent myoferlin cleavage, regardless of cell injuries and subsequent Ca^{2+} influx [108]. The resulting cleaved myoferlin increases ERK phosphorylation in an overexpressing HEK293 system. It would be of interest to further study the link between mini-myoferlin and KRAS mutated cancers as ERK is a mid-pathway signalling protein in this context.

6.2. Pancreas and Colon Cancers

In pancreas adenocarcinoma (PAAD), myoferlin is overexpressed in high grade PAAD in comparison to low grade [73]. The patients with high myoferlin PAAD had a significantly worse prognosis than those with low myoferlin PAAD, with myoferlin appearing as an independent prognosis factor. The experiments undertaken with pancreatic cell lines and siRNA-mediated silencing demonstrated that myoferlin requested to maintain a high proliferation rate. The authors reported that myoferlin is a key element in VEGF exocytosis by PAAD cell lines, correlating with microvessel density in PAAD tissue [109]. Recently, it was demonstrated that myoferlin is critical to maintain mitochondrial structure and oxidative phosphorylation [110]. This discovery was extended to colon cancer where myoferlin seemed also to protect cells from p53-driven apoptosis [111]. The concept claiming that metastatic dissemination relies on oxidative phosphorylation is broadly accepted [112,113]. Based on these reports, the authors discovered that myoferlin was overexpressed in PAAD cells with a high metastatic potential, where it controls mitochondrial respiration [114].

Recently, FER1L4 methylated DNA marker in pancreatic juice has been strongly associated with pancreatic ductal adenocarcinoma suggesting its use as a biomarker for early detection [115].

6.3. Lung Cancer

In mice bearing solid LLC lung tumours, the intratumoral injection of myoferlin siRNA mixed with a lipidic vector reduced the tumour volume by 73%. The observed reduction was neither the consequence of a difference in blood vessel density nor of VEGF secretion. However, a significant reduction of the proportion of the Ki67-positive cells indicated a decrease in cell proliferation [75]. Myoferlin was reported as expressed in human non-small cell lung cancer tissues where it was correlated with VEGFR2, thyroid transcription factor (TTF)-1 and transformation-related protein (p63), especially in the low stage tumours [116].

Recently, it was suggested that long non-coding RNA Fer1L4 negatively controlled proliferation and migration of lung cancer cells, probably through the PI3K/AKT pathway [117]. The same observation was made in osteosarcoma cells [118], esophageal squamous cell carcinoma [119], and hepatocellular carcinoma [120].

6.4. Liver Cancer

In the hepatocellular carcinoma (HCC) cell line, the silencing of the transcriptional coactivator of the serum response factor (SRF), Megakaryoblastic Leukemia 1/2 (MKL1/2), induced a reduction of myoferlin gene expression. It was shown by chromatin immunoprecipitation that MKL1/2 binds effectively to the myoferlin promoter [76]. As in other cancer types, HCC required myoferlin to proliferate and perform invasion or anchorage-independent cell growth. Its depletion enhanced EGFR phosphorylation, in agreement with the concept of myoferlin being a regulator of RTK recycling.

6.5. Head and Neck Cancer

A myoferlin expression pattern was investigated in oropharyngeal squamous carcinoma (OPSCC). It was reported that myoferlin was overexpressed in 50% of the cases and significantly associated with worse survival. Moreover, HPV-negative patients had significantly higher expressions of myoferlin. A subgroup survival analysis indicates the interaction between these two parameters as HPV-negative has the worst prognosis when myoferlin is highly expressed. Nuclear myoferlin expression appeared to be highly predictive of the clinical outcome and associated with IL-6 and nanog overexpression [77]. Upon HNSCC cell line stimulation with IL-6, myoferlin dissociates from EHD2 and binds activated STAT3 to drive it in the nucleus. The observation was extended to breast cancer cell lines [69].

6.6. Gastric Cancer

Recently, a profiling study reported that FER1L4 was a long non-coding RNA (lncRNA) strongly downregulated in gastric cancer tissue [96], in plasma from gastric cancer patients [121] and in human gastric cancer cell lines [122]. In gastric cancer tissues, FER1L4 lncRNA was associated with the tumour diameter, differentiation state, tumour classification, invasion, metastasis, TNM stage and serum CA72-4. Interestingly, the abundance of this lncRNA decreases in plasma shortly after surgery [121]. The same team reported that the FER1L4 lncRNA is a target of miR-106a-5p [122,123]. The cell depletion in FER1L4 lncRNA resulted in an increase in miR-106a-5p and in a decrease of its endogenous target PTEN, suggesting a competing endogenous RNA (ceRNA) [124] role for FER1L4 lncRNA [122]. The control of miR-106a-5p by FER1L4 lncRNA was extended to colon cancer [125] and HCC [126], while it was described over miR-18a-5p in osteosarcoma [127].

6.7. Gynecological Cancers

Lnc Fer1L4 was briefly investigated in ovarian cancer where it was described as downregulated in cancer cells in comparison to normal ovarian epithelial cells [128]. Interestingly, the Fer1L4 expression correlates negatively with the paclitaxel resistance and its re-expression restore the paclitaxel sensitivity through the inhibition of a MAPK signalling pathway.

7. Conclusions

This review clearly shows that all ferlin proteins are membrane-based molecular actors sharing structural similarities. Far beyond their well-described involvement in physiological membrane fusion, several correlations apparently link ferlins, and most particularly myoferlin, to cancer prognosis. However, further investigations are still needed to discover the direct link between myoferlin and cancer biology. Encouragingly, there are many indications that myoferlin depletion interferes with growth factor exocytosis, surface receptor fate determination, exosome composition, and metabolism, indicating the future research axes.

Self-sufficiency in growth factor signalling is a hallmark of cancer cells. Cancer cells overproduce the growth factor to stimulate unregulated proliferation in an autocrine, juxtacrine or paracrine fashions. In this context, myoferlin could be considered as a cancer growth promoter as it helps the exocytosis of the growth factors, at least VEGF. In normal cells, myoferlin was described as involved in receptor tyrosine kinase (EGFR and VEGFR) recycling or expression, allowing as such, the cell response to the growth factors. Knowing that some cancer cells exhibit mutations in tyrosine kinase receptors, which lead to a constitutive receptor activation triggering the downstream pathways, it can be speculated that myoferlin depletion could impede cell proliferation in these cases. This role was indeed described in breast cancer cells [104].

Exosomes are small extracellular vesicles released on exocytosis of multivesicular bodies filled with intraluminal vesicles. They represent an important role in intercellular communication, serving as carrier for the transfer of miRNA and proteins between cells. The exosomes are increasingly described as cancer biomarkers [129] and involved in the preparation of the tumour microenvironment [130].

Interestingly, myoferlin was demonstrated to be present in exosomes isolated from several cancer cell types. However, the biological significance of this localization has still to be investigated.

Metabolism recently integrated the hallmarks of cancer [131], and mitochondria were recognised as key players in cancer metabolism [132]. The indications that myoferlin is necessary for optimal mitochondrial function is a promising avenue in the search for an innovative therapy.

Myoferlin, being overexpressed in several cancer types, offers very promising advantages for cancer diagnosis and targeting. Targeting myoferlin at the expression or functional levels remains, however, the next challenge. Interestingly, recent studies identified new small compounds interacting with the myoferlin C2D domain and demonstrating promising anti-tumoral/metastasis properties in breast and pancreas cancer [133,134].

Gene transfer strategies have undergone profound development in recent years and this is particularly applicable for recessive disorders. The adeno-associated virus (AAV) is a non-pathogenic vector used in a treatment strategy aiming at delivering full-length dysferlin or shorter variants to skeletal muscle in dysferlin-null mice. Several well documented reports demonstrate an improvement in the outcome measures after dysferlin gene therapy [135–138]. Similar AAV vectors were used as a gene delivery system in cancer [139,140], allowing the dream of myoferlin negative-dominant delivery to cancer cells. Moreover, the sleeping beauty transposon system [141] may overcome some of the limitations associated with viral gene transfer vectors and transient non-viral gene delivery approaches that are being used in the majority of ongoing clinical trials.

8. Statistical Methods

The multivariate Cox regressions (Table 3) were performed with the coxph function from the R survival library. For each cancer and data type, OncoLnc attempted to construct a model with gene expression, sex, age, and grade or histology as multivariates [90]. The clinical information was obtained from TCGA and only patients who contained all the necessary clinical information were included in the analysis. The patients were split into low and high expressing according to the median gene expression.

Funding: This research was funded by "Fonds Léon Fredericq" and by the "Patrimoine de l'Université de Liège".

Acknowledgments: The results published here are in whole or part based upon data generated by the TCGA Research Network: http://cancergenome.nih.gov/. AB is a Research Director at the National Fund for Scientific Research (FNRS), Belgium. SA is supported by a FNRS FRIA grant. AT acknowledges LabEx MAbImprove for financial support.

Conflicts of Interest: The authors declare no conflicts of interest. The funders had no role in the design of the study; in the collection, analyses, or interpretation of data; in the writing of the manuscript, or in the decision to publish the results.

References

1. Bernardes, N.; Fialho, A.M. Perturbing the Dynamics and Organization of Cell Membrane Components: A New Paradigm for Cancer-Targeted Therapies. *Int. J. Mol. Sci.* **2018**, *19*, 3871. [CrossRef] [PubMed]
2. Achanzar, W.E.; Ward, S. A nematode gene required for sperm vesicle fusion. *J. Cell Sci.* **1997**, *110*, 1073–1081. [PubMed]
3. Bashir, R.; Britton, S.; Strachan, T.; Keers, S.; Vafiadaki, E.; Lako, M.; Richard, I.; Marchand, S.; Bourg, N.; Argov, Z.; et al. A gene related to caenorhabditis elegans spermatogenesis factor fer-1 is mutated in limb-girdle muscular dystrophy type 2B. *Nat. Genet.* **1998**, *20*, 37–42. [CrossRef] [PubMed]
4. Yasunaga, S.; Grati, M.; Cohen-Salmon, M.; El-Amraoui, A.; Mustapha, M.; Salem, N.; El-Zir, E.; Loiselet, J.; Petit, C. A mutation in OTOF, encoding otoferlin, a FER-1-like protein, causes DFNB9, a nonsyndromic form of deafness. *Nat. Genet.* **1999**, *21*, 363–369. [CrossRef] [PubMed]
5. Davis, D.B.; Delmonte, A.J.; Ly, C.T.; McNally, E.M. Myoferlin, a candidate gene and potential modifier of muscular dystrophy. *Hum. Mol. Genet.* **2000**, *9*, 217–226. [CrossRef] [PubMed]
6. Britton, S.; Freeman, T.; Vafiadaki, E.; Keers, S.; Harrison, R.; Bushby, K.; Bashir, R. The third human FER-1-like protein is highly similar to dysferlin. *Genomics* **2000**, *68*, 313–321. [CrossRef]

7. Liu, J.; Aoki, M.; Illa, I.; Wu, C.; Fardeau, M.; Angelini, C.; Serrano, C.; Urtizberea, J.A.; Hentati, F.; Hamida, M.B.; et al. Dysferlin, a novel skeletal muscle gene, is mutated in Miyoshi myopathy and limb girdle muscular dystrophy. *Nat. Genet.* **1998**, *20*, 31–36. [CrossRef] [PubMed]
8. Choi, B.Y.; Ahmed, Z.M.; Riazuddin, S.; Bhinder, M.A.; Shahzad, M.; Husnain, T.; Griffith, A.J.; Friedman, T.B. Identities and frequencies of mutations of the otoferlin gene (OTOF) causing DFNB9 deafness in Pakistan. *Clin. Genet.* **2009**, *75*, 237–243. [CrossRef]
9. Tekin, M.; Akcayoz, D.; Incesulu, A. A novel missense mutation in a C2 domain of OTOF results in autosomal recessive auditory neuropathy. *Am. J. Med. Genet. A* **2005**, *138*, 6–10. [CrossRef]
10. Doherty, K.R.; Cave, A.; Davis, D.B.; Delmonte, A.J.; Posey, A.; Earley, J.U.; Hadhazy, M.; McNally, E.M. Normal myoblast fusion requires myoferlin. *Development* **2005**, *132*, 5565–5575. [CrossRef]
11. Kiselev, A.; Vaz, R.; Knyazeva, A.; Sergushichev, A.; Dmitrieva, R.; Khudiakov, A.; Jorholt, J.; Smolina, N.; Sukhareva, K.; Fomicheva, Y.; et al. Truncating variant in myof gene is associated with limb-girdle type muscular dystrophy and cardiomyopathy. *Front. Genet.* **2019**, *10*, 608. [CrossRef] [PubMed]
12. Aoki, M.; Liu, J.; Richard, I.; Bashir, R.; Britton, S.; Keers, S.M.; Oeltjen, J.; Brown, H.E.; Marchand, S.; Bourg, N.; et al. Genomic organization of the dysferlin gene and novel mutations in Miyoshi myopathy. *Neurology* **2001**, *57*, 271–278. [CrossRef] [PubMed]
13. Demonbreun, A.R.; Lapidos, K.A.; Heretis, K.; Levin, S.; Dale, R.; Pytel, P.; Svensson, E.C.; McNally, E.M. Myoferlin regulation by NFAT in muscle injury, regeneration and repair. *J. Cell Sci.* **2010**, *123*, 2413–2422. [CrossRef] [PubMed]
14. Finn, R.D.; Coggill, P.; Eberhardt, R.Y.; Eddy, S.R.; Mistry, J.; Mitchell, A.L.; Potter, S.C.; Punta, M.; Qureshi, M.; Sangrador-Vegas, A.; et al. The Pfam protein families database: Towards a more sustainable future. *Nucleic Acids Res.* **2016**, *44*, D279–D285. [CrossRef] [PubMed]
15. Corbalan-Garcia, S.; Gómez-Fernández, J.C. Signaling through C2 domains: More than one lipid target. *Biochim. Biophys. Acta* **2014**, *1838*, 1536–1547. [CrossRef] [PubMed]
16. Zhang, D.; Aravind, L. Identification of novel families and classification of the C2 domain superfamily elucidate the origin and evolution of membrane targeting activities in eukaryotes. *Gene* **2010**, *469*, 18–30. [CrossRef]
17. Nalefski, E.A.; Falke, J.J. The C2 domain calcium-binding motif: Structural and functional diversity. *Protein Sci.* **1996**, *5*, 2375–2390. [CrossRef]
18. Shin, O.-H.; Han, W.; Wang, Y.; Südhof, T.C. Evolutionarily conserved multiple C2 domain proteins with two transmembrane regions (MCTPs) and unusual Ca^{2+} binding properties. *J. Biol. Chem.* **2005**, *280*, 1641–1651. [CrossRef]
19. Min, S.-W.; Chang, W.-P.; Südhof, T.C. E-Syts, a family of membranous Ca^{2+}-sensor proteins with multiple C2 domains. *Proc. Natl. Acad. Sci. USA* **2007**, *104*, 3823–3828. [CrossRef]
20. Rizo, J.; Sudhof, T.C. C2-domains, structure and function of a universal Ca^{2+}-binding domain. *J. Biol. Chem.* **1998**, *273*, 15879–15882. [CrossRef]
21. Von Poser, C.; Ichtchenko, K.; Shao, X.; Rizo, J.; Sudhof, T.C. The evolutionary pressure to inactivate. A subclass of synaptotagmins with an amino acid substitution that abolishes Ca^{2+} binding. *J. Biol. Chem.* **1997**, *272*, 14314–14319. [CrossRef] [PubMed]
22. Lek, A.; Lek, M.; North, K.N.; Cooper, S.T. Phylogenetic analysis of ferlin genes reveals ancient eukaryotic origins. *BMC Evol. Biol.* **2010**, *10*, 231. [CrossRef] [PubMed]
23. Washington, N.L.; Ward, S. FER-1 regulates Ca^{2+}-mediated membrane fusion during C. elegans spermatogenesis. *J. Cell Sci.* **2006**, *119*, 2552–2562. [CrossRef] [PubMed]
24. Yan, M.; Rachubinski, D.A.; Joshi, S.; Rachubinski, R.A.; Subramani, S. Dysferlin domain-containing proteins, Pex30p and Pex31p, localized to two compartments, control the number and size of oleate-induced peroxisomes in Pichia pastoris. *Mol. Biol. Cell.* **2008**, *19*, 885–898. [CrossRef] [PubMed]
25. Patel, P.; Harris, R.; Geddes, S.M.; Strehle, E.-M.; Watson, J.D.; Bashir, R.; Bushby, K.; Driscoll, P.C.; Keep, N.H. Solution Structure of the Inner DysF Domain of Myoferlin and Implications for Limb Girdle Muscular Dystrophy Type 2B. *J. Mol. Biol.* **2008**, *379*, 981–990. [CrossRef] [PubMed]
26. Fuson, K.; Rice, A.; Mahling, R.; Snow, A.; Nayak, K.; Shanbhogue, P.; Meyer, A.G.; Redpath, G.M.I.; Hinderliter, A.; Cooper, S.T.; et al. Alternate splicing of dysferlin C2A confers Ca^{2+}-dependent and Ca^{2+}-independent binding for membrane repair. *Structure* **2014**, *22*, 104–115. [CrossRef] [PubMed]

27. Aartsma-Rus, A.; Van Deutekom, J.C.T.; Fokkema, I.F.; Van Ommen, G.-J.B.; Den Dunnen, J.T. Entries in the Leiden Duchenne muscular dystrophy mutation database: An overview of mutation types and paradoxical cases that confirm the reading-frame rule. *Muscle Nerve* **2006**, *34*, 135–144. [CrossRef] [PubMed]
28. Bernatchez, P.N.; Acevedo, L.; Fernandez-Hernando, C.; Murata, T.; Chalouni, C.; Kim, J.; Erdjument-Bromage, H.; Shah, V.; Gratton, J.-P.; McNally, E.M.; et al. Myoferlin regulates vascular endothelial growth factor receptor-2 stability and function. *J. Biol. Chem.* **2007**, *282*, 30745–30753. [CrossRef]
29. Miyatake, Y.; Yamano, T.; Hanayama, R. Myoferlin-Mediated Lysosomal Exocytosis Regulates Cytotoxicity by Phagocytes. *J. Immunol.* **2018**, *201*, 3051–3057. [CrossRef]
30. Redpath, G.M.I.; Sophocleous, R.A.; Turnbull, L.; Whitchurch, C.B.; Cooper, S.T. Ferlins Show Tissue-Specific Expression and Segregate as Plasma Membrane/Late Endosomal or Trans-Golgi/Recycling Ferlins. *Traffic* **2016**, *17*, 245–266. [CrossRef]
31. Davis, D.B.; Doherty, K.R.; Delmonte, A.J.; McNally, E.M. Calcium-sensitive phospholipid binding properties of normal and mutant ferlin C2 domains. *J. Biol. Chem.* **2002**, *277*, 22883–22888. [CrossRef] [PubMed]
32. Bootman, M.D.; Rietdorf, K.; Hardy, H.; Dautova, Y.; Corps, E.; Pierro, C.; Stapleton, E.; Kang, E.; Proudfoot, D. Calcium Signalling and Regulation of Cell Function. In *eLS*; John Wiley & Sons, Ltd.: Chichester, UK, 2012; pp. 1–14.
33. Harsini, F.M.; Bui, A.A.; Rice, A.M.; Chebrolu, S.; Fuson, K.L.; Turtoi, A.; Bradberry, M.; Chapman, E.R.; Sutton, R.B. Structural Basis for the Distinct Membrane Binding Activity of the Homologous C2A Domains of Myoferlin and Dysferlin. *J. Mol. Biol.* **2019**, *431*, 2112–2126. [CrossRef] [PubMed]
34. Therrien, C.; Fulvio, S.D.; Pickles, S.; Sinnreich, M. Characterization of lipid binding specificities of dysferlin C2 domains reveals novel interactions with phosphoinositides. *Biochemistry* **2009**, *48*, 2377–2384. [CrossRef] [PubMed]
35. Marty, N.J.; Holman, C.L.; Abdullah, N.; Johnson, C.P. The C2 domains of otoferlin, dysferlin, and myoferlin alter the packing of lipid bilayers. *Biochemistry* **2013**, *52*, 5585–5592. [CrossRef] [PubMed]
36. Johnson, C.P.; Chapman, E.R. Otoferlin is a calcium sensor that directly regulates SNARE-mediated membrane fusion. *J. Cell Biol.* **2010**, *191*, 187–197. [CrossRef] [PubMed]
37. Helfmann, S.; Neumann, P.; Tittmann, K.; Moser, T.; Ficner, R.; Reisinger, E. The Crystal Structure of the C2A Domain of Otoferlin Reveals an Unconventional Top Loop Region. *J. Mol. Biol.* **2011**, *406*, 479–490. [CrossRef]
38. Harsini, F.M.; Chebrolu, S.; Fuson, K.L.; White, M.A.; Rice, A.M.; Sutton, R.B. FerA is a Membrane-Associating Four-Helix Bundle Domain in the Ferlin Family of Membrane-Fusion Proteins. *Sci. Rep.* **2018**, *8*, 10949. [CrossRef]
39. De Morrée, A.; Hensbergen, P.J.; van Haagen, H.H.; Dragan, I.; Deelder, A.M.; AC't Hoen, P.; Frants, R.R.; van der Maarel, S.M. Proteomic analysis of the dysferlin protein complex unveils its importance for sarcolemmal maintenance and integrity. *PLoS ONE* **2010**, *5*, e13854. [CrossRef]
40. Doherty, K.R.; Demonbreun, A.R.; Wallace, G.Q.; Cave, A.; Posey, A.D.; Heretis, K.; Pytel, P.; McNally, E.M. The endocytic recycling protein EHD2 interacts with myoferlin to regulate myoblast fusion. *J. Biol. Chem.* **2008**, *283*, 20252–20260. [CrossRef]
41. Bansal, D.; Miyake, K.; Vogel, S.S.; Groh, S.; Chen, C.-C.; Williamson, R.; McNeil, P.L.; Campbell, K.P. Defective membrane repair in dysferlin-deficient muscular dystrophy. *Nature* **2003**, *423*, 168–172. [CrossRef]
42. Lukyanenko, V.; Muriel, J.M.; Bloch, R.J. Coupling of excitation to Ca^{2+} release is modulated by dysferlin. *J. Physiol.* **2017**, *595*, 5191–5207. [CrossRef] [PubMed]
43. Lennon, N.J.; Kho, A.; Bacskai, B.J.; Perlmutter, S.L.; Hyman, B.T.; Brown, R.H. Dysferlin Interacts with Annexins A1 and A2 and Mediates Sarcolemmal Wound-healing. *J. Biol. Chem.* **2003**, *278*, 50466–50473. [CrossRef] [PubMed]
44. Vincent, A.E.; Rosa, H.S.; Alston, C.L.; Grady, J.P.; Rygiel, K.A.; Rocha, M.C.; Barresi, R.; Taylor, R.W.; Turnbull, D.M. Dysferlin mutations and mitochondrial dysfunction. *Neuromuscul. Disord.* **2016**, *26*, 782–788. [CrossRef]
45. Pramono, Z.A.D.; Lai, P.S.; Tan, C.L.; Takeda, S.; Yee, W.C. Identification and characterization of a novel human dysferlin transcript: Dysferlin_v1. *Hum. Genet.* **2006**, *120*, 410–419. [CrossRef] [PubMed]
46. Lek, A.; Evesson, F.J.; Lemckert, F.A.; Redpath, G.M.I.; Lueders, A.-K.; Turnbull, L.; Whitchurch, C.B.; North, K.N.; Cooper, S.T. Calpains, cleaved mini-dysferlinC72, and L-type channels underpin calcium-dependent muscle membrane repair. *J. Neurosci.* **2013**, *33*, 5085–5094. [CrossRef]

47. Redpath, G.M.I.; Woolger, N.; Piper, A.K.; Lemckert, F.A.; Lek, A.; Greer, P.A.; North, K.N.; Cooper, S.T. Calpain cleavage within dysferlin exon 40a releases a synaptotagmin-like module for membrane repair. *Mol. Biol. Cell.* **2014**, *25*, 3037–3048. [CrossRef] [PubMed]
48. O'Connor, V.; Lee, A.G. Synaptic vesicle fusion and synaptotagmin: 2B or not 2B? *Nat. Neurosci.* **2002**, *5*, 823–824. [CrossRef]
49. Przybylski, R.J.; Szigeti, V.; Davidheiser, S.; Kirby, A.C. Calcium regulation of skeletal myogenesis. II. Extracellular and cell surface effects. *Cell Calcium* **1994**, *15*, 132–142. [CrossRef]
50. Demonbreun, A.R.; Posey, A.D.; Heretis, K.; Swaggart, K.A.; Earley, J.U.; Pytel, P.; McNally, E.M. Myoferlin is required for insulin-like growth factor response and muscle growth. *FASEB J.* **2010**, *24*, 1284–1295. [CrossRef]
51. Zhou, Y.; Xiong, L.; Zhang, Y.; Yu, R.; Jiang, X.; Xu, G. Quantitative proteomics identifies myoferlin as a novel regulator of A Disintegrin and Metalloproteinase 12 in HeLa cells. *J. Proteom.* **2016**, *148*, 94–104. [CrossRef]
52. Galliano, M.F.; Huet, C.; Frygelius, J.; Polgren, A.; Wewer, U.M.; Engvall, E. Binding of ADAM12, a marker of skeletal muscle regeneration, to the muscle-specific actin-binding protein, α-actinin-2, is required for myoblast fusion. *J. Biol. Chem.* **2000**, *275*, 13933–13939. [CrossRef] [PubMed]
53. Posey, A.D.; Pytel, P.; Gardikiotes, K.; Demonbreun, A.R.; Rainey, M.; George, M.; Band, H.; McNally, E.M. Endocytic recycling proteins EHD1 and EHD2 interact with fer-1-like-5 (Fer1L5) and mediate myoblast fusion. *J. Biol. Chem.* **2011**, *286*, 7379–7388. [CrossRef] [PubMed]
54. Roux, I.; Safieddine, S.; Nouvian, R.; Grati, M.; Simmler, M.-C.; Bahloul, A.; Perfettini, I.; Le Gall, M.; Rostaing, P.; Hamard, G.; et al. Otoferlin, defective in a human deafness form, is essential for exocytosis at the auditory ribbon synapse. *Cell* **2006**, *127*, 277–289. [CrossRef] [PubMed]
55. Chapman, E.R.; Hanson, P.I.; An, S.; Jahn, R. Ca^{2+} regulates the interaction between synaptotagmin and syntaxin 1. *J. Biol. Chem.* **1995**, *270*, 23667–23671. [CrossRef] [PubMed]
56. Mohrmann, R.; de Wit, H.; Connell, E.; Pinheiro, P.S.; Leese, C.; Bruns, D.; Davletov, B.; Verhage, M.; Sørensen, J.B. Synaptotagmin interaction with SNAP-25 governs vesicle docking, priming, and fusion triggering. *J. Neurosci.* **2013**, *33*, 14417–14430. [CrossRef] [PubMed]
57. Ramakrishnan, N.A.; Drescher, M.J.; Drescher, D.G. Direct interaction of otoferlin with syntaxin 1A, SNAP-25, and the L-type voltage-gated calcium channel Cav1.3. *J. Biol. Chem.* **2009**, *284*, 1364–1372. [CrossRef] [PubMed]
58. Ramakrishnan, N.A.; Drescher, M.J.; Morley, B.J.; Kelley, P.M.; Drescher, D.G. Calcium regulates molecular interactions of otoferlin with soluble NSF attachment protein receptor (SNARE) proteins required for hair cell exocytosis. *J. Biol. Chem.* **2014**, *289*, 8750–8766. [CrossRef]
59. Hams, N.; Padmanarayana, M.; Qiu, W.; Johnson, C.P. Otoferlin is a multivalent calcium-sensitive scaffold linking SNAREs and calcium channels. *Proc. Natl. Acad. Sci. USA* **2017**, *114*, 8023–8028. [CrossRef] [PubMed]
60. Sharma, A.; Yu, C.; Leung, C.; Trane, A.; Lau, M.; Utokaparch, S.; Shaheen, F.; Sheibani, N.; Bernatchez, P. A new role for the muscle repair protein dysferlin in endothelial cell adhesion and angiogenesis. *Arterioscler. Thromb. Vasc. Biol.* **2010**, *30*, 2196–2204. [CrossRef]
61. Yu, C.; Sharma, A.; Trane, A.; Utokaparch, S.; Leung, C.; Bernatchez, P. Myoferlin gene silencing decreases Tie-2 expression in vitro and angiogenesis in vivo. *Vascul. Pharmacol.* **2011**, *55*, 26–33. [CrossRef]
62. Bernatchez, P.N.; Sharma, A.; Kodaman, P.; Sessa, W.C. Myoferlin is critical for endocytosis in endothelial cells. *Am. J. Physiol. Cell. Physiol.* **2009**, *297*, C484–C492. [CrossRef] [PubMed]
63. Han, W.Q.; Xia, M.; Xu, M.; Boini, K.M.; Ritter, J.K.; Li, N.J.; Li, P.L. Lysosome fusion to the cell membrane is mediated by the dysferlin C2A domain in coronary arterial endothelial cells. *J. Cell Sci.* **2012**, *125*, 1225–1234. [CrossRef] [PubMed]
64. Leung, C.; Shaheen, F.; Bernatchez, P.; Hackett, T.-L. Expression of myoferlin in human airway epithelium and its role in cell adhesion and zonula occludens-1 expression. *PLoS ONE* **2012**, *7*, e40478. [CrossRef] [PubMed]
65. Stamer, W.D.; Hoffman, E.A.; Luther, J.M.; Hachey, D.L.; Schey, K.L. Protein profile of exosomes from trabecular meshwork cells. *J. Proteom.* **2011**, *74*, 796–804. [CrossRef] [PubMed]
66. Iacobuzio-Donahue, C.A.; Maitra, A.; Shen-Ong, G.L.; van Heek, T.; Ashfaq, R.; Meyer, R.; Walter, K.; Berg, K.; Hollingsworth, M.A.; Cameron, J.L.; et al. Discovery of Novel Tumor Markers of Pancreatic Cancer using Global Gene Expression Technology. *Am. J. Pathol.* **2002**, *160*, 1239–1249. [CrossRef]
67. Han, H.; Bearss, D.J.; Browne, L.W.; Calaluce, R.; Nagle, R.B.; Von Hoff, D.D. Identification of differentially expressed genes in pancreatic cancer cells using cDNA microarray. *Cancer Res.* **2002**, *62*, 2890–2896. [PubMed]

68. Amatschek, S.; Koenig, U.; Auer, H.; Steinlein, P.; Pacher, M.; Gruenfelder, A.; Dekan, G.; Vogl, S.; Kubista, E.; Heider, K.-H.; et al. Tissue-wide expression profiling using cDNA subtraction and microarrays to identify tumor-specific genes. *Cancer Res.* **2004**, *64*, 844–856. [CrossRef]
69. Yadav, A.; Kumar, B.; Lang, J.C.; Teknos, T.N.; Kumar, P. A muscle-specific protein "myoferlin" modulates IL-6/STAT3 signaling by chaperoning activated STAT3 to nucleus. *Oncogene* **2017**, *36*, 6374–6382. [CrossRef]
70. McKinney, K.Q.; Lee, Y.Y.; Choi, H.S.; Groseclose, G.; Iannitti, D.A.; Martinie, J.B.; Russo, M.W.; Lundgren, D.H.; Han, D.K.; Bonkovsky, H.L.; et al. Discovery of putative pancreatic cancer biomarkers using subcellular proteomics. *J. Proteom.* **2011**, *74*, 79–88. [CrossRef]
71. Turtoi, A.; Musmeci, D.; Wang, Y.; Dumont, B.; Somja, J.; Bevilacqua, G.; De Pauw, E.; Delvenne, P.; Castronovo, V. Identification of novel accessible proteins bearing diagnostic and therapeutic potential in human pancreatic ductal adenocarcinoma. *J. Proteome Res.* **2011**, *10*, 4302–4313. [CrossRef]
72. McKinney, K.Q.; Lee, J.-G.; Sindram, D.; Russo, M.W.; Han, D.K.; Bonkovsky, H.L.; Hwang, S.-I. Identification of differentially expressed proteins from primary versus metastatic pancreatic cancer cells using subcellular proteomics. *Cancer Genom. Proteom.* **2012**, *9*, 257–263.
73. Wang, W.S.; Liu, X.H.; Liu, L.X.; Lou, W.H.; Jin, D.Y.; Yang, P.Y.; Wang, X.L. ITRAQ-based quantitative proteomics reveals myoferlin as a novel prognostic predictor in pancreatic adenocarcinoma. *J. Proteom.* **2013**, *91*, 453–465. [CrossRef] [PubMed]
74. Adam, P.J.; Boyd, R.; Tyson, K.L.; Fletcher, G.C.; Stamps, A.; Hudson, L.; Poyser, H.R.; Redpath, N.; Griffiths, M.; Steers, G.; et al. Comprehensive proteomic analysis of breast cancer cell membranes reveals unique proteins with potential roles in clinical cancer. *J. Biol. Chem.* **2003**, *278*, 6482–6489. [CrossRef] [PubMed]
75. Leung, C.; Yu, C.; Lin, M.I.; Tognon, C.; Bernatchez, P. Expression of myoferlin in human and murine carcinoma tumors: Role in membrane repair, cell proliferation, and tumorigenesis. *Am. J. Pathol.* **2013**, *182*, 1900–1909. [CrossRef] [PubMed]
76. Hermanns, C.; Hampl, V.; Holzer, K.; Aigner, A.; Penkava, J.; Frank, N.; Martin, D.E.; Maier, K.C.; Waldburger, N.; Roessler, S.; et al. The novel MKL target gene myoferlin modulates expansion and senescence of hepatocellular carcinoma. *Oncogene* **2017**, *36*, 3464–3476. [CrossRef] [PubMed]
77. Kumar, B.; Brown, N.V.; Swanson, B.J.; Schmitt, A.C.; Old, M.; Ozer, E.; Agrawal, A.; Schuller, D.E.; Teknos, T.N.; Kumar, P. High expression of myoferlin is associated with poor outcome in oropharyngeal squamous cell carcinoma patients and is inversely associated with HPV-status. *Oncotarget* **2016**, *7*, 18665–18677. [CrossRef] [PubMed]
78. Song, D.H.; Ko, G.H.; Lee, J.H.; Lee, J.S.; Yang, J.W.; Kim, M.H.; An, H.J.; Kang, M.H.; Jeon, K.N.; Kim, D.C. Prognostic role of myoferlin expression in patients with clear cell renal cell carcinoma. *Oncotarget* **2017**, *8*, 89033–89039. [CrossRef]
79. Koh, H.M.; An, H.J.; Ko, G.H.; Lee, J.H.; Lee, J.S.; Kim, D.C.; Seo, D.H.; Song, D.H. Identification of Myoferlin Expression for Prediction of Subsequent Primary Malignancy in Patients With Clear Cell Renal Cell Carcinoma. *In Vivo* **2019**, *33*, 1103–1108. [CrossRef]
80. Kim, M.H.; Song, D.H.; Ko, G.H.; Lee, J.H.; Kim, D.C.; Yang, J.W.; Lee, H.I.; An, H.J.; Lee, J.S. Myoferlin expression and its correlation with FIGO histologic grading in early-stage endometrioid carcinoma. *J. Pathol. Transl. Med.* **2018**, *52*, 93–97. [CrossRef]
81. Welton, J.L.; Khanna, S.; Giles, P.J.; Brennan, P.; Brewis, I.A.; Staffurth, J.; Mason, M.D.; Clayton, A. Proteomics analysis of bladder cancer exosomes. *Mol. Cell. Proteom.* **2010**, *9*, 1324–1338. [CrossRef]
82. Mathivanan, S.; Lim, J.W.E.; Tauro, B.J.; Ji, H.; Moritz, R.L.; Simpson, R.J. Proteomics analysis of A33 immunoaffinity-purified exosomes released from the human colon tumor cell line LIM1215 reveals a tissue-specific protein signature. *Mol. Cell. Proteom.* **2010**, *9*, 197–208. [CrossRef] [PubMed]
83. Beckler, M.D.; Higginbotham, J.N.; Franklin, J.L.; Ham, A.-J.; Halvey, P.J.; Imasuen, I.E.; Whitwell, C.; Li, M.; Liebler, D.C.; Coffey, R.J. Proteomic analysis of exosomes from mutant KRAS colon cancer cells identifies intercellular transfer of mutant KRAS. *Mol. Cell. Proteom.* **2013**, *12*, 343–355. [CrossRef] [PubMed]
84. Ji, H.; Greening, D.W.; Barnes, T.W.; Lim, J.W.; Tauro, B.J.; Rai, A.; Xu, R.; Adda, C.; Mathivanan, S.; Zhao, W.; et al. Proteome profiling of exosomes derived from human primary and metastatic colorectal cancer cells reveal differential expression of key metastatic factors and signal transduction components. *Proteomics* **2013**, *13*, 1672–1686. [CrossRef] [PubMed]

85. Choi, D.-S.; Choi, D.-Y.; Hong, B.S.; Jang, S.C.; Kim, D.-K.; Lee, J.; Kim, Y.-K.; Kim, K.P.; Gho, Y.S. Quantitative proteomics of extracellular vesicles derived from human primary and metastatic colorectal cancer cells. *J. Extracell. Vesicles* **2012**, *1*, 18704. [CrossRef] [PubMed]
86. Liang, B.; Peng, P.; Chen, S.; Li, L.; Zhang, M.; Cao, D.; Yang, J.; Li, H.; Gui, T.; Li, X.; et al. Characterization and proteomic analysis of ovarian cancer-derived exosomes. *J. Proteom.* **2013**, *80*, 171–182. [CrossRef] [PubMed]
87. Sandvig, K.; Llorente, A. Proteomic analysis of microvesicles released by the human prostate cancer cell line PC-3. *Mol. Cell. Proteom.* **2012**, *11*, M111-012914. [CrossRef]
88. Blomme, A.; Fahmy, K.; Peulen, O.J.; Costanza, B.; Fontaine, M.; Struman, I.; Baiwir, D.; De Pauw, E.; Thiry, M.; Bellahcène, A.; et al. Myoferlin is a novel exosomal protein and functional regulator of cancer-derived exosomes. *Oncotarget* **2016**, *7*, 83669–83683. [CrossRef]
89. Lawrence, M.S.; Stojanov, P.; Mermel, C.H.; Robinson, J.T.; Garraway, L.A.; Golub, T.R.; Meyerson, M.; Gabriel, S.B.; Lander, E.S.; Getz, G. Discovery and saturation analysis of cancer genes across 21 tumour types. *Nature* **2014**, *505*, 495–501. [CrossRef]
90. Anaya, J. OncoLnc: Linking TCGA survival data to mRNAs, miRNAs, and lncRNAs. *PeerJ Comp. Sci.* **2016**, *2*, e67. [CrossRef]
91. Tang, H.; Wei, P.; Chang, P.; Li, Y.; Yan, D.; Liu, C.; Hassan, M.; Li, D. Genetic polymorphisms associated with pancreatic cancer survival: A genome-wide association study. *Int. J. Cancer* **2017**, *141*, 678–686. [CrossRef]
92. Ding, F.; Tang, H.; Nie, D.; Xia, L. Long non-coding RNA Fer-1-like family member 4 is overexpressed in human glioblastoma and regulates the tumorigenicity of glioma cells. *Oncol. Lett.* **2017**, *14*, 2379–2384. [CrossRef] [PubMed]
93. Xia, L.; Nie, D.; Wang, G.; Sun, C.; Chen, G. FER1L4/miR-372/E2F1 works as a ceRNA system to regulate the proliferation and cell cycle of glioma cells. *J. Cell. Mol. Med.* **2019**, *23*, 3224–3233. [CrossRef] [PubMed]
94. You, Z.; Ge, A.; Pang, D.; Zhao, Y.; Xu, S. Long noncoding RNA FER1L4 acts as an oncogenic driver in human pan-cancer. *J. Cell. Physiol.* **2019**, *1859*, 46. [CrossRef] [PubMed]
95. Chen, Z.-X.; Chen, C.-P.; Zhang, N.; Wang, T.-X. Low-expression of lncRNA FER1L4 might be a prognostic marker in osteosarcoma. *Eur. Rev. Med. Pharmacol. Sci.* **2018**, *22*, 2310–2314.
96. Song, H.; Sun, W.; Ye, G.; Ding, X.; Liu, Z.; Zhang, S.; Xia, T.; Xiao, B.; Xi, Y.; Guo, J. Long non-coding RNA expression profile in human gastric cancer and its clinical significances. *J. Transl. Med.* **2013**, *11*, 225. [CrossRef] [PubMed]
97. Kong, Y.; Ren, Z. Overexpression of LncRNA FER1L4 in endometrial carcinoma is associated with favorable survival outcome. *Eur. Rev. Med. Pharmacol. Sci.* **2018**, *22*, 8113–8118.
98. Eisenberg, M.C.; Kim, Y.; Li, R.; Ackerman, W.E.; Kniss, D.A.; Friedman, A. Mechanistic modeling of the effects of myoferlin on tumor cell invasion. *Proc. Natl. Acad. Sci. USA* **2011**, *108*, 20078–20083. [CrossRef]
99. Li, R.; Ackerman, W.E.; Mihai, C.; Volakis, L.I.; Ghadiali, S.; Kniss, D.A. Myoferlin depletion in breast cancer cells promotes mesenchymal to epithelial shape change and stalls invasion. *PLoS ONE* **2012**, *7*, e39766. [CrossRef]
100. Volakis, L.I.; Li, R.; Ackerman, W.E.; Mihai, C.; Bechel, M.; Summerfield, T.L.; Ahn, C.S.; Powell, H.M.; Zielinski, R.; Rosol, T.J.; et al. Loss of myoferlin redirects breast cancer cell motility towards collective migration. *PLoS ONE* **2014**, *9*, e86110. [CrossRef]
101. Blackstone, B.N.; Li, R.; Ackerman, W.E.; Ghadiali, S.N.; Powell, H.M.; Kniss, D.A. Myoferlin depletion elevates focal adhesion kinase and paxillin phosphorylation and enhances cell-matrix adhesion in breast cancer cells. *Am. J. Physiol. Cell. Physiol.* **2015**, *308*, C642–C649. [CrossRef]
102. Barnhouse, V.R.; Weist, J.L.; Shukla, V.C.; Ghadiali, S.N.; Kniss, D.A.; Leight, J.L. Myoferlin regulates epithelial cancer cell plasticity and migration through autocrine TGF-β1 signaling. *Oncotarget* **2018**, *9*, 19209–19222. [CrossRef] [PubMed]
103. Zhang, W.; Zhou, P.; Meng, A.; Zhang, R.; Zhou, Y. Down-regulating Myoferlin inhibits the vasculogenic mimicry of melanoma via decreasing MMP-2 and inducing mesenchymal-to-epithelial transition. *J. Cell. Mol. Med.* **2017**, *155*, 739. [CrossRef] [PubMed]
104. Turtoi, A.; Blomme, A.; Bellahcène, A.; Gilles, C.; Hennequière, V.; Peixoto, P.; Bianchi, E.; Noël, A.; De Pauw, E.; Lifrange, E.; et al. Myoferlin is a key regulator of EGFR activity in breast cancer. *Cancer Res.* **2013**, *73*, 5438–5448. [CrossRef] [PubMed]
105. Nylandsted, J.; Becker, A.C.; Bunkenborg, J.; Andersen, J.S.; Dengjel, J.; Jäättelä, M. ErbB2-associated changes in the lysosomal proteome. *Proteomics* **2011**, *11*, 2830–2838. [CrossRef] [PubMed]

106. Örtegren, U.; Aboulaich, N.; Öst, A.; Strålfors, P. A new role for caveolae as metabolic platforms. *Trends Endocrinol. Metab.* **2007**, *18*, 344–349. [CrossRef] [PubMed]
107. Blomme, A.; Costanza, B.; de Tullio, P.; Thiry, M.; Van Simaeys, G.; Boutry, S.; Doumont, G.; Di Valentin, E.; Hirano, T.; Yokobori, T.; et al. Myoferlin regulates cellular lipid metabolism and promotes metastases in triple-negative breast cancer. *Oncogene* **2017**, *36*, 2116–2130. [CrossRef] [PubMed]
108. Piper, A.-K.; Ross, S.E.; Redpath, G.M.; Lemckert, F.A.; Woolger, N.; Bournazos, A.; Greer, P.A.; Sutton, R.B.; Cooper, S.T. Enzymatic cleavage of myoferlin releases a dual C2-domain module linked to ERK signalling. *Cell. Signal.* **2017**, *33*, 30–40. [CrossRef]
109. Fahmy, K.; Gonzalez, A.; Arafa, M.; Peixoto, P.; Bellahcène, A.; Turtoi, A.; Delvenne, P.; Thiry, M.; Castronovo, V.; Peulen, O.J. Myoferlin plays a key role in VEGFA secretion and impacts tumor-associated angiogenesis in human pancreas cancer. *Int. J. Cancer* **2016**, *138*, 652–663. [CrossRef]
110. Rademaker, G.; Hennequière, V.; Brohée, L.; Nokin, M.-J.; Lovinfosse, P.; Durieux, F.; Gofflot, S.; Bellier, J.; Costanza, B.; Herfs, M.; et al. Myoferlin controls mitochondrial structure and activity in pancreatic ductal adenocarcinoma, and affects tumor aggressiveness. *Oncogene* **2018**, *66*, 1–15. [CrossRef]
111. Rademaker, G.; Costanza, B.; Bellier, J.; Herfs, M.; Peiffer, R.; Agirman, F.; Maloujahmoum, N.; Habraken, Y.; Delvenne, P.; Bellahcène, A.; et al. Human colon cancer cells highly express myoferlin to maintain a fit mitochondrial network and escape p53-driven apoptosis. *Oncogenesis* **2019**, *8*, 21. [CrossRef]
112. LeBleu, V.S.; O'Connell, J.T.; Gonzalez Herrera, K.N.; Wikman, H.; Pantel, K.; Haigis, M.C.; de Carvalho, F.M.; Damascena, A.; Domingos Chinen, L.T.; Rocha, R.M.; et al. PGC-1α mediates mitochondrial biogenesis and oxidative phosphorylation in cancer cells to promote metastasis. *Nat. Cell Biol.* **2014**, *16*, 992–1003. [CrossRef] [PubMed]
113. Porporato, P.E.; Payen, V.L.; Pérez-Escuredo, J.; De Saedeleer, C.J.; Danhier, P.; Copetti, T.; Dhup, S.; Tardy, M.; Vazeille, T.; Bouzin, C.; et al. A mitochondrial switch promotes tumor metastasis. *Cell Rep.* **2014**, *8*, 754–766. [CrossRef] [PubMed]
114. Rademaker, G.; Costanza, B.; Anania, S.; Agirman, F.; Maloujahmoum, N.; Di Valentin, E.; Goval, J.J.; Bellahcène, A.; Castronovo, V.; Peulen, O.J. Myoferlin Contributes to the Metastatic Phenotype of Pancreatic Cancer Cells by Enhancing Their Migratory Capacity through the Control of Oxidative Phosphorylation. *Cancers* **2019**, *11*, 853. [CrossRef] [PubMed]
115. Majumder, S.; Raimondo, M.; Taylor, W.R.; Yab, T.C.; Berger, C.K.; Dukek, B.A.; Cao, X.; Foote, P.H.; Wu, C.W.; Devens, M.E.; et al. Methylated DNA in Pancreatic Juice Distinguishes Patients with Pancreatic Cancer from Controls. *Clin. Gastroenterol. Hepatol.* **2019**. [CrossRef] [PubMed]
116. Song, D.H.; Ko, G.H.; Lee, J.H.; Lee, J.S.; Lee, G.-W.; Kim, H.C.; Yang, J.W.; Heo, R.W.; Roh, G.S.; Han, S.-Y.; et al. Myoferlin expression in non-small cell lung cancer: Prognostic role and correlation with VEGFR-2 expression. *Oncol. Lett.* **2016**, *11*, 998–1006. [CrossRef] [PubMed]
117. Gao, X.; Wang, N.; Wu, S.; Cui, H.; An, X.; Yang, Y. Long non-coding RNA FER1L4 inhibits cell proliferation and metastasis through regulation of the PI3K/AKT signaling pathway in lung cancer cells. *Mol. Med. Rep.* **2019**, *20*, 182–190. [CrossRef] [PubMed]
118. Ma, L.; Zhang, L.; Guo, A.; Liu, L.C.; Yu, F.; Diao, N.; Xu, C.; Wang, D. Overexpression of FER1L4 promotes the apoptosis and suppresses epithelial-mesenchymal transition and stemness markers via activating PI3K/AKT signaling pathway in osteosarcoma cells. *Pathol. Res. Pract.* **2019**, *215*, 152412. [CrossRef] [PubMed]
119. Ma, W.; Zhang, C.-Q.; Li, H.-L.; Gu, J.; Miao, G.-Y.; Cai, H.-Y.; Wang, J.-K.; Zhang, L.-J.; Song, Y.-M.; Tian, Y.-H.; et al. LncRNA FER1L4 suppressed cancer cell growth and invasion in esophageal squamous cell carcinoma. *Eur. Rev. Med. Pharmacol. Sci.* **2018**, *22*, 2638–2645. [PubMed]
120. Wang, X.; Dong, K.; Jin, Q.; Ma, Y.; Yin, S.; Wang, S. Upregulation of lncRNA FER1L4 suppresses the proliferation and migration of the hepatocellular carcinoma via regulating PI3K/AKT signal pathway. *J. Cell. Biochem.* **2019**, *120*, 6781–6788. [CrossRef]
121. Liu, Z.; Shao, Y.; Tan, L.; Shi, H.; Chen, S.; Guo, J. Clinical significance of the low expression of FER1L4 in gastric cancer patients. *Tumour Biol.* **2014**, *35*, 9613–9617. [CrossRef] [PubMed]
122. Xia, T.; Chen, S.; Jiang, Z.; Shao, Y.; Jiang, X.; Li, P.; Xiao, B.; Guo, J. Long noncoding RNA FER1L4 suppresses cancer cell growth by acting as a competing endogenous RNA and regulating PTEN expression. *Sci. Rep.* **2015**, *5*, 13445. [CrossRef] [PubMed]
123. Xia, T.; Liao, Q.; Jiang, X.; Shao, Y.; Xiao, B.; Xi, Y.; Guo, J. Long noncoding RNA associated-competing endogenous RNAs in gastric cancer. *Sci. Rep.* **2014**, *4*, 6088. [CrossRef] [PubMed]

124. Salmena, L.; Poliseno, L.; Tay, Y.; Kats, L.; Pandolfi, P.P. A ceRNA hypothesis: The rosetta stone of a hidden RNA language? *Cell* **2011**, *146*, 353–358. [CrossRef] [PubMed]
125. Yue, B.; Sun, B.; Liu, C.; Zhao, S.; Zhang, D.; Yu, F.; Yan, D. Long non-coding RNA Fer-1-like protein 4 suppresses oncogenesis and exhibits prognostic value by associating with miR-106a-5p in colon cancer. *Cancer Sci.* **2015**, *106*, 1323–1332. [CrossRef] [PubMed]
126. Wu, J.; Huang, J.; Wang, W.; Xu, J.; Yin, M.; Cheng, N.; Yin, J. Long non-coding RNA Fer-1-like protein 4 acts as a tumor suppressor via miR-106a-5p and predicts good prognosis in hepatocellular carcinoma. *Cancer Biomark.* **2017**, *20*, 55–65. [CrossRef]
127. Fei, D.; Zhang, X.; Liu, J.; Tan, L.; Xing, J.; Zhao, D.; Zhang, Y. Long Noncoding RNA FER1L4 Suppresses Tumorigenesis by Regulating the Expression of PTEN Targeting miR-18a-5p in Osteosarcoma. *Cell. Physiol. Biochem.* **2018**, *51*, 1364–1375. [CrossRef] [PubMed]
128. Liu, S.; Zou, B.; Tian, T.; Luo, X.; Mao, B.; Zhang, X.; Lei, H. Overexpression of the lncRNA FER1L4 inhibits paclitaxel tolerance of ovarian cancer cells via the regulation of the MAPK signaling pathway. *J. Cell. Biochem.* **2018**, *120*, 7581–7589. [CrossRef]
129. Théry, C. Cancer: Diagnosis by extracellular vesicles. *Nature* **2015**, *523*, 161–162. [CrossRef]
130. Ciardiello, C.; Cavallini, L.; Spinelli, C.; Yang, J.; Reis-Sobreiro, M.; de Candia, P.; Minciacchi, V.R.; Di Vizio, D. Focus on Extracellular Vesicles: New Frontiers of Cell-to-Cell Communication in Cancer. *Int. J. Mol. Sci.* **2016**, *17*, 175. [CrossRef]
131. Hanahan, D.; Weinberg, R.A. Hallmarks of cancer: The next generation. *Cell* **2011**, *144*, 646–674. [CrossRef]
132. Anderson, R.G.; Ghiraldeli, L.P.; Pardee, T.S. Mitochondria in cancer metabolism, an organelle whose time has come? *Biochim. Biophys. Acta Rev. Cancer* **2018**, *1870*, 96–102. [CrossRef] [PubMed]
133. Zhang, T.; Jingjie, L.; He, Y.; Yang, F.; Hao, Y.; Jin, W.; Wu, J.; Sun, Z.; Li, Y.; Chen, Y.; et al. A small molecule targeting myoferlin exerts promising anti-tumor effects on breast cancer. *Nat. Commun.* **2018**, *9*, 3726. [CrossRef] [PubMed]
134. Li, Y.; He, Y.; Shao, T.; Pei, H.; Guo, W.; Mi, D.; Krimm, I.; Zhang, Y.; Wang, P.; Wang, X.; et al. Modification and Biological Evaluation of a Series of 1,5-Diaryl-1,2,4-triazole Compounds as Novel Agents against Pancreatic Cancer Metastasis through Targeting Myoferlin. *J. Med. Chem.* **2019**, *62*, 4949–4966. [CrossRef] [PubMed]
135. Sondergaard, P.C.; Griffin, D.A.; Pozsgai, E.R.; Johnson, R.W.; Grose, W.E.; Heller, K.N.; Shontz, K.M.; Montgomery, C.L.; Liu, J.; Clark, K.R.; et al. AAV.Dysferlin Overlap Vectors Restore Function in Dysferlinopathy Animal Models. *Ann. Clin. Transl. Neurol.* **2015**, *2*, 256–270. [CrossRef] [PubMed]
136. Escobar, H.; Schöwel, V.; Spuler, S.; Marg, A.; Izsvák, Z. Full-length Dysferlin Transfer by the Hyperactive Sleeping Beauty Transposase Restores Dysferlin-deficient Muscle. *Mol. Ther. Nucleic Acids* **2016**, *5*, e277. [CrossRef] [PubMed]
137. Potter, R.A.; Griffin, D.A.; Sondergaard, P.C.; Johnson, R.W.; Pozsgai, E.R.; Heller, K.N.; Peterson, E.L.; Lehtimäki, K.K.; Windish, H.P.; Mittal, P.J.; et al. Systemic Delivery of Dysferlin Overlap Vectors Provides Long-Term Gene Expression and Functional Improvement for Dysferlinopathy. *Hum. Gene Ther.* **2017**. hum.2017.062. [CrossRef]
138. Llanga, T.; Nagy, N.; Conatser, L.; Dial, C.; Sutton, R.B.; Hirsch, M.L. Structure-Based Designed Nano-Dysferlin Significantly Improves Dysferlinopathy in BLA/J Mice. *Mol. Ther.* **2017**, *25*, 2150–2162. [CrossRef]
139. Lee, J.H.; Kim, Y.; Yoon, Y.-E.; Kim, Y.-J.; Oh, S.-G.; Jang, J.-H.; Kim, E. Development of efficient adeno-associated virus (AAV)-mediated gene delivery system with a phytoactive material for targeting human melanoma cells. *New Biotechnol.* **2017**, *37*, 194–199. [CrossRef]
140. Chow, R.D.; Guzman, C.D.; Wang, G.; Schmidt, F.; Youngblood, M.W.; Ye, L.; Errami, Y.; Dong, M.B.; Martinez, M.A.; Zhang, S.; et al. AAV-mediated direct in vivo CRISPR screen identifies functional suppressors in glioblastoma. *Nat. Neurosci.* **2017**, *20*, 1329–1341. [CrossRef]
141. Hodge, R.; Narayanavari, S.A.; Izsvák, Z.; Ivics, Z. Wide Awake and Ready to Move: 20 Years of Non-Viral Therapeutic Genome Engineering with the Sleeping Beauty Transposon System. *Hum. Gene Ther.* **2017**, *28*, 842–855. [CrossRef]